Crystallization, Separation, Extraction, and Quantification on a Microfluidic Platform

A Thesis Submitted in

Partial Fulfilments of the Requirement for the Degree of

DOCTOR OF PHILOSOPHY

by

Sunil Kumar Singh

(Roll No. 156107038)

Department of Chemical Engineering

Indian Institute of Technology Guwahati

Guwahati - 781039, Assam, India

June 2022

Crystallization, Separation, Extraction, and Quantification on a Microfluidic Platform

A Thesis Submitted in

Partial Fulfilments of the Requirement for the Degree of

DOCTOR OF PHILOSOPHY

by

Sunil Kumar Singh

(Roll No. 156107038)

Department of Chemical Engineering

Indian Institute of Technology Guwahati

Guwahati - 781039, Assam, India

June 2022

Dedicated

To

My Loving Family and Friends

Department of Chemical Engineering
Indian Institute of Technology Guwahati
Guwahati, Assam 781039

STATEMENT

I hereby declare that the content embodied in this thesis entitled **"Crystallization, Separation, Extraction, and Quantification on a Microfluidic Platform"** is the result of investigation carried out by me at the Department of Chemical Engineering, Indian Institute of Technology Guwahati, India, under the guidance of Dr. Partho Sarathi Gooh Pattader. In keeping with the standar practice of reporting scientific observations, due acknowledgements have been made wherever the work described is based on the findings of other investigators.

Guwahati
June, 2022

Sunil Kumar Singh

Department of Chemical Engineering
Indian Institute of Technology Guwahati
Guwahati, Assam 781039

CERTIFICATE

It is certified that the work described in this thesis entitled **"Crystallization, Separation, Extraction, and Quantification on a Microfluidic Platform"**, done by **Mr. Sunil Kumar Singh** (Roll No. 156107038) for the award of degree of Doctor of Philosophy is an authentic record of the results obtained from the research work carried out under my supervision in the Department of Chemical Engineering, Indian Institute of Technology Guwahati, India, and this work has not been submitted elsewhere for the award of any other degree or diploma.

This thesis in my opinion, has reached the standard fulfilling the requirements for the award of degree of Doctor of Philosophy in accordance with the regulations of the institute.

Guwahati
June, 2022

(Dr. Partho Sarathi Gooh Pattader)
Associate Professor
Department of Chemical Engineering
Indian Institute of Technology Guwahati
Guwahati, Assam - 781039, India

ACKNOWLEDGEMENTS

This thesis becomes a reality with the kind support and help of many individuals. It is a genuine pleasure to express my deep sense of thanks and gratitude to them who helped me in the completion of the thesis.

Foremost, I would like to express my sincere thanks to my thesis supervisor ***Dr. Partho Sarathi Gooh Pattader*** *for the continuous support in the various stages of my research journey. He provided me an excellent atmosphere to work with freedom of thinking and execution which grew my interest towards the topic. Also, his positive attitude and encouragement helped me to perform and complete the research objectives. His support is doing the experiments, analysis of data and preparing the manuscripts are invaluable. I am fortunate enough to complete my thesis under his supervision. It has really been a notable working experience with him.*

I would like to extend my sincere gratitude to my doctoral committee chairman ***Prof. Ashok Kumar Dasmahapatra,*** *Department of Chemical Engineering, for his valuable suggestions, evaluation and proper direction during my annual progress seminars. I shall always be obliged to other doctoral committee members,* ***Prof. Tapas Kumar Mandal,*** *Department of Chemical Engineering and* ***Prof. Lalmohan Kundu,*** *Department of Chemistry, for their valuable suggestions, time and efforts.*

I am deeply indebted to the ***thesis examiners*** *for their valuable suggestions to improve the quality of the thesis.*

I would like to acknowledge all the centers and Departments for providing me various instrument facilities required for characterization during the research work carried out at IIT Guwahati specifically, Analytical Lab Facility (Department of Chemical Engineering), Centre for Nanotechnology, Centre for the Environment, Central Instrument Facility (CIF), Department of Bioscience & Bioengineering, and Department of Chemistry for Polarimeter analysis.

I am also grateful to all the staff and faculty members of the Department of Chemical Engineering for helping and providing me the necessary facilities.

*I would like to thank all my **seniors** (Dr. Pritam Roy, Dr. Nilanjan Mandal, Dr. Shirsendu Mitra, Dr. Ankur Pandey), **colleagues** (Kaniska Murmu, Prerona Gogoi, and Aniruddhha Deb), **friends** (Dr. Awadh Kishor Kumar, Shivam Tiwari, Dr. Rupam Sinha, Dr. Nirmal Roy, Nabendu Paul, and Vanarse Vinod Babasaheb) and other well-wisher who helped me to complete my research.*

*My final words go to my family whom I want to thank for showering their love, care, sacrifices and encouragement. I am greatly indebted to my **Mother** whose support made it possible for me to come so far.*

Sunil Kumar Singh

Abstract

The primary focus of the thesis is to explore, design and develop a microfluidic platform for the efficient resolution of enantiomers, surfactant separation, dye extraction, and Hemoglobin quantification. A continuous or semi-continuous process of chiral separation with simultaneous reaction and crystallization, in a microfluidic platform is still challenging but utmost desired for industrial applications especially in pharmaceutical industries. To address this issue, a micro continuous process is developed for chiral separation of racemic molecules exploiting a "classical" method of diastereomer formation and subsequent crystallization. A flexible μ-reactor and a μ-crystallizer are fabricated for the continuous production of diastereomer salt crystals from racemic α-phenylethylamine (I) where optically active L-(+)-tartaric acid (II) is used as a resolving agent. The crystallized S-(-)-I.L-(+)-II diastereomeric salt obtained from the micro-continuous process is purer or at least of similar quality to that obtained from a batch process. The process produces pure crystals at about ~ 33 times faster rate compared to the batch process with identical feed concentrations. Another major problem that is commonly seen nowadays is that most of the industrial effluents discharged into the water bodies contain cationic, anionic, non-ionic, and amphoteric surfactants in different concentrations. These surfactants are not only dangerous to aquatic life but also affect human beings directly or indirectly. To overcome this problem, a microfluidic platform was developed to separate both anionic and cationic surfactant simultaneously from its mixture under the influence of ultra-low electric voltage. For this, a PDMS Y-shape microchannel was fabricated by the use of a high-end 3D printer and then thin copper sheet electrodes were placed across the channel. A constant DC voltage (~ 1.2 V, lower than electrolysis point of water) across the microchannel electrodes was applied using a DC power source. It was found that separation efficiency solely depends on the residence time of the

fluid inside the microchannel. It turns out that, at lower feed flow rate i.e. high residence time favored a higher degree of separation and vice-versa. Moreover, these days various innovative technologies for refining industrial wastewater are adopted to meet the lower toxicity level of pollutants and to satisfy the treatment standards. In this regard, the present study focuses on the component transfer from one liquid phase to another liquid phase, commonly known as the extraction process, in which both the liquids are flowing through a microchannel in the presence of an applied external electric field. We have explored interfacial instability in the presence of an external electric field inside the microchannel for the extraction of methylene blue dye from the aqueous phase using N-amyl alcohol. It was observed that the interfacial mass transfer process occurs through local instability, and hence extraction occurred. The relative strength of mass transfer rate for different cases, such as flow rate, numbers of electrodes, intensity of electric field, have also been reported in detail. Decreasing the intensity of pollution is very important to curb the gradual rise in health issues among the population. Moreover, due to the lack of hospitals and testing labs, dealing with deadly diseases has become a major issue. For instance, Hemoglobin (Hb) level in the blood is one of the vital components associated with causing various unhealthy conditions. In this regard, we attempt to develop a simple, low-cost, easy to use point of care (POC) device based on the spectrophotometric principle for the quantification of Hemoglobin (Hb) on a microfluidic platform. The optical sensitivities of carbon quantum dots (CDs) are found to be highly responsive, while there is a selective reaction between Hb and a reduced form of Methylene Blue (MB_{red}). The interaction of Hb, MB_{red}, and CDs is delineated using UV-Visible (UV-Vis) spectroscopy. The specific interactions of Methylene Blue (MB) with Hb in the presence of CDs show a unique characteristic optical feature, and the same is exploited for the quantitative estimation of Hb. These responses are exploited to quantify Hb

concentration with a limit of detection (LOD) as low as ~ 2 g dL^{-1} in a developed POC device, and the results are validated with the clinical data obtained from a local hospital with reasonably good agreement. In this way, this work encourages us to envision the utilization of microfluidic platform for different applications.

CONTENTS		Page no.
Acknowledgments		*i*
Abstract		*iii*
Contents		*v*
List of Figures		*ix*
List of Tables		*xii*
CHAPTER 1	**Microfluidic Platform Overview, Literature Review, Research Objectives, and Layout of the Thesis**	**1 – 50**
1.1 Introduction and overview		1
1.2 Literature review		2
1.2.1	Chiral Resolution of Racemic Amines in µ-Reactor-Crystallizer	5
1.2.2	Separation of Anionic and Cationic Surfactant in a Microchannel Using Ultra-Low Electric field	6
1.2.3	Liquid-Liquid Efficient Micro Extraction of Dye in a Microfluidic Platform by Creating Electric Field Induced Instability at the Interface of Fluids	6
1.2.4	Carbon dots and Methylene Blue Facilitated Photometric Quantification of Hemoglobin	7
1.3 Objectives of the work		8
1.4 Outline of the thesis		12
References		*38*
CHAPTER 2	**Chiral Resolution of Racemic Amines in µ-Reactor-Crystallizer**	**51 – 64**
2.1 Introduction		51
2.2. Experimental section		52

2.2.1 Materials 54
2.2.2 Apparatus 54
2.2.3 Methods 55
2.2.3.1 Solution preparation 56
2.2.3.2 Batch process 58
2.2.3.3 μ-mixture reactor and μ-crystallizer fabrication 59
2.3 Results and discussion 62
2.3.1 Resolution in μ-reactor-crystallizer 63
2.3.1.1 Rate of formation of prism-shaped crystal 63
2.3.1.2 Image analysis 63
2.3.1.3 Growth rate calculation for the crystals in the micro-continuous process 63
2.3.2 Circular dichroism (CD) spectroscopy 64
2.3.3 UV-Visible spectroscopy 64
2.3.4 Differential scanning calorimetry (DSC) 65
2.3.5 Attenuated total reflectance Fourier transform infrared (ATR-FTIR) spectroscopy 66
2.3.6 Raman spectroscopy 66
2.3.7 X-ray diffraction (XRD) 65
2.3.8 FETEM analysis 55
2.3.9 Energy dispersive X-ray (EDX) analysis 54
2.3.10 ^{1}H NMR analysis and sample calculation of salt crystal 55
2.3.10.1 The calculation for Mole fraction of batch process salt crystal 56
2.3.10.2 Sample calculation for Mole fraction of μ-continuous process salt crystal 56
2.3.11 DSC and XRD of needle-shaped crystals and R-(+)-I.L-(+)-II diastereomeric salt 14
2.3.12 Recovery of the amine 55
2.3.12.1 Calculation of percentage yield and enantiomeric excess 63
2.4 Conclusions 63

References *64*

CHAPTER 3 **Separation of Anionic and Cationic Surfactant in a Microchannel Using Ultra-Low Electric Voltage** **63 - 83**

3.1 Introduction 65
3.2 Experimental section 66
3.2.1 Materials 66
3.2.2 Apparatus 65
3.2.3 Methods 66
3.2.3.1 Solution preparation 74
3.2.3.2 Fabrication of electrode embedded microchannel 75
3.3 Results and discussion 77
3.3.1 Separation of SDS and CTAB from its catanionic mixture in a microchannel 66
3.3.2 Image analysis 66
3.3.3 UV-Vis Spectra Analysis 66
3.3.4 Langmuir–Blodgett (LB) Characteristics of Langmuir Monolayer of Pure Surfactants and Their Mixtures and its Surface Pressure-Area (π-A) Isotherm Measurements 66
3.3.5 Raman Spectroscopy Analysis 66
3.3.6 FT-IR Analysis 66
3.3.7 Measurement of Zeta Potential 66
3.3.8 FETEM analysis 66
3.3.9 HPLC Analysis 66
3.4 Conclusions 79

References *82*

CHAPTER 4 **Liquid-Liquid Efficient Micro Extraction of Dye in a Microfluidic Platform by Creating Electric Field Induced Instability at the Interface of Fluids** **85– 100**

4.1 Introduction 85
4.2. Experimental section 86
4.2.1 Materials 66
4.2.2 Apparatus 66
4.2.3 Methods 66
4.2.3.1 μ-mixture extractor fabrication 74
4.2.3.2 Fabrication of electrodes on the ITO coated glass substrate 33
4.3 Experimental section 86
4.3.1 Liquid-liquid extraction of methylene blue in a microchannel using electric field 66
4.3.2 Effect of various intensity of interfacial electric field and numbers of electrodes on dye extraction 45
4.3.3 Raman spectroscopy 66
4.3.4 Image analysis 33
4.3.5 FETEM analysis 66
4.3.6 Energy dispersive X-ray (EDX) analysis 88
4.4 Conclusions 96
References 98

CHAPTER 5 Carbon Dots and Methylene Blue Facilitated Photometric Quantification of Hemoglobin 101 – 122

5.1 Introduction 101
5.2 Experimental section 102
5.2.1 Materials 66
5.2.2 Apparatus 66
5.2.3 Methods 22
5.2.3.1 Synthesis of Carbon Dots (CDs) 74
5.2.3.2 Preparation of reduced form of Methylene Blue (MB_{red}) 74
5.2.3.3 Preparation of complex reaction matrix with CDs/Nafion/MB_{red}/Hb 55

5.2.3.4 Solution preparation of KI_3 and $Fe(NO_3)_3$ 22
5.3 Characterization of CDs 167
5.3.1 Photoluminescence and UV-Vis Spectrophotometric analysis of CDs 66
5.3.2 FETEM analysis of CDs 66
5.3.3 Energy dispersive X-ray (EDX) analysis 66
5.4 Results and discussion 167
5.4.1 UV-Vis spectroscopic analysis 66
5.4.2 FT-IR analysis 66
5.4.3 Zeta potential measurement 66
5.4.4 Reaction mechanism of MB_{red} with Hb 66
5.4.5 Fabrication of the device 66
5.4.6 LED selection/optimization of wavelength 66
5.4.7 Interference study 66
5.4.8 Quantification of Hb and calibration curve 66
5.4.9 Quantification of Hb on a microfluidic platform 66
5.4.10 Storage conditions, stability test, and reproducibility assay 66
5.4.11 Limit of detection (LOD) calculation of the optical device 66
5.4.12 Comparison of methods adopted for the quantification of Hb 66
5.5 Conclusions 167
References *122*

CHAPTER 6 Overall Conclusions and Recommendations for Future Work **125 – 126**

6.1 Major Conclusions 125
6.2 Recommendations for Future Research Work 126

Research Output 129

LIST OF FIGURES

	Title	Page no.
Figure 2.1	Schematic representation of the experimental setup for the separation of S-(-)-α-phenylethylamine from its racemic mixture in a continuous manner at a microfluidic platform. An optical image of the serpentine microchannel (right) and the micrograph of the salt crystals inside a μ-crystallizer is shown in the top right.	2
Figure 2.2	Shows the reaction mechanism of L-(+)-tartaric acid with racemic α-phenylethylamine and formed two diastereomers salts S-(-)-I.L-(+)-II (less soluble) and R-(+)-I.L-(+)-II (more soluble).	3
Figure 2.3	Optical micrographs (10X magnification) of diastereomer salt crystals in the μ-crystallizer at different flow rates ranging from 5-30 μL/min. The image shows the formation of the crystals for the feed concentration of 0.92 mM racemic α-phenylethylamine and 0.92 mM L-(+)-tartaric acid at different time duration (10-30 min). (i_1-i_6), (j_1-j_6) and (k_1-k_6) represent the growth of the crystals at τ = 10 min, 20 min, and 30 min, respectively. All the images were recorded at a position, l ~ 22 cm of the μ-crystallizer. The scale bar for all the figures is 200 μm.	5
Figure 2.4	Optical micrographs (10X magnification) of diastereomer salt crystals in the μ-crystallizer at different flow rates ranging from 5-30 μL/min. The image shows the formation of crystals in the μ-crystallizer for the feed concentration of 0.61 mM racemic α-phenylethylamine and 0.61 mM L-(+)-tartaric acid at different time duration (20-60 min). At τ = 20 min, image (i_1-i_6) shows the growth of crystals. At τ = 40 min, image (j_1-j_6) shows the growth of crystals. At τ = 60 min, image (k_1-k_6) shows the growth of crystals. All the images were recorded at a position, l ~ 22 cm of the μ-crystallizer. The scale bar for all the figures is 200 μm.	9
Figure 2.5	Optical micrographs (10X magnification) of diastereomer salt crystals in the μ-crystallizer at different flow rates ranging from 5-30 μL/min. The image shows the	11

	formation of crystals in the μ-crystallizer for the feed concentration of 0.31 mM racemic α-phenylethylamine and 0.31 mM L-(+)-tartaric acid at different duration (30-130 min). (i_1-i_6), (j_1-j_6) and (k_1-k_6) represent the growth of the crystals at τ = 30 min, 80 min, and 130 min, respectively. All the images were recorded at a position, l ~ 22 cm of the μ-crystallizer. The scale bar for all the figures is 200 μm.	
Figure 2.6	A plausible mechanism of the formation of relatively pure S-(-)-I.L-(+)-II salt formation in the micro-continuous process.	11
Figure 2.7	Dynamics of both needle and prism type of diastereomer salt in a μ-continuous crystallizer. **(a)** Different stages of the growth-evolution of the prism-shaped diastereomer salt with time. **(b)** Represents the crystal shape-map of the diastereomer salt (needle, mixed, and prism) for different feed concentrations and flow rates. **(c)** The development of salt nucleation reveals three distinct phases: (I) initial slow nucleation stage, (II) rapid growth, and (III) final stages characterized by different growth rates measured.	14
Figure 2.8	The graphs show the growth rate (dA_c/dt) of salt crystals with time (t) and its linear fitted line for different concentrations of feed. **(a)** Different stages of the growth-evolution of the prism-shaped diastereomer salt with time. **(b)** 0.92 mM **(c)** 0.61 mM **(d)** 0.31 mM.	21
Figure 2.9	(Colour line) CD spectra of chemical mixture of R-(+)-I and L-(+)-II (orange) **(a)**, chemical mixture of S-(-)-I and L-(+)-II chemical (black) **(b)**, chemical mixture of S-(-)-I and D-(-)-II chemical (cyan) **(c)**, chemical mixture of R-(+)-I and D-(-)-II chemical (blue) **(d)** before crystallization. CD spectra of methanol solution of S-(-)-I.L-(+)-II diastereomers salt crystals obtained from batch process (custom green) **(e)** and μ-process (custom pink) **(f)**.	28
Figure 2.10	(Colour line) CD spectra of pure chemicals, L-(+)-II (black) **(a)**, D-(-)-II (red) **(b)**, R-(+)-I (blue) **(c)**, S-(-)-I (pink) **(d)**, and racemic α-phenylethylamine (green) **(e)**.	53
Figure 2.11	Characterization of diastereomer salt crystals synthesized by batch process (green) and μ-continuous process (custom pink): **(a)** UV-Vis spectroscopy. **(b)** DSC.	55

Figure 2.12	Show **(a)** UV-Vis plot of needle-shape (S-(-)-I.L-(+)-II) diastereomer salt crystal. **(b)** UV-Vis plot of R-(+)-I.L-(+)-II diastereomer salt. **(c)** UV-Vis plot of needle-shape (S-(-)-I.L-(+)-II) diastereomer salt crystal and (R-(+)-I.L-(+)-II) diastereomer salt.	56
Figure 2.13	Characterization of diastereomer salt crystals synthesized by batch process (green) and µ-continuous process (custom pink): **(a)** and **(b)** ATR-FTIR spectroscopy. **(c)** and **(d)** Raman spectroscopy.	57
Figure 2.14	Show the XRD plots of synthesized diastereomer salt crystals: **(a)** batch process. **(b)** µ-continuous process. The W-H plot **(c)** and **(d)** show $\frac{\beta cos\theta}{\lambda}$ versus $\frac{sin\theta}{\lambda}$. **(c)** compares the W-H plots for crystals obtained from the batch and µ-continuous process with similar crystallite sizes. The W-H plot for two additional crystallite sizes for the µ-continuous process is shown in **(d)**.	58
Figure 2.15	Shows the images of synthesized diastereomer salt crystals by the µ-continuous process. **(a)** FETEM image of the diastereomer salt **(b)** Magnified image of the salt crystals with HRTEM image at the inset showing the lattice fringes of ~ 0.21 nm. **(c)** Selected area electron diffraction (SAED) pattern of the diastereomer salt crystals. **(d)** EDX spectrum of the salt crystals, the inset image depicts the scanning area for EDX analysis. Elemental mapping of C **(e)**, N **(f)**, and O **(g)** of a selected area on the diastereomer salt crystals are shown.	60
Figure 2.16	^{1}H NMR of diastereomer salt crystal. **(a)** Batch process. **(b)** µ-continuous process.	61
Figure 2.17	Show **(a)** DSC plot of needle-shape (S-(-)-I.L-(+)-II) diastereomer salt crystal. **(b)** XRD plot of needle-shape (S-(-)-I.L-(+)-II) diastereomer salt crystal. **(c)** DSC plot of needle-shape (S-(-)-I.L-(+)-II) diastereomer salt crystal and (R-(+)-I.L-(+)-II) diastereomer salt. **(d)** XRD plot of needle-shape (S-(-)-I.L-(+)-II) diastereomer salt crystal and (R-(+)-I.L-(+)-II) diastereomer salt.	63
Figure 2.18	**(a)** Optical rotation of chiral α-phenylethylamines mixed at different %. **(b)** Optical image of the test tube having recovered amine (organic phase) from the diastereomeric crystals.	69
Figure 3.1	Shows the optical image of Y-shaped electrode embedded	70

microchannel.
Figure 3.2 Schematic representation of the experimental setup for the separation of anionic (SDS) and cationic (CTAB) surfactants in a microfluidic platform using ultra low DC electric voltage mixture in a continuous manner. 71
Figure 3.3 Shows the images of glass vials containing **(a)** Aqueous solution of pure SDS, CTAB, and catanionic surfactant. **(b)** Outlet streams at different flow rates. 71
Figure 3.4 (Colour online) UV-Vis spectra of SDS, CTAB, catanionic mixture (SDS/CTAB = 50/50), and outlet streams of various flow rates. 75
Figure 3.5 (Colour online) **(a)** Pressure – area (π–A) isotherm of the SDS, CTAB, catanionic mixture surfactant with different composition. **(b)** Pressure – area (π–A) isotherm of the outlet streams of various flow rates. 75
Figure 3.6 (Colour online) **(a)** Raman spectra of the SDS, CTAB, catanionic mixture (SDS/CTAB = 50/50) surfactant, and outlet - 1 stream of various flow rates. **(b)** Raman spectra of the SDS, CTAB, catanionic mixture (SDS/CTAB = 50/50) surfactant, and outlet - 2 stream of various flow rates. 76
Figure 3.7 (Colour online) shows the FTIR spectra of the SDS (blue curve), CTAB (light green curve), catanionic mixture (SDS/CTAB = 50/50) surfactant (pink curve), outlet – 1 (black curve), outlet – 2 (orange curve). 77
Figure 3.8 Shows the images of the outlet strams of the flow rate 20 μL min^{-1}. **(a)** Elemental mapping spectrum of the outlet –1. **(b)** FETEM image of the outlet –1. **(c)** Elemental mapping spectrum of the outlet –2. **(d)** FETEM image of the outlet –2. 78
Figure 3.9 Plot **(a)** HPLC spectra of SDS. Plot **(b)** HPLC spectra of CTAB. 79
Figure 3.10 Plot **(a)** show the calibration curve for SDS. Plot **(b)** show the calibration curve for CTAB. Plot **(c)** depicts the effect of flow rate on % separation. 78
Figure 4.1 Shows the optical image of serpentine-shaped microchannel. 90
Figure 4.2 Schematic representation of the experimental setup for the extraction of methylene blue from aqueous phase in a continuous manner at a microfluidic platform. 91

Figure 4.3 (Colour online) Plot **(a)** Aqueous phase UV-Vis spectra of methylene blue of feed (black), 0 V (red), 50 V (blue), 100 V (pink), 150 V (green), 200 V (light yellow), 250 V (purple), and 300 V (cyan) for lowest (E1) number of electrodes. **(b)** Aqueous phase UV-Vis spectra of 0 V (red), 50 V (blue), 100 V (pink), 150 V (green), 200 V (light yellow), 250 V (purple), and 300 V (cyan) for E2 number of electrodes. **(c)** Aqueous phase UV-Vis spectra of 0 V (red), 50 V (blue), 100 V (pink), 150 V (green), 200 V (light yellow), 250 V (purple), and 300 V (cyan) for E3 number of electrodes. **(d)** Aqueous phase UV-Vis spectra of 0 V (red), 50 V (blue), 100 V (pink), 150 V (green), 200 V (light yellow), 250 V (purple), and 300 V (cyan) for E4 number of electrodes. **(e)** Aqueous phase UV-Vis spectra of 0 V (red), 50 V (blue), 100 V (pink), 150 V (green), 200 V (light yellow), 250 V (purple), and 300 V (cyan) for highest (E2) number of electrodes. **(f)** Aqueous phase Raman spectra of 50 V (blue), 100 V (pink), 150 V (green), 200 V (light yellow), 250 V (purple), and 300 V (cyan) for highest (E5) number of electrodes. 95

Figure 4.4 (Colour online) Plot **(a)** Organic phase UV-Vis spectra of methylene blue of 0 V (red), 50 V (blue), 100 V (pink), 150 V (green), 200 V (light yellow), 250 V (purple), and 300 V (cyan) for lowest (E1) number of electrodes. **(b)** Organic phase UV-Vis spectra of methylene blue of 0 V (red), 50 V (blue), 100 V (pink), 150 V (green), 200 V (light yellow), 250 V (purple), and 300 V (cyan) for E2 number of electrodes. **(c)** Organic phase UV-Vis spectra of methylene blue of 0 V (red), 50 V (blue), 100 V (pink), 150 V (green), 200 V (light yellow), 250 V (purple), and 300 V (cyan) for E3 number of electrodes. **(d)** Organic phase UV-Vis spectra of methylene blue of 0 V (red), 50 V (blue), 100 V (pink), 150 V (green), 200 V (light yellow), 250 V (purple), and 300 V (cyan) for E4 number of electrodes. **(e)** Organic phase UV-Vis spectra of methylene blue of 0 V (red), 50 V (blue), 100 V (pink), 150 V (green), 200 V (light yellow), 250 V (purple), and 300 V (cyan) for highest (E5) number of electrodes.

Figure 4.5 (Colour online) Plot **(a)** show the calibration curve for the methylene blue at different concentration (0 mg L^{-1} to 10 mg L^{-1}) as a function of absorbance. Plot **(b)** depicts the effect of various intensity of electric field on % extraction keeping constant numbers of electrodes. Plot **(c)** represents the effect of various numbers of electrodes on % extraction keeping constant electric field.

Figure 4.6 Shows the images of glass vials containing aqueous phase samples of feed, 0 V, 50 V, 100 V, 150 V, 200 V, 250 V, and 300 V for highest (E5) number of electrodes.

Figure 4.7 Shows the images of aqueous and organic phase **(a)** FETEM image of the aqueous phase. **(b)** Magnified image of aqueous phase with HRTEM image at the inset showing the lattice fringes of ~ 0.20 nm. **(c)** Selected area electron diffraction (SAED) pattern of the aqueous phase. **(d)** FETEM image of the organic phase. **(e)** Magnified image of organic phase with HRTEM image at the inset showing the lattice fringes of ~ 0.18 nm. **(f)** Selected area electron diffraction (SAED) pattern of the organic phase.

Figure 4.8 Shows the images of the aqueous phase extraction in a continuous manner at a microfluidic platform. **(a)** EDX spectrum of the methylene blue, the inset image depicts the scanning area for EDX analysis. Elemental mapping of C **(b)**, N **(c)**, S **(g),** and Cl **(e)** of a selected area are shown.

Figure 4.9 Shows the images of the organic phase extraction in a continuous manner at a microfluidic platform. **(a)** EDX spectrum of the methylene blue, the inset image depicts the scanning area for EDX analysis. Elemental mapping of C **(b)**, N **(c)**, S **(g),** and Cl **(e)** of a selected area are shown.

Figure 5.1 (Colour online) **(a)** Schematic representation of the reaction for Hb detection and **(b)** spectrophotometric sensing mechanism. 104

Figure 5.2 (Colour online) Plot **(a)** shows the PL emission spectra of CDs at different monochromatic excitations. Plot **(b)** depicts the TRPL curve of CDs at an excitation wavelength of 375 nm. Plot **(c)** shows the UV-Vis absorption spectrum (red line) of the synthesized CDs. The blue line portrays the PL emission spectrum of the synthesized CDs in an aqueous solution after excitation with light having a wavelength of 360 nm. The green line 105

represents the PL excitation spectrum of the synthesized CDs in an aqueous solution. The inset optical images depict the aqueous solution of CDs under visible light which is in pale yellow (left) and blue when illuminated under a UV lamp (right) **(d)** FETEM image of the synthesized CDs of size ~ 4.2 ± 2 nm indicated by the dark circular spots. **(e)** Magnified image of CDs and in the inset HRTEM image of lattice fringes of the CDs with an equal interplanar spacing of ~ 0.22 nm. **(f)** Selected area electron diffraction (SAED) pattern of synthesized CDs. **(g)** EDX spectrum of the synthesized CDs, the inset image depicts the scanning area for EDX analysis. Elemental mapping of synthesized CDs is depicted in **(h)** C, **(i)** O, and **(j)** N.

Figure 5.3 **(a)** EDX spectrum of the complex matrix. **(b)** Scanning area for EDX analysis. Elemental mapping of complex matrix **(c)** C, **(d)** O, **(e)** S, **(f)** F, **(g)** N, **(h)** Cl. 106

Figure 5.4 **(a)** EDX spectrum of the complex matrix and Hb hybrid. **(b)** Scanning area for EDX analysis. Elemental mapping of complex matrix and Hb hybrid **(c)** C, **(d)** O, **(e)** N, **(f)** S, **(g)** F, **(h)** Cl, **(i)** Fe. 107

Figure 5.5 (Colour online) **(a)** UV-Vis spectra of CDs (magenta), MB_{ox} (blue), H_2A (green), MB_{red} (violet colored short dash dotted line), Hb (red), Nf (dark cyan), and complex reaction matrix with Hb (maroon). **(b)** UV-Vis spectra of reaction matrix with various concentrations of Hb: 2 g dL^{-1} (blue), 6 g dL^{-1} (custom blue), 10 g dL^{-1} (green), 14 g dL^{-1} (magenta), 18 g dL^{-1} (orange), and 20 g dL^{-1} (red). Inset of (b) shows magnified spectra in the range of 630 – 690 nm. 108

Figure 5.6. (Colour online) Plots **(a)** to **(e)** show FTIR spectra for pure CDs, Nf, Hb, MB_{ox}, MB_{red} samples, respectively. Plot **(f)** depicts FTIR spectra of CDs with Nf. Plot **(g)** represents FTIR spectra of Hb with Nf. Plot **(h)** shows the further change in peak on the addition of Hb to CDs and Nf solution. Plot **(i)** shows the FTIR spectra of the complex matrix solution containing CDs, Nf, Hb, and MB_{red}. 109

Figure 5.7 (Colour online) **(a)** Schematic representation of the electronic interactions of CDs, Nf, MB_{red}, and Hb 110

molecules. Plot **(b)** shows the zeta potential of Hb, CDs, Nf, MB_{red}, complex, and complex/Hb hybrid solution.

Figure 5.8 (Colour online) **(a)** Schematic of the device setup and **(b)** a developed prototype device for the Hb detection unit. (Colour online) Shows the sensitivity of the fabricated device. Plot **(c)** shows the response of the device for different types of LEDs, blue LED (blue square dots), white LED (black hollow square), red LED (red dots), yellow LED (magenta hollow circle dots), and green LED (green triangle dots). **(d)** shows the response of the Hb (red dots), $Fe(NO_3)_3$ (green square dots), $CuSO_4$ (purple triangles), and KI_3 (maroon square dots) in the complex matrix. **(e)** demonstrates the response of the device for Hb (4 g dL^{-1}) (red filled circle), 1 kb DNA Ladder (filled blue diamond), human blood plasma of person 1 (hollow violet circle), person 2 (hollow green triangle), person 3 (hollow orange square), person 4 (hollow purple hexagonal), and person 5 (hollow magenta inverted triangle) in the complex matrix. The inset of the figures shows the magnified image at the low normalized resistance value (Y-axis). 111

Figure 5.9 Plot **(a)** shows the response of UV-Vis for different concentration of Hb, normalized absorbance values of CDs peak (magenta triangle) and the normalized absorbance values of MB_{ox} (blue square dots). Plot **(b)** shows the response of the optical device of lab samples (green square dots) for a wide range of hemoglobin concentrations (4 g dL^{-1} to 18 g dL^{-1}), and clinical samples (red dots) for different concentration of Hb (5.2 to 15.7 g dL^{-1}). 111

Figure 5.10 (Colour online) **(a)** Calibration curve for the Hb concentration (4 g dL^{-1} to 18 g dL^{-1}) as a function of the normalized resistance. Plot **(b)** shows the comparison of the clinical reading (obtained from a local hospital) of Hb concentration from 17 patients with the readings obtained from the optical device developed in this work using the calibration curve **(a)**. Deviation from the diagonal blue line indicates the deviation between hospital readings and the device reading. **(c)** Depicts the stability of the complex reaction matrix: response of the device for a particular 162

concentration of Hb (9 g dL^{-1}) over the period of 8 weeks.
Figure 5.11 shows the Hb quantification on a microfluidic platform. 120

Figure 5.12 Plot shows the response of the optical device of lab samples (dark cyan square dots) for a wide range of hemoglobin concentrations (4 g dL^{-1} to 18 g dL^{-1}).

LIST OF TABLES

	Title	Page no.
Table 2.1	Diastereomeric crystal structure with concentration and flow rate in μ-crystallizer	5
Table 2.2	Mole fraction of individual components in the salt crystal	8
Table 3.1	Zeta potential of pure surfactants and samples	51
Table 5.1	Cost estimation of the fabricated device	71
Table 5.2	Comparison of detection methods from various published works	73

CHAPTER 1

Microfluidic Platform Overview, Literature Review, Research Objectives, and Layout of the Thesis

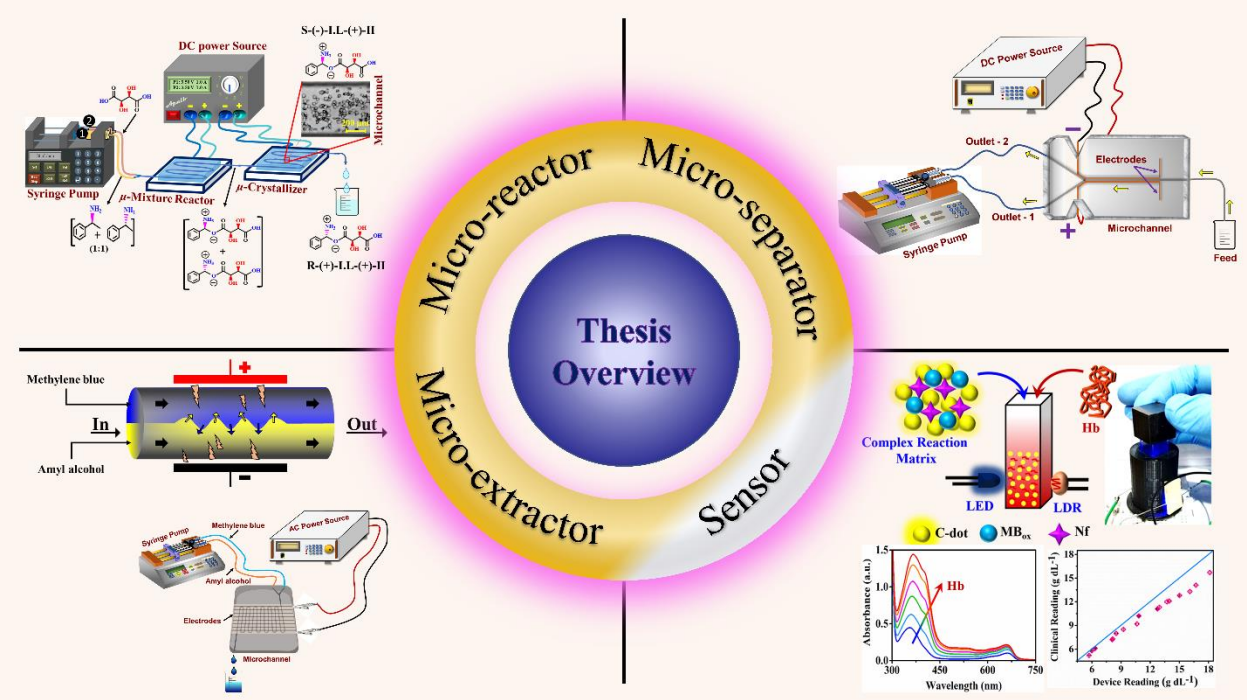

CHAPTER 1

Microfluidic Platform Overview, Literature Review, Research Objectives, and Layout of the Thesis

In this particular chapter, resolution of enantiomers, separation of surfactant, extraction of dye, and Hemoglobin detection methods have been discussed in brief. The microfluidic based technology has been highlighted based on its advantages, efficiency, and suitability for the particular application at an industrial scale. Finally, based on the knowledge gap and challenges, the research objectives have been defined and at the end layout of the thesis has been mentioned.

1.1 Introduction and overview

In the present thesis, we explore various microfluidic platforms for the crystallization, separation, extraction, and quantification of molecules in a microchannel. Micro-nano fluidics is a multidisciplinary field that includes engineering, physics, chemistry, biochemistry, and biotechnology, with practical applications in designing and developing systems. In the recent decades, microfluidic platform gains high attention due its wide variety of application such as reaction [1], cell sorting [2], synthesis of micro/nanomaterials [3,4], emulsification [5,6], energy harvesting [7,8], crystallization [9], separation [10], extraction [11], detection [12], micro-electro-mechanical devices (MEMS) [13], and many more. Although the manufacturing of these micro-nano fluidic structures is a complex process, the constant high-rising demand for miniaturization keeps pace with technological advancement and serves as the foundation for technological innovations. In particular, this field has picked the interest of scientists due to some distinct advantages over their macroscopic counterparts such as (i) availability of high surface to

volume ratio for enhanced momentum, heat and mass transfer, (ii) usage and ability to handle smaller volumes of any fluid, (iii) well controlled endothermic and exothermic reactions, (iv) high performance due to process intensification, (v) great control over the process parameters, and (vi) suitability to hazardous chemicals [14].

For the last few decades, pharmaceutical industries are looking for new process technologies to reduce the cost of drugs [15–17]. Thus, continuous or semi-continuous production, separation, or extraction processes are receiving significant attention as the end products have improved purity, yield, and efficiency [18,19]. Along with this, process intensification has become the central requirement which can be achieved on a microfluidic platform due to recent advancements in μ-mixture, μ-reactor, μ-crystallizer, and μ-extractor [20,21]. Performing micro-scale multi-step chemical synthesis and separation requires the development of reaction and separation techniques in microfluidic devices. Although microreactors have been developed for a wide range of chemical applications [1,22], further development in continuous flow chemical separators is needed for implementing continuous, multi-step microchemical synthesis and separation. Common separation processes, such as crystallization, liquid–liquid extraction are complicated as the phase separation process is performed continuously after mixing and contacting the phases. In addition, extrinsic fields such as electric, magnetic, and electromagnetic fields have increased their usefulness and applicability by enhancing turbulence, mixing, chemical synthesis, and reaction. The diffusive length and time scales commonly limit mass, momentum, and heat transmission inside extremely constrained microsystems, thus limiting their efficiency and applicability. On the flip side, compared to the traditional macroscale procedure, using a smaller volume of reagent has made the technology less expensive, safe, and waste-free. Modern microscale applications necessitate advancement in

rate-limiting diffusive transport for effective mixing, crystallization, extraction, detection, dissolution, reaction, separation, cooling, or heating. In this context, advancement in groovy or twisted channels, serpentine channels, spiral channels, Y-shaped channels, multiple fluid flow paths enhances the requirement for a particular application. Because of its superior conversion, yield, and efficiency, processes such as continuous flow synthesis inside the microreactor, continuous synthesis of crystals inside the micro-crystallizer, continuous flow liquid-liquid extraction inside the micro-extractor, and continuous flow separation inside the micro-separator have picked the interest of many industries. Furthermore, in modern human life, personal care practices have become an indispensable part to maintain a minimum quality of health. For this, there have been significant advancements in the area of design and development of the point-of-care testing (POCT) devices by implementing advanced technologies like bio-process reaction engineering, nanotechnology, micro or nanoelectronics, microfluidics, smart soft materials, data analytics, and connectivity [23–28]. In particular, micro and nanoscale objects such as the nanoparticles, nanofibers, nanodots, nanopores, and microfluidic devices have shown the immense potential to improve the efficiency of various highly selective detection techniques by enhancing the accuracy, sensitivity and response time [27,29–31], and resulting in immediate detection of diverse ailments. The guidelines as laid by World Health Organization (WHO) for developing efficient POCT devices are known as ASSURED,which stands for affordable, sensitive, specific, user-friendly, rapid/robust, equipment-free or minimal, and delivered at time of need [32,33]. Nowadays, it is evident that bigger things come as smaller packages in almost all routine and high-tech gadgets. For example, earlier health care diagnostic tests were conducted in labs, but now we have moved forward to tests being conducted on chips. Hence, the assembly of different microfluidic devices on a single chip creates avenues for ‘μTAS’ or ‘lab-

on-a-chip' for a host of biological and chemical assays. Therefore, microfluidic platform gains high attention in present day technological avenue.

1.2 Literature review

1.2.1 Chiral Resolution of Racemic Amines in μ-Reactor-Crystallizer

The focus of this chapter is on chiral resolution of molecules from its racemic mixture. Many biological molecules exist in different stereoisomeric conformations. These molecules usually contain the same atoms and groups with similar connectivity but have different orientations in space. If stereoisomers are mirror images of each other, it is called enantiomers. Enantiomers possess similar physical and chemical properties in an achiral environment. However, they differ only in the way they interact with other chiral molecules [34] or in a chiral environment, viz. they rotate plane-polarized light in opposite directions. However, the enantiomers being similar in terms of physical or chemical properties are difficult to separate from each other using conventional techniques. For this, extensive work has been reported on the resolution of enantiomers from its racemic mixture by different groups of scientist.

The "classical" enantiomer resolution method (Pasteurian resolution) was discovered in 1853 [35,36] which is still extensively used to prepare chirally pure compounds on an industrial scale. In this method, the mixture of enantiomers [(±)A] is converted into a pair of diastereomeric salts by reacting it with a pure chiral resolving agent [(+)B or (-)B], [37] e.g.,

$$(\pm)A + (+)B \longrightarrow (+)A(+)B + (-)A(+)B$$

The diastereomeric salts, thus formed via acid-base type reactions, have different physical properties. Hence, they can be separated by precipitating the least soluble diastereomeric salt out of the mixture with a proper choice of both the concentration and

temperature of the system. The variations of the Louis Pasteur resolution method were adopted by selecting the appropriate resolving agent and it was proved to be an effective technique for chiral resolution [38,39]. Along with this, other enzymatic or chemical approaches were also explored [40,41]. However, as the cost and time requirement for the resolution is very high, these techniques were not widely accepted for commercial applications. The most versatile and commonly accepted technique is chiral chromatography, which separates most of the racemates [42,43]. However, this technique requires costly chiral stationary phase column, high amount of solvents, and low mass throughput. This prompts the researchers to develop new technologies which include, liquid-liquid extraction [44,45], chiral membrane separation [46], dynamic resolution [47–49], preferential crystallization [50–53] diastereomeric resolution [54] and semi-batch or continuous crystallization by seeding method [55–57]. Most of these techniques follow complicated multi-step batch processes and generate low fractional recrystallization of pure enantiomeric form. Hence, for the last few decades, to adopt a continuous or semi-continuous mode of operation and to improve the yield, several industries are rapidly approaching microfluidic platforms for chemical and biological synthesis [28]. Microfluidics has its unique advantages, such as a large surface-to-volume ratio, highly stable laminar flow, diffusion-dominated mass transfer effect, the handling of small sample size, parallel operations, low reaction time, low operation cost, etc. [58–60]. Swift development in microfluidics is encouraged by the vision of integrating an entire chemical or biochemical laboratory onto a small single microchip called "lab-on-a-chip". Of late, the separation of chiral compounds on a microfluidic platform using different methods such as functionalizing the chromatographic column materials or microchannel wall [61–64], membrane [65,66], chip-based HPLC [67], magnetic separation

[68–70], etc. are also reported. However, these techniques are not attractive at the industrial scale because of the complicated process, high cost, low throughput, and low efficiency.

In view of the above discussion, a continuous or semi-continuous process of chiral separation with simultaneous reaction and crystallization in a microfluidic platform is still challenging but utmost desired for industrial applications. This work focuses on developing a robust but flexible, efficient but sensitive, and cost-effective technique for the production of optically pure chiral molecules on a microfluidic platform in a semi-continuous fashion. Specifically, we have chosen the resolution of chiral amines, α-phenylethylamine, from its racemic mixture using L-(+)-tartaric acid as a chiral resolving agent. Sequential µ-reactor and µ-crystallizer are employed for the resolution and the investigation is focused on the controlling parameters such as the concentrations and the flow rate of the reagents to ensure the purity of the enantiomer. We also provide a comparative study of the purity of the synthesized µ-crystals, obtained from the bulk batch process and the continuous microfluidics.

1.2.2 Separation of Anionic and Cationic Surfactant in a Microchannel Using Ultra-Low Electric Voltage

The focus of this chapter is on the separation of anionic and cationic surfactants in a microchannel using an ultra low electric voltage. Water pollution has become a global concern due to its deteriorating impact on both human health as well as aquatic life. There are numerous sources of water pollution where surfactants are considered major pollutants [71,72]. A huge amount of different types of surfactants (e.g., soaps and detergents) is released not only from laundries, washing and cleaning operations but also from various industries such as (sugar, petroleum, personal care products, food, fabric, and pulp and paper [73]. Surfactant-based products can have a negative impact on the surface water such as–decrease in oxygen transfer,

damage in water quality due to foaming, and reduction in the self-cleaning capacity of the river. Human health can be adversely affected by drinking water contaminated with these surfactants. A variety of diseases such as skin irritation, liver damage, stomach cramps, sore throat, and nausea can occur in a human. This can also lead to death in many severe cases. High concentrations of surfactants can also have toxic and harmful effects on all types of amphibian life. They can damage the outer mucus layers, which protect the fishes from bacteria and parasites. Surfactants can cause severe damage to their gills too [74]. If the surface tension of the water becomes low, fishes may consume toxic organic chemicals like phenol and pesticides. Since most surfactants reduce the surface tension of water, fishes are seen to easily consume these chemicals. Moreover, when such fish is consumed as food, humans can undergo liver and kidney damage.

The breeding capability of the amphibian organisms reduces due to surfactants and detergents used for industrial purposes and household products. The phosphate-rich surfactants initiate algal bloom in the freshwater which decrease oxygen in the waterways. The decomposition of the algae consumes oxygen present, which would otherwise have been utilized by the aquatic life [75]. Wastewater containing chemicals like phosphates and ammonia is a nuisance for humans as it generates large amount of foam in the lake and river. Such excessive foaming creates an unbearable stench causing suffocation to the nearby residents and passers-by. To meet stringent environmental regulations as directed by various governmental bodies, the surfactant concentration in the effluent streams must be reduced.

The physiochemical process that involves the extraction of surface-active molecules from a growing foam and separating them from the solution is known as foam fractionation. It is one of the most promising strategies used today for separating surfactants from wastewater [76–81].

Moreover, it is considered to be a well-explored topic presently applied to various industries, including biological protein and metabolite purification, mineral processing, and agriculture [82–85]. Hence, interest in foam fractionation has grown in the recent years, which brought about better knowledge of the process and also generated novel ideas for what may appear to be a well-established technique. Foam fractionation is considered a better alternative to the existing modern municipal wastewater treatment process due to its efficient capacity to remove refractory chemicals [86]. The inherent advantages of foam fractionation as a water treatment technique namely low capital cost, low energy requirement, environmental friendliness, and low operational expenses [87]. Recently, Burghoff [77] offered comprehensive study that focusses mainly on biotechnological applications of phytonutrient, metabolites, and protein enrichment. Jenkins [88] studied the applicability of an integrated system of foam fractionation with the industrial wastewater treatment plants where surface-active chemicals do not cause any hindrance in the microbial degradation process. A few scientists have demonstrated the possible application of foam fractionation in removal and concentrating of pollutants from a waste stream [89]. Boonyasuwat et al. [79] showed that complete removal of surfactant from water depends on several variables such as decreasing airflow rate, increasing foam height, and increasing the number of stages in a multi-stage foam fractionator. Tharapiwattananon et al. [90] investigated the effects of airflow rate, foam height, liquid height, surfactant concentration in the liquid feed and sparger porosity on the recovery of surfactant. They found that the rate of surfactant recovery can be increased and the enrichment ratio can be decreased by increasing the airflow ratio. Kumpabooth et al. [91] studied the effects of temperature and added salt on foam flow rate, enrichment ratio, foam wetness, and the rate of surfactant recovery. They found that an increase

in temperature generally had a positive impact on foam fractionation as a more concentrated foam liquid was recovered as the overhead.

Moreover, Rubin and Jorne [92] found that based on the relative distribution coefficient the foam fractionation technique can separate two different surfactants. The calculations were based on Langmuir isotherm which gave the conservative estimation of relative distribution coefficient at very low surfactant concentrations. Šonc and Grilc [78] developed a mathematical model to describe the changes occurring while varying the concentration of the surfactant and found the optimal conditions of many processes and material parameters on an actual industrial sample. A model was prepared where optimal parameters for the surfactant solutions were given as input for purification of actual wastewater samples containing surfactants from various industrial cleaning operations. Qu et al. [93] investigated the recovery of surfactants and metal ions accumulated in the permeate phase of micellar-enhanced ultrafiltration (MEUF) process and found that changes in the airflow rate have a substantial effect on the enrichment ratio during removal of SDS and Cd^{2+}. Srinet et al. [94] observed that the foam volume increased by increasing the rate of airflow. Higher separation efficiency and surfactant recovery are achievable at lower initial surfactant concentration. The Presence of salt reduces the surfactant recovery and separation efficiency. Tadakamalla and Marathe [95] optimized some important parameters such as the airflow rate, foam height, influent concentration, variation of the pH of the feed solution, and duration of operation using cationic surfactant, cetyl pyridinium chloride. They also found that a single surfactant can be recovered better than that of a mixture of cationic and nonionic surfactants using the foam fractionation process.

A range of conventional techniques are being employed for the treatment of wastewater such as biological, chemical, and combined chemical and biological. Numerous research have

looked at the aerobic degradation of surfactants [96–98] and several kinds of bacteria have been found to be capable of decomposing a surfactant [99]. Citrobacter braakii strains have been found to degrade a wide range of anionic surfactants [100]. Because of the intensive agitation and aeration required by the culture medium, high surfactant concentrations have been observed to cause substantial foaming problems in several reactors (both aerobic and anaerobic) [101,102]. As a result of this problem, biodegradation is not always the best option for surfactant treatment. Using a chemical pre-treatment before the wastewater enters the treatment facility is one technique for mitigating the concerns [100]. Chemical pre-treatment of biorecalcitrant chemicals is intended to transform them to products that can be biodegraded more easily via biological processes rather than to entirely mineralize them [103]. Fenton's reaction decomposes hydrogen peroxide (H_2O_2) into water and oxygen using a combination of H_2O_2 and ferrous irons. The initial concentration of ferrous ions and hydrogen peroxide are affect the type of surfactant being degraded [102,104]. In most cases, the procedure takes only 40 to 50 minutes to achieve the requisite surfactant elimination [104,105]. The distinctive foaming of surfactants in oxygenated water causes biological and combination treatment operations to be problematic [106]. Hence, purely chemical methods were discussed such as Coagulation-flocculation surfactant treatment was proposed by [107,108] found poor removal rates for anionic surfactants. They discovered that certain improvements, such as the addition of activated carbon or the removal of polyelectrolytes, improved the efficiency of the process. Activated carbon is a good adsorbent for adsorption of surfactants [109].

On the basis of the above discussion we could deduce that simultaneous continuous separation of cationic and anionic surfactant on a microfluidic platform is still challenging.

Hence, this work focuses on developing a technique for the efficient separation of surfactant molecules on a microfluidic platform.

1.2.3 Liquid-Liquid Efficient Micro Extraction of Dye in a Microfluidic Platform by Creating Electric Field Induced Instability at the Interface of Fluids

The aim of this chapter is to efficiently extract dye in a microfluidic platform by creating electric field-induced instability at the interface of fluids. The study of interfacial instability in the presence of external force fields such as surface tension gradient [110], electric field [111,112], magnetic field [113], viscosity imbalance, and density imbalance has been an important area of scientific research owing to its various applications in the field of heat and mass transfer, reaction kinetics, thermodynamics, and biological processes. A plethora of literature focuses on the interfacial instability phenomena [114–116], which are ubiquitous in many natural and artificial processes, such as capillary instability [117,118], Kelvin-Helmholtz instability [119], and Saffman-Taylor instability [120,121]. Interfacial instability can always be associated with enhanced transfer processes such as heat, mass, and momentum transfer with economic benefits in the fields of extraction, separation, absorption, desorption, cooling, and heating. Liquid-liquid extraction is an important unit operation where one component is extracted from a particular liquid phase onto another liquid phase. Macroscale batch extraction processes are routinely used in chemical industries [122], oil refineries [123], pharmaceutical industries [124,125], and food industries [126]. A few previous studies highlight the spontaneous interfacial mass transfer processes, where the component transfer is enhanced as a result of interfacial convection [127] induced by interfacial Marangoni instability [128].

In the microextraction process [129], a component, dissolved in a phase, is extracted by another immiscible phase in microfluidic channels or conduits. This process is associated with

high mass transfer rates owing to the larger specific surface area. Contactors with propeller agitators [130], packed bed columns [131], RTL extractors [132], etc. were in use for various chemical process industries to perform liquid-liquid extraction on a mass scale and in a batch fashion. Microscale extraction [133] has attracted attention recently because of its continuous throughput with high efficiency. Due to the low diffusion path lengths, microchannels are very effective in analyzing two-phase processes, which are limited by mass transfer. Microfluidic systems are characterized by a dimension which is essentially less than 1 mm. Microfluidics is also preferred in multiphase flow processes in industries such as pharmaceuticals and fine chemicals where the amount of the desired product is very less [134]. Sarkar *et al.* [135] and Zhao and Middelberg [136] reported flow morphologies in a serpentine glass and a PMMA microchannel, respectively. Both of their research revealed different flow patterns such as slug flow, slug and droplet flow, droplet flow, unstable annular flow, annular flow, annular dispersed flow, fully dispersed flow, etc. associated with the enhancement of mass transfer which found different industrial applications. In recent times, importance is being paid to the development of several micro extractors [11]. Inertial force, which is essential for enhanced transport, is very much important in the microfluidic scenario and is characterized by strong internal circulations induced by shear. This gives rise to convection in the individual slugs [137], which greatly enhances the extraction. Kashid *et al.* [132] reported the extraction process for the water acetone-toluene system in the flow regimes such as slug, slug-drop, deformed interface, parallel/annular, slug-dispersed, and dispersed flows. The mass transfer coefficient for these different kinds of flow patterns is individually calculated and is was found to be a function of channel cross section, flow rates, and surface area. Fries *et al.* [138] examined the extraction of vanillin from aqueous solution to an organic phase. Their results concluded that reduction of channel cross-

section enhances the mass transfer coefficient, which were one of the initial detailed preliminary reports on the extraction process in microfluidic channels. Vir *et al.* [139] provided a semi-analytical solution for the extraction process occurring in core-annular and stratified configurations. They showed a comparison between their model and available experimental literature. Malengier *et al.* [137] reported extraction efficiency for both cocurrent and countercurrent systems and concluded that the extraction efficiency of the countercurrent flow is higher than that of the cocurrent flow. Ghaini *et al.* [140] analyzed mass transfer to determine the effective interfacial area in slug flow using physical and chemical methods. Tamagawa and Muto [141] studied an extraction process where the cesium ion (Cs+) present in aqueous cesium nitrate solution was extracted by a solvent [di(2- ethylhexyl)phosphoric acid ester in cyclohexane]. They compared the results obtained from microchannel extraction with those of batch extraction processes. It was concluded that the slug flow shows high extraction efficiency, and it could be obtained at a low residence time. Naleini *et al.* [142] also performed a comparative study of the extraction process of oleuropein from ethyl acetate into the aqueous phase in a microchannel with a corresponding batch system. They reported that the extraction yield using a microchannel with a processing time of 0.13 min was 18% better than that in the batch process at 45 min. Nandagopal *et al.* [143] studied the extraction of phenol from dodecane into distilled water. They compared the slug flow based extraction performance with that of conventional extraction techniques such as batch extraction, microwave assisted extraction, and ultrasound assisted extraction. They observed 94.18% extraction in the slug flow regime at a residence time of 3 min.

This chapter studies a two-phase flow with the simultaneous extraction process, where a component is transferred from phase 1 to phase 2. It is well established that the convective mode

of transport processes is always higher than the diffusive mode of transport processes. The flow inside a microchannel is basically laminar in nature. Hence, the interface is perturbed externally in the presence of the electric field. The effect of the electric field is discussed in this article along with the salient features, which lead to an efficient extraction process in the microscale system. Moreover, in this current study, we have extensively studied the effect of electric field driven instability. Under these conditions, the amplitude of the interfacial perturbation is augmented, and miniaturized droplets were produced to have an emulsified flow. Due to the formation of the tiny droplets, the surface to volume ratio and the local interfacial convection are increased enormously to enhance the mass transfer and extraction efficiency by many folds.

1.2.4 Carbon Dots and Methylene Blue Facilitated Photometric Quantification of Hemoglobin

The goal of this chapter is detection and quantification of Hemoglobin in blood sample. Early diagnosis of diseases has become important due to the gradual rise of human health issues. Moreover, due to the hectic lifestyle, visiting a medical practitioner or a hospital is also becoming a tedious job for people with a tight schedule. To address these conditions, engineers and scientists across the globe have developed many point of care (POC) diagnostic kits. For qualitative or quantitative detection of various malfunctioning conditions inside a human body, medical science monitors various biomarkers found in different body fluids, such as blood [144], urine [145], sputum [146], sweat [147], tears [148], soft tissues [149], etc. Numerous selective biochemical and chemical reactions, such as lock and key interactions of enzymes [150], antigen-antibody interactions [151], RNA aptamer interactions [152], are exploited to develop optical [153,154], electrochemical [155], resistive [156], and capacitive [157] sensors. In this regard, identifying a particular foreign antigen or a specific indicator molecule associated with

the respective health condition is necessary. Regular monitoring of health parameters like blood sugar, lipid, serum albumin, hemoglobin, urinary proteins, thyroid, and other components have become essential. As the infection from foreign bacteria and viruses is the most discussed matter of today's world, along with all the available regular testing, exploration for new biomarkers for malaria [158], dengue [159,160], and others have always been in demand to improve the medical condition in a society.

Hemoglobin (Hb) is one among the various other vital components associated with multiple unhealthy conditions such as anemia [161], leukemia [162], porphyria [163], thalassemia [164], heart diseases [165], and many others [166]. Hb present in red blood cells is a tetrameric metalloprotein [167], made up of a globin protein with four iron protoporphyrin (heme). There are just four types of globin protein present in human body, namely, myoglobin (Mb), neuroglobin (Ngb), cytoglobin (Cygb), and hemoglobin (Hb). Myoglobin (Mb) is a protein, which is mainly found in muscles and heart [168,169]. Neuroglobin (Ngb) and cytoglobin (Cygb) are found mostly in cerebrospinal fluid (CSF) and in almost all body tissues respectively to protect the brain and other parts of the body from hypoxia [170,171]. Hb is responsible for the transportation of oxygen (O_2) from the lungs to different parts of the body through the blood and also carries carbon dioxide (CO_2) from other parts of the body to the lungs [172]. The normal level of Hb in blood lies between 13.0 – 18.0 g dL^{-1} for males and 12.0 – 16.0 g dL^{-1} for females [173]. Hb level below this normal level of Hb concentration causes anaemia. Therefore, accurate quantification of Hb in clinical diagnostics is especially essential to detect the associated diseases at an early stage.

The World Health Organization (WHO) has recognized various available techniques for the determination of Hb levels in blood samples [173,174]. All of the presently available

methods have their respective limitations and advantages despite being used in most clinical laboratories. Among these methods, spectrophotometric [175] and cyanmethemoglobin [176] methods are the most popular in clinical laboratories. These methods require highly specialized clinical expertise owing to the complexity of sample pretreatment, high reaction time, and requirement of a large amount of sample.

Of late, numerous analytical methods have been reported, such as colorimetric [177], fluorimetric [178–182], electrochemical [155,183], and chemiluminescence [184,185], based methods for the measurement of Hb. Nonetheless, most of the methods are not sensitive to measure the shallow concentration of Hb in the blood sample. Therefore, the development of a highly sensitive, user-friendly, and economic Hb sensor to measure very low concentration of Hb in human blood samples is still of great interest.

In the domain of biosensors, recently, carbon quantum dots (CDs) have gained considerable attention [186–189] due to their unique and enhanced optical signals when interacted with other chemical reagents. CDs are of the size < 10 nm having sp^2 and sp^3 hybridized carbon atoms with functional groups like −COOH and −OH [190]. CDs have exceptional characteristics such as fluorescence, water-solubility, biomolecule compatibility, and stability in terms of optical and chemical properties [191,192]. Fluorescence intensity of CDs is normally stable while changing the physical or chemical environment such as pH, electric and magnetic field, ionic strength, or in the presence of other chemicals. By exploiting the fluorescence quenching of CDs, a portable device for the quantification of Hb in blood samples can be targeted.

In view of the above discussions, here we report the fabrication of a portable device to quantify Hb. The specific interactions of Methylene Blue (MB) with Hb in the presence of CDs

show a unique characteristic optical feature, which is exploited for the quantitative estimation of Hb. The fabrication of a portable Hb quantification device based on the spectrophotometric principle using a light-emitting diode (LED) and a light-dependent resistor (LDR) is elaborated. Finally, the results obtained from the device are validated with clinical samples along with the interference study and stability analysis.

1.3 Objectives of the work

In view of the above context, the present thesis explores the usage of the microfluidic platform for the efficient resolution of enantiomers, surfactant separation, dye extraction, and Hemoglobin quantification. The objectives of the present work are as follows:

1. Chiral Resolution of Racemic Amines in μ-Reactor-Crystallizer.
2. Separation of Anionic and Cationic Surfactant in a Microchannel Using Ultra-Low Electric Voltage.
3. Liquid-Liquid Efficient Micro Extraction of Dye in a Microfluidic Platform by Creating Electric Field Induced Instability at the Interface of Fluids.
4. Carbon Dots and Methylene Blue Facilitated Photometric Quantification of Hemoglobin.

1.4 Outline of the thesis

On the basis of the above discussion, the thesis work has been divided into six chapters. A brief overview of each chapter is presented below.

Chapter 1. This chapter presents the general overview of various microfluidic platforms and their applications. Also, this chapter comprises a detailed literature review on chiral resolution,

surfactant separation, dye extraction, and haemoglobin quantification. Finally, the research problem is identified, and the objectives of this thesis are given to accomplish the research goal.

Chapter 2. This chapter shows the resolution of enantiomers in a continuous manner and for this, a microfluidic platform was developed to separate S-(-)-α-phenylethylamine from its racemic mixture using L-(+)-tartaric acid as a resolving agent via diastereomeric salt formation. The optimum resolution conditions were determined such as reactor temperature, feed concentration, feed flow rate, etc. and a crystal shape map was developed using concentration and the flow rate as process parameters. Various characterization like CD, DSC, FTIR, Raman, XRD, NMR, Polarimeter, UV-Vis, etc. has been carried out to investigate the purity of crystals. Alongside, a comparative study of diastereomer salt obtained from µ-continuous and batch has been carried out.

Chapter 3. In this study, we demonstrated a simultaneous separation of cationic and anionic surfactant from the water using ultra low electric voltage. The goal is to improve the existing physical and chemical processes for industrial wastewater treatment (e.g., chemical precipitation, synthetic organic resins, adsorption on active coal, etc.). A localized non-invasive DC electric voltage integrated into a microchannel can facilitate the separation of charged molecules in and around the flow stream.

Chapter 4. This chapter explores the pathways to enhance the extraction efficiency of methylene blue dye from the aqueous phase to the organic phase in a microchannel under the influence of an external electric field. It is intuitive that the surface-to-volume ratio increases as we do hydrodynamic two-phase flows in a microscale system. The effect of number of electrodes and

electric field intensity on extraction efficiency was also investigated. The results were analyzed using UV-Vis.

Chapter 5. In this chapter, we report the development of a prototype hand-held device for the quantitative detection of Hb exploiting the optical properties of CDs and its interaction with Hb. Also, we developed a portable device, based on a simple colourimetric principle, by integrating a light source (LED) and a detector (LDR). A calibration curve was prepared using this device to quantify the Hb concentration. Using the calibration curve for our developed portable device analysis for real blood samples was demonstrated. A comparison of the device reading with the local hospital data was also performed.

Chapter 6. This chapter draws an appropriate overall conclusion based on the investigation in the present study. This chapter also provides some new useful directions for future work.

References

[1] K.F. Jensen, *Microreaction Engineering.* 56 (**2001**) 293–303.

[2] J. Autebert, B. Coudert, F.C. Bidard, J.Y. Pierga, S. Descroix, L. Malaquin, J.L. Viovy, Microfluidic: An innovative tool for efficient cell sorting, *Methods.* 57 (**2012**) 297–307.

[3] L. Capretto, D. Carugo, S. Mazzitelli, C. Nastruzzi, X. Zhang, Microfluidic and lab-on-a-chip preparation routes for organic nanoparticles and vesicular systems for nanomedicine applications, *Adv. Drug Deliv. Rev.* 65 (**2013**) 1496–1532.

[4] K.S. Krishna, Y. Li, S. Li, C.S.S.R. Kumar, Lab-on-a-chip synthesis of inorganic nanomaterials and quantum dots for biomedical applications, *Adv. Drug Deliv. Rev.* 65 (**2013**) 1470–1495.

[5] L. Shui, A. Van Den Berg, J.C.T. Eijkel, Interfacial tension controlled W/O and O/W 2-phase flows in microchannel, *Lab Chip.* 9 (**2009**) 795–801.

[6] J.H. Xu, S.W. Li, J. Tan, Y.J. Wang, G.S. Luo, Controllable preparation of monodisperse O/W and W/O emulsions in the same microfluidic device, *Langmuir.* 22 (**2006**) 7943–7946.

[7] Á.G. Marín, W. Van Hoeve, P. García-Sánchez, L. Shui, Y. Xie, M.A. Fontelos, J.C.T. Eijkel, A. Van Den Berg, D. Lohse, The microfluidic Kelvin water dropper, *Lab Chip.* 13 (**2013**) 4503–4506.

[8] E. Yıldırım, H. Külah, Electrostatic energy harvesting by droplet-based multi-phase microfluidics, *Microfluid. Nanofluidics.* 13 (**2012**) 107–111.

[9] S.K. Singh, P. Gogoi, A. Deb, P.S. Gooh Pattader, Chiral resolution of racemic amines in μ-reactor-crystallizer, *Chem. Eng. Sci.* 256 (**2022**) 117686.

[10] A. Jain, L.L. Munn, Biomimetic postcapillary expansions for enhancing rare blood cell separation on a microfluidic chip, *Lab Chip.* 11 (**2011**) 2941–2947.

[11] Y.A. Olcer, M. Tascon, A.E. Eroglu, E. Boyacı, Thin film microextraction: Towards faster and more sensitive microextraction, *TrAC - Trends Anal. Chem.* 113 (**2019**) 93–101.

[12] P. Cui, S. Wang, Application of microfluidic chip technology in pharmaceutical analysis: A review, *J. Pharm. Anal.* 9 (**2019**) 238–247.

[13] K.A. Cook-Chennault, N. Thambi, A.M. Sastry, Powering MEMS portable devices - A review of non-regenerative and regenerative power supply systems with special emphasis on piezoelectric energy harvesting systems, *Smart Mater. Struct.* 17 (**2008**) 043001.

[14] V. Kumar, M. Paraschivoiu, K.D.P. Nigam, Single-phase fluid flow and mixing in microchannels, *Chem. Eng. Sci.* 66 (**2011**) 1329–1373.

[15] P. Suresh, P.K. Basu, Improving pharmaceutical product development and manufacturing: Impact on cost of drug development and cost of goods sold of pharmaceuticals, *J. Pharm. Innov.* 3 (**2008**) 175–187.

[16] J.A. DiMasi, R.W. Hansen, H.G. Grabowski, The price of innovation: New estimates of

drug development costs, *J. Health Econ.* 22 (**2003**) 151–185.

[17] P. Basu, G. Joglekar, S. Rai, P. Suresh, J. Vernon, Analysis of manufacturing costs in pharmaceutical companies, *J. Pharm. Innov. 3* (**2008**) 30–40.

[18] K.M. Christensen, M.J. Pedersen, K. Dam-Johansen, T.L. Holm, T. Skovby, S. Kiil, Design and operation of a filter reactor for continuous production of a selected pharmaceutical intermediate, *Chem. Eng. Sci.* 71 (**2012**) 111–117.

[19] M. Sean, Special report: Continuous technology update, *Pharm. Technol. Eur.* 24 (**2012**) 35.

[20] A.I. Shallan, C. Priest, Microfluidic process intensification for synthesis and formulation in the pharmaceutical industry, *Chem. Eng. Process. - Process Intensif.* 142 (**2019**) 107559.

[21] S. Mitra, S.K. Singh, E. Shevchenko, M. Sachan, A. Ghosh, M. Basak, P.S. Gooh Pattader, Efficient microextraction process exploiting spontaneous interfacial convection driven by Marangoni and electric field induced instability: A computational fluid dynamics study, *Phys. Fluids.* 32 (**2020**) 1–13.

[22] V. Hessel, H. Löwe, Organische Synthese mit mikrostrukturierten Reaktoren, *Chemie-Ingenieur-Technik.* 76 (**2004**) 535–554.

[23] N. Bhattacharjee, A. Urrios, S. Kang, A. Folch, The upcoming 3D-printing revolution in microfluidics, *Lab Chip.* 16 (**2016**) 1720–1742.

[24] P. Gogoi, D.K. Bhattacharyya, B. Borah, J.K. Kalita, A survey of outlier detection methods in network anomaly identification, *Comput. J.* 54 (**2011**) 570–588.

[25] L.J. Kricka, O. Nozaki, S. Heyner, W.T. Garside, P. Wilding, Applications of a microfabricated device for evaluating sperm function, *Clin. Chem.* 39 (**1993**) 1944–1947.

[26] L.J. Kricka, Microchips, microarrays, biochips and nanochips: Personal laboratories for the 21st century, *Clin. Chim. Acta.* 307 (**2001**) 219–223.

[27] T. Vo-Dinh, B. Cullum, Biosensors and biochips: Advances in biological and medical diagnostics, *Fresenius. J. Anal. Chem.* 366 (**2000**) 540–551.

[28] G.M. Whitesides, The origins and the future of microfluidics, *Nature.* 442 (**2006**) 368–373.

[29] R. Bashir, BioMEMS: State-of-the-art in detection, opportunities and prospects, *Adv. Drug Deliv. Rev.* 56 (**2004**) 1565–1586.

[30] D. Grieshaber, R. MacKenzie, J. Vörös, E. Reimhult, Electrochemical biosensors - Sensor principles and architectures, *Sensors.* 8 (**2008**) 1400–1458.

[31] J. Homola, Surface plasmon resonance sensors for detection of chemical and biological species, *Chem. Rev.* 108 (**2008**) 462–493.

[32] P.B. Luppa, A. Bietenbeck, C. Beaudoin, A. Giannetti, Clinically relevant analytical techniques, organizational concepts for application and future perspectives of point-of-

care testing, *Biotechnol. Adv.* 34 (**2016**) 139–160.

[33] R.W. Peeling, D. Mabey, Point-of-care tests for diagnosing infections in the developing world, *Clin. Microbiol. Infect.* 16 (**2010**) 1062–1069.

[34] G. Gübitz, M.G. Schmid, Chiral separation principles in chromatographic and electromigration techniques, *Mol. Biotechnol.* 32 (**2006**) 159–179.

[35] L. Pasteur, Transformation des acides tartriques en acide racémique. Découverte de l'acide tartrique inactif. Nouvelle méthode de séparation de l'acide racémique en acides tartriques droit et gauche, *Comptes Rendus l'Académie Des Sci.* 37 (**1853**) 162–166.

[36] P. Newman, Optical Resolution Procedures for Chemical Compounds, Vol 2, Acids: Optical Resolution Information Center, New York, **1981**.

[37] P. Louis, The first examples described by Pasteur were the two pairs ammonium hydrogen (+)-tartrate-ammonium hydrogen (-)-malate and (+)-tartramide-(-)-malaminde, *Ann. Chim.* 3 (**1853**) 437–483.

[38] W.J. Pope, S.J. Peachey, CVIII–The application of powerful optically active acids to the resolution of externally compensated basic substances. Resolution of tetrahydroquinaldine., *J. Chem. Soc.* 75 (**1899**) 1066–1093.

[39] N.B. Báthori, L.R. Nassimbeni, Selectivity and enantiomeric resolution in inclusion chemistry: A systematic study of chiral discrimination through crystallization, *Cryst. Growth Des.* 10 (**2010**) 1782–1787.

[40] A.N. Collins, G.N. Sheldrake, J. Crosby, eds., Chirality in Industry II: Developments in the Commercial Manufacture and Applications of Optically Active Compounds, John Wiley & Sons Ltd., **1997**.

[41] H. Murakami, From racemates to single enantiomers - Chiral synthetic drugs over the last 20 years, in: K. Sakai, N. Hirayama, R. Tamura (Eds.), Top. Curr. Chem., Springer-Verlag, Berlin, Heidelberg, **2007**: pp. 273–299.

[42] G. Subramanian, Chiral Separation Techniques: A Practical Approach, 3rd ed., Wiley-VCH, **2007**.

[43] E. Francotte, Enantioselective chromatography: From its emergence to its successful implementation in the pharmaceutical environment, *Chimia (Aarau).* 63 (**2009**) 867–871.

[44] K. Tang, L. Song, Y. Liu, Y. Pan, X. Jiang, Separation of flurbiprofen enantiomers by biphasic recognition chiral extraction, *Chem. Eng. J.* 158 (**2010**) 411–417.

[45] J.M. Yi, S.J. Huang, Y.R. Jiang, K.W. Tang, Enantioselective extraction of fenvaleric acid enantiomers by two-phase (W/O) recognition chiral extraction, *J. Incl. Phenom. Macrocycl. Chem.* 68 (**2010**) 271–275.

[46] R. Xie, L.Y. Chu, J.G. Deng, Membranes and membrane processes for chiral resolution, *Chem. Soc. Rev.* 37 (**2008**) 1243–1263.

[47] K. Würges, U. MacKfeld, M. Pohl, S. Lütz, S. Wilhelm, W. Wiechert, T. Kubitzki, An efficient route to both enantiomers of allo-threonine by simultaneous amino acid

racemase-catalyzed isomerization of threonine and crystallization, *Adv. Synth. Catal.* 353 (**2011**) 2431–2438.

[48] E.A. Manoel, K.C. Pais, A.G. Cunha, A.B.C. Simas, M.A.Z. Coelho, D.M.G. Freire, Kinetic resolution of 1,3,6-tri-O-benzyl-myo-inositol by Novozym 435: Optimization and enzyme reuse, *Org. Process Res. Dev.* 16 (**2012**) 1378–1384.

[49] R. Yoshioka, Racemization, optical resolution and crystallization-induced asymmetric transformation of amino acids and pharmaceutical intermediates, in: K. Sakai, N. Hirayama, R. Tamura (Eds.), Top. Curr. Chem., Springer-Verlag, Berlin, Heidelberg, **2007**: pp. 83–132.

[50] M.P. Elsner, G. Ziomek, A. Seidel-Morgenstern, Simultaneous preferential crystallization in a coupled batch operation mode. Part II: Experimental study and model refinement, *Chem. Eng. Sci.* 66 (**2011**) 1269–1284.

[51] K. Petruševska-Seebach, A. Seidel-Morgenstern, M.P. Elsner, Preferential crystallization of l -asparagine in water, *Cryst. Growth Des.* 11 (**2011**) 2149–2163.

[52] G. Coquerel, Preferential Crystallization. In: Novel Optical Resolution Technologies, in: K. Sakai, N. Hirayama, R. Tamura (Eds.), Top. Curr. Chem., Springer-Verlag, Berlin, Heidelberg, **2007**: pp. 1–51.

[53] K. Galan, M.J. Eicke, M.P. Elsner, H. Lorenz, A. Seidel-Morgenstern, Continuous preferential crystallization of chiral molecules in single and coupled mixed-suspension mixed-product-removal crystallizers, *Cryst. Growth Des.* 15 (**2015**) 1808–1818.

[54] M. Balawejder, D. Kiwala, H. Lorenz, A. Seidel-Morgenstern, W. Piatkowski, D. Antos, Resolution of a diasteromeric salt of citalopram by multistage crystallization, *Cryst. Growth Des.* 12 (**2012**) 2557–2566.

[55] R.R.E. Steendam, J.H. Ter Horst, Continuous Total Spontaneous Resolution, *Cryst. Growth Des.* 17 (**2017**) 4428–4436.

[56] C. Xiouras, G. Belletti, R. Venkatramanan, A. Nordon, H. Meekes, E. Vlieg, G.D. Stefanidis, J.H. Ter Horst, Toward Continuous Deracemization via Racemic Crystal Transformation Monitored by in Situ Raman Spectroscopy, *Cryst. Growth Des.* 19 (**2019**) 5858–5868.

[57] F. Cameli, C. Xiouras, G.D. Stefanidis, High-throughput on demand access of single enantiomers by a continuous flow crystallization process, *CrystEngComm.* 22 (**2020**) 3519–3525.

[58] S.K. Sia, G.M. Whitesides, Microfluidic devices fabricated in poly(dimethylsiloxane) for biological studies, *Electrophoresis.* 24 (**2003**) 3563–3576.

[59] D.J. Beebe, G.A. Mensing, G.M. Walker, Physics and applications of microfluidics in biology, *Annu. Rev. Biomed. Eng.* 4 (**2002**) 261–286.

[60] H.A. Stone, A.D. Stroock, A. Ajdari, Engineering flows in small devices: Microfluidics toward a lab-on-a-chip, *Annu. Rev. Fluid Mech.* 36 (**2004**) 381–411.

[61] Z. Zhang, M. Wu, R. Wu, J. Dong, J. Ou, H. Zou, Preparation of perphenylcarbamoylated β-cyclodextrin-silica hybrid monolithic column with "one-pot" approach for enantioseparation by capillary liquid chromatography, *Anal. Chem.* 83 (**2011**) 3616–3622.

[62] R.P. Liang, C.M. Liu, X.Y. Meng, J.W. Wang, J.D. Qiu, A novel open-tubular capillary electrochromatography using β-cyclodextrin functionalized graphene oxide-magnetic nanocomposites as tunable stationary phase, *J. Chromatogr. A.* 1266 (**2012**) 95–102.

[63] P. Qu, J. Lei, L. Zhang, R. Ouyang, H. Ju, Molecularly imprinted magnetic nanoparticles as tunable stationary phase located in microfluidic channel for enantioseparation, *J. Chromatogr. A. 1217* (**2010**) 6115–6121.

[64] M. Ludwig, D. Belder, Coated microfluidic devices for improved chiral separations in microchip electrophoresis, *Electrophoresis.* 24 (**2003**) 2481–2486.

[65] T.H. Yoon, L.Y. Hong, D.P. Kim, Chiral separation by a pseudo membrane in a triple-laminar flow with a microfluidic contactor, *Chem. - An Asian J.* 6 (**2011**) 1015–1018.

[66] P.C. Wang, J. Gao, C.S. Lee, High-resolution chiral separation using microfluidics-based membrane chromatography, *J. Chromatogr. A.* 942 (**2002**) 115–122.

[67] S. Thurmann, C. Lotter, J.J. Heiland, B. Chankvetadze, D. Belder, Chip-based high-performance liquid chromatography for high-speed enantioseparations, *Anal. Chem*. 87 (**2015**) 5568–5576.

[68] X. Ye, J. Cui, B. Li, N. Li, R. Wang, Z. Yan, J. Tan, J. Zhang, X. Wan, Enantiomer-selective magnetization of conglomerates for quantitative chiral separation, *Nat. Commun.* 10 (**2019**) 1–7.

[69] K. Banerjee-Ghosh, O. Ben Dor, F. Tassinari, E. Capua, S. Yochelis, A. Capua, S.H. Yang, S.S.P. Parkin, S. Sarkar, L. Kronik, L.T. Baczewski, R. Naaman, Y. Paltiel, Separation of enantiomers by their enantiospecific interaction with achiral magnetic substrates, *Science.* 360 (**2018**) 1331–1334.

[70] F. Tassinari, J. Steidel, S. Paltiel, C. Fontanesi, M. Lahav, Y. Paltiel, R. Naaman, Enantioseparation by crystallization using magnetic substrates, *Chem. Sci.* 10 (**2019**) 5246–5250.

[71] A.M. Becker, S. Gerstmann, H. Frank, Perfluorooctane surfactants in waste waters, the major source of river pollution, *Chemosphere.* 72 (**2008**) 115–121.

[72] E. Önder, A.S. Koparal, Ü.B. Öğütveren, An alternative method for the removal of surfactants from water: Electrochemical coagulation, *Sep. Purif. Technol.* 52 (**2007**) 527–532.

[73] P. Wungrattanasopon, J.F. Scamehorn, S. Chavedej, C. Saiwan, J.H. Harwell, Use of foam flotation to remove tert-butylphenol from water, *Sep. Sci. Technol.* 31 (**1996**) 1523–1540.

[74] P.D. Abel, Toxicity of synthetic detergents to fish and aquatic invertebrates, *J. Fish Biol.* 6 (**1974**) 279–298.

[75] D. Bajpai, V.K. Tyagi, Laundry detergents: an overview., *J. Oleo Sci.* 56 (**2007**) 327–340.

[76] S. Chen, M.B. Timmons, J.J. Bisogni, D.J. Aneshansley, Modeling surfactant removal in foam fractionation: II - Experimental investigations, *Aquac. Eng.* 13 (**1994**) 183–200.

[77] B. Burghoff, Foam fractionation applications, *J. Biotechnol.* 161 (**2012**) 126–137.

[78] A. Šonc, V. Grilc, Batch foam fractionation of surfactants from aqueous solutions, *Acta Chim. Slov.* 51 (**2004**) 687–698.

[79] S. Boonyasuwat, S. Chavadej, P. Malakul, J.F. Scamehorn, Anionic and cationic surfactant recovery from water using a multistage foam fractionator, *Chem. Eng. J.* 93 (**2003**) 241–252.

[80] S. Boonyasuwat, S. Chavadej, P. Malakul, J.F. Scamehorn, Surfactant recovery from water using a multistage foam fractionator: Part i effects of air flow rate, foam height, feed flow rate and number of stages, *Sep. Sci. Technol.* 40 (**2005**) 1835–1853.

[81] S. Boonyasuwat, S. Chavadej, P. Malakul, J.F. Scamehorn, Surfactant recovery from water using a multistage foam fractionator: Effect of surfactant type, *Sep. Sci. Technol.* 44 (**2009**) 1544–1561.

[82] Z. Zhang, Z. Wu, G. Liu, Interfacial adsorption of methyl orange in liquid phase of foam fractionation using dodecyl dimethyl betaine as the collector, *J. Ind. Eng. Chem.* 28 (**2015**) 184–189.

[83] W. Bae, H. Won, B. Hwang, R.A. de Toledo, J. Chung, K. Kwon, H. Shim, Characterization of refractory matters in dyeing wastewater during a full-scale Fenton process following pure-oxygen activated sludge treatment, *J. Hazard. Mater.* 287 (**2015**) 421–428.

[84] A. Lopez, G. Ricco, R. Ciannarella, A. Rozzi, A.C. Di Pinto, R. Passino, Textile wastewater reuse: Ozonation of membrane concentrated secondary effluent, *Water Sci. Technol.* 40 (**1999**) 99–105.

[85] C.H. Tung, S.Y. Shen, J.H. Chang, Y.M. Hsu, Y.C. Lai, Treatment of real printing wastewater with an electrocatalytic process, *Sep. Purif. Technol.* 117 (**2013**) 131–136.

[86] G. Morgan, U. Wiesmann, Single and multistage foam fractionation of rinse water with alkyl ethoxylate surfactants, *Sep. Sci. Technol.* 36 (**2001**) 2247–2263.

[87] A.K. Kumar, N. Rawat, P. Ghosh, Removal and recovery of a cationic surfactant from its aqueous solution by foam fractionation, *J. Environ. Chem. Eng.* 8 (**2020**) 103555.

[88] D. Jenkins, Application of foam fractionation to wastewater treatment., *J. Water Pollut. Control Fed.* 38 (**1966**) 1737–1766.

[89] R.B. Grieves, R.K. Wood, Continuous foam fractionation: The effect of operating variables on separation, *AIChE J.* 10 (**1964**) 456–460.

[90] N. Tharapiwattananon, J.F. Scamehorn, S. Osuwan, J.H. Harwell, K.J. Haller, Surfactant recovery from water using foam fractionation, *Sep. Sci. Technol.* 31 (**1996**) 1233–1258.

[91] K. Kumpabooth, J.F. Scamehorn, S. Osuwan, J.H. Harwell, Surfactant recovery from water using foam fractionation: Effect of temperature and added salt, *Sep. Sci. Technol.* 34

(**1999**) 157–172.

[92] E. Rubin, J. Jorne, Foam separation of solutions containing two ionic surface-active solutes, *Ind. Eng. Chem. Fundam.* 8 (**1969**) 474–483.

[93] Y.H. Qu, G.M. Zeng, J.H. Huang, K. Xu, Y.Y. Fang, X. Li, H.L. Liu, Recovery of surfactant SDS and Cd2+ from permeate in MEUF using a continuous foam fractionator, *J. Hazard. Mater.* 155 (**2008**) 32–38.

[94] S.S. Srinet, A. Basak, P. Ghosh, J. Chatterjee, Separation of anionic surfactant in paste form from its aqueous solutions using foam fractionation, *J. Environ. Chem. Eng.* 5 (**2017**) 1586–1598.

[95] K. Tadakamalla, K. V. Marathe, Hydrodynamic study and optimization strategy for the surfactant recovery from aqueous solutions, *Desalination.* 266 (**2011**) 98–107.

[96] P.H. Brunner, S. Capri, A. Marcomini, W. Giger, Occurrence and behaviour of linear alkylbenzenesulphonates, nonylphenol, nonylphenol mono- and nonylphenol diethoxylates in sewage and sewage sludge treatment, *Water Res.* 22 (**1988**) 1465–1472.

[97] D. Prats, F. Ruiz, B. Vázquez, M. Rodriguez-Pastor, Removal of anionic and nonionic surfactants in a wastewater treatment plant with anaerobic digestion. A comparative study, *Water Res.* 31 (**1997**) 1925–1930.

[98] S. González, M. Petrovic, D. Barceló, Removal of a broad range of surfactants from municipal wastewater - Comparison between membrane bioreactor and conventional activated sludge treatment, *Chemosphere.* 67 (**2007**) 335–343.

[99] C.G. Van Ginkel, Complete degradation of xenobiotic surfactants by consortia of aerobic microorganisms, *Biodegradation.* 7 (**1996**) 151–164.

[100] F. Aloui, S. Kchaou, S. Sayadi, Physicochemical treatments of anionic surfactants wastewater: Effect on aerobic biodegradability, *J. Hazard. Mater.* 164 (**2009**) 353–359.

[101] J. Varley, A.K. Brown, J.W.R. Boyd, P.W. Dodd, S. Gallagher, Dynamic multi-point measurement of foam behaviour for a continuous fermentation over a range of key process variables, *Biochem. Eng. J.* 20 (**2004**) 61–72.

[102] X.J. Wang, Y. Song, J.S. Mai, Combined Fenton oxidation and aerobic biological processes for treating a surfactant wastewater containing abundant sulfate, *J. Hazard. Mater.* 160 (**2008**) 344–348.

[103] C.D. Adams, J.J. Kuzhikannil, Effects of UV/H2O2 preoxidation on the aerobic biodegradability of quaternary amine surfactants, *Water Res.* 34 (**2000**) 668–672.

[104] M. Kitis, C.D. Adams, G.T. Daigger, The effects of Fenton's reagent pretreatement on the biodegradability of nonionic surfactants, *Water Res.* 33 (**1999**) 2561–2568.

[105] A. Babuponnusami, K. Muthukumar, A review on Fenton and improvements to the Fenton process for wastewater treatment, *J. Environ. Chem. Eng.* 2 (**2014**) 557–572.

[106] A. Dhouib, N. Hamad, I. Hassaïri, S. Sayadi, Degradation of anionic surfactants by Citrobacter braakii, *Process Biochem.* 38 (**2003**) 1245–1250.

[107] M.A. Aboulhassan, S. Souabi, A. Yaacoubi, M. Baudu, https://doi.org/10.1007/BF03325941, *Int. J. Environ. Sci. Technol.* 3 (**2006**) 327–332.

[108] J. Kaleta, M. Elektorowicz, The removal of anionic surfactants from water in coagulation process, *Environ. Technol.* 34 (**2013**) 999–1005.

[109] S.H. Wu, P. Pendleton, Adsorption of anionic surfactant by activated carbon: Effect of surface chemistry, ionic strength, and hydrophobicity, *J. Colloid Interface Sci.* 243 (**2001**) 306–315.

[110] S. Kalliadasis, A. Kiyashko, E.A. Demekhin, Marangoni instability of a thin liquid film heated from below by a local heat source, *J. Fluid Mech.* 475 (**2003**) 377–408.

[111] B. Ray, P.D.S. Reddy, D. Bandyopadhyay, S.W. Joo, A. Sharma, S. Qian, G. Biswas, Surface instability of a thin electrolyte film undergoing coupled electroosmotic and electrophoretic flows in a microfluidic channel, *Electrophoresis.* 32 (**2011**) 3257–3267.

[112] R. Verma, A. Sharma, K. Kargupta, J. Bhaumik, Electric field induced instability and pattern formation in thin liquid films, *Langmuir.* 21 (**2005**) 3710–3721.

[113] A. Pedchenko, I. Grants, Instability of rotating magnetic field driven flow in a counter-rotating cylinder, *Phys. Fluids.* 17 (**2005**) 104102.

[114] T. Pfeil, H. Klahr, Mapping the Conditions for Hydrodynamic Instability on Steady-State Accretion Models of Protoplanetary Disks, *Astrophys. J.* 871 (**2019**) 150.

[115] Q. An, A.M. Steinberg, The role of strain rate, local extinction, and hydrodynamic instability on transition between attached and lifted swirl flames, *Combust. Flame.* 199 (**2019**) 267–278.

[116] B. Zhang, M. Shahsavari, Z. Rao, S. Yang, B. Wang, Contributions of hydrodynamic features of a swirling flow to thermoacoustic instabilities in a lean premixed swirl stabilized combustor, *Phys. Fluids.* 31 (**2019**) 075106.

[117] S. Shabahang, J.J. Kaufman, D.S. Deng, A.F. Abouraddy, Observation of the Plateau-Rayleigh capillary instability in multi-material optical fibers, Appl. *Phys. Lett.* 99 (**2011**) 161909.

[118] Q. Wang, Capillary instability of a viscous liquid thread in a cylindrical tube, *Phys. Fluids.* 25 (**2013**) 112104.

[119] M.K. Awasthi, Study on kelvin-helmholtz instability with heat and mass transfer, *J. Fluids Eng. Trans. ASME.* 136 (**2014**) 1–8.

[120] M. Kawaguchi, S. Yamazaki, K. Yonekura, T. Kato, Viscous fingering instabilities in an oil in water emulsion, *Phys. Fluids.* 16 (**2004**) 1908–1914.

[121] A.C. Callan-Jones, J.F. Joanny, J. Prost, Viscous-fingering-like instability of cell fragments, *Phys. Rev. Lett.* 100 (**2008**) 27–30.

[122] J.K. Novev, N. Panchev, R.I. Slavchov, Evaporating foam films of pure liquid stabilized via the thermal Marangoni effect, *Chem. Eng. Sci.* 171 (**2017**) 520–533.

[123] K.R. Semkov, N. Kolev, On the evaluation of the interfacial turbulence (the Marangoni effect) in gas (vapour)-liquid mass transfer. Part I. A method for estimating the interfacial turbulence effect, *Chem. Eng. Process.* 29 (**1991**) 77–82.

[124] P.R. Byron, M.J. Rathbone, Prediction of interfacial transfer kinetics. II. Solute ionization and aqueous phase ionic strength effects in two-phase transfer and rotating diffusion cells, *Int. J. Pharm.* 29 (**1986**) 103–111.

[125] D.G. Lopes, I. Koutsamanis, K. Becker, O. Scheibelhofer, P. Laggner, D. Haack, M. Stehr, A. Zimmer, S. Salar-Behzadi, Microphase separation in solid lipid dosage forms as the cause of drug release instability, *Int. J. Pharm.* 517 (**2017**) 403–412.

[126] E.F. Skurygin, V. V. Dil'man, On Marangoni instability during desorption accompanied by evaporation, *J. Food Eng.* 43 (**2000**) 125–131.

[127] E. Ruckenstein, C. Berbente, The occurrence of interfacial turbulence in the case of diffusion accompanied by chemical reaction, *Chem. Eng. Sci.* 19 (**1964**) 329–347.

[128] M. Morozov, S. Michelin, Self-propulsion near the onset of Marangoni instability of deformable active droplets, *J. Fluid Mech.* 860 (**2019**) 711–738.

[129] B. Sobac, P. Colinet, L. Pauchard, Influence of Bénard-Marangoni instability on the morphology of drying colloidal films, *Soft Matter.* 15 (**2019**) 2381–2390.

[130] J. B. FERNANDE and M. M. SHARMA, Effective interfacial area in agitated liquid-liquid continuous reactors, *Chem. Eng. Sci.* 22 (**1967**) 1267–1282.

[131] R.P. Verma, M.M. Sharma, Mass transfer in packed liquid-liquid extraction columns, *Chem. Eng. Sci.* 30 (**1975**) 279–292.

[132] M.N. Kashid, A. Renken, L. Kiwi-Minsker, Influence of flow regime on mass transfer in different types of microchannels, *Ind. Eng. Chem. Res.* 50 (**2011**) 6906–6914.

[133] T.W. Phillips, J.H. Bannock, J.C. DeMello, Microscale extraction and phase separation using a porous capillary, *Lab Chip.* 15 (**2015**) 2960–2967.

[134] P. Derboven, P.H.M. Van Steenberge, J. Vandenbergh, M.F. Reyniers, T. Junkers, D.R. D'Hooge, G.B. Marin, Improved Livingness and Control over Branching in RAFT Polymerization of Acrylates: Could Microflow Synthesis Make the Difference?, Macromol. *Rapid Commun.* 36 (**2015**) 2149–2155.

[135] P.S. Sarkar, K.K. Singh, K.T. Shenoy, A. Sinha, H. Rao, S.K. Ghosh, Liquid-liquid two-phase flow patterns in a serpentine microchannel, *Ind. Eng. Chem. Res.* 51 (**2012**) 5056–5066.

[136] C.X. Zhao, A.P.J. Middelberg, Two-phase microfluidic flows, *Chem. Eng. Sci.* 66 (**2011**) 1394–1411.

[137] M.N. Kashid, I. Gerlach, S. Goetz, J. Franzke, J.F. Acker, F. Platte, D.W. Agar, S. Turek, Internal circulation within the liquid slugs of a liquid-liquid slug-flow capillary microreactor, *Ind. Eng. Chem. Res.* 44 (**2005**) 5003–5010.

[138] D.M. Fries, T. Voitl, P.R. von Rohr, Liquid extraction of vanillin in rectangular

microreactors, *Chem. Eng. Technol.* 31 (**2008**) 1182–1187.

[139] A.B. Vir, A.S. Fabiyan, J.R. Picardo, S. Pushpavanam, Performance comparison of liquid-liquid extraction in parallel microflows, *Ind. Eng. Chem. Res.* 53 (**2014**) 8171–8181.

[140] A. Ghaini, M.N. Kashid, D.W. Agar, Effective interfacial area for mass transfer in the liquid-liquid slug flow capillary microreactors, *Chem. Eng. Process. Process Intensif.* 49 (**2010**) 358–366.

[141] O. Tamagawa, A. Muto, Development of cesium ion extraction process using a slug flow microreactor, *Chem. Eng. J.* 167 (**2011**) 700–704.

[142] N. Naleini, M. Rahimi, R. Heydari, Oleuropein extraction using microfluidic system, *Chem. Eng. Process. Process Intensif.* 92 (**2015**) 1–6.

[143] M.S.G. Nandagopal, R. Antony, N. Selvaraju, Comparative study of liquid–liquid extraction in miniaturized channels over other conventional extraction methods, *Microsyst. Technol.* 22 (**2016**) 349–356.

[144] J.D. Cohen, L. Li, Y. Wang, C. Thoburn, B. Afsari, L. Danilova, C. Douville, A.A. Javed, F. Wong, A. Mattox, R.H. Hruban, C.L. Wolfgang, M.G. Goggins, M.D. Molin, T.L. Wang, R. Roden, A.P. Klein, J. Ptak, L. Dobbyn, J. Schaefer, N. Silliman, M. Popoli, J.T. Vogelstein, J.D. Browne, R.E. Schoen, R.E. Brand, J. Tie, P. Gibbs, H.L. Wong, A.S. Mansfield, J. Jen, S.M. Hanash, M. Falconi, P.J. Allen, S. Zhou, C. Bettegowda, L.A. Diaz, C. Tomasetti, K.W. Kinzler, B. Vogelstein, A.M. Lennon, N. Papadopoulos, Detection and localization of surgically resectable cancers with a multi-analyte blood test, *Science.* 359 (**2018**) 926–930.

[145] L. Van Neste, R.J. Hendriks, S. Dijkstra, G. Trooskens, E.B. Cornel, S.A. Jannink, H. de Jong, D. Hessels, F.P. Smit, W.J.G. Melchers, G.H.J.M. Leyten, T.M. de Reijke, H. Vergunst, P. Kil, B.C. Knipscheer, C.A. Hulsbergen-van de Kaa, P.F.A. Mulders, I.M. van Oort, W. Van Criekinge, J.A. Schalken, Detection of High-grade Prostate Cancer Using a Urinary Molecular Biomarker–Based Risk Score, *Eur. Urol.* 70 (**2016**) 740–748.

[146] A.T. Hastie, F.J. Martinez, J.L. Curtis, C.M. Doerschuk, N.N. Hansel, S.A. Christenson, N. Putcha, V.E. Ortega, X. Li, R.G. Barr, E.E. Carretta, D.J. Couper, C.B. Cooper, E.A. Hoffman, R.E. Kanner, E.C. Kleerup, W.K. O'Neal, R. Paine, S.P. Peters, N.E. Alexis, P.G. Woodruff, M.L.K. Han, D.A. Meyers, E.R. Bleecker, W.H. Anderson, R.C. Boucher, R.P. Bowler, A.P. Comellas, G.J. Criner, R.G. Crystal, M.T. Dransfield, C.M. Freeman, R.J. Kaner, J.A. Krishnan, L.M. LaVange, S.C. Lazarus, J.D. Newell, E.C. Oelsner, S.I. Rennard, D.P. Tashkin, M.B. Scholand, J.M. Wells, R.A. Wise, Association of sputum and blood eosinophil concentrations with clinical measures of COPD severity: an analysis of the SPIROMICS cohort, *Lancet Respir. Med.* 5 (**2017**) 956–967.

[147] F.J. Accurso, F. Van Goor, J. Zha, A.J. Stone, Q. Dong, C.L. Ordonez, S.M. Rowe, J.P. Clancy, M.W. Konstan, H.E. Hoch, S.L. Heltshe, B.W. Ramsey, P.W. Campbell, M.A. Ashlock, Sweat chloride as a biomarker of CFTR activity: Proof of concept and ivacaftor clinical trial data, *J. Cyst. Fibros.* 13 (**2014**) 139–147.

[148] N. von Thun und Hohenstein-Blaul, S. Funke, F.H. Grus, Tears as a source of biomarkers for ocular and systemic diseases, *Exp. Eye Res.* 117 (**2013**) 126–137.

[149] M.C. Hu, M. Shi, J. Zhang, H. Quiñones, C. Griffith, M. Kuro-o, O.W. Moe, Klotho deficiency causes vascular calcification in chronic kidney disease, *J. Am. Soc. Nephrol.* 22 (**2011**) 124–136.

[150] A. Küchler, M. Yoshimoto, S. Luginbühl, F. Mavelli, P. Walde, Enzymatic reactions in confined environments, *Nat. Publ. Gr.* 11 (**2016**) 409–420.

[151] M.H.V. Van Regenmortel, D. Altschuh, J. Chatellier, L. Christensen, N. Rauffer-Bruyère, P. Richalet-Secordel, J. Witz, G. Zeder-Lutz, Measurement of antigen-antibody interactions with biosensors, *J. Mol. Recognit.* 11 (**1998**) 163–167.

[152] Y. Xiao, A.A. Lubin, A.J. Heeger, K.W. Plaxco, Label-free electronic detection of thrombin in blood serum by using an aptamer-based sensor, *Angew. Chemie - Int. Ed.* 44 (**2005**) 5456–5459.

[153] M.S. Steiner, A. Duerkop, O.S. Wolfbeis, Optical methods for sensing glucose, *Chem. Soc. Rev.* 40 (**2011**) 4805–4839.

[154] R. Cush, J.M. Cronin, W.J. Stewart, C.H. Maule, J. Molloy, N.J. Goddard, The resonant mirror: a novel optical biosensor for direct sensing of biomolecular interactions Part I: Principle of operation and associated instrumentation, *Biosens. Bioelectron.* 8 (**1993**) 347–354.

[155] E. Matysiak, M. Donten, A. Kowalczyk, M. Bystrzejewski, I.P. Grudzinski, A.M. Nowicka, A novel type of electrochemical sensor based on ferromagnetic carbon-encapsulated iron nanoparticles for direct determination of hemoglobin in blood samples, *Biosens. Bioelectron.* 64 (**2015**) 554–559.

[156] L.G. Carrascosa, M. Moreno, M. Álvarez, L.M. Lechuga, Nanomechanical biosensors: A new sensing tool, *TrAC - Trends Anal. Chem.* 25 (**2006**) 196–206.

[157] C. Berggren, B. Bjarnason, G. Johansson, Capacitive biosensors, *Electroanalysis.* 13 (**2001**) 173–180.

[158] P.K. Sahu, S. Satpathi, P.K. Behera, S.K. Mishra, S. Mohanty, S.C. Wassmer, Pathogenesis of cerebral malaria: New diagnostic tools, biomarkers, and therapeutic approaches, *Front. Cell. Infect. Microbiol.* 5 (**2015**) 1–13.

[159] D.V. John, Y.S. Lin, G.C. Perng, Biomarkers of severe dengue disease - A review, *J. Biomed. Sci.* 22 (**2015**) 1–7.

[160] P. Antunes, D. Watterson, M. Parmvi, R. Burger, A. Boisen, P. Young, M.A. Cooper, M.F. Hansen, A. Ranzoni, M. Donolato, Quantification of NS1 dengue biomarker in serum via optomagnetic nanocluster detection, *Sci. Rep.* 5 (**2015**) 1–10.

[161] E. Beutler, J. Waalen, The definition of anemia: What is the lower limit of normal of the blood hemoglobin concentration?, *Blood.* 107 (**2006**) 1747–1750.

[162] S. Wu, C. Zheng, S. Chen, X. Cai, Y. Shi, B. Lin, Y. Chen, Overexpression of long non- coding RNA HOTAIR predicts a poor prognosis in patients with acute myeloid leukemia, *Oncol. Lett.* 10 (**2015**) 2410–2414.

[163] D.M. Bissell, K.E. Anderson, H.L. Bonkovsky, Porphyria, *N. Engl. J. Med.* 377 (**2017**) 862-872.

[164] S. Kradtap, B. Srisawang, P. Kongtawelert, D. Christian, K. Grudpan, Review on screening and analysis techniques for hemoglobin variants and thalassemia, *Talanta.* 65 (**2005**) 1149–1161.

[165] T. Options, Anemia and Chronic Heart Failure, *J. Am. Coll. Cardiol.* 52 (**2008**) 501–511.

[166] M. Chonchol, C. Nielson, Hemoglobin levels and coronary artery disease, *Am. Heart J.* 155 (**2008**) 494–498.

[167] C.J. Wilson, D. Apiyo, P. Wittung-Stafshede, Role of cofactors in metalloprotein folding, *Q. Rev. Biophys.* 37 (**2004**) 285–314.

[168] J.B. Wittenberg, B.A. Wittenberg, Myoglobin function reassessed, *J. Exp. Biol.* 206 (**2003**) 2011–2020.

[169] G.A. Ordway, D.J. Garry, Myoglobin: An essential hemoprotein in striated muscle, *J. Exp. Biol.* 207 (**2004**) 3441–3446.

[170] T. Burmester, B. Ebner, B. Weich, T. Hankeln, Cytoglobin: A novel globin type ubiquitously expressed in vertebrate tissues, *Mol. Biol. Evol.* 19 (**2002**) 416–421.

[171] B. Casado, L.K. Pannell, G. Whalen, D.J. Clauw, J.N. Baraniuk, Human neuroglobin protein in cerebrospinal fluid, *Proteome Sci.* 3 (**2005**) 1–8.

[172] H. Mairbäurl, R.E. Weber, Oxygen transport by hemoglobin, *Compr. Physiol.* 2 (**2012**) 1463–1489.

[173] Path, Anemia Detection Methods in Low-Resource Settings: A Manual For Health Workers, Http//Www.Path.Org/Publications/Files/TS_anemia_guide_ Heal. (**1997**).

[174] R.D. Whitehead, Z. Mei, C. Mapango, M.E.D. Jefferds, Methods and analyzers for hemoglobin measurement in clinical laboratories and field settings, *Ann. N. Y. Acad. Sci.* (**2019**) 1–25.

[175] G.G. Nahas, Spectrophotometric determination of hemoglobin and oxyhemoglobin in whole hemolyzed blood, *Science.* 113 (**1951**) 723–725.

[176] P. Bhaskaram, N. Balakrishna, K. V. Radhakrishna, K. Krishnaswamy, Validation of hemoglobin estimation using Hemocue, *Indian J. Pediatr.* 70 (**2003**) 25–28.

[177] N. Pourreza, H. Golmohammadi, Hemoglobin detection using curcumin nanoparticles as a colorimetric chemosensor, *RSC Adv.* 5 (**2015**) 1712–1717.

[178] G. Kalaiyarasan, A. Venugopal, N. Kumar, C. Sivakumar, J. Joseph, Photoluminescence of oligomers of aniline-2-sulfonic acid formed in the presence of AuCl4 − and sodium citrate : Application in the optical detection of hemoglobin, *Sensors Actuators B. Chem.* 209 (**2015**) 883–888.

[179] S. Pang, S. Liu, X. Su, A novel fl uorescence assay for the detection of hemoglobin based on the G-quadruplex / hemin complex, *Talanta.* 118 (**2014**) 118–122.

[180] A. Barati, M. Shamsipur, H. Abdollahi, Hemoglobin detection using carbon dots as a fluorescence probe, *Biosens. Bioelectron.* 71 (**2015**) 470–475.

[181] P. Lv, D. Xie, Z. Zhang, Magnetic carbon dots based molecularly imprinted polymers for fluorescent detection of bovine hemoglobin, *Talanta.* 188 (**2018**) 145–151.

[182] S. Huang, E. Yang, Y. Liu, J. Yao, W. Su, Q. Xiao, Low-temperature rapid synthesis of nitrogen and phosphorus dual-doped carbon dots for multicolor cellular imaging and hemoglobin probing in human blood, *Sensors Actuators, B Chem.* 265 (**2018**) 326–334.

[183] Z. Wang, F. Li, J. Xia, L. Xia, F. Zhang, S. Bi, G. Shi, Y. Xia, J. Liu, Y. Li, L. Xia, An ionic liquid-modified graphene based molecular imprinting electrochemical sensor for sensitive detection of bovine hemoglobin, *Biosens. Bioelectron.* 61 (**2014**) 391–396.

[184] K.S. Ahn, J.H. Lee, J.M. Park, H.N. Choi, W.Y. Lee, Luminol chemiluminescence biosensor for glycated hemoglobin (HbA1c) in human blood samples, *Biosens. Bioelectron.* 75 (**2016**) 82–87.

[185] Z.S. Traore, S.M. Shah, X. Su, Flow-injection chemiluminescence determination of haemoglobin in the blood, *Luminescence.* 28 (**2013**) 56–62.

[186] H. Li, X. Yan, S. Qiao, G. Lu, X. Su, Yellow-Emissive Carbon Dot-Based Optical Sensing Platforms: Cell Imaging and Analytical Applications for Biocatalytic Reactions, *ACS Appl. Mater. Interfaces.* 10 (**2018**) 7737–7744.

[187] J. Wang, J. Qiu, A review of carbon dots in biological applications, *J. Mater. Sci.* 51 (**2016**) 4728–4738.

[188] P. Das, M. Maruthapandi, A. Saravanan, M. Natan, G. Jacobi, E. Banin, A. Gedanken, Carbon Dots for Heavy-Metal Sensing, pH-Sensitive Cargo Delivery, and Antibacterial Applications, *ACS Appl. Nano Mater.* 3 (**2020**) 11777–11790.

[189] A. Saravanan, M. Maruthapandi, P. Das, S. Ganguly, S. Margel, J.H.T. Luong, A. Gedanken, Applications of N-Doped Carbon Dots as Antimicrobial Agents, Antibiotic Carriers, and Selective Fluorescent Probes for Nitro Explosives, *ACS Appl. Bio Mater.* 3 (**2020**) 8023–8031.

[190] N. Jamaludin, S.A. Rashid, T. Tan, Natural biomass as carbon sources for the synthesis of photoluminescent carbon dots, Elsevier Inc., (**2019**) 109-134.

[191] P. Namdari, B. Negahdari, A. Eatemadi, Synthesis, properties and biomedical applications of carbon-based quantum dots: An updated review, *Biomed. Pharmacother.* 87 (**2017**) 209–222.

[192] P. Zuo, X. Lu, Z. Sun, Y. Guo, H. He, A review on syntheses, properties, characterization and bioanalytical applications of fluorescent carbon dots, *Microchim. Acta.* 183 (**2016**) 519–542.

CHAPTER 2

Chiral Resolution of Racemic Amines in µ-Reactor-Crystallizer

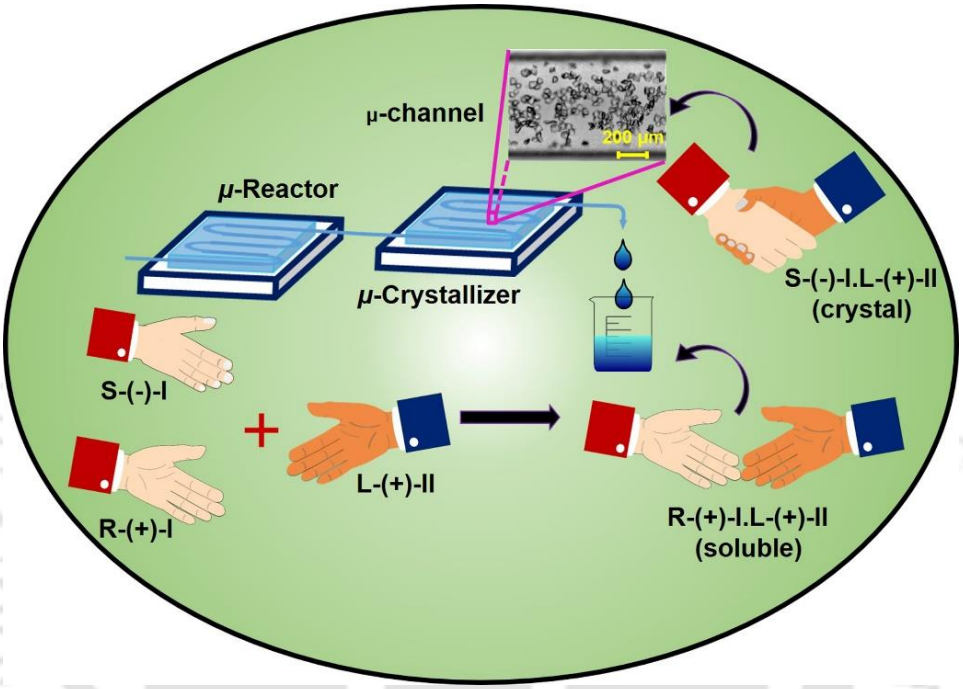

CHAPTER 2

Chiral Resolution of Racemic Amines in μ-Reactor-Crystallizer

The production of pure chiral drugs in a continuous manner is one of the major issues for pharmaceutical industries. A micro continuous process is developed for chiral separation of racemic molecule exploiting a "classical" method of diastereomer formation and subsequent crystallization. A flexible μ-reactor and μ-crystallizer are fabricated for the continuous production of diastereomer salt crystals from racemic α-phenylethylamine (I) where optically active L-(+)-tartaric acid (II) is used as resolving agent. The process described in this work is capable to produce pure crystals at ~ 33 times faster rate compared to the batch process at identical feed concentrations. The better control over purity and faster resolution suggest that this low-cost micro-continuous process could be implemented in industries through very-large-scale integration (VLSI). This work is scientifically acknowledged in ***"Chemical Engineering Science"****.*

2.1 Introduction

Stereoisomers contain the same atoms and groups with the same connectivity, but different orientations in the space. If stereoisomers are mirror images of each other, it is called enantiomers. Enantiomers possess similar physical and chemical properties in an achiral environment. They differ only in the way they interact with other chiral molecules [1] or in a chiral environment, viz. they rotate plane-polarized light in opposite directions. In general, most pharmaceutical drugs are chiral [2]. Several components used in the pharmaceuticals, foods, fine-chemicals, agrochemicals, and cosmetic industries, are available in racemic mixtures (an

equimolar mixture (50% - 50%) of enantiomers) due to their inherent entropic benefit toward equilibrium. Only one of the enantiomers of the racemic mixture is usually biologically active. The presence of another enantiomer can be treated as an impurity and this often causes adverse pharmacological or toxicological side effects in humans [3]. Hence, with strict regulation, Food and Drug Administration (FDA) regularly promotes pharmaceutical industries to analyze the impact of each enantiomer individually and to produce drugs that contain only the pure, therapeutically active enantiomer [4].

Industrial processes generally prefer a continuous mode of operation which have advantages over a batch process. However, the majority of the pharmaceutical productions still follow a batch approach specially for bulk chemicals and where purity is not much of a concern. For the last few decades, pharmaceutical industries, to reduce the cost of drugs, are looking for new process technologies [5,6]. Thus, continuous or semi-continuous production, separation, or extraction processes are receiving significant attention with improved purity, yield, and efficiency [7,8]. Along with this, process intensification also has become the central requirement which can be achieved on a microfluidic platform due to recent advancements in µ-mixture, µ-reactor, µ-crystallizer, and µ-extractor [9,10].

This work focuses on developing a semi-continuous process for the resolution of chiral molecules with simultaneous reaction and crystallization in a microfluidic platforms for the production of optically pure chiral molecules. Specifically, we have chosen the resolution of chiral amines, α-phenylethylamine, from its racemic mixture using L-(+)-tartaric acid as a chiral resolving agent. Sequential µ-reactor and µ-crystallizer are employed for the resolution and the investigation is focused on the controlling parameters such as the concentrations and the flow rate of the reagents to ensure the purity of the enantiomer. We also provide a comparative study

of the purity of the synthesized μ-crystals, obtained from the bulk batch process and the continuous microfluidics.

2.2 Experimental section

2.2.1 Materials

The commercially available enantiomers, R-(+)-α-phenylethylamine, S-(-)-α-phenylethylamine, L-(+)-tartaric acid, D-(-)-tartaric acid, NaOH powder, and diethyl ether were purchased from HiMedia, (India). Methanol solvent was procured from SRL, (India). All reagents and solvents were used without further purifications unless otherwise specified. Sylgard^{TM} 184 Silicone Elastomer Kit for the preparation of polydimethylsiloxane (PDMS) was purchased from Dow Chemical International PVT. LTD. USA. Acrylonitrile Butadiene Styrene (ABS) filament was obtained from Ultimaker, Netherlands. Filter paper (100R) was acquired from Axiva, India. Silicone rubber tubes and non-toxic polyethylene tubing were bought from Sigma-Aldrich USA and Pro Lab Marketing PVT. LTD. India, respectively. 10 mL Dispo Van disposable syringes were purchased from 1mg, India. Peltier elements were purchased from Robotbanao, India.

2.2.2 Apparatus

For the study of material properties, Circular dichroism spectroscopy (CD), Polarimeter, UV-Vis spectroscopy (UV-Vis), Differential scanning calorimetry (DSC), Attenuated Total Reflectance Fourier transform infrared (ATR-FTIR), Raman spectroscopy, X-Ray diffraction (XRD), Field emission transmission electron microscope (FETEM), Field emission scanning electron microscope (FESEM), and Nuclear magnetic resonance (^{1}H NMR) were used.

The formation of diastereomeric salt was examined using CD (JASCO J-815 CD) Spectrometer. The spectra of each sample (5 mg/mL) were examined with the help of the JASCO spectra manager of version 2.0. The CD spectra were recorded in an inert N_2 environment using methanol as a solvent and a high-precision Quartz SUPRASIL cuvette that has a path length of 1 mm. The percentage of enantiomeric excess (% ee) of diastereomeric salt was calculated using a polarimeter (Rudolph, 14-8.5-100-6.0). The specific rotations of each pure enantiomer and their mixture ((R-(+)-α-phenylethylamine, S-(-)-α-phenylethylamine)) dissolved in methanol were measured at 589 nm on a Rudolph polarimeter equipped with a sodium lamp at ~ 25 °C. The process was repeated for the unknown sample. The cell volume was 7 mL and the optical path length was 10 cm. The UV-Vis (Shimadzu, UV-2600 230 V EN spectrophotometer) absorbance of the samples (0.5 mg/mL) was measured to quantify the diastereomer in the UV visible region (200 nm – 800 nm). DSC (Netzsch, STA449F3A00) was used to determine the thermal properties of the crystals. The samples (4 mg) were heated from 0 °C to 250 °C at a heating rate of 10 K/min to determine the exact melting temperature (T_m). The presence of functional groups of crystal was examined by ATR-FTIR (PerkinElmer Spectrum Two) in the frequency range of 400 cm^{-1} – 4000 cm^{-1}. Micro-Raman spectroscopy (Horiba Jobin Vyon, LabRam HR) was used to validate functional groups. The spectra were acquired at an acquisition duration of 10 s with an excitation wavelength of 532 nm. The XRD (Rigaku, Micromax-007HF using Cu-Kα-Kβ radiations at λ = 1.54 A°, 40 kV, 40 mA) was performed in the angle range of 10° – 40° at a scan rate of 5° per minute to analyze the structure of crystals. FETEM (JEOL, JEM 2100F at the acceleration voltage of 200 kV) was used to get the detailed morphology of the salt crystal. The sample was prepared by depositing a methanol drop containing salt crystals on a 400-mesh carbon-coated copper grid (SPI, USA), and then dried at room temperature in a vacuum oven.

FESEM (Zeiss, Gemini 300 at the acceleration voltage of 30 kV) was performed for elemental mapping of materials. ^{1}H NMR (600 MHz, Bruker) was used for the compositional analysis of materials. A small quantity (2 mg) of sample salt was dissolved in 600 µL deuterated solvent (methanol – d_4) in a sealed Thrift Grade tube to perform NMR. A syringe pump (Harvard Apparatus, PHD 2000) was used to infuse the fluids inside the µ-mixture reactor at a controlled flow rate. The flow connection from the syringe to the µ-reactor was accomplished by silicone rubber tubes (Sigma-Aldrich, I.D. × O.D. 1/16 inch × 1/8 inch) and micropipette tips (Tarson, 0.2 µL – 10 µL). Whereas the µ-reactor to µ-crystallizer was connected using non-toxic polyethylene tubing (Intramedic Clay Adams, I.D. × O.D. 1/67 inch × 1/23 inch). The raffinate of µ-crystallizer was also collected using polyethylene tubing. 3D printer (Ultimaker 3, Netherlands) was used to mold the ABS wire in a round serpentine shape. This 3D-printed ABS wire was then used as a sacrificial mold for the fabrication of a PDMS microfluidic channel having an inner diameter of ~ d = 500 µm. Peltier elements were used as heating and cooling elements in µ-reactor and in µ-crystallizer, respectively. A regulated DC (0 – 30 V, TD3202M Apalb, India) power supply was used as a voltage source for Peltier elements. All videos and images were recorded using a CCD camera (Zeiss Axiocam 503 color) attached with an optical microscope (Carl Zeiss, Axio Scope.A1, Model AIMAT HAL 100).

2.2.3 Methods

2.2.3.1 Solution preparation

First, ~ 0.92 mM solutions of L-(+)-tartaric acid and racemic α-phenylethylamine were prepared separately in methanol. These solutions were then heated up to ~ 70 °C for 5 to 10 min and then

cooled down to room temperature of ~ 25 °C. Subsequently, these solutions were filtered through filter paper to remove the dust particles (if any) and used for further experiments.

2.2.3.2 Batch process

The L-(+)-tartaric acid solution was heated to ~ 70 °C in a conical flask and the equimolar racemic α-phenylethylamine solution was carefully added into it in a dropwise manner to avoid foaming while stirring. This solution was then stirred for another 5 to 10 min and then filtered through a filter paper to remove any dust particles present in it. The solution was then cooled down to room temperature and kept in a refrigerator at ~ 4 °C. It takes ~ 72 h to form the crystals of (S-(-)-α-phenylethylamine. L-(+)-tartaric acid) salt at this condition. Often needle-shaped impure salt crystals also develop instead of pure prismatic crystals. This impure needle-shaped crystal can be redissolved by raising the temperature of the solution along with the addition of a small amount of methanol and again recrystallizing the salt following the procedure described above. The white prismatic salt crystals were separated using a filter paper and washed with a small volume (~ 5 mL) of fresh methanol to remove any unwanted adhered components. The crystals were then dried at low pressure in a vacuum desiccator before further use.

2.2.3.3 μ-mixture reactor and μ-crystallizer fabrication

A 3D printed serpentine microfilament (~ d = 500 μm) was fabricated by extruding ABS using the 3D printer (Ultimaker 3).

A molding technique was used to fabricate a microchannel in PDMS. First, part A (oligomer) and part B (crosslinker) of the Sylgard^{TM} 184 elastomer kit were mixed thoroughly in a ratio of 10:1. The mixture was then degassed in a vacuum desiccator for 40 min to remove all the air

bubbles trapped inside. On a cleaned glass slide with the help of double-sided tape, a rectangular mold was prepared. A small amount of the oligomer-crosslinker mixture was poured into it and shaken to make a thin film of oligomer over the glass slide. The film was then partially cured at 85 °C in a hot air oven for half an hour and subsequently cooled down to room temperature. The prefabricated 3D printed serpentine ABS microfilament was then cleaned with DI water, dried with nitrogen flow, and then placed on top of the thin partially cured PDMS film. Again some of the degassed oligomer-crosslinker (10:1) mixture was poured on top of it. It was ensured that no bubbles were trapped inside the liquid oligomers-crosslinker mixture after pouring. The arrangement was then kept in a hot air oven at 85 °C for 6 h to fully crosslink the PDMS. It was made sure that the ends of the ABS filament were outside the PDMS block. After curing, the ABS microfilament embedded PDMS block was dipped into an acetone bath for 12 h. The acetone dissolved the ABS microfilament, and a microchannel was formed inside the PDMS block. Later, the microchannel embedded PDMS block was further ultra-sonicated in the acetone bath for 5 h to remove any trace of ABS completely. The microchannel was then repeatedly washed with acetone and DI water for 10 – 15 min. Finally, the cleaned micro-channel was dried by blowing nitrogen gas and then keeping it in a hot air oven for 30 min at 75 °C. **Figure 2.1** shows a schematic as well as an optical image of a serpentine-shaped circular microchannel with an inner diameter of ~ d = 500 µm, and a total path length of ~ l = 45 cm.

2.3 Results and discussion

2.3.1 Resolution in µ-reactor-crystallizer

Figure 2.1 shows the schematic of the experimental setup for the chiral resolution of S-(-)-α-phenylethylamine in a microfluidic platform by fractional crystallization of its diastereomeric

salts with L-(+)-tartaric acid. From now on, α-phenylethylamine and tartaric acid will be denoted by (I) and (II), respectively. Briefly, syringe 1 and syringe 2 (Cyan and red-colored syringe in **Figure 2.1**) were filled with racemic α-phenylethylamine (0.92 mM) (I) and L-(+)-tartaric acid (0.92 mM) (II) solutions, respectively. These solutions were injected with the help of a syringe pump into the µ-reactor at a constant flow rate of 5 µL/min. The µ-reactor was maintained at a constant temperature of (~ 70 °C) using Peltier element 1. The residence time of reactants, t_r, was ~ 18 min inside the µ-reactor. Two diastereomer salts [S-(-)-I.L-(+)-II, and R-(+)-I.L-(+)-II] were formed in the µ-reactor as per the reaction mechanism shown in **Figure 2.2.**

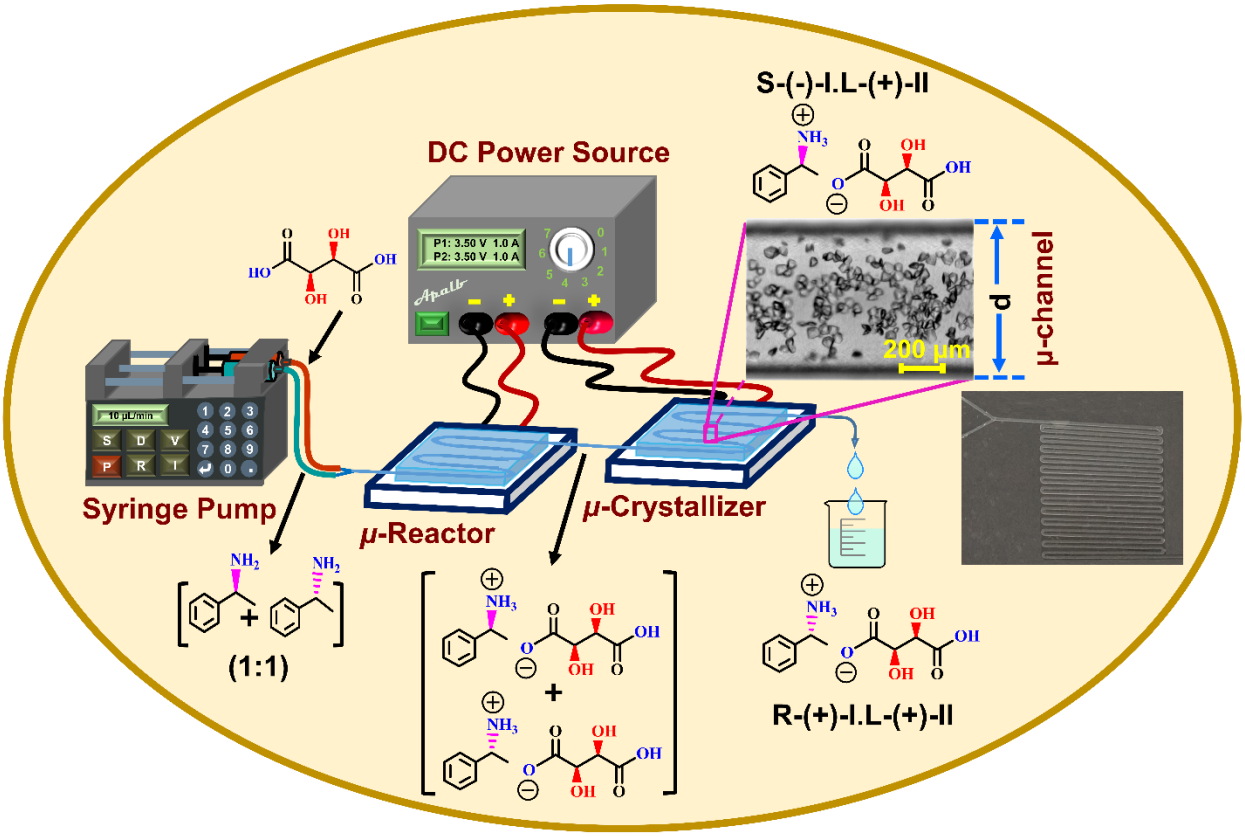

Figure 2.1 Schematic representation of the experimental setup for the separation of S-(-)-α-phenylethylamine from its racemic mixture in a continuous manner at a microfluidic platform. An optical image of the serpentine microchannel (right) and the micrograph of the salt crystals inside a µ-crystallizer is shown in the top right.

Among these two diastereomers, R-(+)-I.L-(+)-II is relatively more soluble compared to S-(-)-I.L-(+)-II. The solubility of the both diastereomers salt in methanol was determined at the experimental temperature of 25 °C. A known amount (~ 50 mg) of both diastereomers salt was weighed in a separate glass vial equipped with a magnetic stirrer, and a known amount of solvent (Methanol) was added. The vials were placed on a magnetic stirrer plate and stirred at 700 rpm for 10 h at 25 °C to ensure attainment of a solid−liquid equilibrium, after which the solubility was determined gravimetrically. It was found that, the solubility of the prism-shape S-(-)-I.L-(+)-II diastereomer salt crystal and R-(+)-I.L-(+)-II diastereomers salt 0.0051 g/mL and 0.6074 g/mL, respectively. Each measurement was conducted at least three times, and the relative deviation was found that less than 5%. Next, the solution containing two diastereomer salts was passed through a μ-crystallizer, connected in series to the μ-reactor. The average temperature of μ-crystallizer was maintained at ~ 4 °C with the help of a second Peltier element 2. Thus, the less soluble salt (S-(-)-I.L-(+)-II) was crystallized inside the μ-crystallizer and the highly soluble salt (R-(+)-I.L-(+)-II) came out of the μ-crystallizer as raffinate. A CCD camera attached with an optical microscope was used for the in-situ recording of the videos as well as capturing the images at different positions of the μ-crystallizer. At the wall surface of the microchannel, the genesis of the S-(-)-I.L-(+)-II nanocrystals were instigated by heterogeneous nucleation. After running the operation for τ ~ 10 min, the first detectable amount of tiny needle-shaped crystals started to appear throughout the channel of the μ-crystallizer. These crystals grew up with time and almost blocked the crystallizer channel in τ ~ 30 min, as shown in **Figure 2.3**. On the other hand, the raffinate of the crystallizer was continuously collected in a beaker, which contained a high amount of R-(+)-I.L-(+)-II diastereomer salt.

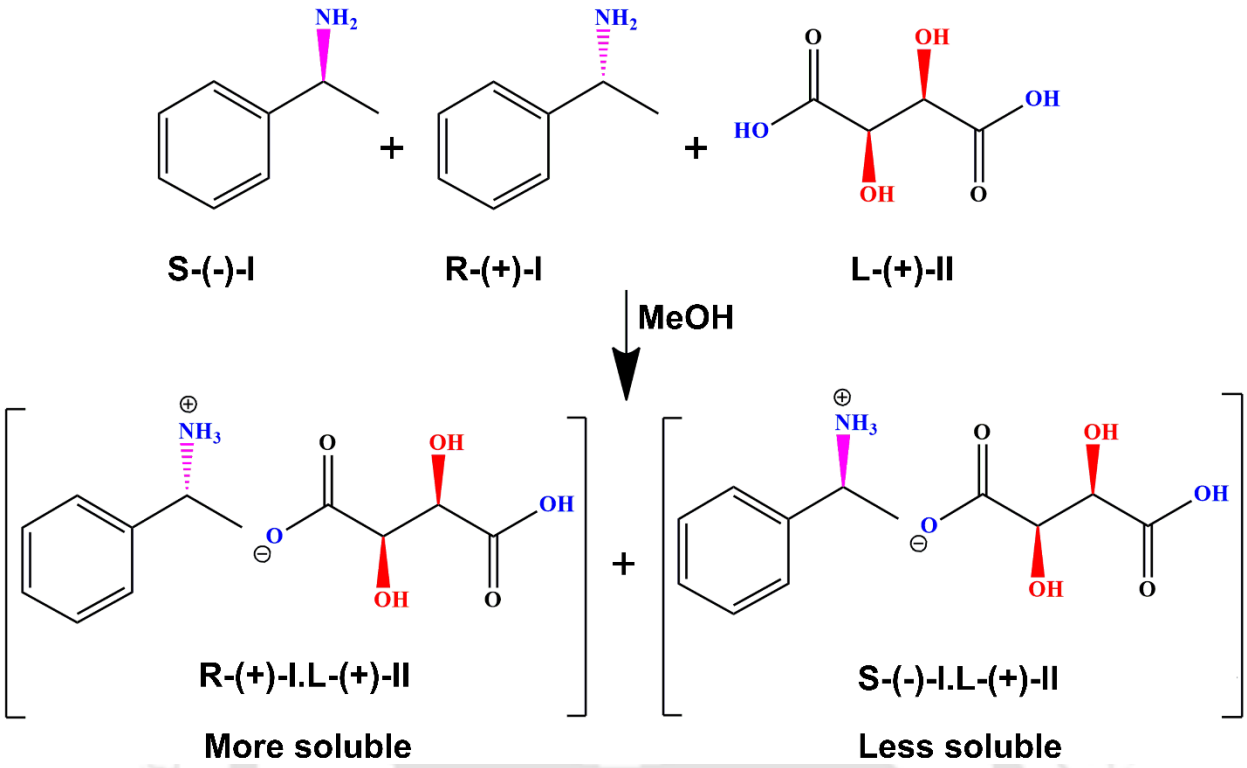

Figure 2.2 Shows the reaction mechanism of L-(+)-tartaric acid with racemic α-phenylethylamine and formed two diastereomers salts S-(-)-I.L-(+)-II (less soluble) and R-(+)-I.L-(+)-II (more soluble).

Generally, S-(-)-I.L-(+)-II diastereomer salt forms two types (shape) of crystals, namely prism and needle shape [11]. The prism-shaped crystals are pure, while the needle-shaped crystals are impure containing some amount of R-(+)-I.L-(+)-II in it [11]. Under the above-specified conditions (**Figure 2.3**), we noticed that most of the formed crystals were in needle shape, which was undesired. Similar experiments were performed with varying feed concentrations ranging from 0.92 mM to 0.31 mM and with flow rates ranging from 5-30 µL/min. It was marked that the time required to form the first detectable tiny crystals as well as to fill up the microchannel with crystals were longer for relatively higher dilution and flow rate. The concentration and flow rate of the feeds are the two parameters that control the purity and

shape of crystals. It was recognized that low feed concentration and the high flow rate is favorable for prism-shaped crystals. Whereas, ample needle-like crystals are found at lower flow rates and high feed concentrations (**Table 2.1**). At the low feed concentration of ~ 0.31 mM, the crystallization rate was decreased by almost ~ 3 times, and the τ for forming the first detectable tiny prism crystals was ~ 30 min when the flow rate of feed was maintained at 5 µL/min (**Figure 2.5**). The µ-crystallizer was almost filled up with crystals after τ = ~ 2 h.

These crystals were collected by injecting fresh methanol at a high flow rate in the µ-crystallizer. Notably, the optimum feed concentration and the flow rate were found to be 0.31 mM and 10 µL/min respectively for the prism-like crystal with maximum yield (**Figure 2.5**). Hence, the experiment was conducted at this optimum condition and the collected diastereomer salt crystals were used for further characterization. The collected micron range crystals (5 µm –10 µm) were dried at 40 °C in a hot air oven for 15 min. The dried crystals were used for qualitative and quantitative characterizations. Interestingly, no crystal formation was observed in the batch process for the optimized temperature and concentration, within the total duration of the continuous process. Generally, for the batch process, the crystal formation takes place at a much longer time, ~ 72 h. Plausibly, the rapid formation of the prism-shaped crystals is due to the laminar flow confinement along with the continuous replenishment of the fresh feed solution surrounding the growing crystal. This maintains the constant concentration of the diastereomer salts. This also facilitates the faster dissolution of the impure R-(+)-I.L-(+)-II (if formed any) at the surface of the crystal, compared to the batch process, where the local concentration of the impure R-(+)-I.L-(+)-II surrounding the crystal is relatively high due to local depletion of S-(-)-I.L-(+)-II. Thus prism-shaped pure S-(-)-I.L-(+)-II crystal was obtained from µ-crystallizer. For this, a possible mathematical reaction model is developed in section 2.3.1.1.

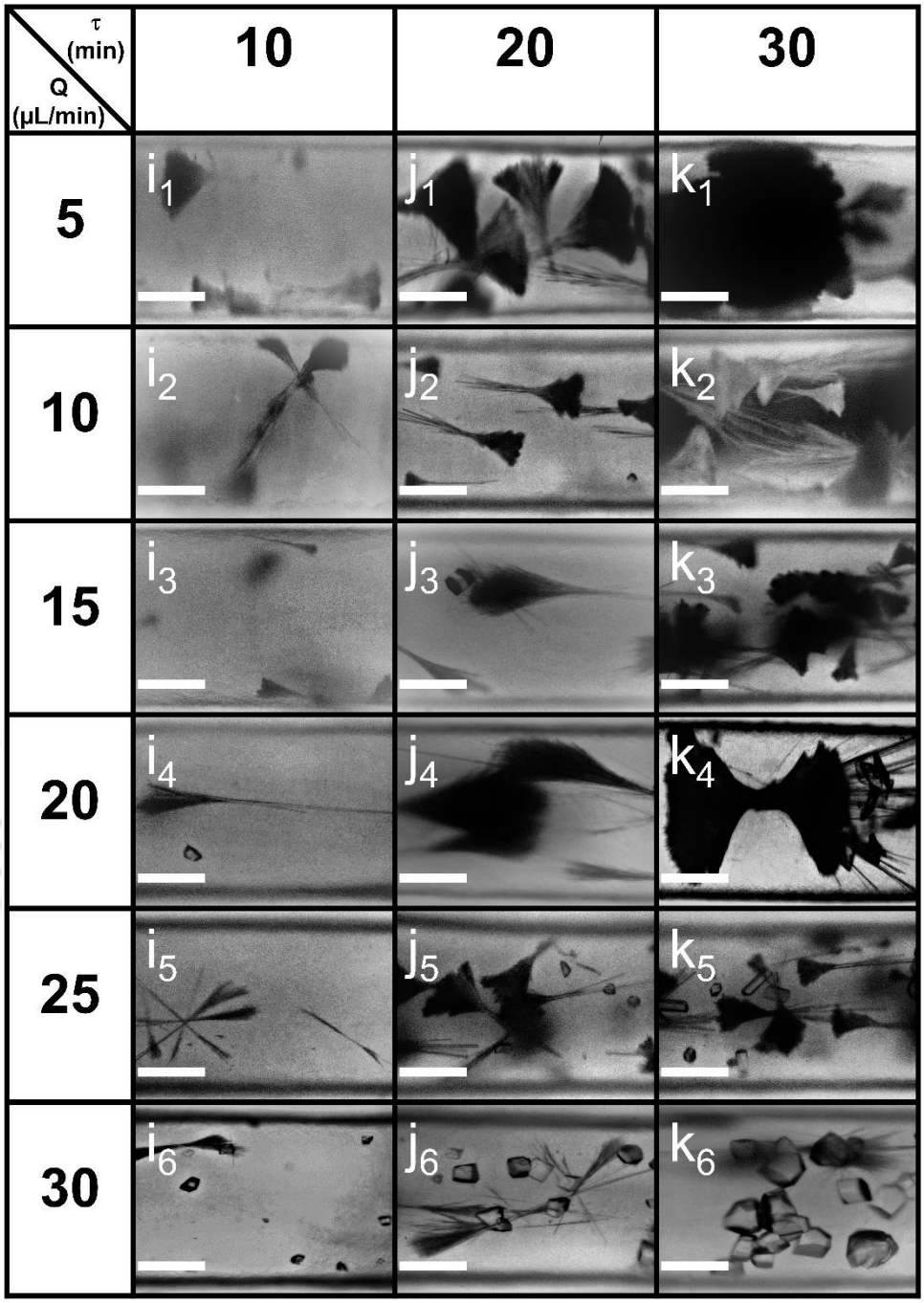

Figure 2.3 Optical micrographs (10X magnification) of diastereomer salt crystals in the μ-crystallizer at different flow rates ranging from 5-30 μL/min. The image shows the formation of the crystals for the feed concentration of 0.92 mM racemic α-phenylethylamine and 0.92 mM L-(+)-tartaric acid at different time duration (10-30 min). (i_1-i_6), (j_1-j_6) and (k_1-k_6) represent the growth of the crystals at τ = 10 min, 20 min, and 30 min, respectively. All the images were recorded at a position, *l* ~ 22 cm of the μ-crystallizer. The scale bar for all the figures is 200 μm.

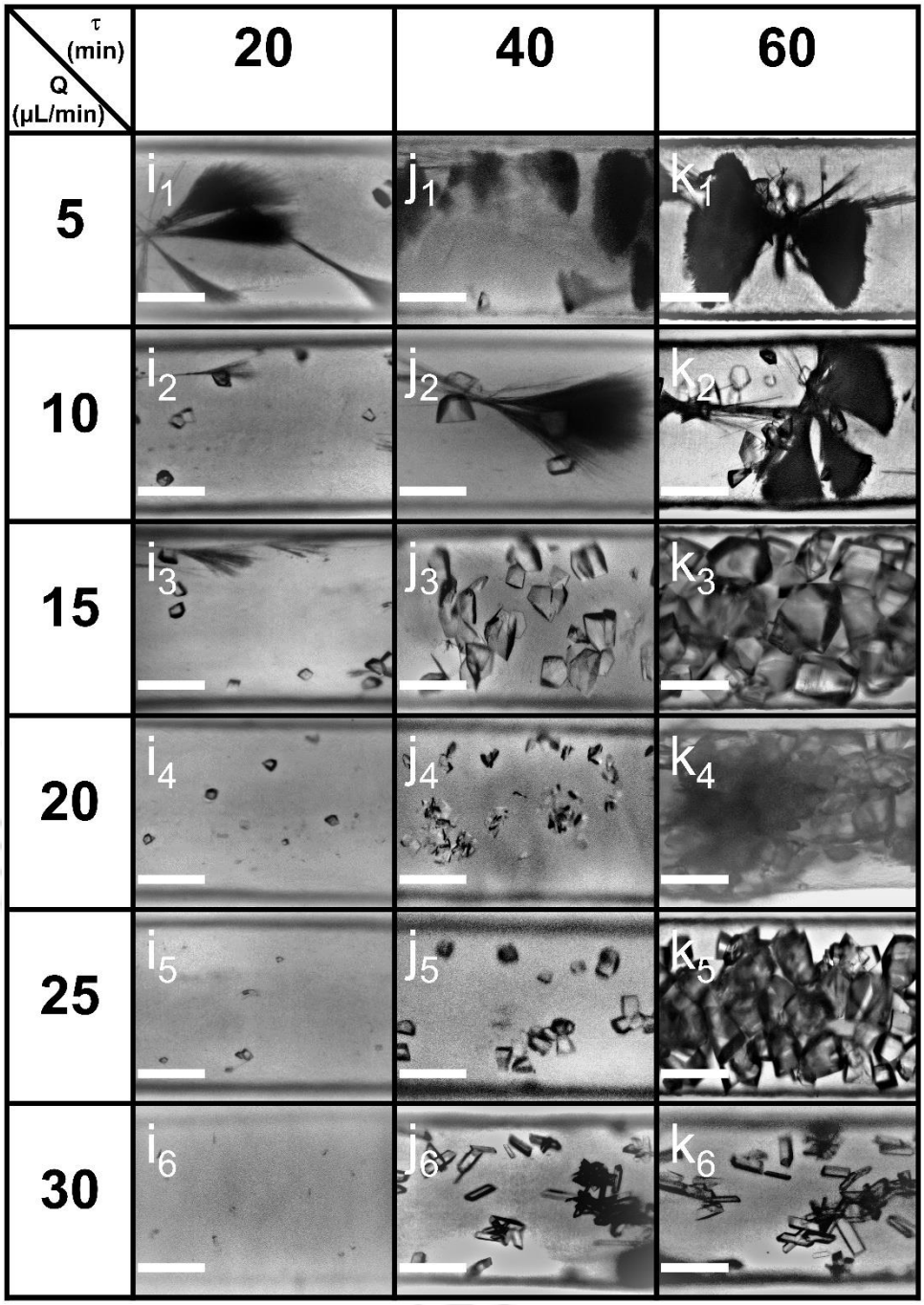

Figure 2.4 Optical micrographs (10X magnification) of diastereomer salt crystals in the μ-crystallizer at different flow rates ranging from 5-30 μL/min. The image shows the formation of crystals in the μ-crystallizer for the feed concentration of 0.61 mM racemic α-phenylethylamine and 0.61 mM L-(+)-tartaric acid at different time duration (20-60 min). At τ = 20 min, image (i_1-i_6) shows the growth of crystals. At τ = 40 min, image (j_1-j_6) shows the growth of crystals. At τ = 60 min, image (k_1-k_6) shows the growth of crystals. All the images were recorded at a position, *l* ~ 22 cm of the μ-crystallizer. The scale bar for all the figures is 200 μm.

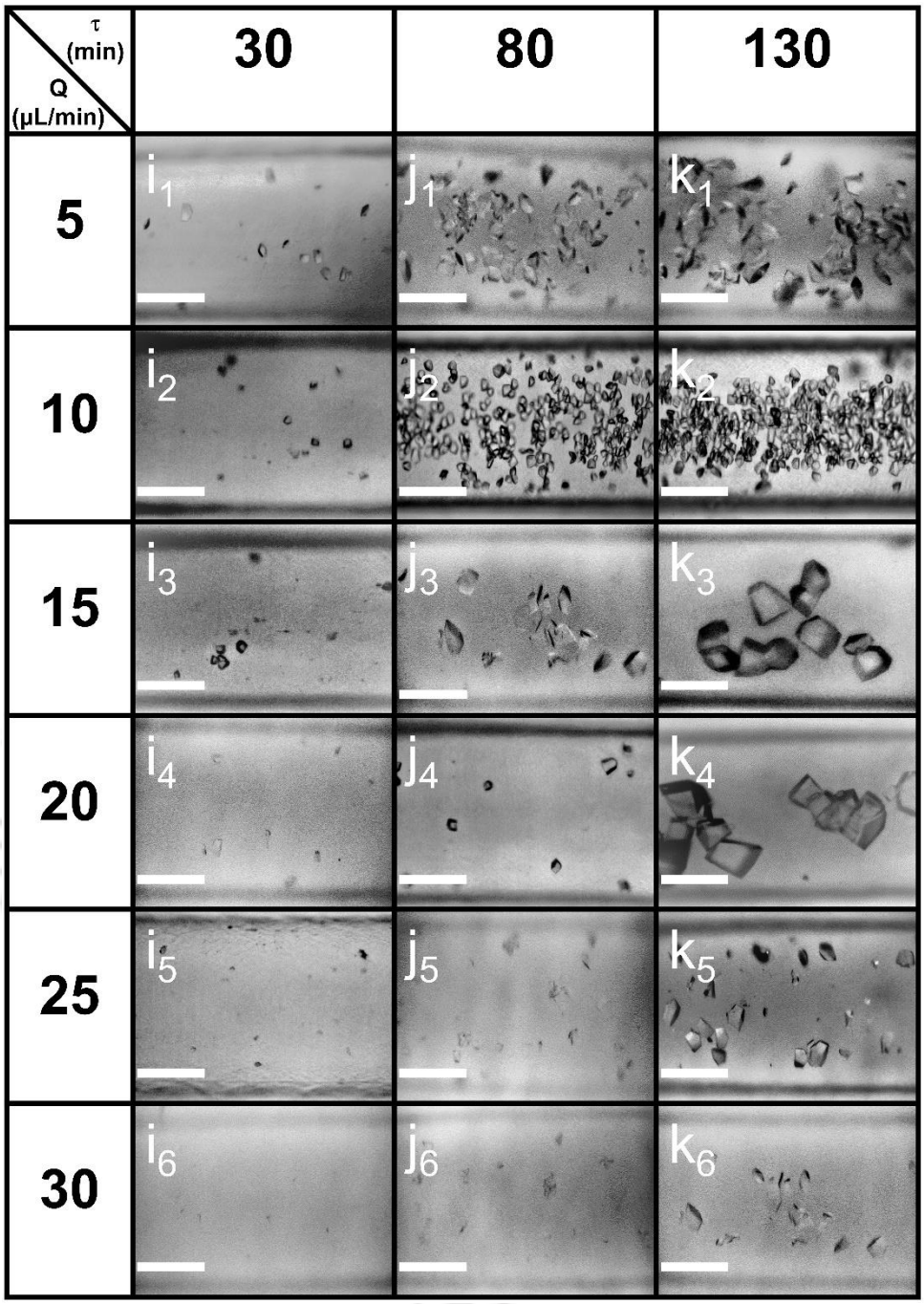

Figure 2.5 Optical micrographs (10X magnification) of diastereomer salt crystals in the μ-crystallizer at different flow rates ranging from 5-30 μL/min. The image shows the formation of crystals in the μ-crystallizer for the feed concentration of 0.31 mM racemic α-phenylethylamine and 0.31 mM L-(+)-tartaric acid at different duration (30-130 min). (i_1-i_6), (j_1-j_6) and (k_1-k_6) represent the growth of the crystals at τ = 30 min, 80 min, and 130 min, respectively. All the images were recorded at a position, *l* ~ 22 cm of the μ-crystallizer. The scale bar for all the figures is 200 μm.

Table 2.1: Diastereomeric crystal structure with concentration and flow rate in µ-crystallizer

Sl. No.	Feed concentration (mM)	Flow rate (µL/min)	Crystal shape (Prism/Needle)
1	0.92	5	Needle
		10	Needle
		15	Needle
		20	Mostly needle
		25	Mostly needle
		30	Almost an equal proportion of needle and prism
2	0.61	5	Needle
		10	Mostly needle
		15	Needle as well as prism
		20	Prism
		25	Prism
		30	Prism
3	0.31	5	Prism
		10	Prism
		15	Prism
		20	Prism
		25	Prism
		30	Prism

2.3.1.1 Rate of formation of prism-shaped crystal

As the feed flows through the µ-reactor-crystallizer at a constant rate, at any instant of time one can assume the process is at a steady state.

Concentration of R-(+)-α-phenylethylamine is [R] mol/m^3,

Concentration of S-(-)-α-phenylethylamine is [S] mol/m^3,

Concentration of L-(+)-tartaric acid is [L] mol/m^3,

Concentration of Methanol is [M] mol/m^3 and [M]>>[R],[S],[L] as the solution is dilute.

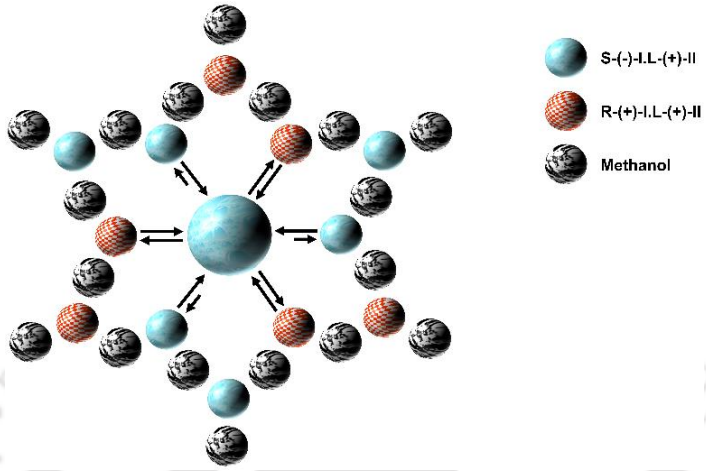

Figure 2.6 A plausible mechanism of the formation of relatively pure S-(-)-I.L-(+)-II salt formation in the micro-continuous process.

Let's us assume the concentration surrounding an infinitesimally small crystal site, the above-mentioned concentrations are constant. This is justified as the growth of the crystal is slow and the fresh feed is always flowing past the crystal site.

The probability of finding an R molecule near the crystal site is =[R]/N; where N=[R]+[S]+[L]+[M].

The probability of finding an S molecule near the crystal site is =[S]/N.

Similarly, the probability of finding L and M molecules are [L]/N and [M]/N, respectively.

Rate of forming S-L complex, $r_{S-L} \propto \left(\frac{[S]}{N}\right).\left(\frac{[L]}{N}\right)$; [as S-L complex is less soluble its dissolution is negligible].

Rate of forming R-L complex, $r_{R-L} \propto \left(\frac{[R]}{N}\right).\left(\frac{[L]}{N}\right)$;

Rate of dissolution of R-L complex, $r_{d(R-L)} \propto \left(\frac{[R-L]}{N}\right).\left(\frac{[M]}{N}\right)$; where [R-L] is the concentration of the already formed R-L complex.

So, the net rate of formation of R-L complex, $r_{R-L} \propto \left[\left(\frac{[R]}{N}\right).\left(\frac{[L]}{N}\right) - \left(\frac{[R-L]}{N}\right).\left(\frac{[M]}{N}\right)\right]$;

Since [M]>>[R],[S],[L] rate of dissolution of R-(+)-I.L-(+)-II complex is high compared to the rate of formation. This shows why the dilute solution favors pure S-(-)-I.L-(+)-II crystals over the concentrated feed solution. Moreover, fresh feed flowing in the µ-continuous process ensures that the surrounding of the S-(-)-I.L-(+)-II crystal is not depleted of S-(-)-I or L-(+)-II molecule to form new S-(-)-I.L-(+)-II salt. This also supports the fact that the high flow rate favors the formation of pure prismatic crystals. Based on the feed concentration and the input flow rate in a µ-reactor crystallizer, a crystal shape map is developed in section 2.3.1.2.

The purity of the recovered amine solely depends on the purity of the diastereomeric crystal formation. Thus in the subsequent section, we focus our discussion on the characterization and the purity of the crystals formed by the optimized feed concentration (0.31 mM) and the flow rate (10 µL/min). The characteristics of the crystals were then compared with the prismatic crystals obtained from the batch process.

2.3.1.2 Image analysis

As shown in **Figure 2.7** and **Figure 2.8**, the size, as well as the number of diastereomer salt crystals, gradually increase with time. The time-evolution of the projected coverage area of the crystals/volume of the µ-crystallizer was monitored with image analysis. The images, recorded at a position of l ~ 22 cm (~ middle of the length of micro-channel) of the µ-crystallizer and at 10 µL/min flow rate of each feed concentration, were analyzed using an open-source software ImageJ at different time intervals. To identify the size or boundary of the salt crystals precisely, the recorded sequences were processed via a color threshold algorithm using ImageJ (See **Figure 2.8**) [12].

By measuring the crystal coverage area $A_c(t)$ at a different time (t), the evolution of the crystal growth dynamics was obtained. Some of the diastereomer salt crystals deposits were not identified by the threshold steps in ImageJ. Therefore, those regions were manually cropped and measured to minimize the errors. The area growth rate (dA_c/dt) of salt-crystals was estimated from the slope of the linear fit of A_c vs t curve (**Figure 2.8**).

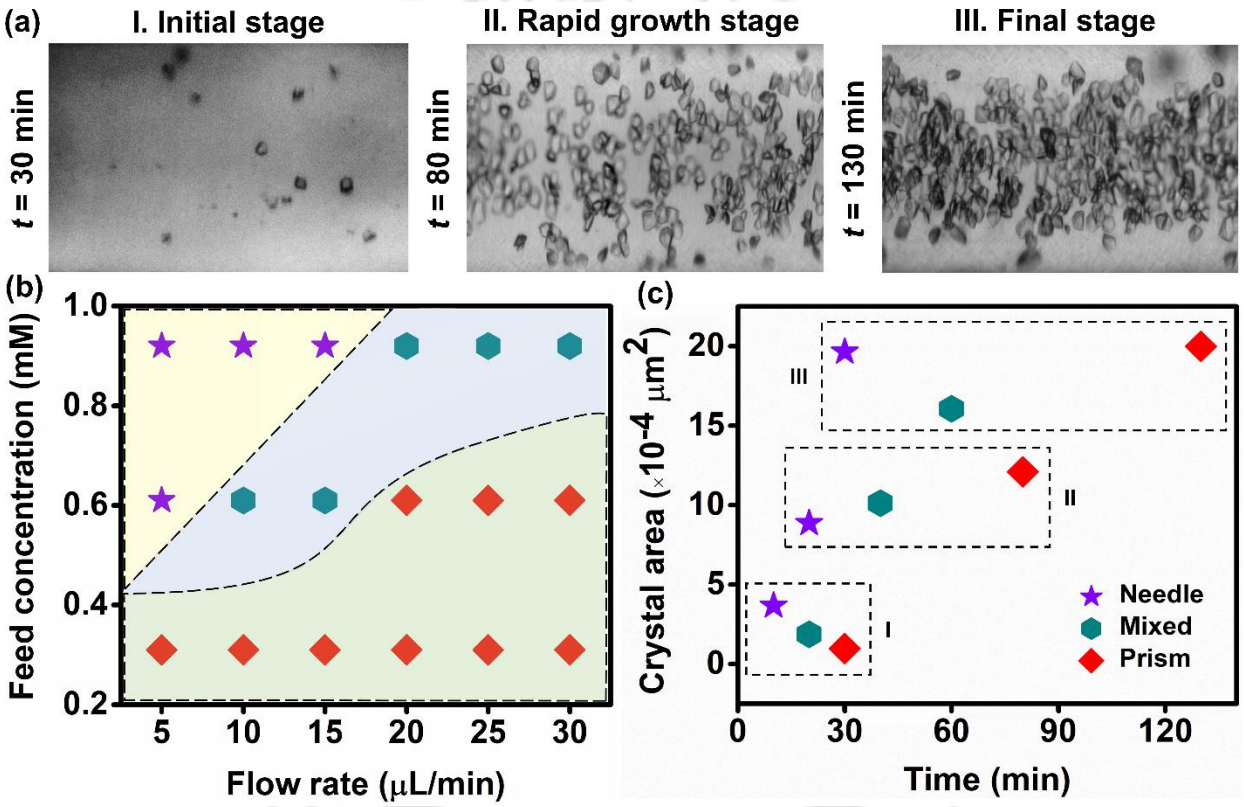

Figure 2.7 Dynamics of both needle and prism type of diastereomer salt in a µ-continuous crystallizer. **(a)** Different stages of the growth-evolution of the prism-shaped diastereomer salt with time. **(b)** Represents the crystal shape-map of the diastereomer salt (needle, mixed, and prism) for different feed concentrations and flow rates. **(c)** The development of salt nucleation reveals three distinct phases: (I) initial slow nucleation stage, (II) rapid growth, and (III) final stages characterized by different growth rates measured.

In the next section, we have characterized and compared the prismatic crystals obtained from both batch and µ-continuous processes. As already shown, by varying the feed concentration and the flow rate, one can easily control the shape of the crystals in a continuous microfluidic platform. However, tuning the shape of the crystals in a batch process is difficult. In an identical condition, the crystal shape appears almost randomly in the batch process. As we are interested in prismatic crystals only, we had to repeatedly dissolve and recrystallize to obtain prismatic crystals from a batch process.

2.3.1.3 Growth rate calculation for the crystals in the micro-continuous process

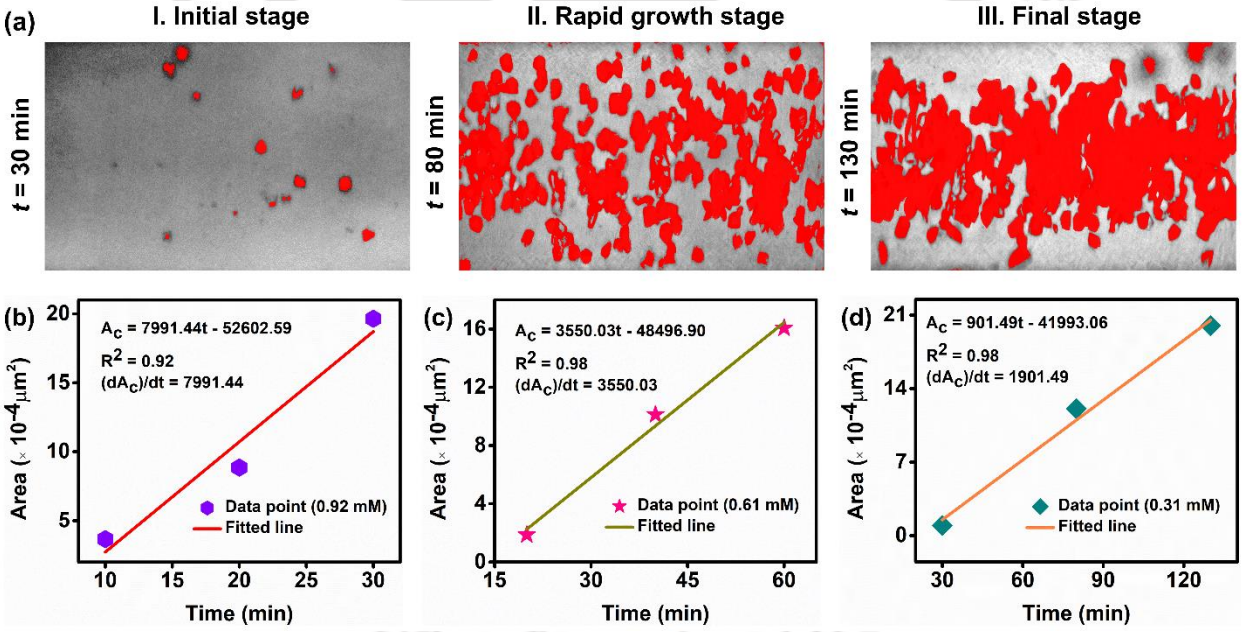

Figure 2.8 The graphs show the growth rate (dA_c/dt) of salt crystals with time (t) and its linear fitted line for different concentrations of feed. **(a)** Different stages of the growth-evolution of the prism-shaped diastereomer salt with time. **(b)** 0.92 mM **(c)** 0.61 mM **(d)** 0.31 mM.

2.3.2 Circular dichroism (CD) spectroscopy

The CD spectra of pure chemicals and the synthesized diastereomers salt crystals (both processes) were recorded at the same concentration (5 mg/mL in methanol) under identical conditions. **Figure 2.9** shows the CD spectra of R-(+) and S-(-)-α-phenylethylamine (I) when mixed with the equivalent amount of L-(+) and D-(-) tartaric acid (II) following the method described in section 2.2.3.2 before refrigeration and crystallization. The solutions show the Cotton effect at around 214 nm [13]. The cotton effect is defined as the characteristic wavelength dependence of the optical rotatory dispersion curve or the circular dichroism curve or both in the vicinity of an absorption band of a substance. The Cotton effect is called positive if the optical rotation first increases as the wavelength decreases, and negative if the rotation first decreases with the decrease in wavelength. The sign of the Cotton effect is governed by the chirality of the tartaric acid (See **Figure 2.10** for CD spectra of the pure components). A positive Cotton effect at ~ 213 nm and a negative Cotton effect at ~ 223 nm are observed for both S-(-)-I.L-(+)-II and R-(+)-I.L-(+)-II. The Cotton effects with the opposite signs are found for S-(-)-I.D-(-)-II and R-(+)-I.D-(-)-II (**Figure 2.9**). To analyze the salt crystals, an equivalent amount of (S-(-)-I.L-(+)-II), obtained from both batch and μ-process, was dissolved in methanol and CD spectra were recorded (**Figure 2.9**). The same Cotton effect of S-(-)-I.L-(+)-II was observed for both the crystals with an additional shallow negative peak at ~ 227 nm, which confirms the salt formation. Notably, the intensity of the two peaks is almost similar for the salt crystals obtained from both methods. The enantiomeric excess of the recovered amine was estimated using a polarimeter and was found to have ~ 78% (see section 2.3.12.1).

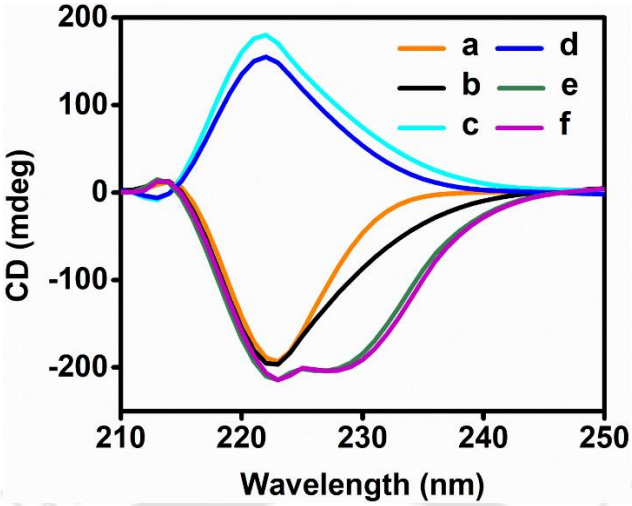

Figure 2.9 (Colour line) CD spectra of chemical mixture of R-(+)-I and L-(+)-II (orange) **(a)**, chemical mixture of S-(-)-I and L-(+)-II chemical (black) **(b)**, chemical mixture of S-(-)-I and D-(-)-II chemical (cyan) **(c)**, chemical mixture of R-(+)-I and D-(-)-II chemical (blue) **(d)** before crystallization. CD spectra of methanol solution of S-(-)-I.L-(+)-II diastereomers salt crystals obtained from batch process (custom green) **(e)** and μ-process (custom pink) **(f)**.

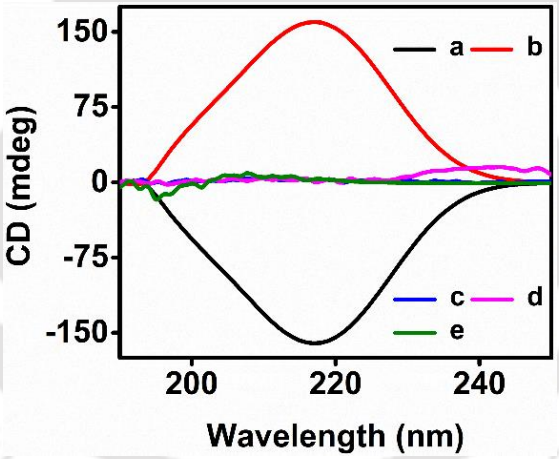

Figure 2.10 (Colour line) CD spectra of pure chemicals, L-(+)-II (black) **(a)**, D-(-)-II (red) **(b)**, R-(+)-I (blue) **(c)**, S-(-)-I (pink) **(d)**, and racemic α-phenylethylamine (green) **(e)**.

2.3.3 UV-Visible spectroscopy

The UV-Vis spectra of diastereomer salt crystals, which are synthesized by both batch and continuous (in μ-reactor and μ-crystallizer) processes are compared in **Figure 2.11a**. Both the

samples for UV-Vis analysis were prepared by dissolving 2 mg of crystal in 4 mL of methanol. Although the absorbance peaks are similar for both the salt crystals, the intensity for the crystals from µ-crystallizer is slightly higher compared to the crystals from the batch process. This may be due to the presence of trace impurities in the salt crystals from the batch process. According to Lambert-Beer Law, an increase in concentration increases the absorbance value. Hence, this result indicates that the salt prepared by the µ-crystallizer process (having slightly higher absorbance compared to that of the crystals from the batch process) is at least as pure as the salt obtained from the batch process. Also, we have performed UV–Vis analysis of both needle-shaped S-(-)-I.L-(+)-II crystals and R-(+)-I.L-(+)-II diastereomeric salt (See **Figure 2.12**). Since both are diastereomeric salt crystals, a big difference was not noticed but a small shift in UV–Vis spectra was observed.

2.3.4 Differential scanning calorimetry (DSC)

Figure 2.11b shows the DSC curve of synthesized diastereomer salt crystal S-(-)-I.L-(+)-II from both the processes, i.e., batch as well as with µ-continuous process. The melting point of S-(-)-I.L-(+)-II salt crystals depends on the purity and composition. Impure solids melt at lower temperatures and over a wider temperature range [14]. However, pure solids exhibit a narrow temperature melting range usually 1 to 2 °C. Impurities cause structural defects in the molecules and weaken the intermolecular bonds. Furthermore, when molecules are tightly packed together, a substance has a higher melting point and requires high energy to break the bond than a substance with molecules that do not pack well [15]. The synthesized S-(-)-I.L-(+)-II salt crystal possesses the melting peak (endothermic) at 198 °C for batch process and 199 °C for the µ-continuous process (**Figure 2.11b**). It revealed that the synthesized salt crystal of the µ-

continuous process is as pure as the crystals obtained from the batch process or purer than that. We have also calculated the enthalpy from the DSC data, by dividing the integrated peak area by the rate of the heating. The enthalpy change for the melting of the crystals obtained from the batch process is ΔH = 360 J/g. Whereas, the same for that obtained from the µ-continuous process, is ΔH = 371 J/g. The higher enthalpy change signifies that higher energy is required to break the bonds in the salt crystals from µ-crystallizer than that from the batch process. These results strongly confirm that the synthesized diastereomers salt crystals obtained from µ-continuous possess higher crystallinity [16,17]. Also, Attenuated total reflectance Fourier transform infrared (ATR-FTIR) spectroscopy and Raman spectroscopy of synthesized diastereomers salt crystals were performed to investigate the functional groups and bonding between the atoms.

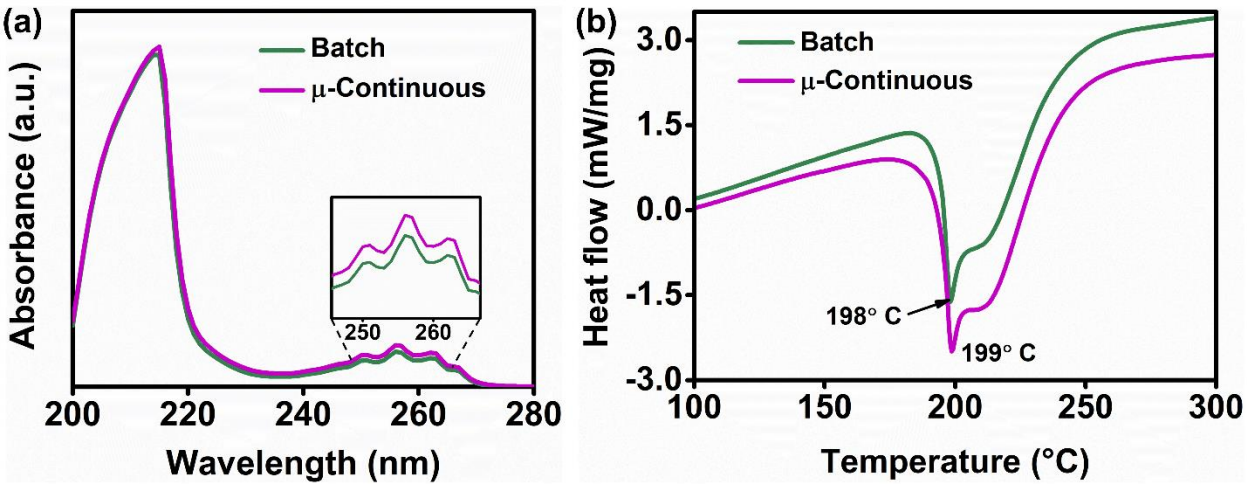

Figure 2.11 Characterization of diastereomer salt crystals synthesized by batch process (green) and µ-continuous process (custom pink): **(a)** UV-Vis spectroscopy. **(b)** DSC.

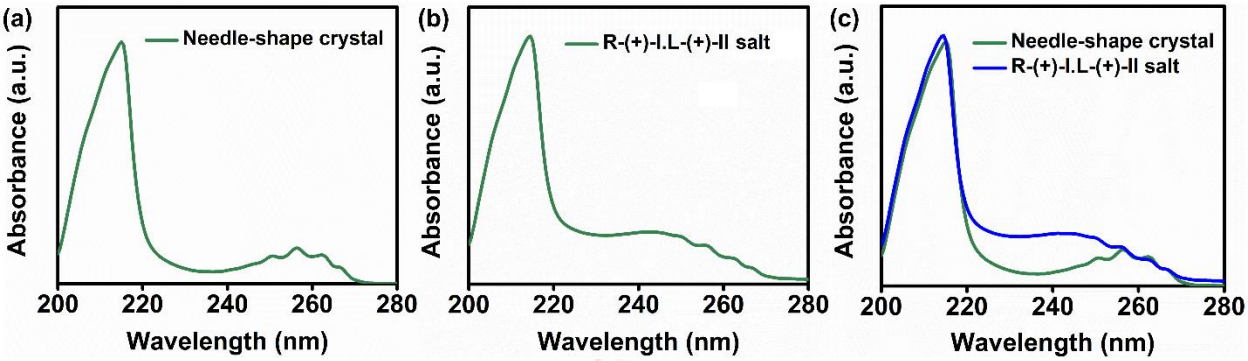

Figure 2.12 Show **(a)** UV-Vis plot of needle-shape (S-(-)-I.L-(+)-II) diastereomer salt crystal. **(b)** UV-Vis plot of R-(+)-I.L-(+)-II diastereomer salt. **(c)** UV-Vis plot of needle-shape (S-(-)-I.L-(+)-II) diastereomer salt crystal and (R-(+)-I.L-(+)-II) diastereomer salt.

2.3.5 Attenuated total reflectance Fourier transform infrared (ATR-FTIR) spectroscopy

Figure 2.13a, b shows ATR-FTIR spectra of diastereomer salt S-(-)-I.L-(+)-II crystals, which were synthesized by batch as well as µ-continuous processes. The characteristic peak at 3565 cm^{-1} is corresponded to –O–H stretching of tartrate whereas, the peak at 3405 cm^{-1} confirms the presence of primary amine (N–H), in the salt crystal. A broad peak at 3109 cm^{-1} and 2927 cm^{-1} is attributed to =C–H and –C–H stretching, respectively. An individual peak at 1735 cm^{-1} represents the strong vibration bond of carbonyl ν(C=O), which indicates the presence of an acid moiety, and peaks at 1610 cm^{-1} and 1375 cm^{-1} signify the asymmetric carbonyl ν_{as}(COO–) and symmetric ν_s(COO–) stretch, respectively [18]. These two vibrational bonds ν_{as}(COO–) and ν_s(COO–) certify the proton transfer from L-(+)-tartaric acid to S-(-)-α-phenylethylamine molecules during the mono-ionized diastereomer salt crystal formation. Overlapped bands were observed between 1475 cm^{-1} to 1380 cm^{-1} due to indistinguishable δ(N–H) and ν_{as}(COO–) vibrations at similar energy. The characteristic peak of synthesized crystalline salt at 1375 cm^{-1} is due to the medium bending mode of C–H while at 1232 cm^{-1} peak for C–N bonding. The

specific peak at 1060 cm^{-1} shows the strong stretching interaction between carbon and oxygen (C–O) atoms. An intense peak at 967 cm^{-1} is assigned for strong bending between carbon atoms (C=C). The particular peaks at 867 cm^{-1}, 766 cm^{-1}, 700 cm^{-1}, 605 cm^{-1}, 539 cm^{-1}, and 460 cm^{-1} all signify the strong bending mode of C–H with sp^3 hybridization [19]. It should be noted that all the peak intensities of the crystals are higher for µ-continuous possess than the batch process.

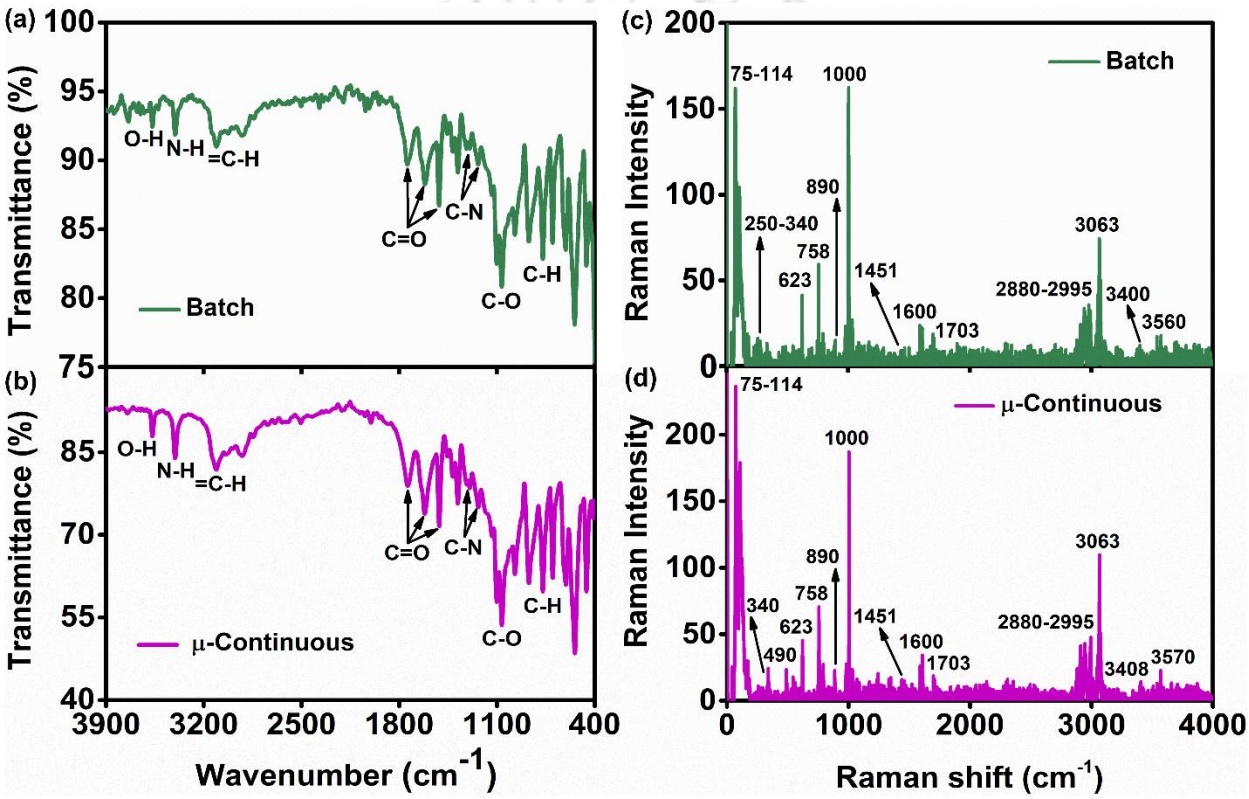

Figure 2.13 Characterization of diastereomer salt crystals synthesized by batch process (green) and µ-continuous process (custom pink): **(a)** and **(b)** ATR-FTIR spectroscopy. **(c)** and **(d)** Raman spectroscopy.

2.3.6 Raman spectroscopy

Raman spectra of salt (S-(-)-I.L-(+)-II) crystal powder was recorded using a microscopic glass slide as a substrate (**Figure 2.13c, d**). The band ranging from 75 – 114 cm^{-1} is due to lattice

vibration in crystals, and the band at 340 cm^{-1} corresponds to linear aliphatic chain vibration/disordered form of D band (C–C) [20]. The Raman shift at 490 cm^{-1} and 623 cm^{-1} are responsible for C–C–N scissoring and phenyl ring in-plane deformation, respectively. The band at 758 cm^{-1} is attributed to C–H aromatic bending and ring bending, whereas the peak at 890 cm^{-1} is for C–O–C vibration. The strongest peak at 1000 cm^{-1} is the typical phenyl ring breathing. The ethyl CH_2 scissoring vibration band shows at 1451 cm^{-1}, and the peak at 1600 cm^{-1} represents the ring in-plane deformation [21]. A large number of vibrational modes between 1200 cm^{-1} to 3000 cm^{-1} are due to a combination of C=C, C–C, and C=O stretching and C–H bending vibrations. An intense peak at 3063 cm^{-1} confirms the presence of =C–H in the aromatic ring of amine salt crystal. The weak bands at ~ 3408 cm^{-1} and ~ 3570 cm^{-1} correspond to the vibrational energy of N–H and O–H bonds, respectively [20]. It can be observed from Raman spectra that the intensity of all functional groups was higher in the case of the µ-continuous process due to its high crystallinity and concentration. This analysis strongly supports DSC and UV-Vis spectroscopy results that the synthesized diastereomers salt crystals by the µ-continuous process are highly crystalline and have a high concentration than the batch process. This statement can also be verified from the XRD pattern of the synthesized salt crystals.

2.3.7 X-ray diffraction (XRD)

The crystallinity of S-(-)-I.L-(+)-II salt, which was synthesized by both processes (µ-continuous and batch process), was determined using the XRD pattern is shown in **Figure 2.14**. Generally, an XRD pattern reveals the crystal structure and unit cell of a molecule. Furthermore, the positions of the atoms and crystallinity can be judged by the intensities of the peaks [22]. To determine the Miller indices, a relation was developed by combining the plane-spacing equation

with Bragg's law [22]. For the synthesized salt crystals, the Miller indices were calculated using MATCH! 3 software, which showed that the cell setting and space group are monoclinic and $P2_1$, respectively. Similar findings were reported earlier [23]. The calculated crystal planes for the synthesized S-(-)-I.L-(+)-II salt by batch process are (0 2 0), (0 1 1), (1 1 -1), (1 2 0), (0 2 1), (1 0 1), (1 3 0), (0 3 1), (0 4 0), (1 4 0), (1 4 -1), (0 2 2), (0 3 2), and (3 1 -1) at 2θ values of 12.46°, 15.84°, 17.28°, 17.54°, 19.22°, 21.76°, 22.48°, 23.84°, 25.08°, 28.02°, 29.94°, 32.04°, 35.10°, and 36.62°, respectively (**Figure 2.14a**). On the other hand, the same obtained from µ-continuous process are (0 1 1), (1 1 1), (2 1 0), (1 2 -1), (1 2 1), (0 0 2), (0 1 2), (1 3 1), (0 2 2), (2 2 -2), (2 4 0), (2 3 -2), (2 3 2), and (4 1 -2) at 2θ values of 12.50°, 15.86°, 17.28°, 17.52°, 19.22°, 21.78°, 22.68°, 23.90°, 25.12°, 27.86°, 29.92°, 31.28°, 35.10°, and 36.62°, respectively (**Figure 2.14b**). The presence of defects in the crystalline structure creates certain strains in the crystals, which ultimately roots a change in the overall crystallite size as well as minor shifting of peaks position. Therefore, the Miller indices of the corresponding peaks of the salt crystals from both the processes are different from each other. The average crystallite size (L) and the strain (ε) in the crystals for both processes were estimated using the modified Williamson-Hall (W-H) method [24,25] by plotting βcosθ/λ vs sinθ/λ. The equation is given below,

$$\frac{\beta cos\theta}{\lambda} = \frac{1}{L} + \frac{\varepsilon sin\theta}{\lambda} \qquad (2.1)$$

where β stands for full-width at half-maxima (FWHM) intensity, θ is the Bragg angle, and λ denotes the wavelength used in XRD (λ = 0.15409 nm). The intercept ($1/L$) and the slope (ε) of the W-H plot give the average crystallite size (L) and the strain (ε) of the salt crystals, respectively (**Figure 2.14c, d**). From the W-H plot, the estimated values of average crystallite sizes are 72.20 nm, and 107.29 nm, whereas the corresponding strain values are -0.00044 and -0.00034 for the crystals obtained from the batch process. For the crystals from the µ-continuous

process, the W-H plot provides four different strain and intercept values. Two crystallite sizes (72.35 nm and 106.72 nm) and strain values (-0.00041 and -0.00038) are similar to the crystals obtained from the batch process (**Figure 2.14c**). The two additional crystallite sizes are 43.21 nm and 53.87 nm with corresponding strain values of -0.00078 and -0.00063, respectively. The dislocation density (δ) was calculated using the following equation [24]:

$$\delta = \frac{1}{L^2} \qquad (2.2)$$

The estimated values of δ for the batch process are 8.68×10^{-5} nm^{-2} and 1.91×10^{-4} nm^{-2}, whereas 8.78×10^{-5} nm^{-2}, 1.91×10^{-4} nm^{-2}, 3.44×10^{-4} nm^{-2} and 5.35×10^{-4} nm^{-2} are for the µ-continuous process. This result confirms that the dislocation densities in lattice planes of the crystals are almost similar for both the µ-continuous and batch process, with more grain boundaries in the crystals from the µ-continuous process due to two additional smaller crystallite sizes (**Figure 2.14d**). All of the above studies prove that the crystals from the µ-continuous process are at least as pure as the diastereomer salt from the batch process.

In the subsequent section, surface morphology and elemental mapping of only µ-continuous process salt crystals were investigated using FETEM and EDX, respectively. Also, the mole fraction of S-(-)-α-phenylethylamine in the salt crystals from both the processes was analyzed using ^{1}H NMR analysis. Additionally, we have performed DSC and XRD analysis of both needle-shaped crystals and R-(+)-I.L-(+)-II diastereomeric salt.

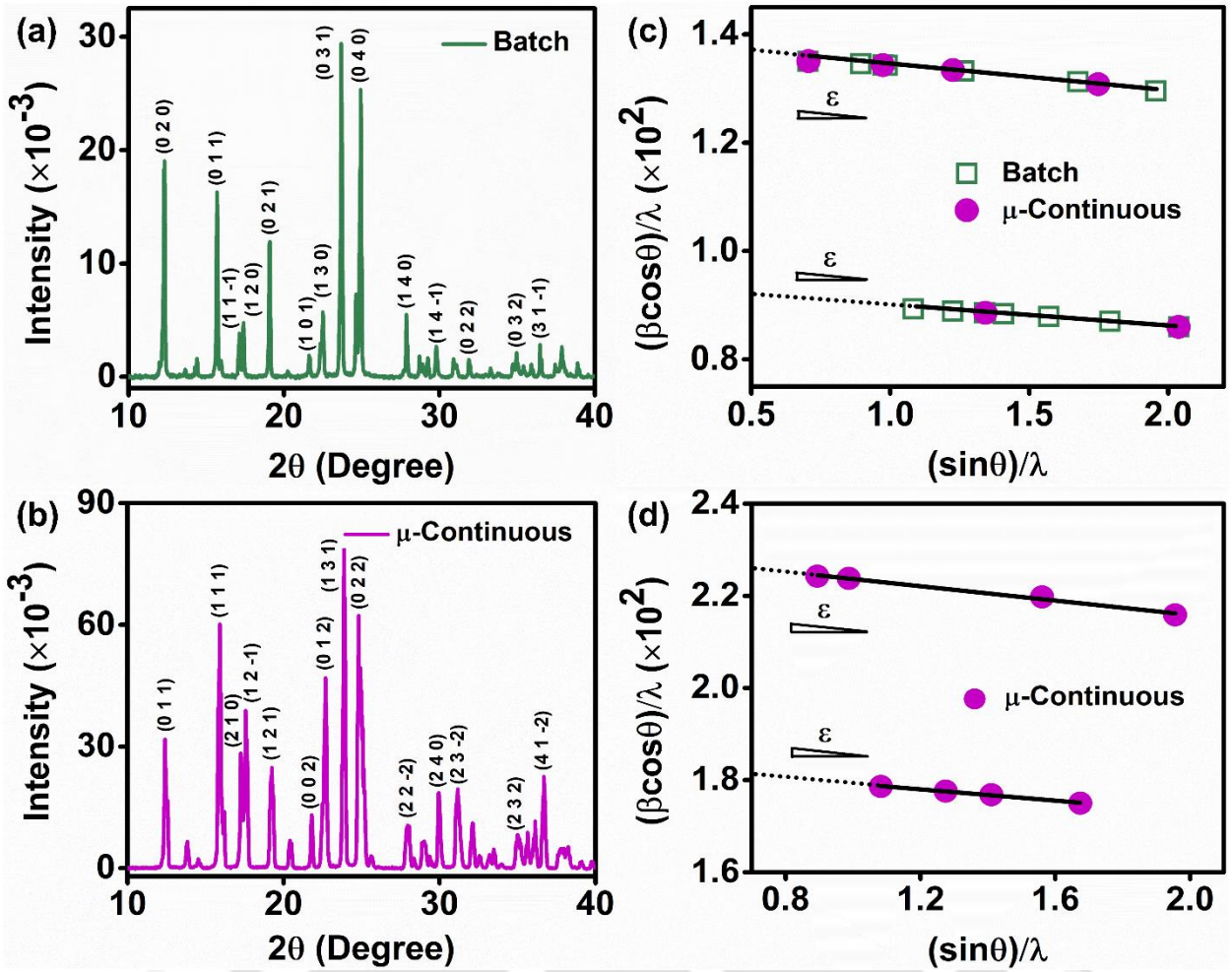

Figure 2.14 Show the XRD plots of synthesized diastereomer salt crystals: **(a)** batch process. **(b)** μ-continuous process. The W-H plot **(c)** and **(d)** show $\frac{\beta cos\theta}{\lambda}$ versus $\frac{sin\theta}{\lambda}$. **(c)** compares the W-H plots for crystals obtained from the batch and μ-continuous process with similar crystallite sizes. The W-H plot for two additional crystallite sizes for the μ-continuous process is shown in **(d)**.

2.3.8 FETEM analysis

The morphology of the synthesized S-(-)-I.L-(+)-II salt crystal using the μ-continuous process was studied using FETEM. The FETEM image (**Figure 2.15a**) shows that the average size of the salt crystals is ~ 5.2 ± 2 nm. HRTEM image (**Figure 2.15b**) depicts that all of the particles are crystalline. Well resolved lattice fringes with an equal interplanar spacing of ~ 0.21 nm are

shown in the inset of **Figure 2.15b**. The SAED pattern shown in **Figure 2.15c** confirms the crystalline structure. The presence of a single circular orbit with prominent dots is evidence of the prominent monolayered crystalline material. This result is in accord with DSC, Raman spectra, and XRD results.

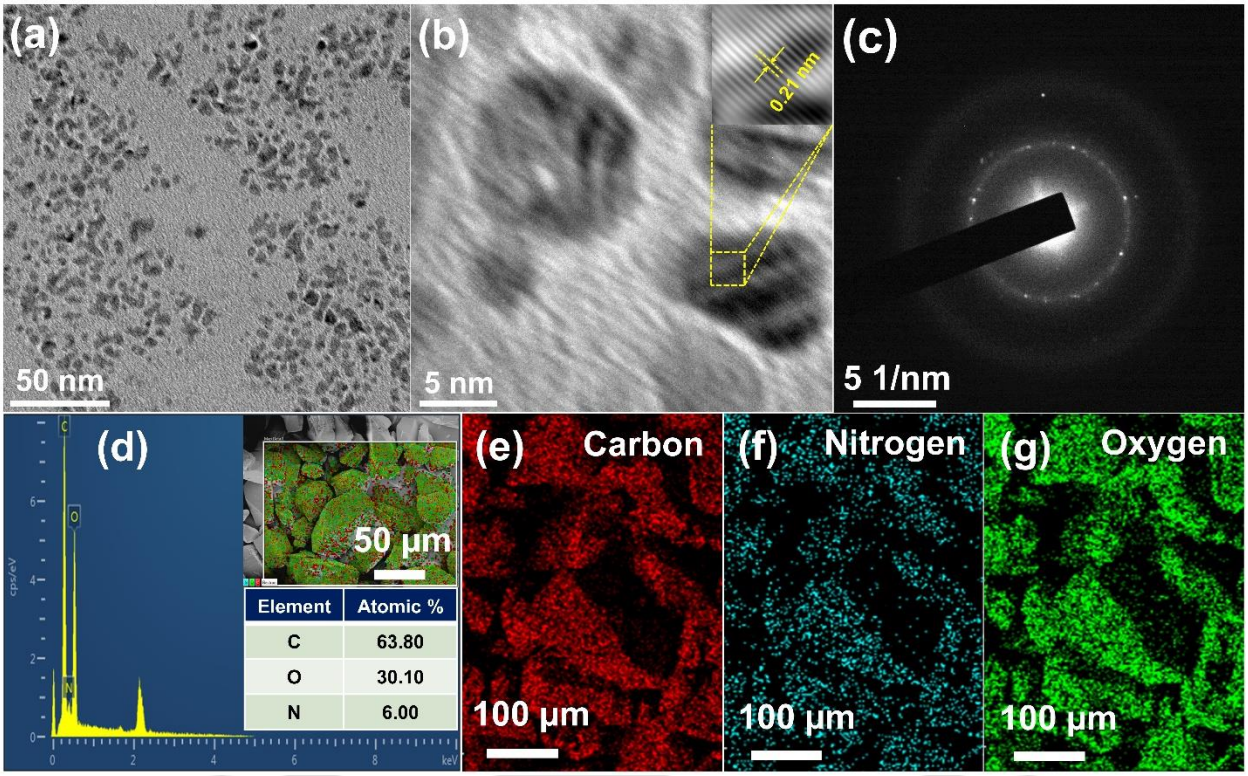

Figure 2.15 Shows the images of synthesized diastereomer salt crystals by the µ-continuous process. **(a)** FETEM image of the diastereomer salt **(b)** Magnified image of the salt crystals with HRTEM image at the inset showing the lattice fringes of ~ 0.21 nm. **(c)** Selected area electron diffraction (SAED) pattern of the diastereomer salt crystals. **(d)** EDX spectrum of the salt crystals, the inset image depicts the scanning area for EDX analysis. Elemental mapping of C **(e)**, N **(f)**, and O **(g)** of a selected area on the diastereomer salt crystals are shown.

2.3.9 Energy dispersive X-ray (EDX) analysis

The cross-sectional FESEM image of S-(-)-I.L-(+)-II salt crystal obtained from the µ-continuous process is shown in **Figure 2.15d** inset. The shape of the synthesized salt crystals is prismatic. The elemental mapping of the salt crystal was carried out by FESEM-EDX (**Figure 2.15e-g**) on a selected rectangular area. Uniform distributions of C, O, and N atoms are found throughout the salt crystals. The FESEM-EDX analysis further confirms the elemental composition (atomic percentages) of the salt to be 63.80%, 30.10%, and 6% for C, O, and N, respectively.

2.3.10 ^{1}H NMR analysis and sample calculation of salt crystal

^{1}H NMR spectroscopy was used to analyze the composition of diastereomers salt crystal for both processes. The proton peak areas of every component were sited in order to get the molar concentration. Three sets of data, corresponding to the crystals obtained from the three independent sets of experiments, were examined to ensure that the average uncertainty is less than 0.001. The ^{1}H NMR spectra of both approaches (batch and µ-continuous process) are shown in **Figure 2.16**. The raw NMR data were processed using ACD/NMR software [26], which showed the reference peak of solvent at 3.31 ppm, and the rest of the peaks correspond to the crystal (**Figure 2.16**). Except for solvent peak, the individual peak areas of NMR spectra were integrated to get the number of hydrogen atoms, which were present in each functional group of the diastereomers salt crystals. The individual mole fraction was calculated using the following equation [27].

$$x_i = \frac{H_i}{\sum_{i=1}^{n} H_i} \qquad (2.3)$$

Here, x_i denotes the mole fraction of the i^{th} component in the sample, H_i represents the peak area of the single 'H' atom corresponding to the i^{th} component, and 'n' signifies the total number of

the components present in the sample. For this case, n = 2 represents S-(-)-α-phenylethylamine and L-(+)-tartaric acid.

From the ^{1}H NMR spectra of diastereomers salt crystal, the single hydrogen atom of S-(-)-α-phenylethylamine is present at ~ 4.46 ppm, which was used to quantify its concentration. Similarly, for L-(+)-tartaric acid concentration, the peak at ~ 4.40 ppm is considered to represent the hydrogen atoms for the 2 sites shown in **Figure 2.16**. The reference peak of solvent (Methanol-d_4) was set to 3.31 ppm. The identified peaks for each compound were used to estimate the mole fraction in both methods using equation (2.3). It was deduced from ^{1}H NMR analysis that salt crystals obtained from both processes are similar.

Table 2.2: Mole fraction of individual components in the salt crystal

Sl. No.	Preparation method	L-(+)-tartaric acid	S-(-)-α-phenylethylamine
1	Batch process	0.4921	0.5079
2	μ-continuous process	0.4878	0.5122

2.3.10.1 The calculation for Mole fraction of batch process salt crystal

Peak area equivalent to 1 Hydrogen of L-(+)-tartaric acid (–CH–) = 8.74/2 = 4.37

Peak area equivalent to 1 Hydrogen of S-(-)- α-phenylethylamine (–CH–) = 4.51/1 = 4.51

Now $\sum_{i=1}^{4} H_i = (4.51 + 4.37) = 8.88$

Mole fraction of S-(-)-α-phenylethylamine = 4.51/8.88 = 0.5079

Mole fraction of L-(+)-tartaric acid = 4.37/8.88 = 0.4921

2.3.10.2 Sample calculation for Mole fraction of μ-continuous process salt crystal

Peak area equivalent to 1 Hydrogen of L-(+)-tartaric acid (–CH–) = 9.22/2 = 4.61

Peak area equivalent to 1 Hydrogen of S-(-)- α-phenylethylamine (–CH–) = 4.84/1 = 4.84

Now $\sum_{i=1}^{4} H_i = (4.61 + 4.84) = 9.45$

Mole fraction of S-(-)-α-phenylethylamine = 4.84/9.45 = 0.5122

Mole fraction of L-(+)-tartaric acid = 4.61/9.45 = 0.4878

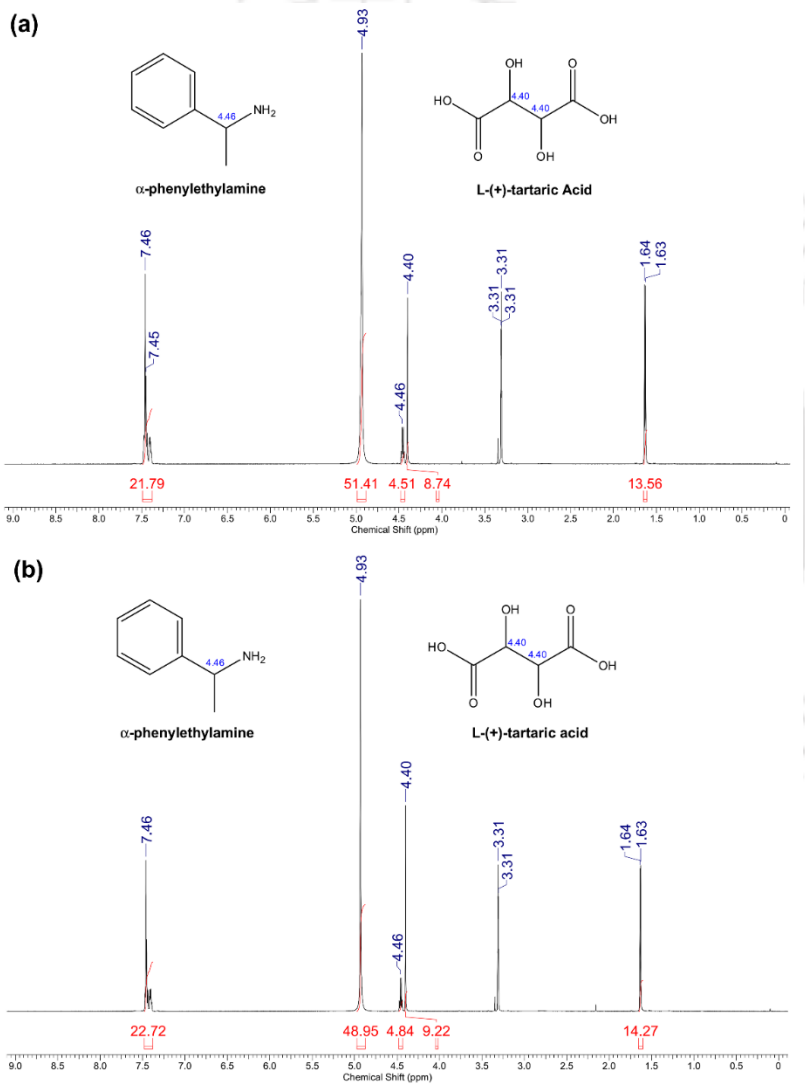

Figure 2.16 ^{1}H NMR of diastereomer salt crystal. **(a)** Batch process. **(b)** µ-continuous process.

2.3.11 DSC and XRD of needle-shaped crystals and R-(+)-I.L-(+)-II diastereomeric salt

DSC graph showed that the melting point of needle-shaped crystals is 181.5°C (**Figure 2.17a**), which is lower than the melting point of prism-shaped crystals i.e. 199°C (**Figure 2.11b**). Furthermore, XRD pattern as well as intensity are different for needle-shaped crystals (**Figure 2.17b**) compared to prism-shaped crystals (**Figure 2.14b**). It might be due to the presence of higher amount of R-(+)-I.L-(+)-II diastereomers in needle-shaped crystals. Additionally, DSC and XRD graph of (R-(+)-I.L-(+)-II) diastereomer salt were different compared to prism-shaped diastereomer salt crystal (**Figure 2.17c,d**). Therefore, we can conclude that the needle-shaped crystals are "impure "compared to prism-shaped crystals.

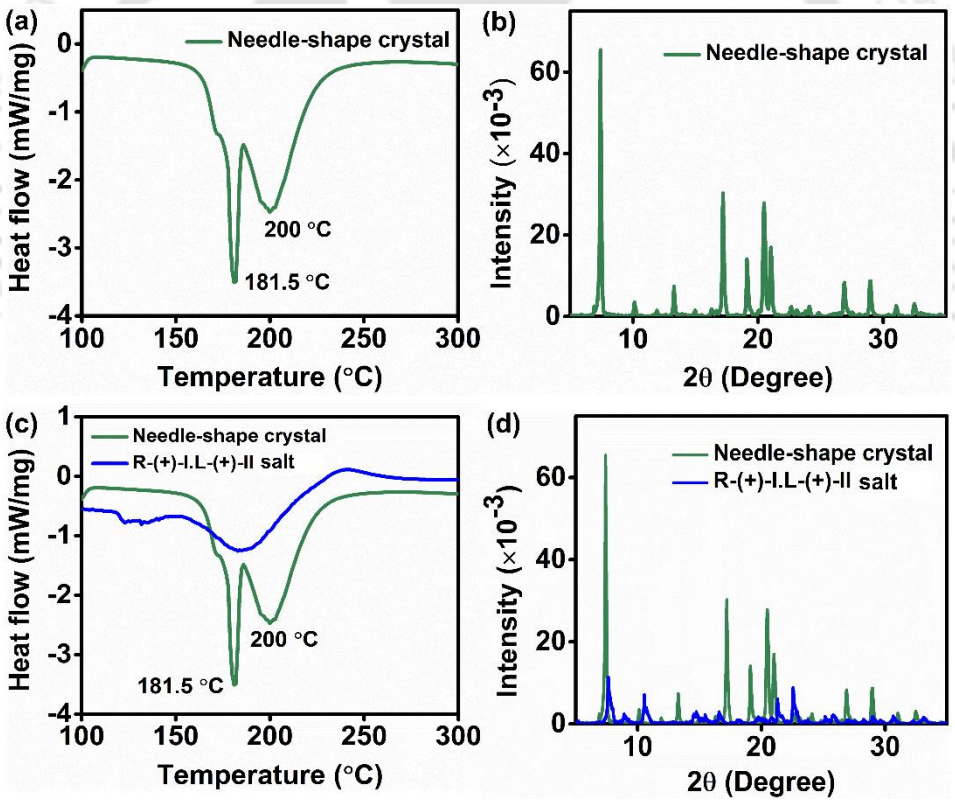

Figure 2.17 Show **(a)** DSC plot of needle-shape (S-(-)-I.L-(+)-II) diastereomer salt crystal. **(b)** XRD plot of needle-shape (S-(-)-I.L-(+)-II) diastereomer salt crystal. **(c)** DSC plot of needle-shape (S-(-)-I.L-(+)-II) diastereomer salt crystal and (R-(+)-I.L-(+)-II) diastereomer salt. **(d)** XRD plot of needle-shape (S-(-)-I.L-(+)-II) diastereomer salt crystal and (R-(+)-I.L-(+)-II) diastereomer salt.

2.3.12 Recovery of the amine

The salt crystal (S-(-)-I.L-(+)-II) obtained from the batch process was partially dissolved in DI water and added 50% NaOH solution to convert the amine salt into the free base. The resulting mixture was shaken vigorously with diethyl ether to extract the amine. As a result, this solution mixture formed two layers, aqueous and organic (**Figure 2.18b**). The entire solution was transferred into a narrow test tube and left for ~ 4 h to separate the organic layer from the aqueous layer. The organic layer was pipetted out and collected into a separate vial and the total obtained amount is ~ 750 µL. Finally, the percentage yield and enantiomeric excess were calculated.

2.3.12.1 Calculation of percentage yield and enantiomeric excess

To calculate the % ee and % yield of batch process salt crystals, firstly, a calibration chart of a mixture of pure enantiomers of the chiral analytes (R-(+)-α-phenylethylamine, S-(-)-α-phenylethylamine) was prepared by measuring specific rotation using a polarimeter, shown in **Figure 2.18a**. This calibration chart was prepared by dissolving a fixed volume of total analytes (75 µL) in 7 mL of methanol. It was observed that the specific rotation of pure R-(+)-α-phenylethylamine is +0.28, whereas for pure S-(-)-α-phenylethylamine is -0.28, and for the mixture of enantiomers, specific rotation lies in between them. The % ee and % yield were calculated by dissolving the same amount of sample, i.e., 75 µL in 7 mL of methanol, and found that 78% and 46.34%, respectively.

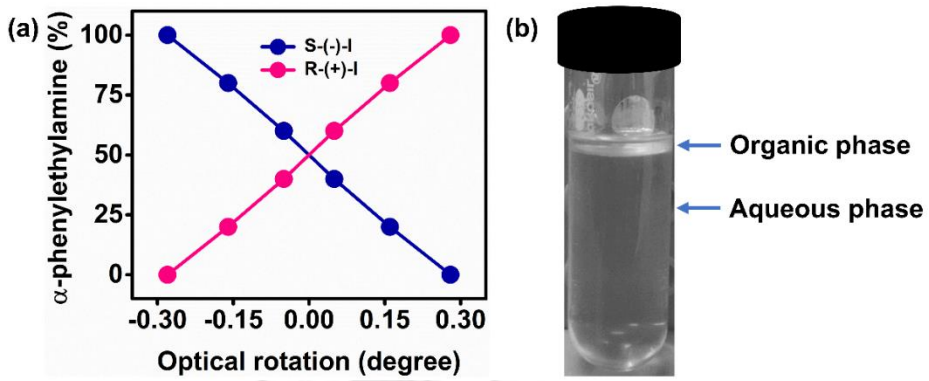

Figure 2.18 (a) Optical rotation of chiral α-phenylethylamines mixed at different %. **(b)** Optical image of the test tube having recovered amine (organic phase) from the diastereomeric crystals.

For pure chemical:

Methanol = 7 mL

S-(-)-α-Phenylethylamine = 75 µL

Observed Optical Rotation = -0.28

Overall concentration (c) = 0.01 g/mL (assuming density of α-Phenylethylamine as 964 kg/m^3)

Path Length (l) = 1 dm

$$\text{Specific rotation} = \frac{Observed\ optical\ rotation}{Concentration\ *\ Path\ length} \quad (2.4)$$

Specific rotation $[\alpha]_{589}^{24.9} = -28°$

For sample:

Methanol = 7 mL

Sample = 75 µL

Observed Optical Rotation = -0.22

Path Length = 1 dm

$$\text{Specific rotation} = \frac{Observed\ optical\ rotation}{Concentration\ *\ Path\ length} \qquad (2.5)$$

$$-28 = \frac{-0.22}{c * l}$$

Overall concentration c = 0.00785 g/mL

i.e. 0.057 g S-α-Phenylethyethyamine is present in 75 µL of sample. Total 750 µL of the organic phase is recovered i.e. 0.57 g from 1.23 g of the S-α-Phenylethyethyamine feed.

% yield = 0.57/1.23, = 46.34%

% Enantiomeric Excess (ee) from the Figure 2.18 (a):

From the observed rotation (-0.22) the percentage of the S-α-Phenylethyethyamine is ~ 89%. Thus R-α-Phenylethyethyamine is ~ 11%.

$$\text{Thus \% enantiomeric excess (ee)} = \frac{(S-R)}{(S+R)} * 100 \qquad (2.6)$$

$$= \frac{(0.89-0.11)}{(0.89+0.11)} * 100$$

$$= 78\%$$

2.4 Conclusions

In the present work, a microfluidic platform was developed to separate S-(-)-α-phenylethylamine from its racemic mixture using L-(+)-tartaric acid as a resolving agent via diastereomeric salt formation. The synthesized diastereomeric crystals thus obtained were as pure or better than the crystals obtained from the batch process as supported by the melting point and DSC data. Assuming the identical purity of the salt crystal, the recovered S-(-)-α-phenylethylamine obtained from such salt crystals was ~ 89%. The optimum resolution conditions were determined

such as reactor temperature, feed concentration, feed flow rate, etc. and a crystal shape map was developed using concentration and the flow rate as process parameters. The total time required for the formation of highly pure diastereomeric crystal is at most 130 min which is 33 fold less compared to the batch process (~ 4320 min). Moreover, in the batch process, there is uncertainty in the formation of impure needle-like crystals, and have less control over it. On the contrary, one can absolutely control the purity (needle-like or prism-like) by controlling the appropriate flow rate and concentration of the feed. It follows a facile one-step workflow that is fully adaptable to expand the range of enantio-separation with great analytical reproducibility at a faster rate compared to the conventional batch process [28] and can be adopted for industrial application with VLSI to achieve high throughput production.

References

[1] G. Gübitz, M.G. Schmid, Chiral separation principles in chromatographic and electromigration techniques, *Mol. Biotechnol.* 32 (**2006**) 159–179.

[2] J.S. Millership, A. Fitzpatrick, Commonly used chiral drugs: A survey, *Chirality.* 5 (**1993**) 573–576.

[3] G. Subramanian, Chiral Separation Techniques: A Practical Approach, 3rd ed., *Wiley-VCH,* **2007**.

[4] FDA Policy Statement for the Development of New, *Chirality.* 4 (**1992**) 338–340.

[5] P. Suresh, P.K. Basu, Improving pharmaceutical product development and manufacturing: Impact on cost of drug development and cost of goods sold of pharmaceuticals, *J. Pharm. Innov.* 3 (**2008**) 175–187.

[6] J.A. DiMasi, R.W. Hansen, H.G. Grabowski, The price of innovation: New estimates of drug development costs, *J. Health Econ.* 22 (**2003**) 151–185.

[7] K.M. Christensen, M.J. Pedersen, K. Dam-Johansen, T.L. Holm, T. Skovby, S. Kiil, Design and operation of a filter reactor for continuous production of a selected pharmaceutical intermediate, *Chem. Eng. Sci.* 71 (**2012**) 111–117.

[8] M. Sean, Special report: Continuous technology update, *Pharm. Technol. Eur.* 24 (**2012**) 35.

[9] A.I. Shallan, C. Priest, Microfluidic process intensification for synthesis and formulation in the pharmaceutical industry, *Chem. Eng. Process. - Process Intensif.* 142 (**2019**) 107559.

[10] S. Mitra, S.K. Singh, E. Shevchenko, M. Sachan, A. Ghosh, M. Basak, P.S. Gooh Pattader, Efficient microextraction process exploiting spontaneous interfacial convection driven by Marangoni and electric field induced instability: A computational fluid dynamics study, *Phys. Fluids.* 32 (**2020**) 1–13.

[11] A. Ault, R(+)- and S(−)-α-Phenylethylamine, *Org. Synth.* (**2003**) 93–93.

[12] M.D. Abràmoff, P.J. Magalhães, S.J. Ram, Image processing with imageJ, *Biophotonics Int.* 11 (**2004**) 36–41.

[13] J.M. Castagnetto, X. Xu, N.D. Berova, J.W. Canary, Absolute configurational assignment of serf-organizing asymmetric tripodal ligand-metal complexes, *Chirality.* 9 (**1997**) 616–622.

[14] C. Hock, S. Straßburg, H. Haberland, B. V. Issendorff, A. Aguado, M. Schmidt, Melting-point depression by insoluble impurities: A finite size effect, *Phys. Rev. Lett.* 101 (**2008**) 1–4.

[15] A.R. Katritzky, R. Jain, A. Lomaka, R. Petrukhin, Perspective on the Relationship between Melting Points and Chemical Structure, *Cryst. GROWTH Des.* 1 (**2001**) 261–265.

[16] Y. Kong, J.N. Hay, The measurement of the crystallinity of polymers by DSC, *Polymer*

(Guildf). 43 (**2002**) 3873–3878.

[17] Yeong-Tarng Shieh, Y.-S. Lin, Y.-K. Twu, H.-B. Tsai, R.-H. Lin, Effect of Crystallinity on Enthalpy Recovery Peaks and Cold-Crystallization Peaks in PET via TMDSC and DMA Studies, *J. Appl. Polym. Sci.* 116 (**2010**) 1334–1341.

[18] H. Wu, A.G. Jones, Crystallization, Dehydration, and Phase Transformations of Diastereomeric Salts: L-Ephedrine and D-Tartaric Acid, *Chem. Eng. Technol.* 35 (**2012**) 1031–1038.

[19] D.L. Pavia, G.M. Lampman, G.S. Kriz, Introduction to Spectroscopy third edition, *Thomson Learn. Inc.* (**2001**).

[20] F.R. Dollish, W.G. Fateley, F.F. Bentley, Characteristic Raman frequencies of organic compounds, *Wiley,* New York, **1974**.

[21] R. Sierpe, E. Lang, P. Jara, A.R. Guerrero, B. Chornik, M.J. Kogan, N. Yutronic, Gold Nanoparticles Interacting with β-Cyclodextrin-Phenylethylamine Inclusion Complex: A Ternary System for Photothermal Drug Release, *ACS Appl. Mater. Interfaces.* 7 (**2015**) 15177–15181.

[22] B.D. Cullity, Elements of X-RAY DIFFRACTION, 2nd ed., *Addison-Wesley Publishing Company,* Inc., Philippines, **1978**.

[23] D.E. Turkington, E.J. MacLean, A.J. Lough, G. Ferguson, C. Glidewell, Supramolecular structures of 1-phenylethylammonium tartrates, *Acta Crystallogr. Sect. B Struct. Sci.* 61 (**2005**) 103–114.

[24] R. Sinha, N. Roy, T.K. Mandal, Growth of Carbon Dot-Decorated ZnO Nanorods on a Graphite-Coated Paper Substrate to Fabricate a Flexible and Self-Powered Schottky Diode for UV Detection, *ACS Appl. Mater. Interfaces.* 12 (**2020**) 33428–33438.

[25] B. Saha, S. Das, K.K. Chattopadhyay, Electrical and optical properties of Al doped cadmium oxide thin films deposited by radio frequency magnetron sputtering, *Sol. Energy Mater. Sol. Cells*. 91 (**2007**) 1692–1697.

[26] ACD/Structure Elucidator, Advanced Chemistry Development, Inc., *Toronto, ON, Canada,* **2010**.

[27] P.K. Naik, S. Paul, T. Banerjee, Liquid Liquid Equilibria measurements for the extraction of poly aromatic nitrogen hydrocarbons with a low cost Deep Eutectic Solvent: Experimental and theoretical insights, *J. Mol. Liq.* 243 (**2017**) 542–552.

[28] E. Pálovics, S. Zsolt, S. Beáta, B. Miklós, F. Elemér, Separation of Chiral Compounds: Enantiomeric and Diastereomeric Mixtures, Lab. *Unit Oper. Exp. Methods Chem. Eng.* (**2018**) 99–122.

CHAPTER 3

Separation of Anionic and Cationic Surfactant in a Microchannel Using Ultra-Low Electric Voltage

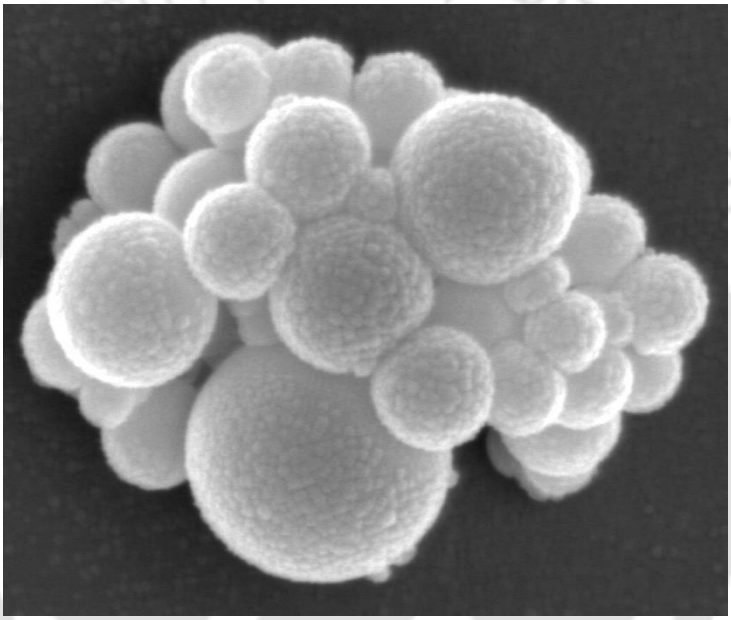

CHAPTER 3

Separation of Anionic and Cationic Surfactant in a Microchannel Using Ultra-Low Electric Voltage

Most industrial effluents contain cationic, anionic, non-ionic, and amphoteric surfactants in different concentrations. These surfactants are dangerous for aquatic life and directly or indirectly affect human. To overcome this problem, a microfluidic platform was developed to separate both anionic and cationic surfactants simultaneously from its mixture under the influence of ultra-low electric voltage. For this, a PDMS Y-shape microchannel was fabricated using a high-end 3D printer, and then thin copper sheet electrodes were placed across the channel. A DC power source applied constant DC voltage of ~ 1.2 V across the microchannel electrodes which is lower than the electrolysis point of water. It was found that separation efficiency solely depends on the residence time of the fluid inside the microchannel. It turns out that for lower feed flow rate i.e., high residence time favored a higher degree of separation and vice-versa. Langmuir Blodgett (LB) and HPLC analysis confirmed that, for below critical micelle concentration (CMC), and the lower flow rate, separation efficiency was more than 90%.

3.1 Introduction

Treating various contaminants found in water bodies, such as surfactants, is one of the major challenges faced in the wastewater treatment process. Water pollution has become a global concern due to its deteriorating impact on human health and aquatic life. There are numerous sources of water pollution where surfactants are considered major pollutants [1,2]. Human health can be adversely affected by drinking water contaminated with these surfactants causing

diseases such as skin irritation, liver damage, stomach cramps, sore throat, nausea, etc. in a human. After all, this can also lead to death in many severe cases.

The physiochemical process that involves the extraction of surface-active molecules from a growing foam and separating them from the solution is known as foam fractionation. It is one of today's most promising strategies for separating surfactants from wastewater [3–8]. Moreover, it is a well-explored topic presently applied to various industries which includes biological protein and metabolite purification, mineral processing, and agriculture. Moreover, Rubin and Jorne found that the foam fractionation technique can separate two different surfactants based on the relative distribution coefficient. A range of conventional methods including biological [9–14], chemical [15,16], combined chemical and biological [12,17,18] are being employed presently for the treatment of wastewater.

Based on the above discussion, we could deduce that simultaneous continuous separation of cationic and anionic surfactant on a microfluidic platform is still challenging. Hence, this work focuses on developing a technique for the efficient separation of surfactant molecules on a microfluidic platform. We have chosen the catanionic solution of SDS and CTAB to separate in a Y-shaped microchannel using ultra-low DC electric voltage.

3.2 Experimental section

3.2.1 Materials

The anionic surfactant sodium dodecyl sulfate (SDS) ($NaC_{12}H_{25}SO_4$, ≥99% purity) and the cationic surfactant cetyltrimethylammonium bromide (CTAB) ($C_{19}H_{42}BrN$, ≥99% purity) were purchased from Sigma-Aldrich (Bangalore, India). Acetonitrile (ACN) (≥99%, HPLC grade)

solvent, and Acetic acid glacial for HPLC (purity >98%) were procured from HiMedia Laboratories Pvt. Ltd. (Mumbai, India). Sylgard^{TM} (R) 184 Silicone Elastomer Kit for the preparation of polydimethylsiloxane (PDMS) was bought from Dow Chemical International PVT. LTD. USA. Acrylonitrile Butadiene Styrene (ABS) filament was obtained from Ultimaker, Netherlands. Silicone rubber tube was acquired from Sigma-Aldrich USA. 10 mL Dispo Van disposable syringes were purchased from 1mg, India. Copper sheet was purchased from the local retail outlet, IIT Guwahati, India. All chemicals were used without any purifications unless otherwise specified. All synthesis and spectroscopic measurement solutions were prepared with Milli-Q water (resistivity ~ 18.2 MΩ.cm), purified by millipore system (France, model: Elixplus Milli-Q).

3.2.2 Apparatus

The UV-Vis (Make: Shimadzu, UV-2600 230 V EN spectrophotometer) absorbance of the samples (200 µL) were measured to quantify the surfactants in the UV visible region (200 nm–800 nm). A Langmuir-Blodgett (LB) (Make: Apex Instruments Co. India) unit was used to measure the surface pressure of surfactant thin layers. The micro-Raman spectroscopy (Make: Horiba Jobin Vyon, LabRam HR) was used to validate functional groups. The spectra were acquired at duration of 10 s with an excitation wavelength of 532 nm. The presence of functional groups was examined by FTIR (Make: PerkinElmer Spectrum Two) in the frequency range of 400 cm^{-1} – 4000 cm^{-1}. The zeta potential of samples was measured using a zeta potentiometer (Make: Beckman Coulter (Nyon, Switzerland), model: Delsa Nano C)), equipped with 658 nm wavelength semiconductor laser diode (40 mW) and 1 cm optical path. FETEM (Make: JEOL, JEM 2100F at the acceleration voltage of 200 kV) was used to get detailed surface morphology

and composition of samples. The samples were prepared by drop casting the solution on a 400-mesh carbon-coated copper grid (SPI, USA) and then dried at room temperature in a vacuum oven. The individual concentration of SDS and CTAB in the samples were analyzed using HPLC system (Make: Agilent LC system, Agilent technologies; model: 1260 Infinity II), which was equipped with evaporative light scattering detector (ELSD), Acclaim^{TM} Surfactant Plus column (Make: Thermo Fisher Scientific, 5 µm, 4.6 × 150 mm) with quaternary pump and an auto sampler (Agilent technologies; model: 1260 Infinity II). A 3D printer (Make: Ultimaker 3, Netherlands) was used to mold the ABS wire in a Y-shape channel. This 3D printed ABS wire was then used as a mold for the fabrication of PDMS microfluidic channel having a width of ~ d = 800 µm. A syringe pump (Make: Harvard Apparatus**,** PHD 2000) was used to suck the fluids inside the µ-channel at a controlled flow rate. The flow connection from the syringe to the µ-channel was accomplished by silicone rubber tubes (Sigma-Aldrich, I.D. × O.D. 1/16 inch × 1/8 inch) and micropipette tips (Tarson, 0.2 µL – 10 µL). The outlets/products of the µ-channel were stored in the glass vials. A programmable AC (Make: 0 – 300 V, Chroma 61601 AC power source) power source was used as a voltage source for the electrodes.

3.2.3 Methods

3.2.3.1 Solution preparation

First, 0.26 mg mL^{-1} solutions of SDS and CTAB were prepared separately in deionized water and these solutions were filtered through filter paper to remove the dust particles (if any) and finally, these solutions were mixed in equal proportion and used for further experiment.

3.2.3.2 Fabrication of electrode embedded microchannel

A PDMS Y-shape microchannel was fabricated using a high-end 3D printer (Ultimaker 3), which works on fused filament fabrication (FFF) technique with a dual extruder. The machine was able to make a fragment with a maximum volume up to 197 mm × 215 mm × 200 mm. The printer machine had layer resolution capacities ranging from 150 - 60 µm, 200 – 20 µm and 600 – 20 µm with 0.25 mm, 0.4 mm, and 0.6 mm nozzles diameter, respectively. The positional resolution of this instrument was 12.5 µm, 12.5 µm, and 2.5 µm in X, Y, and Z directions, respectively. The 3D printer could print materials with maximum building speed of 24 mm^3/s. Additionally, it could print different types of filament materials such as ABS, polylactic acid (PLA), polyvinyl acetate (PVA), and Nylon of 2.85 mm material diameter.

Initially, the CAD model of the 3D printing specimen was created by free CAD and saved as a STL file. Consequently, the STL file was transferred to the Ultimaker Cura (Ultimaker 3D printer software) to slice the file. The process variables of Ultimaker Cura were adjusted and exported the final instructions as a G Cod file. Subsequently, the G Cod file is transferred to the 3D printer as a final command to print the model. The 3D printer molded the Y-shape microchannel having equivalent diameter ~ D_e = 800 µm (thickness ~ D = 800 µm and width ~ W = 800 µm) by extruding the ABS filament and deposited layer by layer. Finally, the printed mold was removed from the 3D printer, followed by detaching the brim mechanically from the channel. At the end, using glue, a thin strip of copper metal was fixed on the two sides of ABS 3D printed mold to make electrodes.

A molding technique was used to fabricate a microchannel in PDMS. First, part A (oligomer) and part B (crosslinker) of the Sylgard^{TM} 184 elastomer kit were mixed thoroughly in a ratio of 10:1. The mixture was then degassed in a vacuum desiccator for 40 min to remove all

the air bubbles trapped inside. On a cleaned glass slide with the help of double-sided tape, a rectangular mold was prepared and the ABS 3D printed mold with electrodes was placed inside it. Subsequently, PDMS was poured on electrodes embedded ABS 3D printed mold followed by curing at 80 °C in a hot air oven overnight. It was ensured that the ends of the ABS filament were outside the PDMS block. After curing, the ABS microfilament embedded PDMS block was dipped into an acetone bath for 12 h. The acetone dissolved the ABS microfilament, and a microchannel was formed inside the PDMS block. Later, the microchannel embedded PDMS block was further ultra-sonicated in the acetone bath for 5 h to remove traces of ABS completely. The microchannel was then repeatedly washed with acetone and DI water for 10 – 15 min. Finally, the cleaned micro-channel was dried by blowing nitrogen gas and then keeping it in a hot air oven for 30 min at 75 °C. **Figure 3.1** shows the optical image of a Y-shaped square microchannel with inner equivalent diameter ~ D_e = 800 μm (thickness ~ D = 800 μm and width ~ W = 800 μm) , and a total path length of ~ l = 3 cm.

Figure 3.1 Shows the optical image of Y-shaped electrode embedded microchannel.

3.3 Results and discussion

3.3.1 Separation of SDS and CTAB from its catanionic mixture in a microchannel

Figure 3.2 shows the schematic of the experimental setup for the separation of anionic (SDS) and cationic (CTAB) surfactants in a microfluidic platform using ultra-low DC electric voltage. Briefly, a syringe pump which contains two syringe (syringe 1 and syringe 2) was used to suck the liquid (feed) through the microchannel at a constant flow rate. The flow rates of the liquid was varied from 20 - 80 µL/min. A DC voltage power source was used to supply the voltage to the electrodes. The electrodes are made of thin copper sheet and placed at two side walls of the microchannel are connected with DC voltage power source. The feed was prepared by mixing the solutions (as mentioned in section 3.2.3.1) in the same volumetric ratio and stored in a volumetric flask to perform the experiment. It is reported that only physical interaction happens between cationic and anionic surfactants [19] and hence it can be separated using this technique. The feed was sucked into the microchannel using a syringe pump. A constant DC voltage ~ 1.2 V (lower than electrolysis point of water) across the microchannel electrodes was applied using a DC power source.

SDS is an anionic surfactant and CTAB is a cationic surfactant which have overall negative and positive charge polarity on the molecules, respectively. The electrodes of the microchannel showed positive and negative charge after application of constant DC voltage. Hence, due to opposite charge of the electrodes, the anionic surfactant (SDS) gets attracted towards positive electrodes while cationic surfactant (CTAB) gets attracted towards negative electrodes and hence separation occurred. It was found that, separation efficiency depends on the residence time. It turns out that, for lower feed flow rate i.e. high residence time is favorable for

higher degree of separation from its mixture and vice-versa. The residence time of feed, t_r, inside the microchannel depends on the feed flow rate and hence for the flow rates of 20, 40, 60, 80 µL min^{-1}, t_r was found to be ~ 46, 23, 15, 11 sec, respectively. Syringe 1 and syringe 2 were connected at the outlets of the microchannel and hence samples were collected in the syringe 1 and syringe 2 continuously. Finally, these samples were stored in separate vials and characterizations were done.

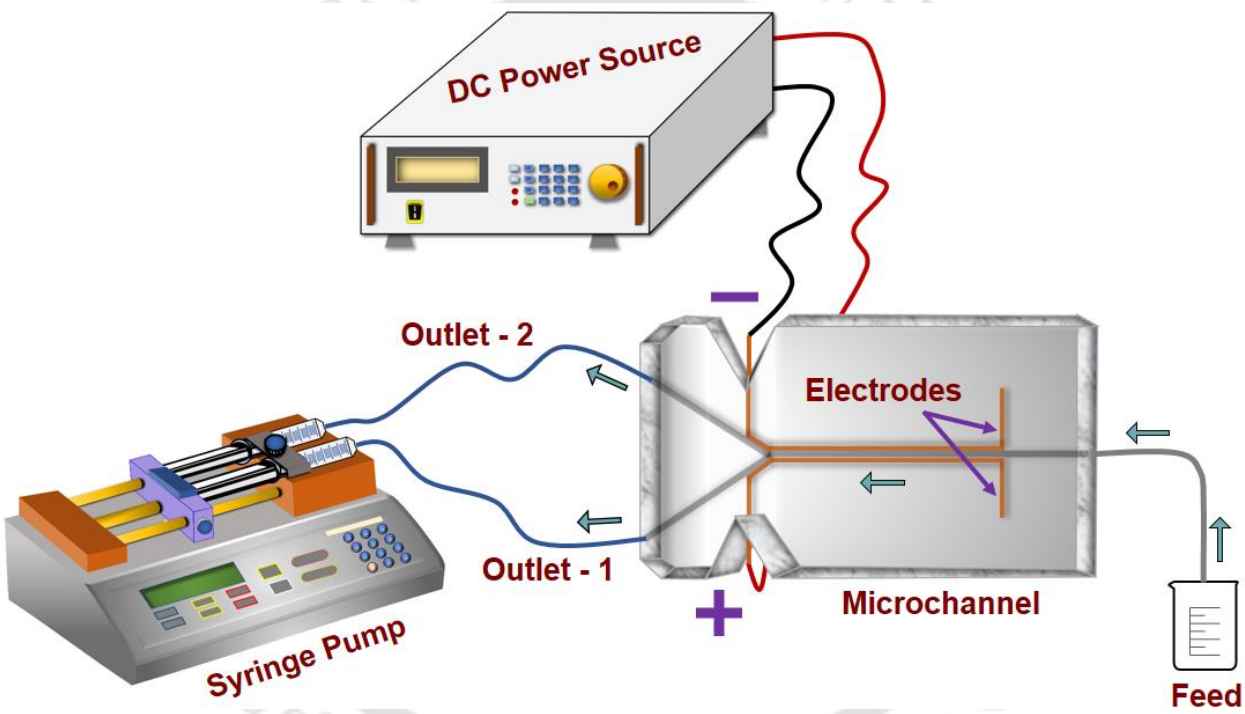

Figure 3.2 Schematic representation of the experimental setup for the separation of anionic (SDS) and cationic (CTAB) surfactants in a microfluidic platform using ultra low DC electric voltage mixture in a continuous manner.

3.3.2 Image analysis

Figure 3.3a shows the images of glass vials containing aqueous phase solution of pure SDS, CTAB, and feed i.e. the mixture of anionic and cationic surfactants (catanionic solution). Generally, pure form of surfactant solution appears clear while mixture of anionic and cationic surfactants (catanionic solution) appears in turbid nature, **Figure 3.3a**. The samples were stored after performing the experiment for analysis, shown in **Figure 3.3b**. The visual appearance of samples shows that, at the lower flow rate, both outlets separated streams solutions appeared almost clear, which indicates that the outlets solution are almost pure. Turbidity of the outlet streams increases with increasing flow rate and hence impure solution. The collected samples were used for qualitative and quantitative analysis for the purity.

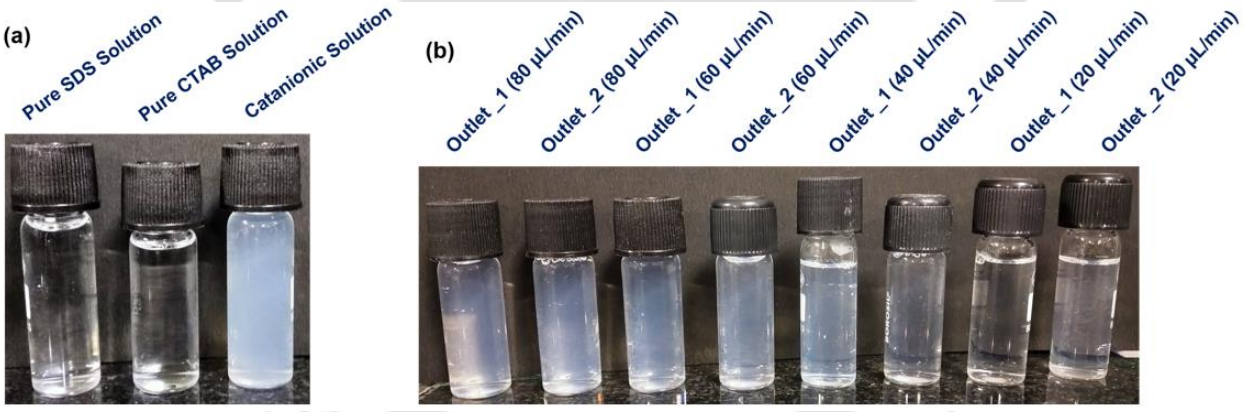

Figure 3.3 Shows the images of glass vials containing **(a)** Aqueous solution of pure SDS, CTAB, and catanionic surfactant. **(b)** Outlet streams at different flow rates.

3.3.3 UV-Vis Spectra Analysis

To characterize the internal construction and interaction of SDS-CTAB bonding/debonding, the ultraviolet-visible spectroscopy (UV-Vis) technology was employed. UV-Vis, an ultraviolet-

visible absorption spectrum, belongs to the electronic spectrum, and is generated by the transition of valence electrons [20]. The ultraviolet visible spectrum and the degree of absorption, produced by the absorption of ultraviolet and visible light from molecules or ions of a sample, can be determined and inferred for the composition and structure of the sample. Generally, this technique measures the absorption of light across the ultraviolet and visible light wavelengths through a liquid sample. With a constant light path length and known absorption coefficient, the concentration of a compound in question can be determined from the light absorbed by the sample according to the Beer-Lambert's law:

$$a = \log_{10} \frac{I_0}{I} = \varepsilon l c \qquad (3.1)$$

Where *a* is the absorbance of the solution, ε is the molar absorptivity, *l* is the thickness, and c is the concentration.

Pure SDS and CTAB show absorption peaks in a range of wavelengths from 250 to 320 nm [21]. The maximum absorption peak is at ~ 280 nm. To determine the purity/amount of cationic surfactant CTAB and anionic surfactant SDS molecules in the compacted/decompacted state, the absorption spectra of outlet 1 and outlet 2 samples at various flow rates are systematically investigated. **Figure 3.4** shows the absorption spectra of pure SDS, CTAB, outlet 1, and outlet 2 at different flow rates. In **Figure 3.4**, displays the absorbance spectra of catanionic surfactant (blue line) where the peak was completely diminished due to compact state or interaction between them. The spectra intensity of outlet 1 and outlet 2 at 280 nm are gradually changing with flow rate. It can be observed clearly from **Figure 3.4**, at higher flow rates (60, and 80 µL min^{-1}), the absorbance of outlet 1 and outlet 2 are almost similar as catanionic surfactant spectra, which indicate the surfactant molecules are still almost in compact state and hence lower degree of separation. Whereas, at the flow rate of 40 µL min^{-1}, the

absorbance peaks of outlet 1 and outlet 2 were clearly visible, which shows some of the surfactant molecules are in the compact state and some them are in the decompact or free state. For the case of lowest flow rate 20 µL min^{-1}, the observed absorbance peak of outlet 1 and outlet 2 were intense, which signifies the surfactant molecules are in almost decompact or free state and hence almost in pure form. This statement can be verified using other analysis of the samples.

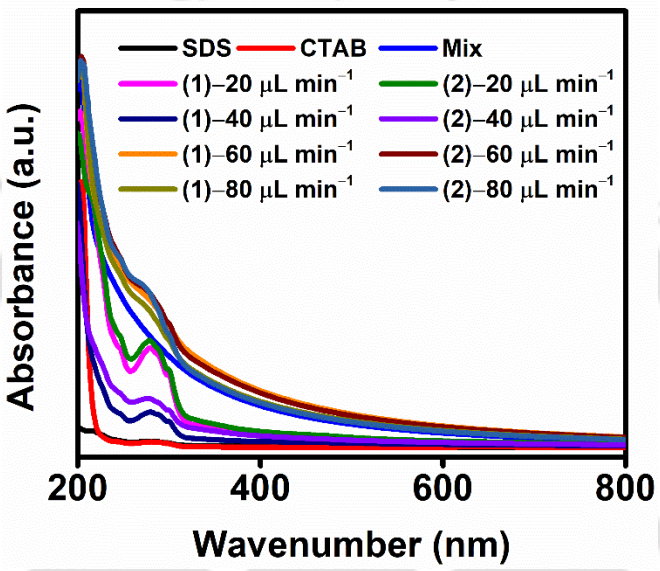

Figure 3.4 (Colour online) UV-Vis spectra of SDS, CTAB, catanionic mixture (SDS/CTAB = 50/50), and outlet streams of various flow rates.

3.3.4 Langmuir–Blodgett (LB) Characteristics of Langmuir Monolayer of Pure Surfactants and Their Mixtures and its Surface Pressure-Area (π-A) Isotherm Measurements

A Langmuir–Blodgett (LB) unit was used to measure the surface pressure of surfactants thin layers. The LB trough was first cleaned with soap solution and then ethanol to get rid of any organic contamination and other particulates matter. For surface pressure–area (π–A) isotherm measurements of pure anionic systems, pure cationic systems, and different ratios of catanionic mixtures on a water sub-phase, stock solutions were prepared. The trough is filled with deionized water which is used as the subphase, and in each case, 200 µL of surfactant solutions are spread

over it at the room temperature (~ 25 °C). The spreading was done using a microsyringe (Hamilton Bonaduz AG, Bonaduz, Switzerland) in such a manner that the surface pressure did not rise above 0.5 mN/m. The numbers of molecules thus spread for pure SDS and CTAB were calculated using their molecular weights as 288.38 and 364.46, respectively. On the other hand, for the mixed surfactants, the number of molecules was represented by the mean molecular weight (*M*) as follows

$$M = \frac{M_1 c_1 v_1 + M_2 c_2 v_2}{c_1 v_1 + c_2 v_2} \qquad (3.2)$$

where M_1 and $M2$ are the molecular weights, c_1 and c_2 are the concentrations (in mM), and v_1 and v_2 are the volume percentages of first and second samples, respectively. The monolayer film was left undisturbed over the water sub-phase for 10 minutes to get surfactant molecules stabilized and uniformly dispersed. The compression speed of the barrier over the trough was controlled at the rate of 10 mm $min^{-1,}$ and hence the monolayer was slowly compressed with a compression speed of 10 mm min^{-1}.

The computerized LB trough used a Teflon-bar-barrier (model LB2007DC, Apex nstruments Co., Kolkata, India) enclosed in a plexiglass box to reduce film contamination. It was equipped with a Wilhelmy-type balance with an accuracy of 0.01 mN/m. The trough width and length were 200 and 600 mm, respectively. The sub-phase Milli-Q water with a pH of 6.5 and a resistivity of 18.2 MΩ cm was purified by millipore system (France, model: Elixplus Milli-Q). All experiments were performed at a temperature of 25 ±1 °C unless otherwise mentioned. At least three independent runs were performed to check the reproducibility.

First, the isotherms were performed to compose the calibration chart for the stock solutions of pure SDS and CTAB at concentration 0.26 mg mL^{-1} prepared in water solvents and mixed in different volume ratios (SDS/CTAB = 90/10, 75/25, 65/35, 50/50, 35/65, 25/75, 10/90)

to form catanionic solutions. It was also investigated for any phase change during compression. These mixtures were spread on the water sub-phase. **Figure 3.5a** displays the surface activities, that is, the variations of surface pressure (π) with time (t) and area (A), of different catanionic mixtures of SDS/CTAB. This figure shows some interesting results about various anionic/cationic mixtures. For the cases of pure surfactants (pink and light yellow curve) and for the extremely cationic-rich (SDS/CTAB = 10/90, maroon curve) and anionic-rich (SDS/CTAB = 90/10, black curve) compositions, the surface pressure remained almost zero. In these cases, the numbers of catanionic complexes were very low, and the rest of the molecules were free surfactants soluble in the sub-phase. Therefore, there was not much of growth in surface pressure. On the other hand, for the remaining compositions [namely, SDS/CTAB = 35/65 (violet curve), 50/50 (deep blue curve), and 65/35 (light green curve)], the curves pass through a peak. Initially, surface pressure increases for a while before it decreases. The rates of increment and decrement of the surface pressure are different for the different compositions. From these observations, it can be concluded that, just after the spreading of the surfactant mixture, both surfactants have a tendency to sink into the sub-phase because of their solubility in water [22,23]. Over time, the electrostatic interaction between the two oppositely charged head groups plays a role in the formation of some catanionic complexes that are insoluble in water. These interaction processes are dynamic in nature. The difference in the nature of π-A curves for the two compositions SDS/CTAB = 35/65 (violet curve) and 65/35 (light green curve) arises because of the different numbers of cationic and anionic molecules having different degrees of solubility. According to Sohrabi et al, CTAB is more surface-active than SDS [24], therefore, the CTAB molecules have a greater probability than the SDS molecules to reside at the surface. For the composition SDS/CTAB = 35/65, the number of CTAB molecules is higher, and these molecules

mostly reside at or near the surface. These cationic CTAB molecules try to minimize their electrostatic repulsive force (i.e., free energy) and attract the anionic SDS molecules at the surface. Finally, they form some catanionic complex structures at the air/water interface which increase the surface pressure. In contrast, for SDS/CTAB = 65/35, the concentration of CTAB molecules is less than that of SDS molecules, and the number of catanionic complexes at the air/water interface is lower. For this reason, the growth of surface pressure is less than for SDS/CTAB = 35/65. In the case of SDS/CTAB = 50/50, the number of catanionic complexes is highest amongst all compositions, and in effect, the graph for this composition show highest pressure (deep blue curve). In CTAB, the head group is $N(CH_3)_3$ (trimethylammonium), whereas in SDS, the head group is OSO_3 (sulfate) [24]. There is an electrostatic interaction between the positively and negatively charged head groups. Insolubility arises because of neutralization of the head-group charges and formation of a bitail structure. Different composition ratios of anionic/cationic mixtures (SDS/CTAB) have different amounts of residual charges, which might be responsible for the formation of different types of aggregates. The involvement of a repulsive steric hydration force cannot be ruled out for the stabilization of these structures [25]. After the complexes are formed, they reach the surface and, over time, form definite two-dimensional assemblies at the air/water interface. Growth of the surface pressure indicates this phenomenon. As time passes, the two-dimensional structures start to convert into three-dimensional structures (hill-like) through reorganization, causing the decrement of the surface pressure. The monolayer is less stable at higher surface pressure. This phenomenon illustrates the fact that the self-assembly of the molecules occurs at high pressure. At high surface pressure, the monolayer is more compressed. This implies that the molecules are closer to each other, initiating different

types of interactions to form organized assemblies and reducing the surface pressure. As a result, the area per molecule decreases to maintain the surface pressure.

This prepared calibration curve can be used to find the approximate/qualitative composition of SDS/CTAB of unknown samples. The π-A curve obtained for different samples matched with the calibration curve, **Figure 3.5b**. It was found that, for the lowest feed flow rate (20 μL min^{-1}, black and cyan curve), the surface pressure of the outlet streams was almost zero, which reflects that higher degree of separation was achieved, and the purity of the outlet streams was found to be more than 90 %. The separation efficiency decreased with increasing the feed flow rate, as the surface pressure of the outlet streams are noted down (red, pink, violet, orange curve). At the highest feed flow rate (80 μL min^{-1}, maroon and deep blue curve), the surface pressure curve of the outlet streams almost matched with SDS/CTAB = 50/50, which concluded that lower degree of separation was achieved.

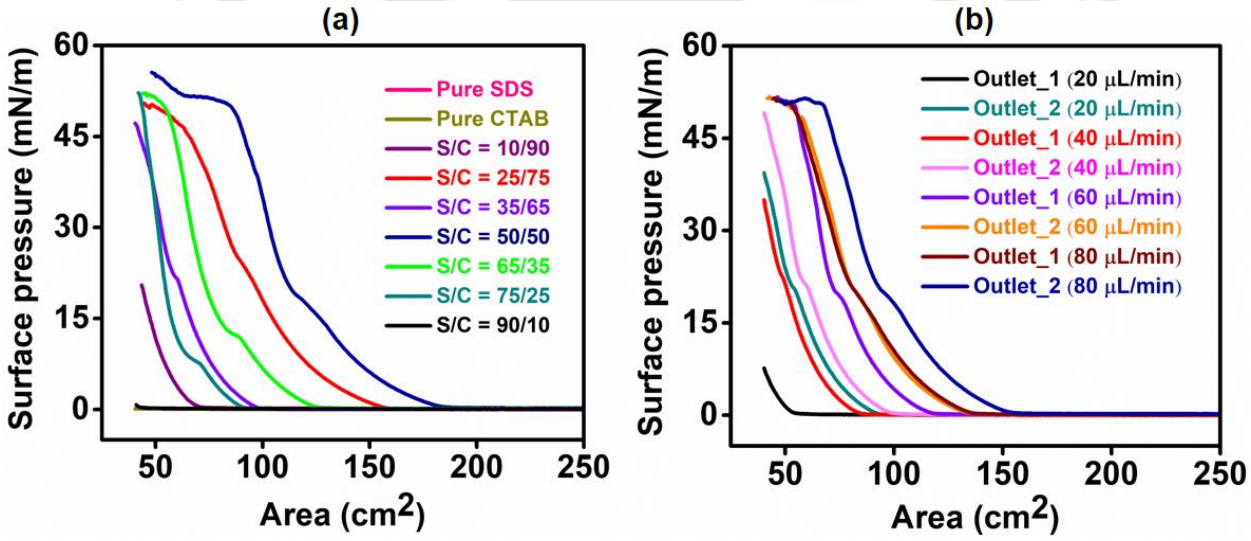

Figure 3.5 (Colour online) **(a)** Pressure – area (π–A) isotherm of the SDS, CTAB, catanionic mixture surfactant with different composition. **(b)** Pressure – area (π–A) isotherm of the outlet streams of various flow rates.

3.3.5 Raman Spectroscopy Analysis

From **Figure 3.6a**, it can be seen clearly that the characteristic Raman peaks of CTAB mainly appear at 758, 830, 901, 942, 957, 1013, 1063, 1125, 1146, 1164, 1212, 1267, 1291, 1393, 1435, 1460 cm^{-1}, and so forth. These characteristic peaks can reflect structural information of CTAB molecule as illustrated [26–29]. The 758 cm^{-1} is attributed to methyl rocking vibration from the $(CH_3)_3N^+$ group. The bands at 830 cm^{-1} correspond to the CH_3 deformation. The 901, 942, and 957 cm^{-1} bands probably correspond to methyl rocking vibration from the $(CH_3)_3N^+$ group and C–N^+ stretching modes. The bands at 1013, 1063, and 1125 cm^{-1} are attributed to the C–C stretching vibration. The 1146 cm^{-1} band is assignable to C–C antisymmetric stretch. The band at 1164 cm^{-1} has its origin in the CH_2 rocking mode, and the 1212 cm^{-1} is attributed to the CH_2 wag vibration. The strongest line at 1267 cm^{-1} is assigned to the δ(C–H) vibrations of the –CH2–$N^+(CH_3)_3$ group. The 1291 cm^{-1} is assigned to the CH_2 twisting, while the bands at 1393 cm^{-1} is assigned to the wag vibration of CH_2 and the deformation vibration of CH_3. The band at 1435 cm^{-1} is attributed to CH_2 bending vibration, and the 1460 cm^{-1} is assigned to CH_2 scissors. Whereas, the characteristic Raman peaks of SDS mainly are at 687, 830, 895, 995, 1060, 1081, 1125, 1217, 1300, 1321, 1365, 1437, 1454, 1478, 1537 cm^{-1}, and so forth. These characteristic peaks reveal structural information of SDS molecular illustrated as follows [30–33]. The bands 687 cm^{-1} belonged to an SO_3 vibration. The 830 cm^{-1} belonged to CO–SO_3 stretching vibration. The 895 cm^{-1} is attributed to CH_3 rocking, and the 995 cm^{-1} is attributed to the stretching vibration of S–OC. The 1060 cm^{-1} is assigned to the full-reflex vibration of the C–C skeleton and may be mixed with SO_3 vibration, and the 1081 cm^{-1} is attributed to twist mode of the C–C skeleton and may be mixed with SO_3 vibration. The band at 1125 cm^{-1} is attributed to the full-

reflex vibration of the C–C skeleton, and the 1217 cm^{-1} is a characteristic of the S–O bond. The 1300 and 1321 cm^{-1} are assigned to the CH_2 twist. The SERS feature at 1365 cm^{-1} can be attributed to the CH_2 wag and the band at 1437, 1454, and 1478 cm^{-1} are attributed to the CH_2 bending modes. The 1537 cm^{-1} is attributed to CH_2 rocking vibration. It can be noted that, in CTAB, the head group is $(CH_3)_3N^+$ group (trimethylammonium), whereas in SDS, the head group is OSO_3^- (sulfate) [12]. There is an electrostatic interaction between the positively and negatively charged head groups forming catanionic complexes. The intensity of all bands increased significantly except particular functional characteristic band of SDS and CTAB for catanionic solution (SDS/CTAB = 50/50). It was found that, for the lowest feed flow rate (20 µL min^{-1}, pink curve), the Raman characteristic bands of the outlet streams are almost same as pure SDS and CTAB, which is the indication of higher degree of separation.

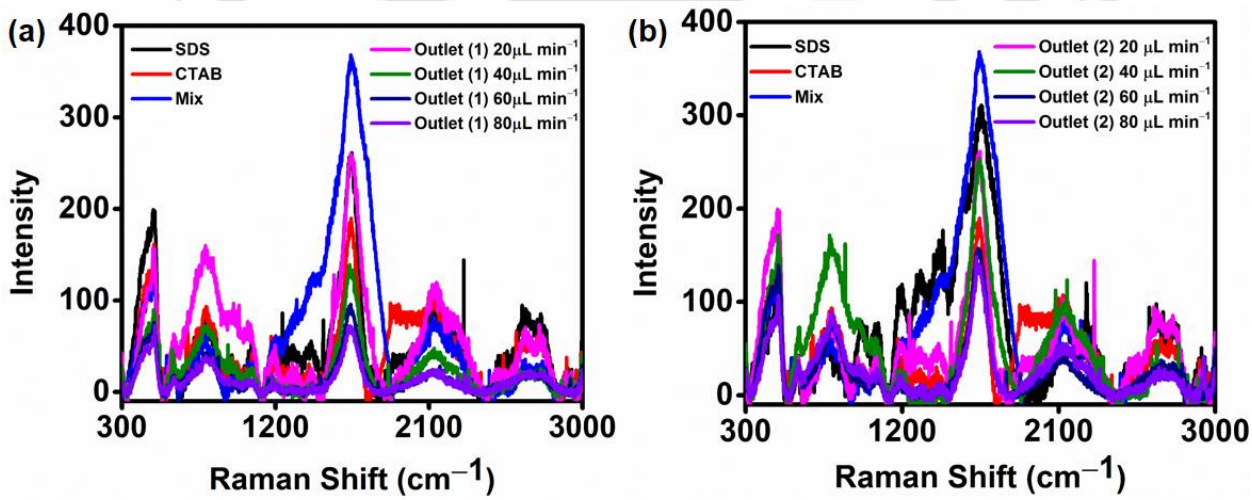

Figure 3.6 (Colour online) **(a)** Raman spectra of the SDS, CTAB, catanionic mixture (SDS/CTAB = 50/50) surfactant, and outlet - 1 stream of various flow rates. **(b)** Raman spectra of the SDS, CTAB, catanionic mixture (SDS/CTAB = 50/50) surfactant, and outlet - 2 stream of various flow rates.

3.3.6 FT-IR Analysis

Figure 3.7 shows the FT-IR spectra of the pure SDS, CTAB, catanionic mixture of surfactant (SDS/CTAB = 50/50), and samples (outlet −1, and outlet −2 of the flow rate 20 µl min^{-1}). It was observed that, pure SDS (blue curve) and outlet −1 (black curve) are having characteristic band and functional group of almost same wavelength. Whereas, pure CTAB (light green curve) and outlet −2 (orange curve) are having characteristic band and functional group of almost same wavelength. These results confirmed that the outlet −1 streams contains mostly SDS surfactant and outlet −2 stream holds CTAB in a major amount. Hence, this analysis supports the results of Raman spectroscopy.

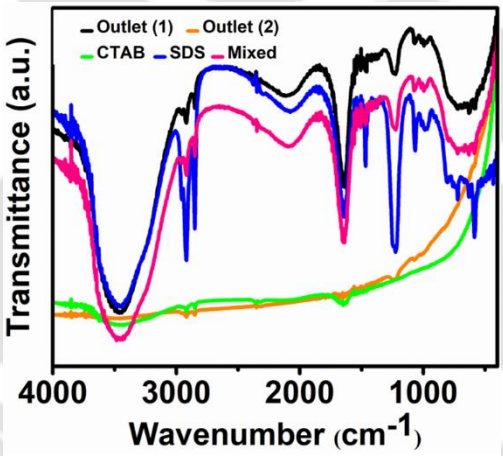

Figure 3.7 (Colour online) shows the FTIR spectra of the SDS (blue curve), CTAB (light green curve), catanionic mixture (SDS/CTAB = 50/50) surfactant (pink curve), outlet – 1 (black curve), outlet – 2 (orange curve).

3.3.7 Measurement of Zeta Potential

The zeta potential at the air–water interface was measured using a zeta potentiometer [make: Beckman Coulter (Switzerland), model: Delsa Nano C]. An ultrasonic water bath [make: Telsonic Ultrasonics (Switzerland), model: TPC 15 H] was used for the sonication of the sample

for 15–30 min to generate the micronanobubbles in the aqueous solution [3]. Next, the dispersion (~1 cm^3) containing the micronanobubbles was immediately transferred to the flow cell of the zeta potentiometer. The micronanobubbles traveled through a confined capillary channel in the flow cell under an electric field. The Doppler frequency shifts of the scattered light were used for measuring the electrophoretic mobility of these micronanobubbles. The Smoluchowski equation was used for the estimation of zeta potential at the air–water interface.

$$\zeta = \left(\frac{\mu}{\varepsilon \varepsilon_0} \right) U \tag{3.3}$$

Where, ζ is valence of ion, ε represents dielectric constant of the medium, ε_0 denotes permittivity of free space, $C^2\ J^{-1}\ m^{-1}$, μ is the solution viscosity, and *U* stand for electrophoretic mobility.

Table 3.1 shows the zeta potential of the pure SDS, CTAB, catanionic mixture of surfactant (SDS/CTAB = 50/50), and samples of different flow rates. It was observed that, pure SDS solution was having net negative charge (-17.90 mV), pure CTAB was having net positive charge (+18.60 mV), and catanionic mixture of surfactant (SDS/CTAB = 50/50) solution was noted net negative charge (-30.45 mV). For the flow rate of 20 μL min^{-1} the zeta potential of outlet –1 was observed at -20.66 mV. Whereas the zeta potential of outlet –2 for the same flow rate was found to be +15.85 mV. This results indicate that, the outlet –1 streams contain mostly SDS surfactant and outlet –2 stream holds CTAB in major amount. Furthermore, with increasing flow rate, the zeta potential of the outlet streams approaches towards the zeta potential of catanionic mixture and for the highest flow rate i.e. 20 μL min^{-1} the zeta potential of both streams (outlet –1, and outlet – 2) becomes almost equal to zeta potential of catanionic mixture. Hence, we can conclude that, at the lower flow rate, separation efficiency was high and vice-versa. It also supports all the above results.

Table 3.1: Zeta potential of pure surfactants and samples

SL. No.	Sample Name	Zeta Potential (mV)
1	Pure SDS	-17.90
2	Pure CTAB	+18.60
3	Catanionic mixture solution	-30.45
4	Outlet (1) – 20 µL min^{-1}	-20.66
5	Outlet (2) – 20 µL min^{-1}	+15.85
6	Outlet (1) – 40 µL min^{-1}	-22.45
7	Outlet (2) – 40 µL min^{-1}	+8.32
8	Outlet (1) – 60 µL min^{-1}	-25.16
9	Outlet (2) – 60 µL min^{-1}	-14.09
10	Outlet (1) – 80 µL min^{-1}	-28.93
11	Outlet (2) – 80 µL min^{-1}	-27.81

3.3.8 FETEM analysis

The morphology and elemental mapping of the outlet streams were studied using FETEM. **Figure 3.8b** and **Figure 3.8d** are the FETEM images of outlet – 1 and outlet – 2 samples for the lowest flow (20 µL min^{-1}) rate, respectively. The elemental mapping was carried out on a selected area. This analysis confirms the elemental composition (atomic and weight percentages) of the outlet streams. In outlet – 1, the atomic % was found to be 89.27 %, 8.84 %, 1.31 %, 0.56 %, and 0.02 % for C, O, Na, S, and Br, respectively. Whereas, in outlet – 2, the atomic % was found to be 94.21 %, 0.31 %, 4.45 %, 0.85 %, and 0.17 % for C, O, Na, S, and Br, respectively.

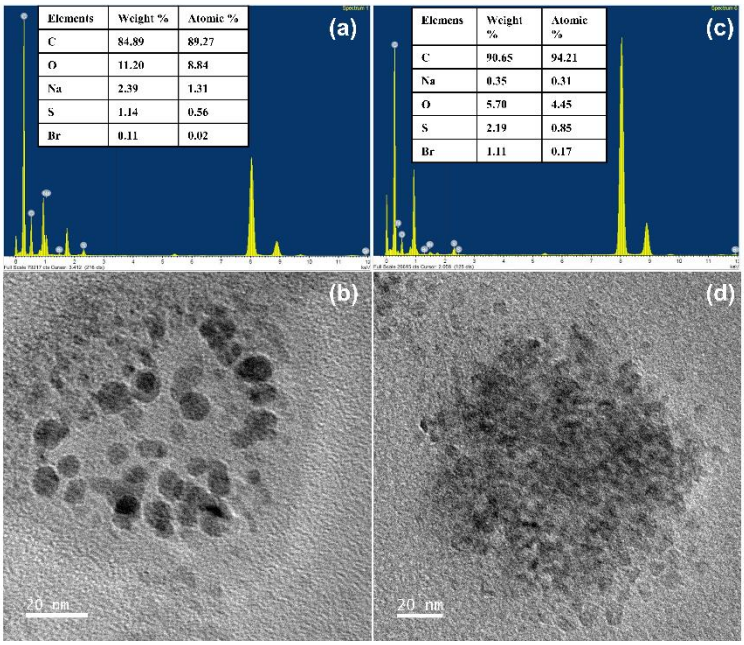

Figure 3.8 Shows the images of the outlet strams of the flow rate 20 µL min^{-1}. **(a)** Elemental mapping spectrum of the outlet –1. **(b)** FETEM image of the outlet –1. **(c)** Elemental mapping spectrum of the outlet –2. **(d)** FETEM image of the outlet –2.

3.3.9 HPLC Analysis

The individual concentration of SDS and CTAB in the samples were analyzed using HPLC. The mobile phase contained a mixture of ACN and ammonium acetate (0.1 M, pH 5.4) flowing at a total flow rate of 1 mL min^{-1} at room temperature which maintained the ACN gradient at (v/v) 25 % – 85 % in 30 min, then hold 85 % ACN for 10 min. The sample injection volume was 20 µL and flow rate of mobile phase was maintained as mentioned above. SDS and CTAB was identified using ELSD detector, and the retention time for SDS and CTAB were 12.72 and 20.33 min, respectively, as shown in **Figure 3.9**.

In order to get the effect of flow rate on the percentage separation, the pure samples (SDS and CTAB) of different concentrations were analyzed and calibration chat was prepared , as shown in **Figure 3.10a and Figure 3.10b**. The HPLC analysis result of the samples shows that percentage separation efficiency decrease with increasing the flow rate. Using the calibration curve, the percentage separation/purity was calculated and found to be ~ 92 %, ~ 82 %, ~ 68 %, and ~ 60 % for the flow rate of 20 µL min^{-1}, 40 µL min^{-1}, 60 µL min^{-1}, and 80 µL min^{-1}, respectively (**Figure 3.10c**). Hence, this result supports the above analysis.

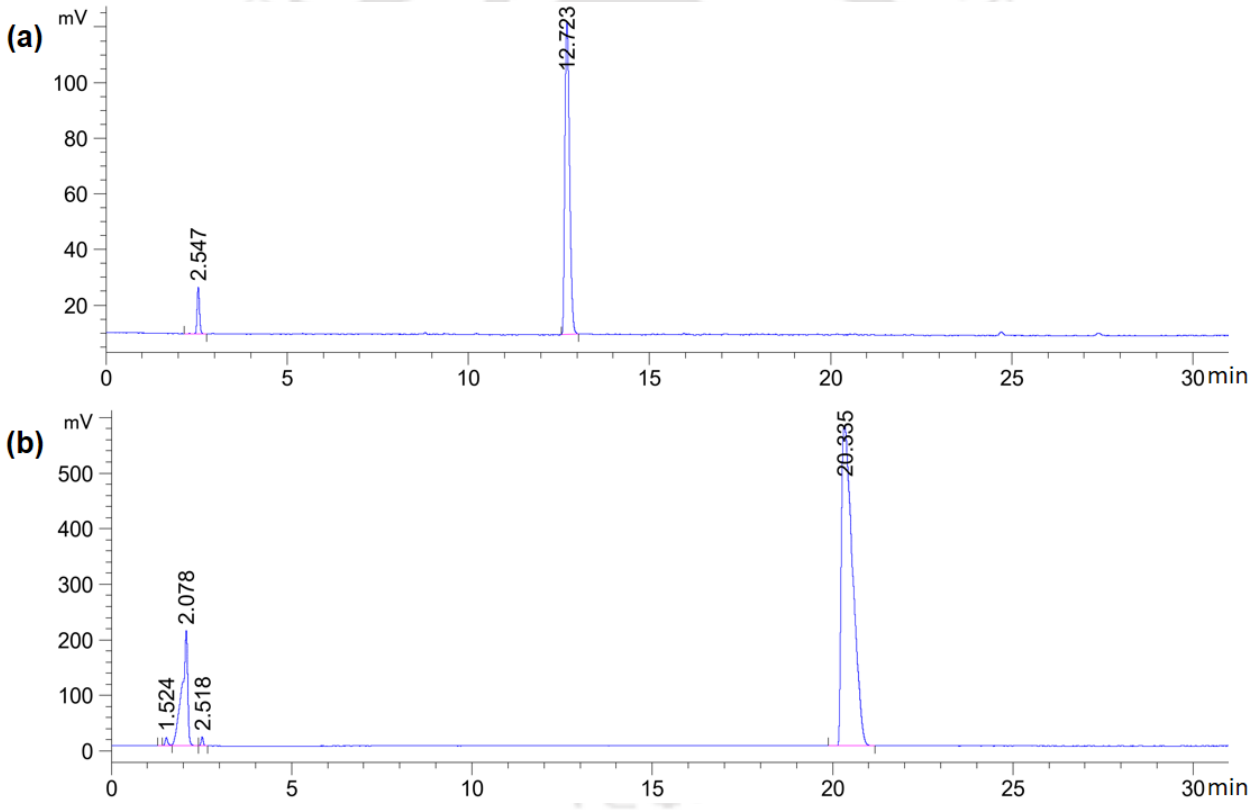

Figure 3.9 Plot **(a)** HPLC spectra of SDS. Plot **(b)** HPLC spectra of CTAB.

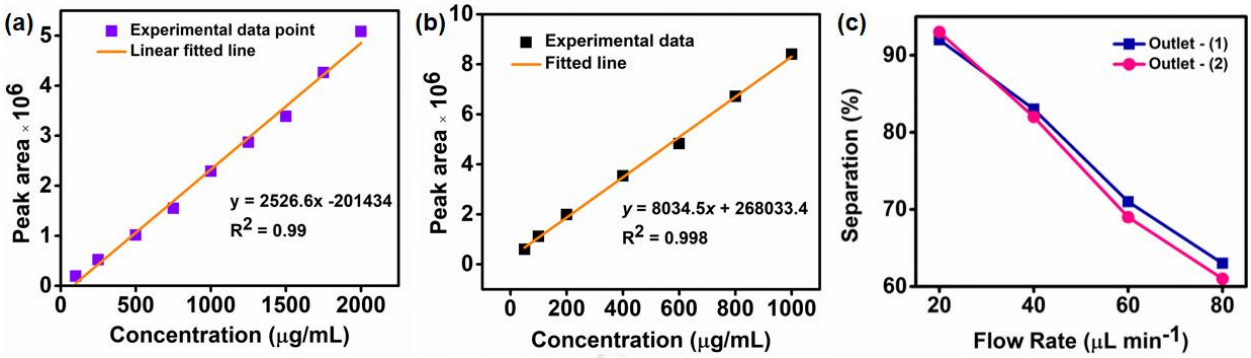

Figure 3.10 Plot **(a)** show the calibration curve for SDS. Plot **(b)** show the calibration curve for CTAB. Plot **(c)** depicts the effect of flow rate on % separation.

3.4 Conclusions

In this study, we have explored a suitable technique to separate anionic and cationic surfactants simultaneously from their mixture under the influence of ultra-low electric voltage on a microfluidic platform. For this, a PDMS Y-shape copper metal sheet electrodes embedded microchannel was fabricated. The constant DC voltage (~ 1.5 V, lower than electrolysis point of water) across the microchannel electrodes was applied. It was found that, the anionic surfactant (SDS) gets attracted towards positive electrodes while cationic surfactant (CTAB) gets attracted towards negative electrodes which results in separation. Separation efficiency depends on the residence time of the fluid inside the microchannel. It turns out that for lower feed flow rate i.e., high residence time favored a higher degree of separation from its mixture and vice-versa. More than 90 % separation efficiency (purity) was achieved at the lower flow rate, which was confirmed through HPLC analysis.

References

[1] F. Tassinari, J. Steidel, S. Paltiel, C. Fontanesi, M. Lahav, Y. Paltiel, R. Naaman, Enantioseparation by crystallization using magnetic substrates, *Chem. Sci.* 10 (**2019**) 5246–5250.

[2] A.M. Becker, S. Gerstmann, H. Frank, Perfluorooctane surfactants in waste waters, the major source of river pollution, *Chemosphere.* 72 (**2008**) 115–121.

[3] S. Chen, M.B. Timmons, J.J. Bisogni, D.J. Aneshansley, Modeling surfactant removal in foam fractionation: II - Experimental investigations, *Aquac. Eng.* 13 (**1994)** 183–200.

[4] B. Burghoff, Foam fractionation applications, *J. Biotechnol.* 161 (**2012**) 126–137.

[5] A. Šonc, V. Grilc, Batch foam fractionation of surfactants from aqueous solutions, *Acta Chim. Slov.* 51 (**2004**) 687–698.

[6] S. Boonyasuwat, S. Chavadej, P. Malakul, J.F. Scamehorn, Anionic and cationic surfactant recovery from water using a multistage foam fractionator, *Chem. Eng. J.* 93 (**2003**) 241–252.

[7] S. Boonyasuwat, S. Chavadej, P. Malakul, J.F. Scamehorn, Surfactant recovery from water using a multistage foam fractionator: Part i effects of air flow rate, foam height, feed flow rate and number of stages, *Sep. Sci. Technol.* 40 (**2005**) 1835–1853.

[8] S. Boonyasuwat, S. Chavadej, P. Malakul, J.F. Scamehorn, Surfactant recovery from water using a multistage foam fractionator: Effect of surfactant type, *Sep. Sci. Technol.* 44 (**2009**) 1544–1561.

[9] P.H. Brunner, S. Capri, A. Marcomini, W. Giger, Occurrence and behaviour of linear alkylbenzenesulphonates, nonylphenol, nonylphenol mono- and nonylphenol diethoxylates in sewage and sewage sludge treatment, *Water Res.* 22 (**1988**) 1465–1472.

[10] D. Prats, F. Ruiz, B. Vázquez, M. Rodriguez-Pastor, Removal of anionic and nonionic surfactants in a wastewater treatment plant with anaerobic digestion. A comparative study, *Water Res.* 31 (**1997**) 1925–1930.

[11] S. González, M. Petrovic, D. Barceló, Removal of a broad range of surfactants from municipal wastewater - Comparison between membrane bioreactor and conventional activated sludge treatment, *Chemosphere.* 67 (**2007**) 335–343.

[12] F. Aloui, S. Kchaou, S. Sayadi, Physicochemical treatments of anionic surfactants wastewater: Effect on aerobic biodegradability, *J. Hazard. Mater.* 164 (**2009**) 353–359.

[13] J. Varley, A.K. Brown, J.W.R. Boyd, P.W. Dodd, S. Gallagher, Dynamic multi-point measurement of foam behaviour for a continuous fermentation over a range of key process variables, *Biochem. Eng. J.* 20 (**2004**) 61–72.

[14] X.J. Wang, Y. Song, J.S. Mai, Combined Fenton oxidation and aerobic biological processes for treating a surfactant wastewater containing abundant sulfate, *J. Hazard. Mater.* 160 (**2008**) 344–348.

[15] M.A. Aboulhassan, S. Souabi, A. Yaacoubi, M. Baudu, Removal of surfactant from industrial wastewaters by coagulation flocculation process, *Int. J. Environ. Sci. Technol.* 3 (**2006**) 327–332.

[16] J. Kaleta, M. Elektorowicz, The removal of anionic surfactants from water in coagulation process, *Environ. Technol.* 34 (**2013**) 999–1005.

[17] C.D. Adams, J.J. Kuzhikannil, Effects of UV/H2O2 preoxidation on the aerobic biodegradability of quaternary amine surfactants, *Water Res.* 34 (**2000**) 668–672.

[18] A. Babuponnusami, K. Muthukumar, A review on Fenton and improvements to the Fenton process for wastewater treatment, *J. Environ. Chem. Eng.* 2 (**2014**) 557–572.

[19] G. Kume, M. Gallotti, G. Nunes, Review on anionic/cationic surfactant mixtures, *J. Surfactants Deterg.* 11 (**2008**) 1–11.

[20] P. Li, J. Hur, Utilization of UV-Vis spectroscopy and related data analyses for dissolved organic matter (DOM) studies: A review, *Crit. Rev. Environ. Sci. Technol.* 47 (**2017**) 131–154.

[21] B. Hao, K. Wang, Y. Zhou, C. Sui, L. Wang, R. Bai, Z. Yang, Label-Free Detecting of the Compaction and Decompaction of ctDNA Molecules Induced by Surfactants with SERS Based on a nanoPAA-ZnCl2-AuLs Solid Substrate, *ACS Omega.* 5 (**2020**) 1109–1119.

[22] J.D. Coppock, K. Krishan, M. Dennin, B.G. Moore, Fluorescence microscopy imaging of Giant folding in a catanionic monolayer, *Langmuir.* 25 (**2009**) 5006–5011.

[23] F. Zhao, J. Xu, Fractal metal nanoparticle aggregates morphology formation mediated by polyelectrolyte/surfactant complex films at interfaces, *Colloid Polym. Sci.* 285 (**2006**) 113–117.

[24] B. Sohrabi, H. Gharibi, B. Tajik, S. Javadian, M. Hashemianzadeh, Molecular interactions of cationic and anionic surfactants in mixed monolayers and aggregates, *J. Phys. Chem. B.* 112 (**2008**) 14869–14876.

[25] E.W. Kaler, K.L. Herrington, A.K. Murthy, J.A.N. Zasadzinski, Phase behavior and structures of mixtures of anionic and cationic surfactants, *J. Phys. Chem. 96* (**1992**) 6698–6707.

[26] A.L. Dendramis, E.W. Schwinn, R.P. Sperline, A surface-enhanced Raman scattering study of CTAB adsorption on copper, *Surf. Sci.* 134 (**1983**) 675–688.

[27] R. Foucault, R.L. Birke, J.R. Lombardi, SERS of Surfactants in Monolayer and Multibilayer Forms on an Electrified Ag Surface, *Langmuir.* 19 (**2003**) 8818–8827.

[28] X. Huang, I.H. El-Sayed, W. Qian, M.A. El-Sayed, Cancer cells assemble and align gold nanorods conjugated to antibodies to produce highly enhanced, sharp, and polarized surface Raman spectra: A potential cancer diagnostic marker, *Nano Lett.* 7 (**2007**) 1591–1597.

[29] H. Duan, L. Jia, M. Chen, S. Ge, X. Guo, Surface-enhanced Raman scattering based on colloidal Ag nanoparticles for quantitative detection of cetyltrimethyl ammonium bromide, *Mater. Express.* 6 (**2016**) 77–82.

[30] R.F.V. Villamil, P. Corio, S.M.L. Agostinho, J.C. Rubim, Effect of sodium dodecylsulfate on copper corrosion in sulfuric acid media in the absence and presence of benzotriazole, *J. Electroanal. Chem.* 472 (**1999**) 112–119.

[31] M. Picquart, Vibrational mode behavior of SDS aqueous solutions studied by Raman scattering, *J. Phys. Chem.* 90 (**1986**) 243–250.

[32] A.R. Paschoal, A.P. Ayala, R.C.F. Pinto, C.W.A. Paschoal, A.A. Tanaka, J.S. Boaventura Filho, N.M. José, About the SDS inclusion in PDMS/TEOS ORMOSIL: A vibrational spectroscopy and confocal Raman scattering study, *J. Raman Spectrosc.* 42 (**2011**) 1601–1605.

[33] J.C. Valmalette, Z. Tan, H. Abe, S. Ohara, Raman scattering of linear chains of strongly coupled Ag nanoparticles on SWCNTs, *Sci. Rep.* 4 (**2014**) 1–8.

CHAPTER 4

Liquid-Liquid Efficient Micro Extraction of Dye in a Microfluidic Platform by Creating Electric Field Induced Instability at the Interface of Fluids

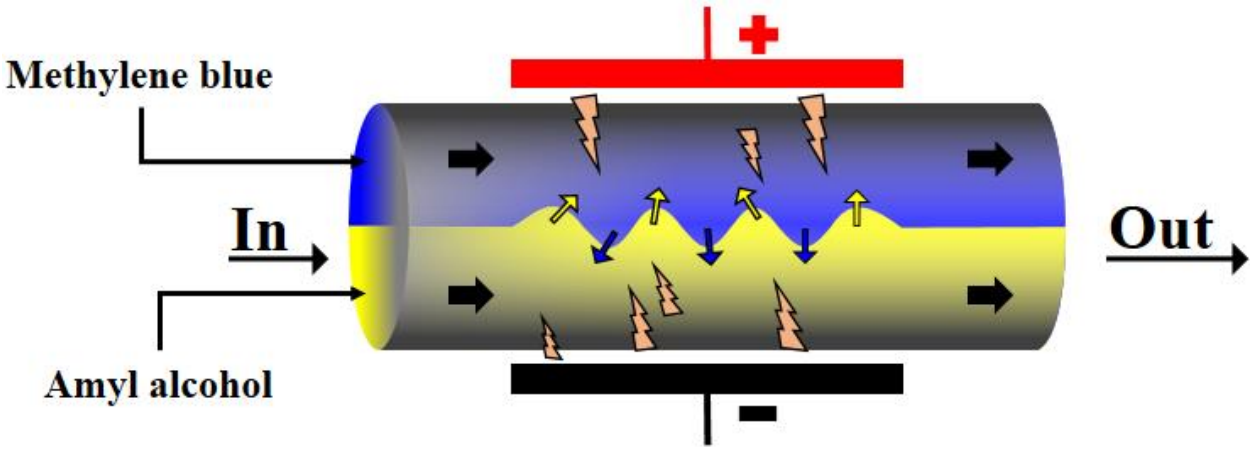

CHAPTER 4

Liquid-Liquid Efficient Micro Extraction of Dye in a Microfluidic Platform by Creating Electric Field Induced Instability at the Interface of Fluids

Nowadays, various innovative process technologies for refining industrial wastewater are often adopted to meet the lower toxicity level of pollutants to satisfy the treatment standards. In this regard, the present study focuses on the component transfer from one liquid phase to another liquid phase, commonly known as the extraction process, in which both the liquids are flowing through a microchannel in the presence of an applied external electric field. We have explored interfacial instability in the presence of an external electric field in the microchannel for the extraction of methylene blue dye from the aqueous phase using N-amyl alcohol. It was observed that the interfacial mass transfer process occurs through local instability, and hence extraction occurred. The relative strength of mass transfer rate for different cases, such as flow rate, numbers of electrodes, intensity of electric field, have been reported in detail. Additionally, effect of spatially varying electric field with different periodicity on component extraction process has been also studied in detail. UV-Vis spectroscopy result shows that, for higher electric field intensity and number of electrodes, extraction efficiency was high.

4.1 Introduction

Colorful consumable commodities, such as food, clothes, leather, vehicles, housing etc. have always lured people since time immemorial. The earliest dyes available to people were Madder extracted from the roots of *Rubia tinctorum* plant and indigo from the leaves of *Indigofera*

tinctoria [1]. The synthetic dyes were cheap, rendered vast combinations of colors, gave excellent properties to the dyed materials but with time researchers studied and put forward its detrimental effects on the living population as well as the environment [2]. Dyes can enter the whole biotic chain either by direct exposure or consumption or indirectly from various air, water or land sources. Extensively used reddish-violet color (Trade name: D & C, Red. No 19) in both textile and food causes skin, eye and respiratory tract irritation and are equally harmful if swallowed in excess [3]. Increasing level of colored pollutants in these water bodies blocks the sunlight from entering the water bodies decreasing the dissolved oxygen and increasing the biological oxygen demand [4]. This situation not only kills the aquatic animals but increasing presence leads to bioaccumulation and eventually biomagnification through the entire food web [5]. Researchers have come up with several chemical and natural techniques to clean the effluent wastewater from industries as well as the dye polluted water bodies. Liquid-liquid extraction is an important unit operation where one component is extracted from a particular liquid phase to another liquid phase.

In this work, we have studied a two-phase flow with the simultaneous extraction process, where a component is transferred from phase 1 to phase 2. In a novel approach, we have made an effort to improve the extraction efficiency by creating the perturbation at the interface in the presence of the electric field.

4.2 Experimental section

4.2.1 Materials

Methylene blue, buffered oxide etchant (BOE), and Silicone rubber tube were purchased from Sigma-Aldrich USA. N-Amyl alcohol and hexamethyldisilazane (HMDS) were bought from

HiMedia, (India). Whereas, Sylgard^{TM} 184 Silicone Elastomer Kit for the preparation of polydimethylsiloxane (PDMS) was obtained from Dow Chemical International Pvt. Ltd. USA. Furthermore, S1813 (positive tone resist) and microposit (MF-319 developer) were acquired from Rohm and Haas Electronic Materials LLC, USA. PG remover was purchased from MicroChem Corp. USA. Acrylonitrile Butadiene Styrene (ABS) filament was procured from Ultimaker, Netherlands. Non-toxic polyethylene tubing was bought from Pro Lab Marketing Pvt. Ltd. India. Additionally,10 mL Dispo Van disposable syringes and ITO coated glass were acquired from 1mg, India and Shilpa Enterprises, India, respectively. All spectroscopic measurement solutions were prepared with Milli-Q water (resistivity ~ 18.2 MΩ.cm) which was purified by a Millipore system (France, model: Elixplus Milli-Q).

4.2.2 Apparatus

For the study of material properties, UV-Vis spectroscopy (UV-Vis), Raman spectroscopy, Field emission transmission electron microscope (FETEM), and Field emission scanning electron microscope (FESEM) were used.

The UV-Vis (Shimadzu, UV-2600 230 V EN spectrophotometer) absorbance of the samples was measured to quantify the concentration of methylene blue in water as well as organic phases in the UV visible region (200 nm – 800 nm). The micro-Raman spectroscopy (Horiba Jobin Vyon, LabRam HR) was used to validate functional groups and concentration of the samples. The spectra were acquired at an acquisition duration of 10 s with an excitation wavelength of 532 nm. FETEM (JEOL, JEM 2100F at the acceleration voltage of 200 kV) was used to get detailed morphology of both phase samples. The samples were prepared by dispensing 100 µL on a 400-mesh carbon-coated copper grid (SPI, USA), and then dried at room

temperature in a vacuum oven. FESEM (Zeiss, Gemini 300 at the acceleration voltage of 30 kV) was performed for elemental mapping of materials.

A syringe pump (Harvard Apparatus, PHD 2000) was used to infuse the fluids inside the µ-mixture extractor at a controlled flow rate. The flow connection from the syringe to the µ-mixture extractor was made by silicone rubber tubes (Sigma-Aldrich, I.D. × O.D. 1/16 inch × 1/8 inch) and micropipette tips (Tarson, 0.2 µL – 10 µL). Whereas, to collect the sample, the outlet of µ- mixture extractor was connected using non-toxic polyethylene tubing (Intramedic Clay Adams, I.D. × O.D. 1/67 inch × 1/23 inch). 3D printer (Ultimaker 3, Netherlands) was used to mold the ABS wire in a flat serpentine shape. This 3D printed ABS wire was then used as a mold for the fabrication of PDMS microfluidic channel having an inner equivalent diameter ~ D_e = 90 µm (thickness ~ D = 40 µm and width ~ W = 200 µm). A programmable AC (0 – 300 V, Chroma 61601 AC power source) power source was used as a voltage source to apply the electric field across the µ-mixture extractor.

4.2.3 Methods

4.2.3.1 µ-mixture extractor fabrication

A 3D printed serpentine microfilament (~ D_e = 90 µm) was fabricated by extruding ABS using the 3D printer (Ultimaker 3). A molding technique was used to fabricate a microchannel in PDMS. First, part A (oligomer) and part B (crosslinker) of the Sylgard^{TM} 184 elastomer kit were mixed thoroughly in the ratio of 10:1. The mixture was then degassed in a vacuum desiccator for 40 min to remove all the air bubbles trapped inside. On a cleaned glass plate, a rectangular well was prepared with the help of double-sided tape. A small amount of the oligomer-crosslinker mixture was poured into it and shaken to make a thin film of oligomer over the glass plate. The film was then partially cured at 85 °C in a hot air oven for half an hour and subsequently cooled

down to room temperature. After that the prefabricated 3D printed serpentine ABS microfilament was cleaned with DI water, dried with nitrogen flow, and then placed on top of the thin partially cured PDMS film. Again, some of the degassed oligomer-crosslinker (10:1) mixture was poured on top of it. It was ensured that no bubbles were trapped inside the liquid oligomers-crosslinker mixture after pouring. The arrangement was then kept in a hot air oven at 85 °C for 6 h to fully crosslink the PDMS. Also, it was made sure that the ends of the ABS filament were outside the PDMS block. After curing, the ABS microfilament embedded PDMS block was dipped into acetone and sonicated for 12 h. The acetone dissolved the ABS microfilament, and a microchannel was formed inside the PDMS block. Later, the microchannel embedded PDMS block was further ultra-sonicated in the acetone bath for 5 h to remove any trace of ABS completely. The microchannel was then repeatedly washed with acetone and DI water for 10 – 15 min. Finally, the cleaned micro-channel was dried first by blowing nitrogen gas and then by keeping it in a hot air oven for 30 min at 75 °C. **Figure 4.1** shows an optical image of a serpentine-shaped microchannel with an inner thickness and width are ~ D = 40 μm and ~ W = 200 μm (~ D_e = 90 μm), respectively. The total path length of the ultra-fine microchannel was found to be ~ l = 60 cm.

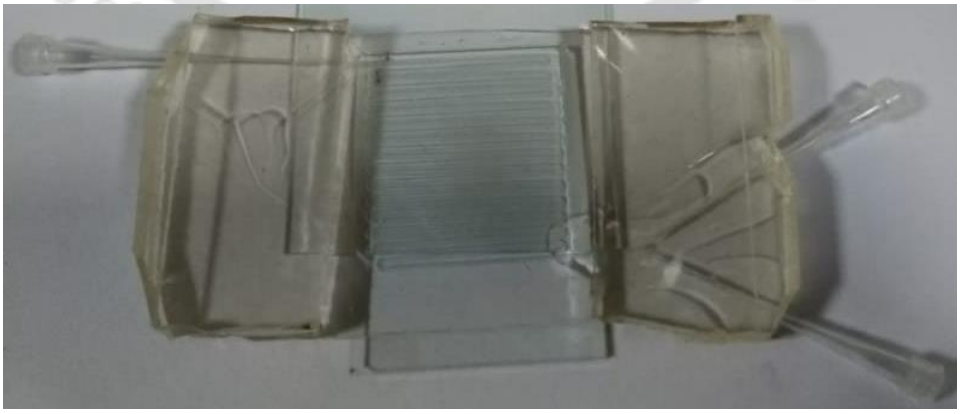

Figure 4.1 Shows the optical image of serpentine-shaped microchannel.

4.2.3.2 Fabrication of electrodes on the ITO coated glass substrate

The electrodes were prepared on an ITO coated glass plate. Initially an instrument called mask writer, was used to fabricate the layout of electrodes on ITO coated glass. At first, the ITO coated glass of dimension 50 mm × 50 mm × 1.1 mm was coated with a primer, hexamethyldisilazane (HMDS) (Himedia, India) at 4000 rpm for 60 sec at ITO coated side, followed by baking for 1 h at a constant temperature of 160 °C, for better adhesiveness in between ITO-glass and photoresist. Furthermore, a positive tone photoresist, S1813 (MicroChem Corp.) was coated above the HMDS layer at 3500 rpm for 60 sec, followed by pre-baking for 3 min. Later, the photoresist coated substrate was exposed under UV-laser light source of wavelength 375 nm, followed by development in a developer solution mixture for 40 sec. Finally, the substrate was hard baked at a temperature of 150 °C for 5 min.

Next, the developed sample was then immersed in a buffered oxide etchant (BOE) which is a mixture of ammonium fluoride and hydrofluoric acid in a ratio of 10:1, for 3 h. Later, rest of the photoresist was washed away by a positive remover, leaving only the ITO-electrodes on the substrate. At last, the substrate was rinsed rigorously with a copious amount of acetone and distilled water followed by the final step of drying the substrate in a nitrogen stream.

The width of each electrode was 300 µm. Here, four types of arrangement could be done while, the maximum achievable gap between two consecutive electrodes, was 3.5 mm and the minimum was 300 µm. When the electrodes were 3.5 mm apart from each other, a minimum number of electrodes participated in the experiment, whereas, when the gap was 300 µm in between the electrodes then, maximum number of electrodes participated in the experiment.

4.3 Results and discussion

4.3.1 Liquid-liquid extraction of methylene blue in a microchannel using electric field

Figure 4.2 shows the schematic of the experimental setup for the liquid-liquid micro extraction of methylene blue from aqueous phase to organic phase in a microfluidic platform using electric field. The two immiscible liquids are flowing in the µ-mixture extractor in a plug flow fashion. In this study methylene blue (cationic dye) solution was prepared in deionized water at a concentration of 10 mg L^{-1} which was maintained throughout the experiment. Briefly, syringe 1 and syringe 2 were filled with methylene blue solution and pure N-Amyl alcohol, respectively. These feeds were injected with the help of a syringe pump into the µ-mixture extractor at a constant flow rate of 5 µL/min. Due to lower fluid velocity and lesser equivalent diameter of the channel, the flow pattern of these fluids inside the µ-mixture extractor was found to be laminar. The residence time of the fluids inside the µ-mixture extractor, t_r, was ~ 8 min. At this condition, it was observed that, the extraction efficiency of methylene blue was high compared to that in the batch process, due to high surface to volume ratio of the fluids in the µ-mixture extractor. The mass transfer rate from one phase to another phase can be further increased by creating turbulence at the interface of the two fluids. For this, the µ-mixture extractor was kept in between a plane and a patterned ITO coated glass i.e. the electrodes were placed outside the channel to apply the electric field on the microchannel. The patterned ITO coated glass was placed on the top of µ-mixture extractor in such a way that the µ-mixture extractor fluids can experience maximum electric field while applying the voltage. It was observed that methylene blue dye was adhering to one side of the microchannel while applying the DC electric field. Methylene blue being a cationic dye, gets attracted towards the negative electrode (Anode) in DC electric field. In this report, target was to enhance the mass transfer rate by creating

instability at the interface. Hence, to overcome this problem, AC electric field was applied in the vertical direction of the channel throughout the experiment.

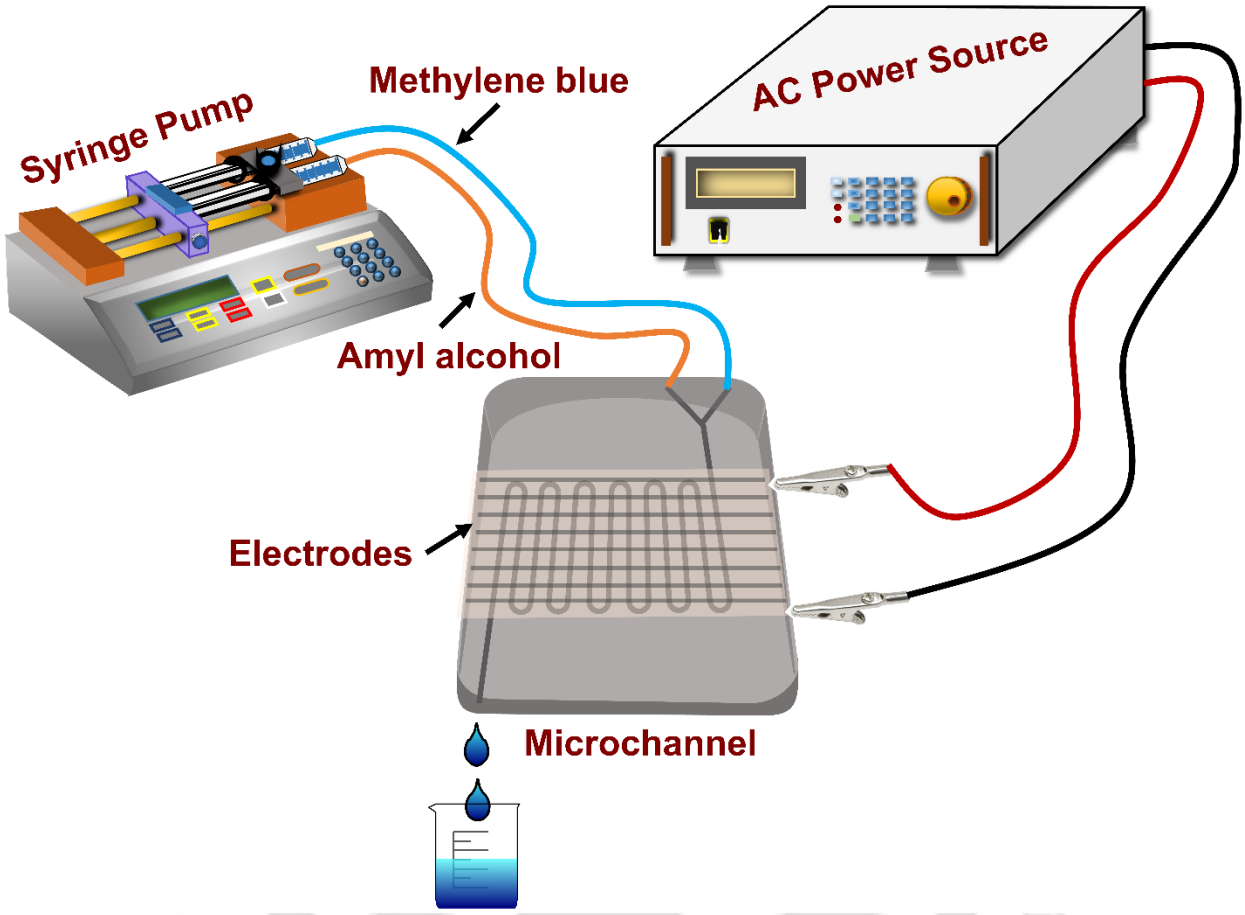

Figure 4.2 Schematic representation of the experimental setup for the extraction of methylene blue from aqueous phase in a continuous manner at a microfluidic platform.

It is well established that the application of external electric field causes interfacial instabilities, pattern formation, and rupture as a result of well developed Maxwell stresses in dielectric [6,7] or leaky dielectric [8] materials . The electric field only gives Maxwell stress within the dielectric liquid, and there is essentially no electric current flow. As the electric field was applied vertically throughout the channel, Maxwell stress experienced at the liquid-air

interface assist the polymer thin film to form columns which resulted in instability at the interface. Hence, the interface gets deformed and ultimately creates instability and breaks into microdroplets. Due to this, a solute component (methylene blue) is dissolved in the aqueous phase, which is extracted by the organic phase (N-Amyl alcohol), during the course of experiment.

The outlet solution from the μ-mixture extractor was collected in a 2 mL glass vial. These two-phase dispersions were allowed to settle for 30 min to form two liquid phases: aqueous and organic phase. Subsequently, the two phases were separated using micro-pipette in separate vials and absorbance of the dye was measured for each individual phases. All the experiments were run three times and mean value was reported to minimize the error. UV-Vis analysis shows that the maximum absorption intensity of the methylene blue dye was ~664 nm [9] which was used for all calculations. The distribution ratio (*D*) and percentage of extraction (*E*) were calculated as per the following equations:

$$D = \frac{[C]_{Org}}{[C]_{Aqu}} \qquad (4.1)$$

$$E = \frac{[C]_{Feed} - [C]_{Aqu}}{[C]_{Feed}} \times 100 \qquad (4.2)$$

Where, $[C]_{Org}$ is the dye concentration in the organic phase (mg L^{-1}), $[C]_{Feed}$ is the initial dye concentration in feed (mg L^{-1}), and $[C]_{Aqu}$ is the dye concentration of aqueous phase after extraction (mg L^{-1}).

4.3.2 Effect of various intensity of interfacial electric field and numbers of electrodes on dye extraction

In order to evaluate the effect of electric field intensity and number of electrodes on the percentage of dye extracted, a series of experiments were performed and characterized using UV-Vis spectroscopy. We have studied the effect of different numbers of electrodes, and different intensities of electric fields to achieve the most efficient one with respect to extraction efficiency. In **Figure 4.3**, E1 – E5 represents the number of electrodes, where, E1 denotes the lowest number of electrodes and E5 indicates the highest number of electrodes. The influence of electric field (0 – 300 V/m) and number of electrodes (E1 – E5) on the extraction efficiency were studied. First the extraction efficiency was studied by varying the electric field from 0 – 300 V/m keeping the number of electrodes constant and vice-versa. After experiment, both the phases were analyzed using different techniques such as UV-Vis, Raman spectroscopy, etc. For the UV-Vis analysis, samples were prepared by dissolving 400 µL of sample in 2 mL of DI water and recording the intensity of the particular sample. **Figure 4.3a** describes the UV-Vis absorbance spectrum of methylene blue (black colored line) in the feed which has a characteristic peak at ~664 nm. The UV-Vis spectra of aqueous phase samples for the lowest (E1) number of electrodes at different intensities of electric field at, 0 V (red colored line), 50 V (blue colored line), 100 V (pink colored line), 150 V (green colored line), 200 V (light yellow colored line), 250 V (purple colored line), and 300 V (light green colored line) are shown in **Figure 4.3a**. It was observed that the absorbance peak intensity decreases with increasing intensity of electric field. The UV-Vis spectra of aqueous phase for the highest (E5) number of electrodes at different intensity of electric field at, 0 V (red colored line), 50 V (blue colored line), 100 V (pink colored line), 150 V (green colored line), 200 V (light yellow colored line), 250 V (purple colored line), and 300 V (cyan colored line) are shown in **Figure 4.3e**. It was observed that the absorbance

peak intensity was drastically decreasing with increasing intensity of electric field. Reverse is true for organic phase as shown in **Figure 4.4**. The rule of thumb for UV-Vis spectroscopy states that, an increase in concentration increases the absorbance values and vice-versa.

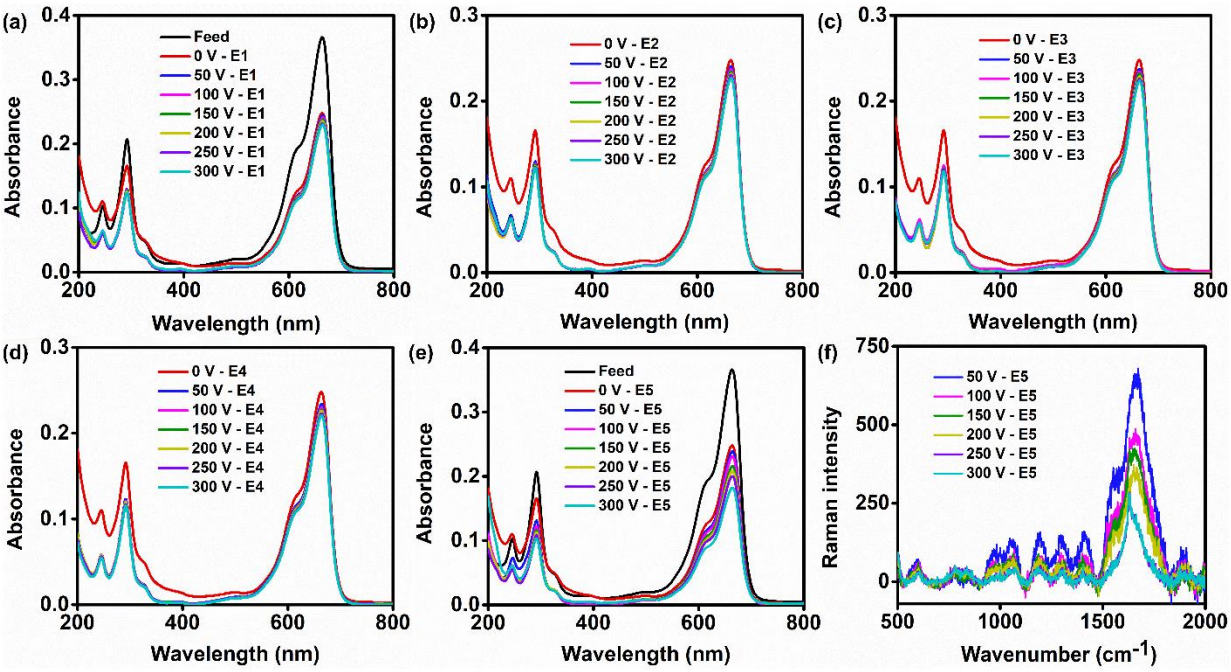

Figure 4.3 (Colour online) Plot **(a)** Aqueous phase UV-Vis spectra of methylene blue of feed (black), 0 V (red), 50 V (blue), 100 V (pink), 150 V (green), 200 V (light yellow), 250 V (purple), and 300 V (cyan) for lowest (E1) number of electrodes. **(b)** Aqueous phase UV-Vis spectra of 0 V (red), 50 V (blue), 100 V (pink), 150 V (green), 200 V (light yellow), 250 V (purple), and 300 V (cyan) for E2 number of electrodes. **(c)** Aqueous phase UV-Vis spectra of 0 V (red), 50 V (blue), 100 V (pink), 150 V (green), 200 V (light yellow), 250 V (purple), and 300 V (cyan) for E3 number of electrodes. **(d)** Aqueous phase UV-Vis spectra of 0 V (red), 50 V (blue), 100 V (pink), 150 V (green), 200 V (light yellow), 250 V (purple), and 300 V (cyan) for E4 number of electrodes. **(e)** Aqueous phase UV-Vis spectra of 0 V (red), 50 V (blue), 100 V (pink), 150 V (green), 200 V (light yellow), 250 V (purple), and 300 V (cyan) for highest (E2) number of electrodes. **(f)** Aqueous phase Raman spectra of 50 V (blue), 100 V (pink), 150 V (green), 200 V (light yellow), 250 V (purple), and 300 V (cyan) for highest (E5) number of electrodes.

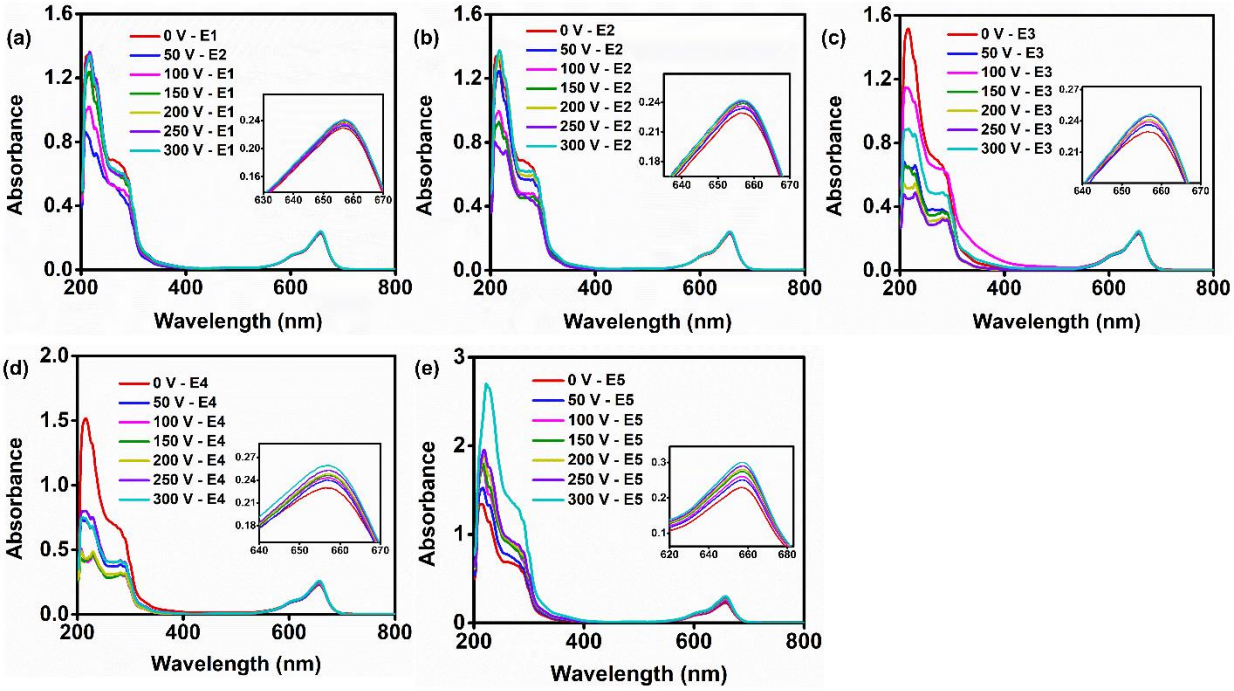

Figure 4.4 (Colour online) Plot **(a)** Organic phase UV-Vis spectra of methylene blue of 0 V (red), 50 V (blue), 100 V (pink), 150 V (green), 200 V (light yellow), 250 V (purple), and 300 V (cyan) for lowest (E1) number of electrodes. **(b)** Organic phase UV-Vis spectra of methylene blue of 0 V (red), 50 V (blue), 100 V (pink), 150 V (green), 200 V (light yellow), 250 V (purple), and 300 V (cyan) for E2 number of electrodes. **(c)** Organic phase UV-Vis spectra of methylene blue of 0 V (red), 50 V (blue), 100 V (pink), 150 V (green), 200 V (light yellow), 250 V (purple), and 300 V (cyan) for E3 number of electrodes. **(d)** Organic phase UV-Vis spectra of methylene blue of 0 V (red), 50 V (blue), 100 V (pink), 150 V (green), 200 V (light yellow), 250 V (purple), and 300 V (cyan) for E4 number of electrodes. **(e)** Organic phase UV-Vis spectra of methylene blue of 0 V (red), 50 V (blue), 100 V (pink), 150 V (green), 200 V (light yellow), 250 V (purple), and 300 V (cyan) for highest (E5) number of electrodes.

Hence, this result indicates that the extraction efficiency increases with increasing number of electrodes and intensity of electric field as the concentration of methylene blue in the aqueous phase was decreasing with increasing the number of electrodes and intensity of electric field. Using a calibration curve, **Figure 4.5a**, the extraction efficiency was calculated and found to be 60% for 0 V/m, 62% for 50 V/m, 65% for 100 V/m, 68% for, 150 V/m, 70% for 200 V/m, 73%

for 250 V/m, and 80% (**Figure 4.5c**) for 300 V/m for the highest numbers of electrodes. The observation made was that the component transfer rate increases with increasing number of electrodes. Hence, extraction efficiency increases with increasing the number of electrodes and voltage across the wall of the μ-mixture extractor. The results show that, at 300 V and E5 numbers of electrodes, the extraction efficiency of methylene blue from the aqueous phase to organic phase was higher compared to other cases. It can be further increased by increasing the electric field and will become constant at a very high electric field. To validate the above results, we further studied the Raman spectra of all the samples.

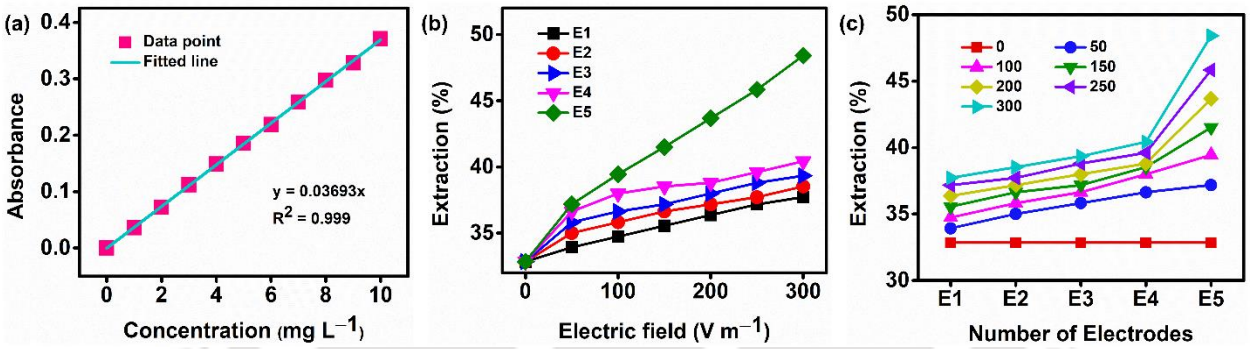

Figure 4.5 (Colour online) Plot **(a)** show the calibration curve for the methylene blue at different concentration (0 mg L^{-1} to 10 mg L^{-1}) as a function of absorbance. Plot **(b)** depicts the effect of various intensity of electric field on % extraction keeping constant numbers of electrodes. Plot **(c)** represents the effect of various numbers of electrodes on % extraction keeping constant electric field.

4.3.3 Raman spectroscopy

Figure 4.3f displays the Raman spectra of the aqueous phase samples. The Raman spectra were recorded using 400 μL sample in 2.5 mL of DI water. The characteristic Raman peaks of methylene blue at 445 cm^{-1} (Skele-tal deformation of C–N–C); 667 cm^{-1} (Out-of-plane bending of C–H); 767, 857 and 900 cm^{-1} (In-plane bending of C–H); 1182 cm^{-1} (Stretching of C–N),

1319 cm^{-1} (In-plane ring deformation of C–H) and 1624 cm^{-1} (Asymmetrical stretching of C–N) were observed [10]. It was seen that; the characteristic Raman peak intensity of MB decreases with increasing number of electrodes and electric field. As Raman intensity is also the function of concentration, we can conclude that extraction efficiency increases with increasing the number of electrodes and voltage across the wall of the μ-mixture extractor. It was noticed that, at 300 V and E5 numbers of electrodes, the extraction efficiency of methylene blue from aqueous phase to organic phase was higher compared to other cases, which supports the UV-Vis spectroscopy results.

4.3.4 Image analysis

Figure 4.6 shows the images of glass vials containing aqueous phase samples of feed namely, 0 V, 50 V, 100 V, 150 V, 200 V, 250 V, and 300 V for the highest (E5) number of electrodes. Each vials contains pure aqueous phase sample without dilution.

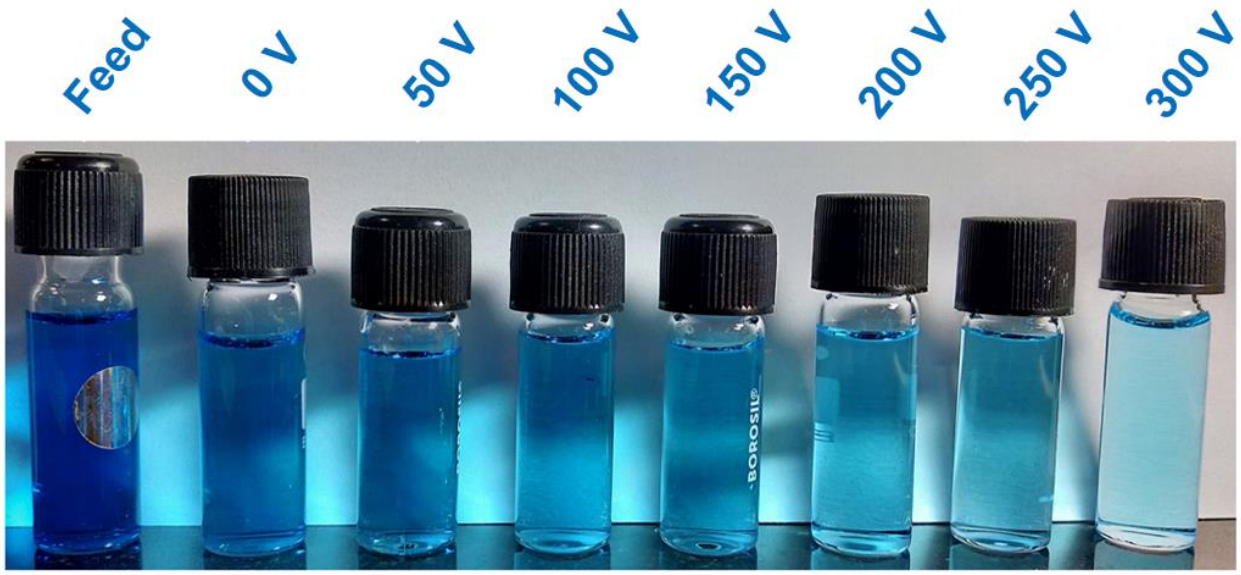

Figure 4.6 Shows the images of glass vials containing aqueous phase samples of feed, 0 V, 50 V, 100 V, 150 V, 200 V, 250 V, and 300 V for highest (E5) number of electrodes.

These images reflect that, the color intensity is highest for feed. The intensity of the methylene blue color decreases with increasing the electric field as well as the number of electrodes. Hence, visually we can see that the concentration of methylene is lowest at 300 V and it increases with decreasing voltage.

4.3.5 FETEM analysis

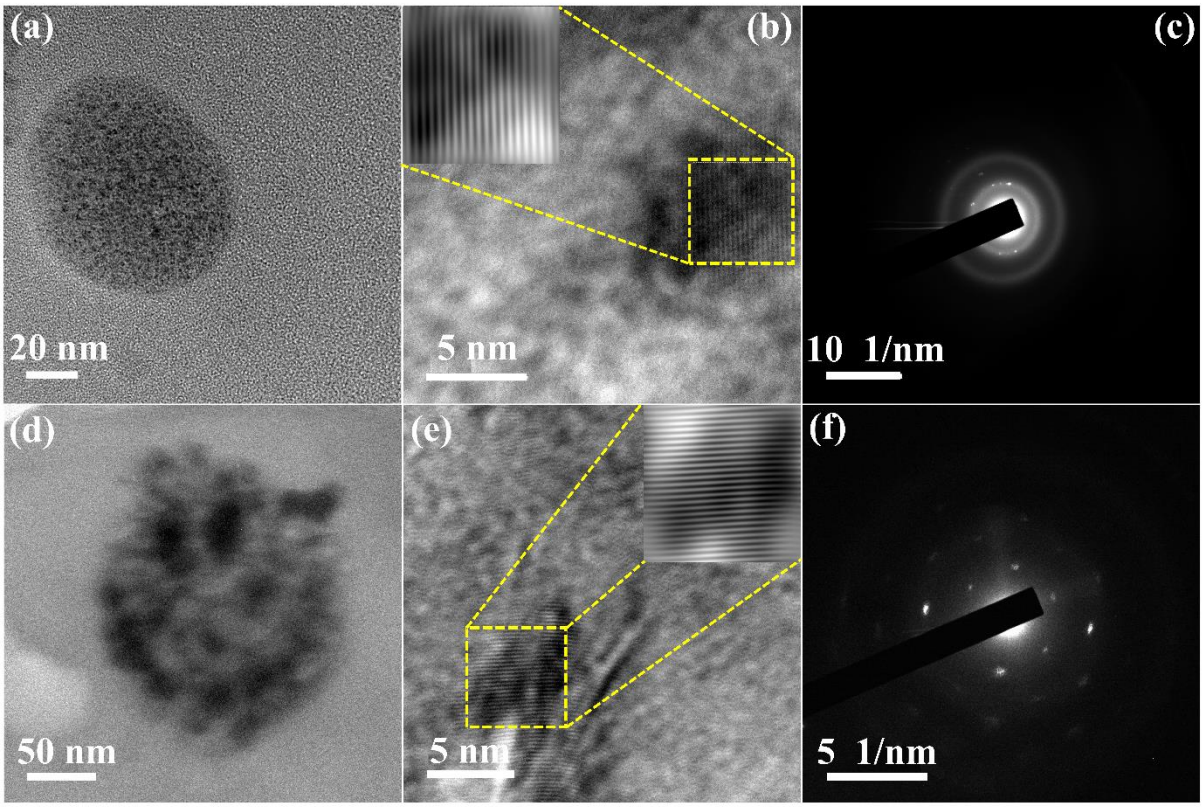

Figure 4.7 Shows the images of aqueous and organic phase **(a)** FETEM image of the aqueous phase. **(b)** Magnified image of aqueous phase with HRTEM image at the inset showing the lattice fringes of ~ 0.20 nm. **(c)** Selected area electron diffraction (SAED) pattern of the aqueous phase. **(d)** FETEM image of the organic phase. **(e)** Magnified image of organic phase with HRTEM image at the inset showing the lattice fringes of ~ 0.18 nm. **(f)** Selected area electron diffraction (SAED) pattern of the organic phase.

The morphology of MB was studied by using FETEM. The sample for the FETEM study was prepared by dropping the aqueous and organic solutions of MB onto a 400-mesh carbon-coated copper grid (SPI, USA) and dried at 40 °C in a vacuum oven. **Figure 4.6a** and **Figure 4.6d** describe the corresponding FETEM images of aqueous and organic phase solution, respectively. The dark regions in the FETEM show the size and shape of the MB. However, the HRTEM images (**Figure 4.6b** and **Figure 4.6e)** of both phases show that most of the MB particles are in quasi-crystalline state. Well resolved lattice fringes with an equal interplanar spacing of ~0.20 nm, ~0.18 nm for aqueous and organic phase are shown in the inset of **Figure 4.6b** and **Figure 4.6e**, respectively. The SAED pattern of aqueous and organic phase are shown in **Figure 4.6c** and **Figure 4.6f**, respectively. This analysis confirms the crystallinity of the material. The presence of a single circular orbit with prominent dots proves the presence of prominent multilayered crystalline material.

4.3.6 Energy dispersive X-ray (EDX) analysis

The cross-sectional FESEM image of both phases are shown in **Figure 4.7**. The samples for the FESEM analysis were prepared by drop-casting on aluminium foil and dried at ~50 °C temperature in a vacuum oven. **Figure 4.7a** and **Figure 4.8a** insets describe the corresponding FESEM images of the aqueous and organic phases, respectively. The elemental mapping of aqueous and organic phase was carried out by selecting a rectangular area of the samples as shown in **Figure 4.7(b-e)** and **Figure 4.8(b-e)**, respectively. The atomic percentages for aqueous phase from elemental mapping analysis of the sample were found to be 57.90 %, 38.30 %, 3.60 %, and 0.10 % for C, N, S and Cl, respectively. Whereas, the atomic percentages for organic

phase from elemental mapping analysis of the sample were found to be 73.40 %, 17.80 %, 6.40 %, and 2.40 % for C, N, S and Cl, respectively.

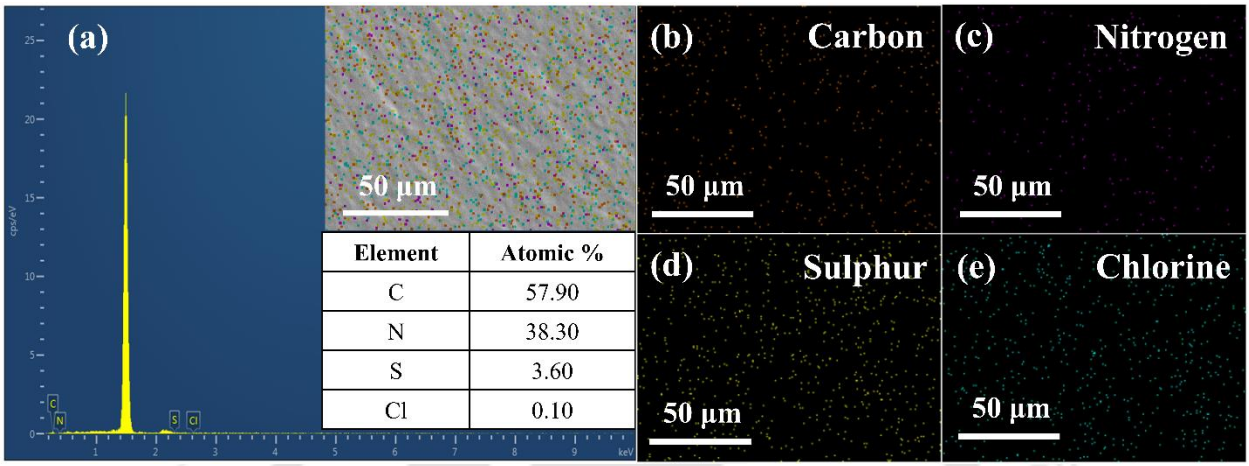

Figure 4.8 Shows the images of the aqueous phase extraction in a continuous manner at a microfluidic platform. **(a)** EDX spectrum of the methylene blue, the inset image depicts the scanning area for EDX analysis. Elemental mapping of C **(b)**, N **(c)**, S **(g),** and Cl **(e)** of a selected area are shown.

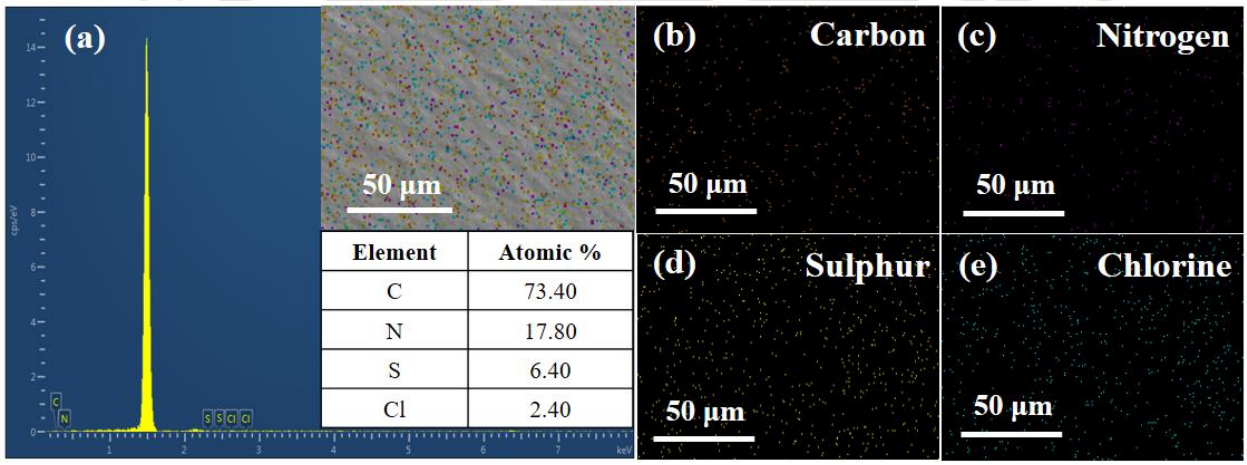

Figure 4.9 Shows the images of the organic phase extraction in a continuous manner at a microfluidic platform. **(a)** EDX spectrum of the methylene blue, the inset image depicts the scanning area for EDX analysis. Elemental mapping of C **(b)**, N **(c)**, S **(g),** and Cl **(e)** of a selected area are shown.

4.4 Conclusions

In this chapter, we have studied the extraction process in a microchannel of equivalent diameter 90 μm and length 60 cm. It is intuitive that surface to volume ratio increases when we do hydrodynamic two-phase flows in microscale systems. The enhanced surface area always speeds up any kind of transport process and the same has been reported long back. However, the flows in such a low dimension channel become very sluggish owing to high frictional forces associated with microscale flows. A few literatures as explained in this article also tried to create local turbulence in microscale flows by various means. The beauty of the present study lies in the fact that we have created a local convection instability at the interface of the two fluids. The key findings of the present study are summarized point wise as,

- An electric field creates instability at the interface of the two-phase system in a microchannel.
- The extraction efficiency of methylene blue in microscale systems was enhanced in the presence of an electric field compared to spontaneous mass transfer.
- It was observed that extraction efficiency was increased with increasing the number of electrodes and vice-versa for the same intensity of the electric field.
- The degree of non-uniformity determines the timescale of the extraction kinetics. We have seen that with higher degree of non-uniformity lower time is required to achieve a predetermined extraction.

References

[1] D.R.W. and G. Hallas, The Chemistry and Application of Dyes, Springer Science & Business Media, **2013**.

[2] P.A. Carneiro, G.A. Umbuzeiro, D.P. Oliveira, M.V.B. Zanoni, Assessment of water contamination caused by a mutagenic textile effluent/dyehouse effluent bearing disperse dyes, *J. Hazard. Mater.* 174 (**2010**) 694–699.

[3] R. Jain, M. Mathur, S. Sikarwar, A. Mittal, Removal of the hazardous dye rhodamine B through photocatalytic and adsorption treatments, *J. Environ. Manage.* 85 (**2007**) 956–964.

[4] A. Ahmad, S.H. Mohd-Setapar, C.S. Chuong, A. Khatoon, W.A. Wani, R. Kumar, M. Rafatullah, Recent advances in new generation dye removal technologies: Novel search for approaches to reprocess wastewater, *RSC Adv.* 5 (**2015**) 30801–30818.

[5] R. Aziam, M. Chiban, E. Eddaoudi, A. Soudani, M. Zerbet, F. Sinan, Factors controlling the adsorption of acid blue 113 dye from aqueous solution by dried C. edulis plant as natural adsorbent, *Arab. J. Geosci.* 9 (**2016**) 1–7.

[6] R.M. Thaokar, V. Kumaran, Electrohydrodynamic instability of the interface between two fluids confined in a channel, *Phys. Fluids.* 17 (**2005**) 1–20.

[7] A. Joshi, M.C. Radhakrishna, N. Rudraiah, Rayleigh-Taylor instability in dielectric fluids, *Phys. Fluids.* 22 (**2010**) 1–10.

[8] R. V. Craster, O.K. Matar, Electrically induced pattern formation in thin leaky dielectric films, *Phys. Fluids.* 17 (**2005**).

[9] S.K. Singh, A. Srinivasan, S. Mitra, P.S. Gooh Pattader, Carbon dots and Methylene blue facilitated photometric quantification of Hemoglobin, *Spectrochim. Acta - Part A Mol. Biomol. Spectrosc.* 271 (**2022**) 120906.

[10] F.R. Dollish, W.G. Fateley, F.F. Bentley, Characteristic Raman frequencies of organic compounds, Wiley, New York, **1974**.

CHAPTER 5

Carbon Dots and Methylene Blue Facilitated Photometric Quantification of Hemoglobin

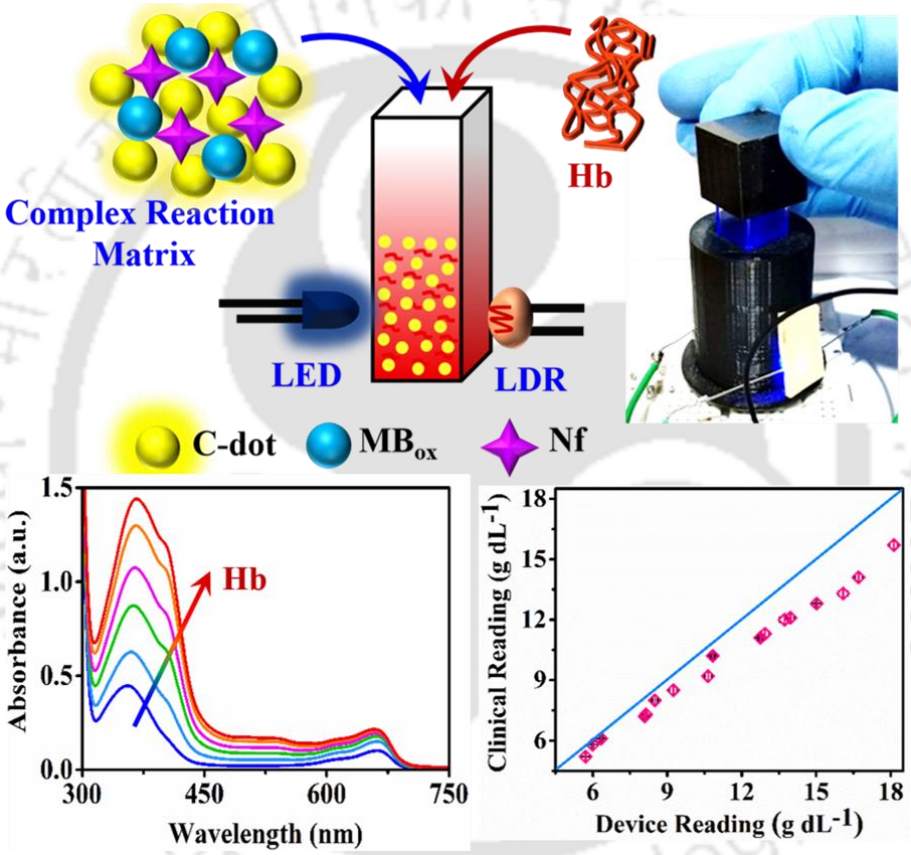

CHAPTER 5

Carbon Dots and Methylene Blue Facilitated Photometric Quantification of Hemoglobin

Early detection and monitoring of Hemoglobin (Hb) is important as this may be related to anemia, leukemia, dengue, etc. To facilitate quantitative detection and monitor the hemoglobin level in the blood, we attempt to develop a low-cost, portable point of care (POC) device based on the spectrophotometric principle. Optical sensitivities of carbon quantum dots (CDs) are found to be highly responsive, while there is a selective reaction between Hb and reduced form of Methylene Blue (MB_{red}). The interaction of Hb, MB_{red}, and CDs is delineated using UV-Visible (UV-Vis) spectroscopy. CDs have a characteristic UV-Vis peak at ~ 347 nm, and it shows a gradual increase of intensity with a slight red shift (~ 355 nm) on the progressive increase in Hb concentration. Simultaneously, the colorless MB_{red} is oxidized to its blue oxidized form MB_{ox} and its characteristic peak starts reappearing at ~ 663 nm. These responses are exploited to quantify Hb concentration with a limit of detection (LOD) as low as ~ 2 g dL^{-1} in a developed POC device, and the results are validated with the clinical data obtained from a local hospital with reasonably good agreement. This photometric detection approach can be adopted for other quantitative biosensors. This work is scientifically acknowledged in ***"Spectrochimica Acta Part A: Molecular and Biomolecular Spectroscopy"****.*

5.1 Introduction

Early diagnosis of diseases has become important in the present day owing to the gradual rise of human health issues. To address these issue, engineers, and scientists across the globe have

developed many point of care (POC) diagnostic kits. For qualitative or quantitative detection of various malfunctioning conditions in a human body, medical science monitors various biomarkers available in different body fluids, such as blood [1], urine [2], sputum [3], sweat [4], tears [5], soft tissues [6], etc. Numerous selective biochemical and chemical reactions, such as lock and key interactions of enzymes [7], antigen-antibody interactions [8], RNA aptamer interactions [9], are exploited to develop optical [10,11], electrochemical [12], resistive [13], and capacitive [14] sensors.

Hemoglobin (Hb) is one among the various other vital components associated with various unhealthy conditions such as anemia [15], leukemia [16], porphyria [17], thalassemia [18], heart diseases [19], and many others [20]. The normal level of Hb in blood lies between 13.0 – 18.0 g dL^{-1} for males and 12.0 – 16.0 g dL^{-1} for females [21]. Hb level below this normal level of Hb concentration causes anemia. Therefore, accurate quantification of Hb in clinical diagnostics is essential to detect the associated diseases at an early stage.

In view of the above discussions, here we report the fabrication of a portable device to quantify Hb. The specific interactions of Methylene Blue (MB) with Hb in the presence of CDs show a unique characteristic optical feature, and the same is exploited for the quantitative estimation of Hb. **Figure 5.1**, schematically shows the main theme of the present work.

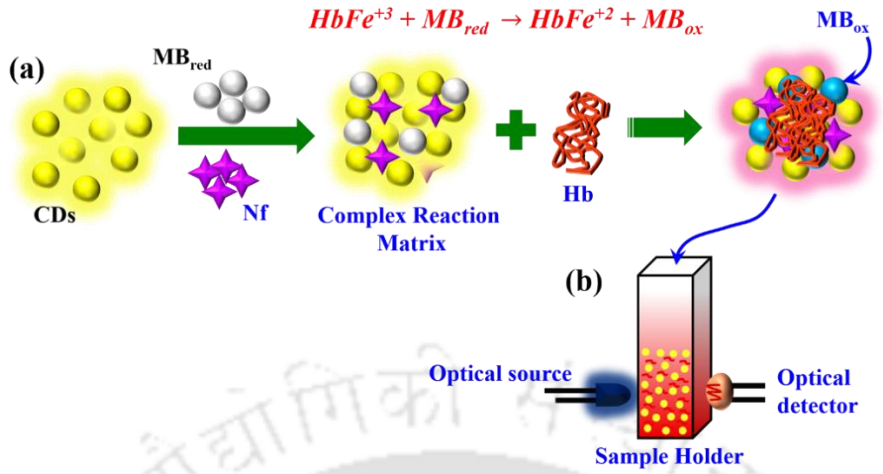

Figure 5.1 (Colour online) **(a)** Schematic representation of the reaction for Hb detection and **(b)** spectrophotometric sensing mechanism.

5.2 Experimental section

5.2.1 Materials

Citric acid (≥ 99%, anhydrous extra pure), L-ascorbic acid (H_2A, ≥ 99.7%, extra pure AR), Ethylenediamine (≥99.5%, GC), Copper sulfate ($CuSO_4$, ≥ 99.5%), Potassium iodide (KI), Iodine (I_2), Nafion (Nf) perfluorinated resin solution, Methylene blue (MB_{ox}), Ethanol (≥ 96%, pure), and Hemoglobin human lyophilized powder (Hb) were procured from Sigma-Aldrich. 1 kb DNA Ladder was purchased from Takara Bio Inc. The human blood plasma and blood samples were obtained from the local Hospital. Whereas, polylactic acid (PLA) filament was obtained from Ultimaker, Netherlands. All chemicals used for the experiments were of analytical grade and used without further purification. All synthesis and spectroscopic measurement solutions were prepared with Milli-Q water (resistivity ~ 18.2 MΩ.cm), purified by a millipore system (France, model: Elixplus Milli-Q). For device fabrication, a digital multimeter (Mastech, M92A(H)), LED, and LDR were used as electronics parts.

5.2.2 Apparatus

Materials were characterized by using Photoluminescent Spectrometer (PL) (Make: Perkin Elmer, LS 45), Time-resolved photoluminescence (TRPL) (Make: LifeSpecII, Edinburgh Instruments), UV-Vis Spectrophotometer (Make: Shimadzu, UV-2600 230 V EN spectrophotometer), PL quantum yield (PLQY) (Make: FM-SPHERE, Horiba), Field Emission Transmission Electron Microscope (FETEM) (Make: JEOL, JEM 2100 at the acceleration voltage of 200 kV), Field Emission Scanning Electron Microscope (FESEM) (Make: Zeiss, Gemini 300 at the acceleration voltage of 30 kV), Fourier Transform Infrared Spectroscopy (FTIR) (Make: PerkinElmer Spectrum Two), and Dynamic light scattering (DLS) (Make: Anton Paar, Litesizer 500). UV-Vis Spectrophotometer (Make: Shimadzu, UV-2600 230 V EN spectrophotometer), Fluorescent property of the CDs was examined by PL. TRPL measurement was carried out using a 375 nm laser excitation source, with an instrument response time of < 50 ps. UV-Vis Spectrophotometer (Make: Shimadzu, UV-2600 230 V EN spectrophotometer). The PLQY of the sample was measured in solution mode using an integrating sphere attached to the fluorimeter. FETEM was used to explore the surface morphology of CDs. FESEM was performed for elemental mapping of materials. The functional groups were examined using FTIR in the wavenumber range of 4000 – 500 cm^{-1}. The zeta potential of samples was evaluated by DLS, equipped with a 658 nm wavelength semiconductor laser diode (40 mW). 3D printer (Make: Ultimaker 3, Netherlands) was used to fabricate the device prototype from polylactic acid (PLA) filament. Teflon-lined stainless-steel autoclave was used for the synthesis of CDs.

5.2.3 Methods

5.2.3.1 Synthesis of Carbon Dots (CDs)

CDs were synthesized following an established hydrothermal technique [22] from non-toxic precursors namely, citric acid, and ethylenediamine. Concisely, 0.42 g of citric acid and 536 µL of ethylenediamine were dissolved in 10 mL milli-Q water. Subsequently, the prepared solution was transferred into a sealed Teflon-lined stainless steel autoclave (50 mL) and heated at 225 °C for 3 hours. After completion of the reaction, the Teflon-lined stainless steel autoclave was cooled to room temperature (25 °C). The resultant solution after the reaction was transparent pale yellow due to the formation of CDs. The prepared CDs solution was purified into two steps. Firstly, the solution was centrifuged at 15000 rpm for 10 min to remove the bigger particles. Then, the supernatant solution was filtered using a microporous syringe filter membrane (pore size: 0.2 µm). The filtrate having CDs was used as a stock solution.

5.2.3.2 Preparation of reduced form of Methylene Blue (MB_{red})

MB is a water-soluble polyaromatic thiazine class of cationic dye molecule, which is stable in its oxidized form 'MB_{ox}' (blue color). It can be easily reduced by a variety of reducing agents [23,24] to its colorless form. In this article, L-ascorbic acid (H_2A), commonly known as vitamin C, was utilized to convert MB_{ox} to MB_{red}. The reaction mechanism of this oxidation-reduction couple conversion is given by Equation 5.1.

$$MB_{ox} + H_2A \rightleftharpoons MB_{red} + D \qquad (5.1)$$

Where D is the dehydroascorbic acid. The stock solutions of MB_{ox} (0.02 mM) and H_2A (0.1 M) were prepared at room temperature, and 300 µL of MB_{ox} solution and 600 µL of H_2A solution

were mixed in a 5 mL glass vial. Subsequently, it was observed that MB changes its color and the mixture became colorless, which confirms the formation of MB_{red}.

5.2.3.3 Preparation of complex reaction matrix with CDs/Nafion/MB_{red}/Hb

The synthesized concentrated CDs stock solution, as mentioned in section 5.2.3.1**,** was diluted five times with milli-Q water to obtain a concentration of 5.5 mg mL^{-1} of CDs. Nafion (Nf) was diluted with ethanol to make 43.7 mg mL^{-1} (0.11 M) solution. The complex reaction matrix was prepared by adding 50 µL of diluted CDs solution, 20 µL of diluted Nf solution, 900 µL of MB_{red} solution (as described in section 5.2.3.2) in 2.5 mL of milli-Q water. Various concentrations of Hb, ranging from 2 g dL^{-1} to 20 g dL^{-1}, were prepared in Milli-Q water, and the electronic interaction of Hb with the complex reaction mixture containing CDs, Nf, MB_{red} was examined. The UV-Vis spectrum of the complex Hb solution was measured in the wavelength range between 200 – 800 nm.

5.2.3.4 Solution preparation of KI_3 and $Fe(NO_3)_3$

Firstly,1.66 g of KI was dissolved in 100 mL of distilled water and then 1.27 g of I_2 was added. This solution was heated at moderate temperature and mixed gently until I_2 is completely dissolved. The KI_3 solution was stored in a dark place and used for further experiment. For $Fe(NO_3)_3$ solution, 241.86 mg of $Fe(NO_3)_3$ was dissolved in 10 mL of distilled water at room temperature and used for further experiment.

5.3 Characterization of CDs

5.3.1 Photoluminescence and UV-Vis Spectrophotometric analysis of CDs

First, to get the optimum excitation wavelength of CDs, the CDs solution was excited at different wavelengths ranging from 300 nm to 400 nm, and corresponding Photoluminescence (PL) emission spectra are shown in **Figure 5.2a**. From this figure, it was found that the maximum PL intensity was obtained at an excitation wavelength of 360 nm. The PL peak emission wavelength was remained almost constant at ~ 444 nm when excited with a wavelength in the range of 300 – 400 nm. The excitation independent emission behavior of CDs result shows that the prepared CDs are having equal particles size with same band gaps [25,26]. Photoluminescence activates the surface states of CDs that are analogous to molecular states, whereas the size effect is a result of quantum dimensions. Both of these contribute to the complexity of the excited states of CDs. In the fluorescence spectra, CDs have maximum emission at ~ 444 nm for an excitation wavelength of 360 nm. A similar observation is also reported by Zhu *et al*. [22]. In order to calculate the lifetime of the excited state of CDs, Time-Resolved Photoluminescence (TRPL) analysis was performed using a 375 nm laser excitation, displayed in **Figure 5.2b**. The observed TRPL decay data were fitted with an exponential decay function represented by, $I(t) = A\exp(-t/\tau)$, Where $I(t)$ is the intensity of the PL at time t and A is the amplitude of the PL decay curve and the time scale of decay signifies the lifetime τ. The average lifetime τ_{avg} of the CDs was found to be 15 ns. Photoluminescence Quantum Yield (PLQY) was measured in solution mode using an integrating sphere attached to the fluorimeter (FM-SPHERE, Horiba with Horiba Jibon Yvon, Fluoromax-4). The following equation was used to estimate the PLQY:

$$\phi = \frac{X_C - X_A}{Y_A - Y_C} \times 100\% \qquad (5.2)$$

Where, X_C denotes integrated luminescence of the CDs due to direct excitation, X_A indicates integrated luminescence from a blank integrating sphere, Y_C is the integrated excitation profile by the sample when it is directly excited by the incident beam, and Y_A is the integrated excitation profile from a blank integrating sphere without the CDs. The integrating sphere was calibrated by measuring the PLQY of the standard samples (Quinine sulfate, Rhodamine 101). PLQY of CDs was measured by adjusting the slit and neutral density filter to get the excitation intensity of ~10^6 counts for the wavelength of 360 nm with a blank integrating sphere. After adjusting the parameters, integrated excitation profile (Y_A) and integrated luminescence (X_A) were recorded from an empty integrating sphere. Then, the sample was placed on the sample holder inside the integrating sphere. Later, the instrument correction file was used to correct the recorded integrated excitation profile (Y_C) and integrated luminescence (X_C) of the sample. Finally, the PLQY of our synthesized CDs sample was estimated to be 86.3%.

The photostability of the CDs was performed using continuous UV light (365 nm) irradiation. The fluorescence intensity of CDs remains more than 80 % after 120 min of illumination, which shows good photostability of CDs. In **Figure 5.2c**, the blue line depicts the emission spectrum of CDs when excited with monochromatic light having a wavelength of 360 nm. Whereas the green line shows the PL excitation spectrum of CDs at its corresponding emission wavelength of ~ 444 nm. The inset of **Figure 5.2c** shows the pale yellowish transparent color of the prepared CDs solution in ambient daylight (left) and bright blue luminescence was observed under UV irradiation lamp (right). The emission maxima that were observed at an excitation wavelength in the UV-Vis domain signifies that the PL property of the CDs was associated with the energy corresponding to the UV-Vis region.

In **Figure 5.2c**, the red line represents the UV-Vis absorption spectra of the synthesized CDs. In general, the UV-Vis optical absorption peak of CDs originates from two kinds of electronic transitions. The first peak of the spectrum is located at ~ 239 nm which represents $\pi-\pi^*$ transition of aromatic C=C and C−C bonds in the sp^2 hybridization of the graphite core, and the second peak of the spectrum is at ~ 347 nm, denoting $n-\pi^*$ transition of C=O, C−N, or C−OH bonds associated with sp^3 hybridized carbon of the carboxyl (−COOH) or amine ($-NH_2$) groups present on CD surface [27,28]. Generally, the presence of all these functional groups instigates excellent water solubility in CDs without any further surface modification. It is reported that the $\pi-\pi^*$ transitions would not produce any remarkable fluorescence signal, whereas, the $n-\pi^*$ transition should have more intense photoluminescence signals [27–29]. Additionally, the high energy tail stretched into the visible region of the absorption spectrum, is the signature of Mie scattering of CDs nanoparticles [30].

5.3.2 FETEM analysis of CDs

The detailed morphology, nanostructure, and size of CDs were studied by using FETEM. The CDs sample for the FETEM study was prepared by dropping the aqueous solution of CDs onto a 400-mesh carbon-coated copper grid (SPI, USA) and dried at room temperature in a vacuum oven. **Figure 5.2d** describes the corresponding FETEM image of the synthesized CDs. The dark regions in the FETEM show the size and shape of the prepared CDs which were found to be spherical with some irregularities. The image also shows the uniform dispersion and distribution of the CDs having an average diameter of 4.2 ± 2 nm without any apparent agglomeration. However, the HRTEM image (**Figure 5.2e)** of CDs shows that most of the particles are quasi-crystalline.

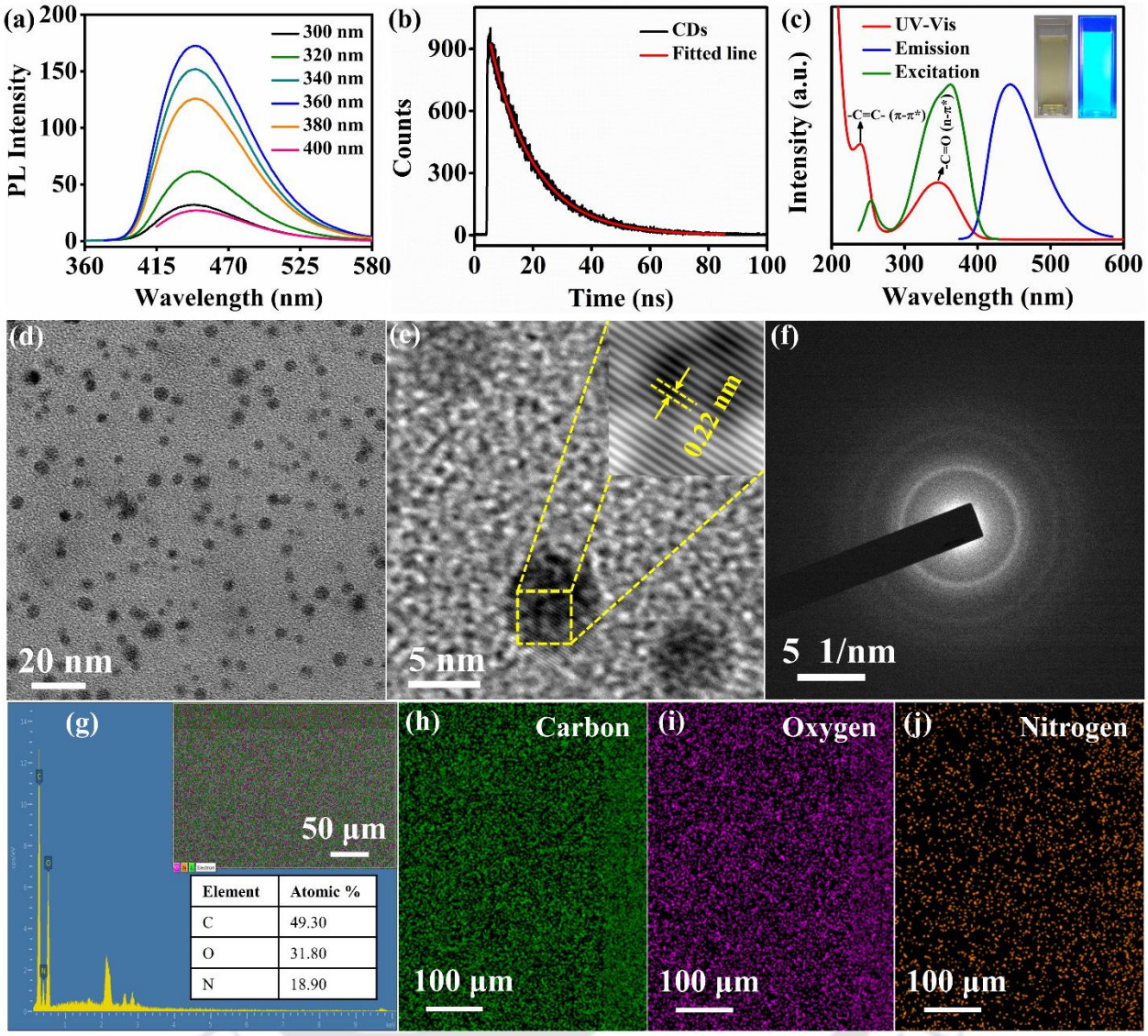

Figure 5.2 (Colour online) Plot **(a)** shows the PL emission spectra of CDs at different monochromatic excitations. Plot **(b)** depicts the TRPL curve of CDs at an excitation wavelength of 375 nm. Plot **(c)** shows the UV-Vis absorption spectrum (red line) of the synthesized CDs. The blue line portrays the PL emission spectrum of the synthesized CDs in an aqueous solution after excitation with light having a wavelength of 360 nm. The green line represents the PL excitation spectrum of the synthesized CDs in an aqueous solution. The inset optical images depict the aqueous solution of CDs under visible light which is in pale yellow (left) and blue when illuminated under a UV lamp (right) **(d)** FETEM image of the synthesized CDs of size ~ 4.2 ± 2 nm indicated by the dark circular spots. **(e)** Magnified image of CDs and in the inset HRTEM image of lattice fringes of the CDs with an equal interplanar spacing of ~ 0.22 nm. **(f)** Selected area electron diffraction (SAED) pattern of synthesized CDs. **(g)** EDX spectrum of the synthesized CDs, the inset image depicts the scanning area for EDX analysis. Elemental mapping of synthesized CDs is depicted in **(h)** C, **(i)** O, and **(j)** N.

Well resolved lattice fringes with an equal interplanar spacing of ~ 0.22 nm are shown in the inset of **Figure 5.2e**. Similar observations were reported earlier for CDs synthesized using citric acid and ethylenediamine [22]. However, the CDs may not be perfectly crystalline due to the intermittent presence of functional groups attached with sp^3 carbons. This is supported by a circular SAED pattern (**Figure 5.2f**), which indicates the amorphous nature of the CDs.

5.3.3 Energy dispersive X-ray (EDX) analysis

The FESEM of the CDs with elemental mapping through EDX analysis reveals the uniform coverage of the elements throughout the CDs. The samples for the FESEM analysis were prepared by drop-casting on aluminium foil and dried at ~ 50 °C temperature in a vacuum oven. **Figure 5.2g** inset describes the corresponding FESEM image of the synthesized CDs. The elemental mapping, shown in **Figure 5.2(h-j)**, illustrates a uniform distribution of C, O, and N atoms throughout the CDs. The atomic percentages from elemental mapping analysis of the CDs were found to be 49.3 %, 31.8 %, and 18.9 % for C, O, and N, respectively. According to EDX mapping data, the elements' relative ratio is constant at all locations. Hence, it concludes that composition is homogeneous throughout the surface. **Figure 5.3** and **Figure 5.4** depict the EDX analysis of complex matrix and complex matrix/Hb hybrid, respectively.

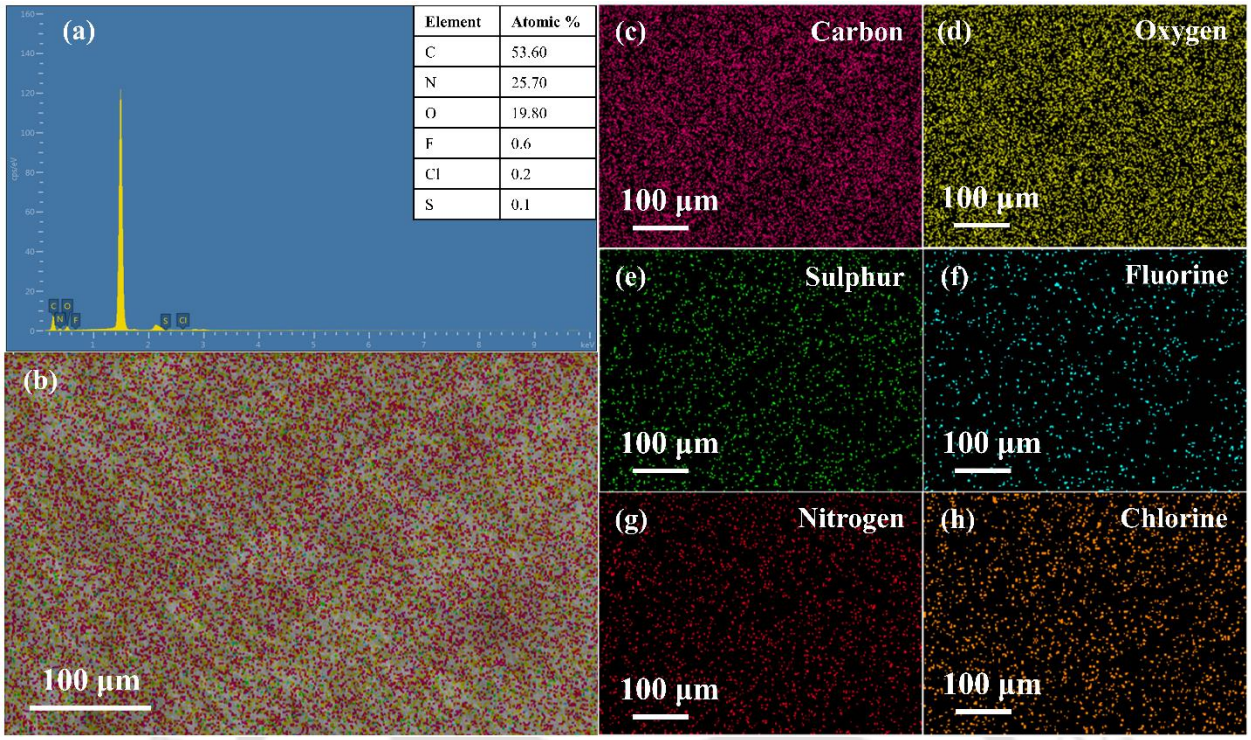

Figure 5.3 (a) EDX spectrum of the complex matrix. **(b)** Scanning area for EDX analysis. Elemental mapping of complex matrix **(c)** C, **(d)** O, **(e)** S, **(f)** F, **(g)** N, **(h)** Cl.

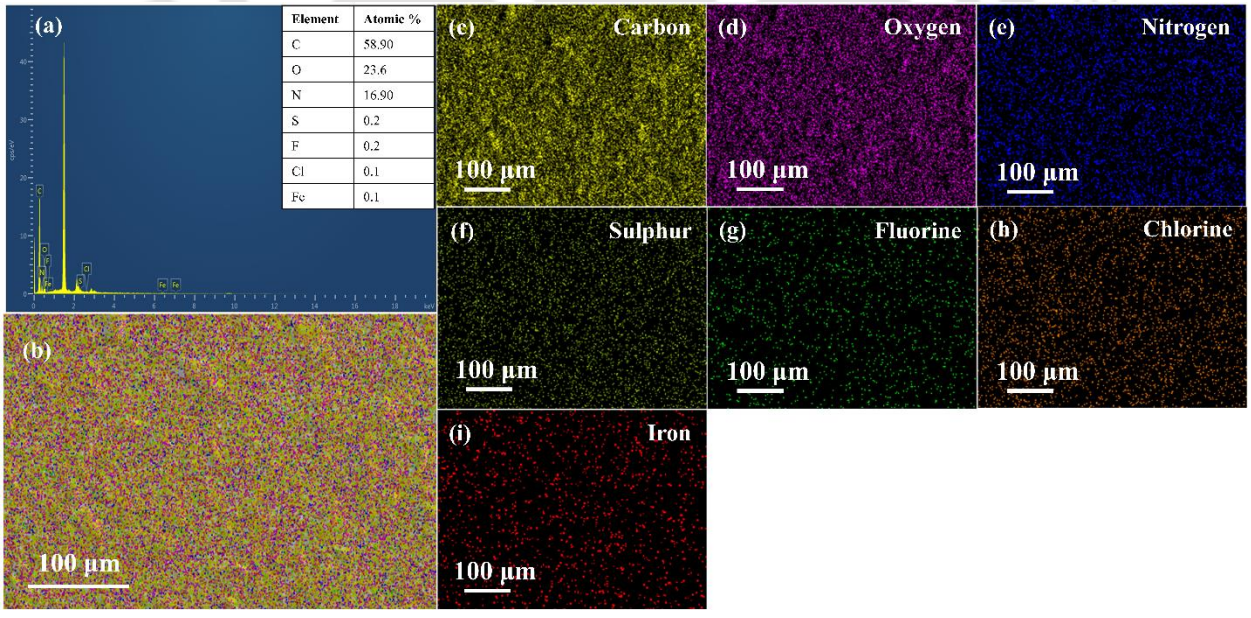

Figure 5.4 (a) EDX spectrum of the complex matrix and Hb hybrid. **(b)** Scanning area for EDX analysis. Elemental mapping of complex matrix and Hb hybrid **(c)** C, **(d)** O, **(e)** N, **(f)** S, **(g)** F, **(h)** Cl, **(i)** Fe.

5.4 Results and discussion

5.4.1 UV-Vis spectroscopic analysis

Figure 5.5a describes the UV-Vis absorbance spectrum of CDs (magenta colored line) that has a peak at ~ 239 nm and ~ 347 nm. Whereas, Nf (dark cyan line) and H_2A (green colored line) do not have any prominent characteristic peaks in the UV-Vis region. However, MB_{ox} (blue colored line) showed its characteristic peak at ~ 664 nm, and later it was noticed that on the addition of very low concentrated (0.1 M) H_2A, the MB_{ox} peak at ~ 664 nm was diminished, which confirms the reaction for the formation of MB_{red} (violet-colored short dash-dotted line) with H_2A. The UV-Vis absorbance peak of pure 0.73 µM of Hb was found at ~ 406 nm (red-colored line)**.** It was noticed that the peak intensity for pure CDs (347 nm) increased significantly with a red shift (355 nm, maroon colored line) (**Figure 5.5a**) after the addition of 4 µL of Hb (2 g dL^{-1}) in the complex reaction matrix and the characteristic peak of pure Hb (406 nm) was diminished. The red shift occurs due to the interaction of Hb molecules with CDs. The results confirmed that MB_{red} accelerated the rate of conversion of $HbFe^{+3}$ to $HbFe^{+2}$ with only minor shifts in the equilibrium of the reaction [31,32]. Simultaneously, due to the cyclic reversible redox reaction of the complex reaction matrix with Hb, the methylene blue peak for the oxidized form started reappearing at ~ 664 nm with a gradual increment of intensity upon the continuous addition of the Hb in the complex reaction matrix, as shown in the inset of **Figure 5.5b**. Conclusively, the complex reaction matrix of CDs could be used to quantify the concentration of the Hb sample from the calibration curve prepared with different known amounts of Hb. To understand the interaction mechanism of different molecules, we further studied the FTIR spectra of all the samples.

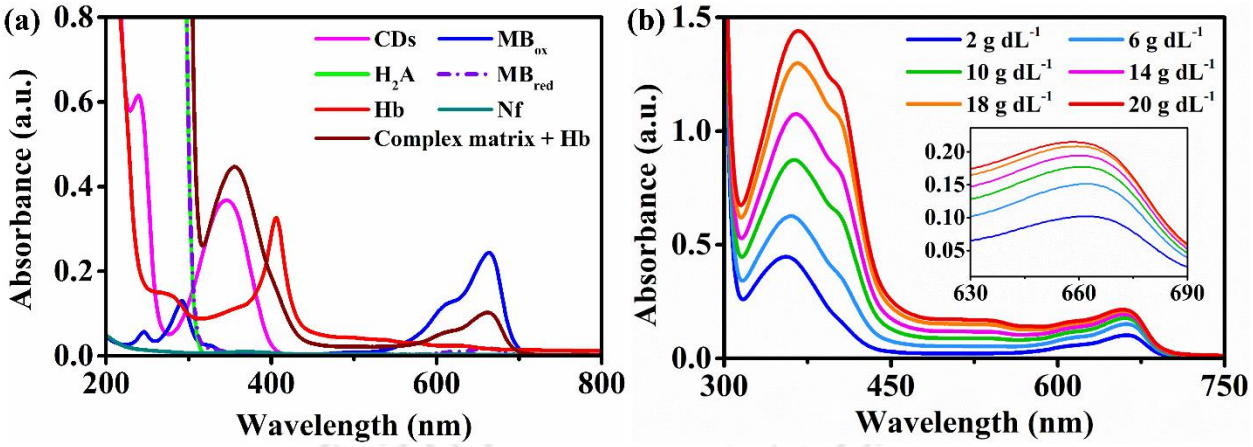

Figure 5.5 (Colour online) **(a)** UV-Vis spectra of CDs (magenta), MB_{ox} (blue), H_2A (green), MB_{red} (violet colored short dash dotted line), Hb (red), Nf (dark cyan), and complex reaction matrix with Hb (maroon). **(b)** UV-Vis spectra of reaction matrix with various concentrations of Hb: 2 g dL^{-1} (blue), 6 g dL^{-1} (custom blue), 10 g dL^{-1} (green), 14 g dL^{-1} (magenta), 18 g dL^{-1} (orange), and 20 g dL^{-1} (red). Inset of (b) shows magnified spectra in the range of 630 – 690 nm.

5.4.2 FT-IR analysis

We performed a detailed FTIR analysis of the complex matrix, its constituent components, and interactions between relevant components. This study is helpful to understand the interaction and changes in terms of bonding during the redox reaction and other electronic interactions that go on in Hb measurement study. FTIR spectrometer in the wavenumber range of 4000 – 500 cm^{-1} was used to characterize all the samples. **Figure 5.6a** shows FTIR spectroscopy data of CDs indicating stretching vibrations of O−H/N−H at 3410 – 3150 cm^{-1}. The medium band at ~ 3015 cm^{-1} suggests the stretching vibrations of C−H. Further, bands at 1645 cm^{-1}, 1570 cm^{-1}, 1390 cm^{-1}, and 1118 cm^{-1} were attributed to C=O, N−H, C−H, and C−NH−C asymmetric stretching [22,33], respectively. For Nf (**Figure 5.6b**), the bands at 1150 cm^{-1} and 1215 cm^{-1} are attributed to the C−F symmetric and asymmetric stretching vibrations, respectively [34]. A band at 1060 cm^{-1} indicates S−O symmetric stretching, and the band at 980 cm^{-1} is indicative of the C−F

stretching (−CF_2−CF(CF_3)−group) [35,36]. Two characteristic amide bands for Hb (**Figure 5.6c**), (1656 cm^{-1}) and (1543 cm^{-1}) show the signatures of the secondary structure of the polypeptide chain [37] that remain unmodified after interactions with Nf (**Figure 5.6g**), CD and Nf (**Figure 5.6h**) or the reaction mixture (**Figure 5.6i**). Highly complex vibrational modes due to the aromatic amine groups in the range of 1271 cm^{-1} to 1365 cm^{-1} are observed for MB_{ox} (**Figure 5.6d**). The majority of the significant vibration bands centered at 3400 – 3500 cm^{-1} (broad), 2926 cm^{-1} and 2855 cm^{-1}, 1600 cm^{-1}, 1395 cm^{-1}, and 1250 cm^{-1} designated to the O−H group, C−H asymmetric stretches of CH_3, C−H symmetric stretches of CH_3, C=N aromatic central rings stretching, multiple ring stretching, N−CH_3 stretch, respectively [38]. **Figure 5.6e** depicts FTIR spectroscopy of MB_{red}. A band at 1117 cm^{-1} corresponds to the C−O−C bend of H_2A [39,40]. The band of C=N aromatic central rings of MB_{ox} stretching group of the host at 1600 cm^{-1} changed to 1630 cm^{-1} for MB_{red}, whereas the band corresponding to N−CH_3 was shifted to 1400 cm^{-1}. These could be attributed to the formation of π-electron interaction. **Figure 5.6f** shows the interaction between CDs and Nf. The characteristic peaks of the composite at 1645 cm^{-1}, 1570 cm^{-1}, 1390 cm^{-1} showed the same band position as that of CDs. Whereas, the bands at 1150 cm^{-1} and 1050 cm^{-1} reflected the presence of Nf without altering the nature of CDs. The interaction between Hb and Nf was also investigated and corresponding FTIR spectra are shown in **Figure 5.6g**. The interaction of HB with both the CDs and Nf is depicted in **Figure 5.6h**. While the characteristic amide bands of Hb (1656 cm^{-1} and 1543 cm^{-1}) remained unaltered, the characteristic band at 1390 cm^{-1} corresponds to C−H, ensures the presence of CDs. FTIR signals of Nf bands were observed with slight shift (1150 – 1158) cm^{-1}, (980 – 985) cm^{-1}, and (1050 – 1070) cm^{-1}, maybe due to the interaction of the hydrophilic and hydrophobic functional groups of Hb with the CDs/Nf system.

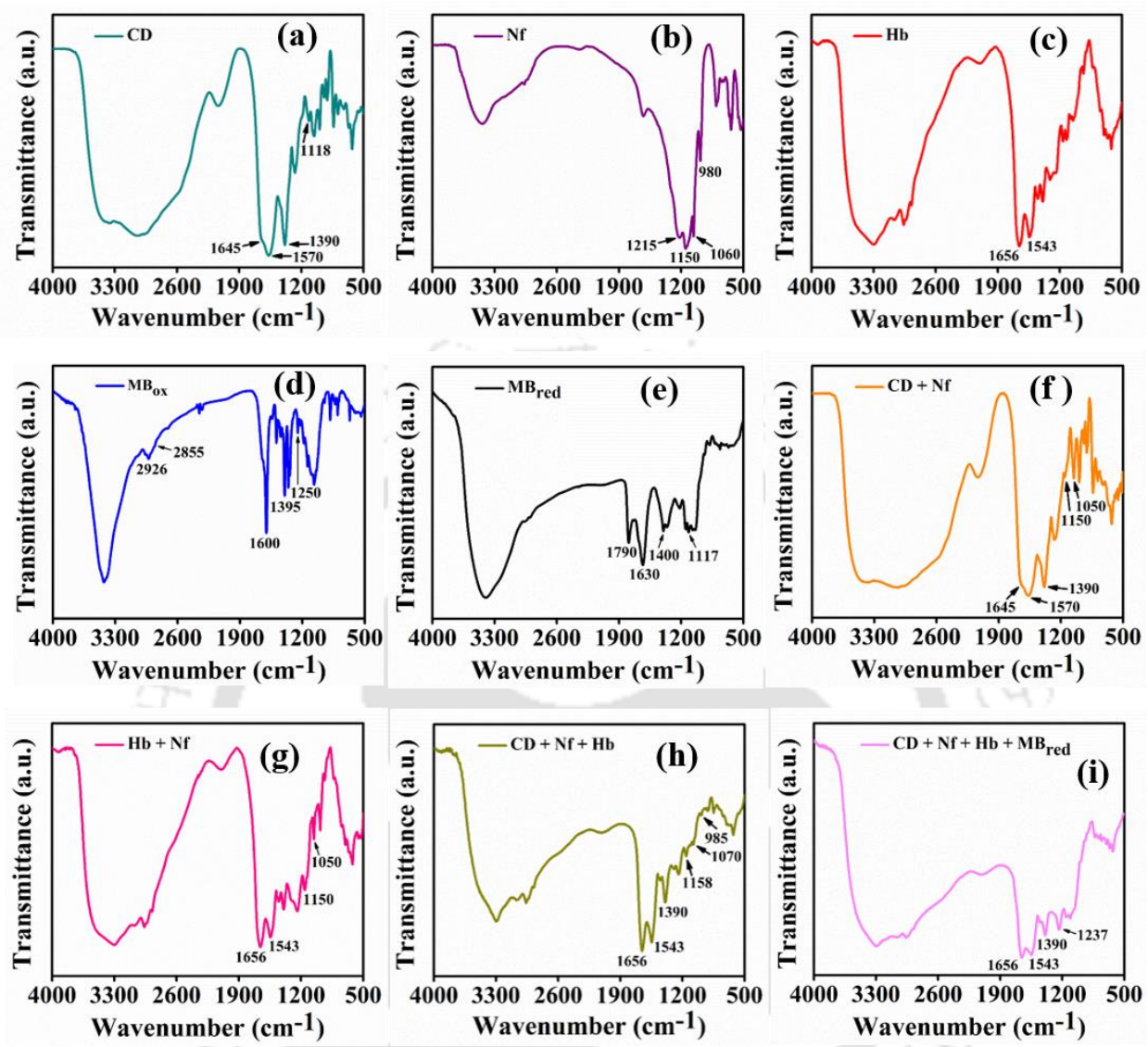

Figure 5.6 (Colour online) Plots **(a)** to **(e)** show FTIR spectra for pure CDs, Nf, Hb, MB_{ox}, MB_{red} samples, respectively. Plot **(f)** depicts FTIR spectra of CDs with Nf. Plot **(g)** represents FTIR spectra of Hb with Nf. Plot **(h)** shows the further change in peak on the addition of Hb to CDs and Nf solution. Plot **(i)** shows the FTIR spectra of the complex matrix solution containing CDs, Nf, Hb, and MB_{red}.

As Nf is extremely stable and has rigid perfluoro polymeric proton containing hydrophobic ($-CF_2-CF_2$) and hydrophilic ($-SO_3H^+$) microchannels [41], it is expected that these channels, along with hydrophobic sites of CDs, can interact with Hb and can stabilize the sandwiched Hb

structure without denaturing it. Therefore, the results reflected that the Hb was completely attached or immobilized on the CDs/Nf complex surface and retained the essential features of its native secondary structures [42,43]. **Figure 5.6i** shows the spectra of the composite mixture. The characteristic bands of CD at 1645 cm^{-1}, 1570 cm^{-1}, and bands of the amides from Hb at 1656 cm^{-1} and 1543 cm^{-1} are almost superimposed on CDs bands. After the addition of MB_{red}, the band at 1237 cm^{-1} reappeared with a small shift (1250 – 1237) cm^{-1} due to the N−CH_3 stretch of MB_{ox}, possibly by π-electron interaction, which confirmed the interaction between Hb and MB_{red}.

5.4.3 Zeta potential measurement

To understand the flocculation behavior and interactions between the entities such as CDs, MB_{red}, Nf, and Hb, zeta potential measurements were carried out at similar experimental concentrations as mentioned in the above section 5.2.3.3. The samples were sonicated for 30 min and zeta potential was measured by taking 500 µL sample solution in a cell. **Figure 5.7a** depicts a schematic representation of electronic interactions at every step and **Figure 5.7b** shows the zeta potential values of the individual components, complex matrix, and the matrix/Hb assembly. It was found that the mean value of zeta potential of CDs was -4.8 mV, which is due to the presence of the electron-donating amine group [44]. For Nf solution, the zeta potential was observed that -0.9 mV, due to the dissociation of sulfonic acid end-groups on side chains which leads to negatively charged molecules in the solution. It was used as a binding agent to attach the Hb on the surface of CD so that Hb gets reduced efficiently. Whereas, the zeta potential of MB_{red} was obtained 6.7 mV, because of the presence of ascorbic acid. The surface charge of the Hb solution was found to be 21.6 mV. It was noticed that the zeta potential of the complex matrix

hybrid solution reduced to -0.5 mV, plausibly due to the flocculation of CDs and MB_{red} in the complex matrix and adsorption of Nf on the surface of CDs/MB_{red} hybrid through electrostatic interaction. The zeta potential of the final solution became 26.3 mV after the addition of 4 µL Hb solution (6 g dL^{-1}) in the complex matrix and progressively increases with the increasing concentration of Hb. This may be due to mostly electrostatic and ionic interactions between Hb protein molecules and complex matrix. Ionic interactions arise from the electrostatic attractions between two groups of opposite charges and by transferring electrons [45,46] between them. It can be deciphered that as the zeta potentials of Hb and complex matrix are positive and negative, respectively, the opposite charges induce the adsorption of Hb on the complex matrix and initiate the ionic interactions by transferring the electrons from the complex matrix to Hb. These results reinforce the proposed reaction mechanism between complex matrix and Hb.

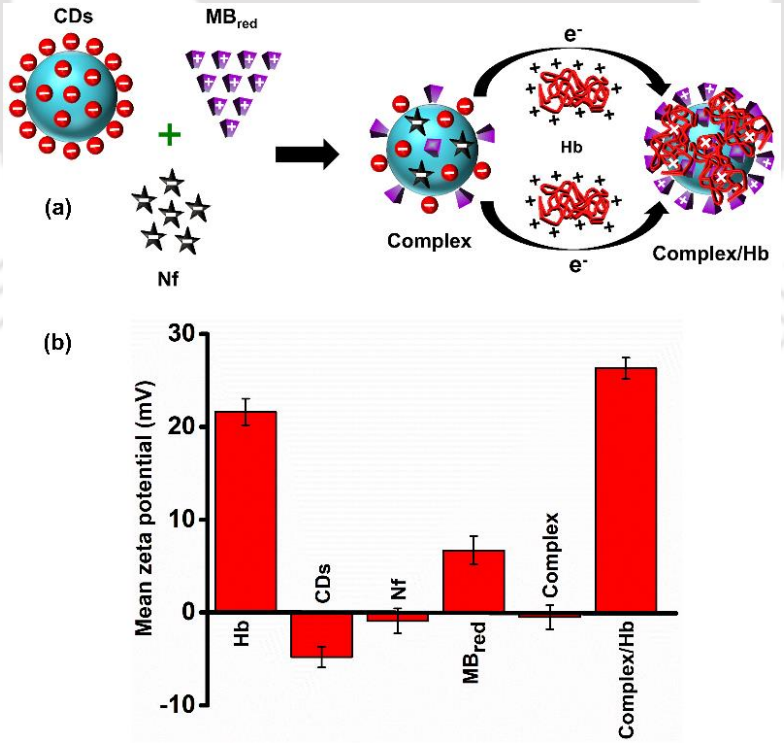

Figure 5.7 (Colour online) **(a)** Schematic representation of the electronic interactions of CDs, Nf, MB_{red}, and Hb molecules. Plot **(b)** shows the zeta potential of Hb, CDs, Nf, MB_{red}, complex, and complex/Hb hybrid solution.

5.4.4 Reaction mechanism of MB_{red} with Hb

Firstly, 900 µL of colorless MB_{red} solution was taken in a quartz cuvette and the mixture was further diluted using 2.5 mL of Milli -Q water. MB_{red} was obtained by mixing the reducing agent H_2A with the blue colored MB_{ox} as described in the experimental section 5.2.3.2. Subsequent addition of Hb solution into this system resulted in a redox reaction, where MB_{red} reduced the ferric form of Hb, ($HbFe^{+3}$), to the ferrous form of Hb, ($HbFe^{+2}$), by transferring an electron and gets itself oxidized to blue $MB_{ox.}$ [47,48]. The associated chemical reactions are shown below:

$$MB_{ox} + H_2A \rightleftharpoons MB_{red} + D$$

$$HbFe^{+3} + MB_{red} \longrightarrow HbFe^{+2} + MB_{ox}$$

In order to quantify Hb, spectrophotometric properties of CDs, MB_{ox}, along with the associated chemical components like H_2A, and Nf, with and without the presence of Hb was studied.

5.4.5 Fabrication of the device

A simple photometer was developed wherein an optical source (a light Emitting Diode), a photo-detector (a light-dependent resistor), a measurement unit (a multimeter), and a sample holding unit (place to put a cuvette) were located. The basic structure of the device was developed using a 3D printer. The LED was placed in the center of one of the side walls of the 3D printed set-up, and an LDR was placed on the opposite side wall, perfectly aligned with the LED in such a way that most of the emitted light from the LED will pass through the solution and reach the LDR. The device was modeled in such a way that the distance between the LED and the LDR remains the same throughout the experiment. The entire experimental setup is shown in **Figure 5.8a**. For the fabrication, initially, the CAD model of the 3D printing specimen was created by using Free

CAD (an open-source software) and saved as an STL file. Consequently, the STL file was transferred to the software of the 3D printing machine Ultimaker Cura (Ultimaker 3D printer software) to slice the file. The process variables of Ultimaker Cura were adjusted and the final instructions were exported as a G Cod file. The G Cod file was then transferred to the 3D printer as a final command to print. The 3D printer molded the device structure as instructed by the G Cod file by extruding the PLA filament and depositing it layer by layer. Subsequently, the 3D printed mold was removed from the 3D printer, and the brim (if any) was detached mechanically from the base of the device. A black color PLA filament was used to fabricate the experimental set-up to ensure zero interference of external light during the experiment.

The 3D printed device prototype thus developed serves as a photometer based on Beer-Lambert's law for the detection of Hb concentration in an unknown solution. The prototype consisted of Light-Emitting Diode (LED), Light Dependent Resistor (LDR), 9 V battery, and a multimeter. LED emitting wavelength near the blue region (450 – 495 nm) was chosen as a light source because the samples of our interests show the maximum absorbance and hence better sensitivity in the aforementioned range of the wavelength. A detailed explanation of the LED selection is given in the next section. LDR was used to detect the transmitted light from the solution that can be obtained as resistance reading using a digital multimeter. Beer-Lambert's law gives the relation between absorbed light, molar concentration, and optical path length of the solution. According to Beer-Lambert's law, absorption depends on the path length and concentration. Therefore, maintaining constant path length is important for comparative absorption study with respect to the concentration. In this setup, we used a cuvette of specific dimensions to maintain a constant path length so that the change in the responses from the device

is only due to the change in Hb concentrations. The rough cost estimation for the device as well as for the unit test is provided below.

Table 5.1: Cost estimation of the fabricated device.

SL. No.	Parts Name	Approx. Cost in Rupees
1	LED	~ 0.60
2	LDR	~ 4.60
3	Cuvette	~ 8.00
4	Multimeter/Arduino	~ 350.00
5	Battery	~ 29.00
6	3D printed model	~ 6.00
		Total = 398.20

The reagent cost per test will be ~ Rs. 1.00

In USD the device cost will be ~ 5.30 USD and per test will cost ~ 0.013 USD.

5.4.6 LED selection/optimization of wavelength

The selection of the LED of a suitable wavelength was proved to be the most important parameter of the device optimization. For this, several tests were performed using various LED light sources that emit lights with wavelengths in red, yellow, green, blue, and also in the white range. The emitted light from LED was transmitted through the complex reaction mixture (as described earlier) having different concentrations of the Hb in it. The transmitted light from the sample was detected by LDR and the LDR gave the response in terms of resistance (**Figure 5.8**). The normalized resistance (NR) was calculated as $NR = \frac{R(C)-R(C_o)}{R(C_o)}$, where $R(C)$ is the resistance at a given concentration C of Hb, and $R(C_o)$ is the resistance of the blank sample (i.e. reading from complex reaction matrix only, without any Hb). From **Figure 5.8c,** it can be inferred that

the device is more sensitive to the blue LED, having wavelength 450 – 490 nm, among all the light sources for the same concentration of Hb in the sample. From the UV-Vis absorbance analysis (**Section 5.4.1, Figure 5.5b)**, it was expected that the device response should be better for UV LED than blue LED. But preliminary experiment with UV LED was giving results with a very high standard deviation. This might be due to the LDR used in this work have lower sensitivity in the UV region as compared to the visible region. Since the aim was to develop an inexpensive Hb quantification device, the cost of the device was minimized as low as possible by using inexpensive (cost-effective) LDRs, LEDs, etc. Hence, expansive LDRs, sensitive to UV, were not used in fabricating the colorimetric photodetector device, and a blue LED, rather than UV-LED was chosen. All the subsequent experiments were performed with the same as well.

5.4.7 Interference study

The fabricated photometer was first utilized to develop a calibration curve for different Hb concentrations so that unknown concentrations of Hb can be quantified. Before developing the calibration curve with the device, the interference study to justify the specificity and selectivity of the detection was performed. The developed device is an optical photodetector, and the working principle is based on the change in resistance of the LDR due to the change in the amount of light transmitted by the sample solution placed in the cuvette. For the interference study, different sets of experiments with nearly similar colored reagents were performed to confirm the resistance change is specific to the Hb.

Here, the interference tests were done using KI_3 and $Fe(NO_3)_3$ solution, which is having nearly the same color as Hb, and it was found that the resistance change was significant only in the case of Hb concentration variation. For other chemicals such as KI_3 and $Fe(NO_3)_3$ the change

was not that significant as shown in **Figure 5.8d.** In this case $R(C)$ in the estimation of the normalized resistance value denotes the resistance obtained from the device for the samples with a concentration of C.

As explained earlier in the UV-Vis spectroscopic analysis, the addition of Hb oxidizes MB_{red} (colorless) to MB_{ox} (blue). The interference of blue-colored compounds was tested using $CuSO_4$ to understand the response of similar colored compounds in the complex reaction matrix. It was seen that blue colored solution did not make a significant change in the resistance value. Furthermore, to prove the selectivity towards Hb and to check if there is any interference from other proteins present in human blood a selectivity study was necessary. Human plasma contains many protein molecules such as albumin, α, β, and γ-globulin, etc., amino acids, along with other inorganic constituents [49]. We collected human blood plasma (from both male and female participants in this study) from the local hospital and different volumes ranging from 2 µL to 30 µL of the plasma was added to the reaction matrix and the response was recorded using the developed device. The normalized resistance found for the blood plasma was below 0.1. This was compared with the very low concentration of Hb solution (4 g dL^{-1}) and for the entire volume range of 2 µL to 30 µL, the device response was found significantly higher for Hb compare to the blood plasma (**Figure 5.8e**). A similar study was performed with 2.5 % (v/v) aqueous solution of 1–10 kilobase pair DNA ladder and the maximum response of normalized resistance was found to be ~ 0.12, which is almost negligible compared to the response from a low concentration of Hb (**Figure 5.8e**). This study ensures the non-interference from other constituents of the blood and proves the specificity of the reaction matrix and the developed device towards the detection of Hb.

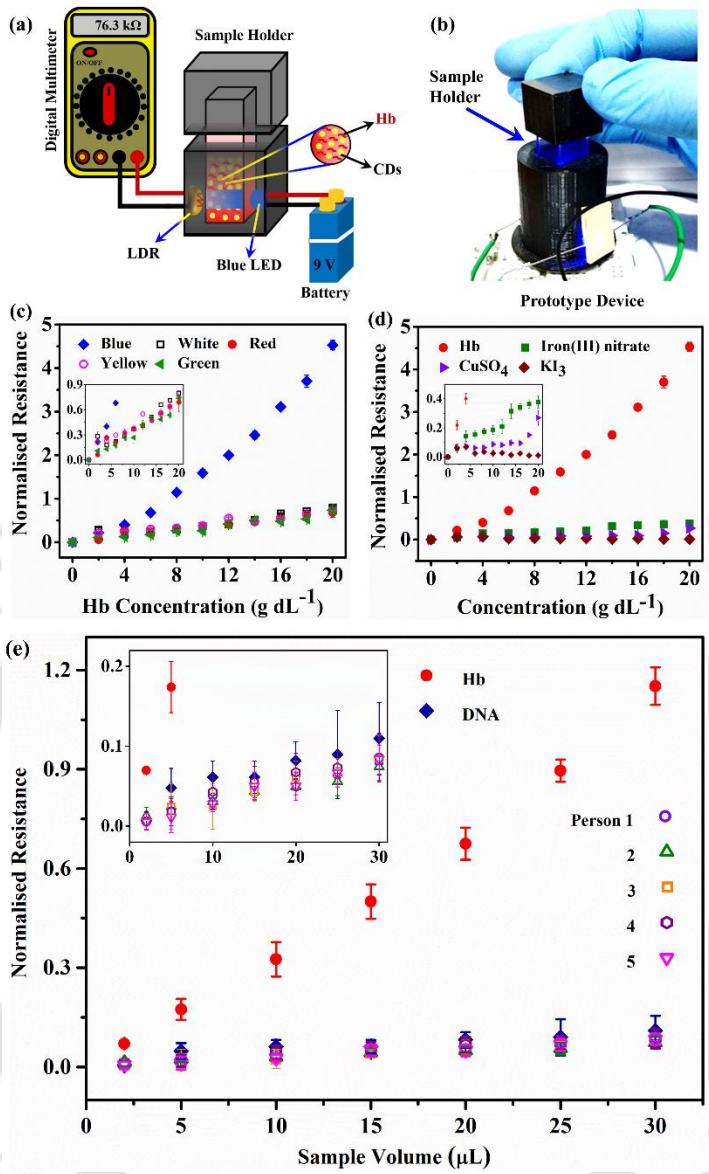

Figure 5.8 (Colour online) **(a)** Schematic of the device setup and **(b)** a developed prototype device for the Hb detection unit. (Colour online) Shows the sensitivity of the fabricated device. Plot **(c)** shows the response of the device for different types of LEDs, blue LED (blue square dots), white LED (black hollow square), red LED (red dots), yellow LED (magenta hollow circle dots), and green LED (green triangle dots). **(d)** shows the response of the Hb (red dots), $Fe(NO_3)_3$ (green square dots), $CuSO_4$ (purple triangles), and KI_3 (maroon square dots) in the complex matrix. **(e)** demonstrates the response of the device for Hb (4 g dL^{-1}) (red filled circle), 1 kb DNA Ladder (filled blue diamond), human blood plasma of person 1 (hollow violet circle), person 2 (hollow green triangle), person 3 (hollow orange square), person 4 (hollow purple hexagonal), and person 5 (hollow magenta inverted triangle) in the complex matrix. The inset of the figures shows the magnified image at the low normalized resistance value (Y-axis).

5.4.8 Quantification of Hb and calibration curve

As discussed, earlier in section 5.4.1, **Figure 5.5b**, with a progressive increment of Hb concentration, UV-Vis peak of CDs at ~ 355 nm (note the red shift of CD peak from 347 nm to 355 nm in presence of Hb) showed a gradual enhancement. On the other hand, with the increase of Hb concentration, MB_{red} (colorless form) converts into MB_{ox} (blue color) and the same showed a progressive increase of the UV-Vis peak intensity of MB_{ox} (blue color) at ~ 664 nm. Change of both the peaks' intensity was considered before preparing the calibration curve for the device. The absorption values at the respective peaks for different concentrations of Hb were normalized by dividing with the corresponding lowest absorbance intensity values. It was found that both the absorbance peaks have sufficient capability to detect the unknown Hb concentration with UV-Vis spectrophotometer (**Figure 5.9**). This spectroscopic analysis is quite sensitive and can be used to detect Hb concentration as low as 1 g dL^{-1} (**Figure 5.9**). Although these calculations were performed using an expensive UV-vis spectrophotometer to justify the capability of detection of the Hb concentration. **Figure 5.9** shows the normalized absorbance peak intensity values of CD (magenta triangle symbols) and that of MB_{ox} (square box symbols with blue) with the change in Hb concentration. The absorption values at the respective peaks were normalized by dividing with the corresponding lowest absorbance intensity values for the **Figure 5.9a**. It was found that both the absorbance peaks have sufficient capability to detect the unknown Hb concentration with a UV-Vis spectrophotometer. For **Figure 5.9b** normalized resistance as a function of the Hb concentration is shown. The normalized resistance (NR) is estimated by as $NR = \frac{R(C)-R(C_o)}{R(C_o)}$, where R(C) is the resistance at a given concentration C of Hb, and R(Co) is the resistance of the blank sample (i.e. reading from complex reaction matrix only, without any Hb).

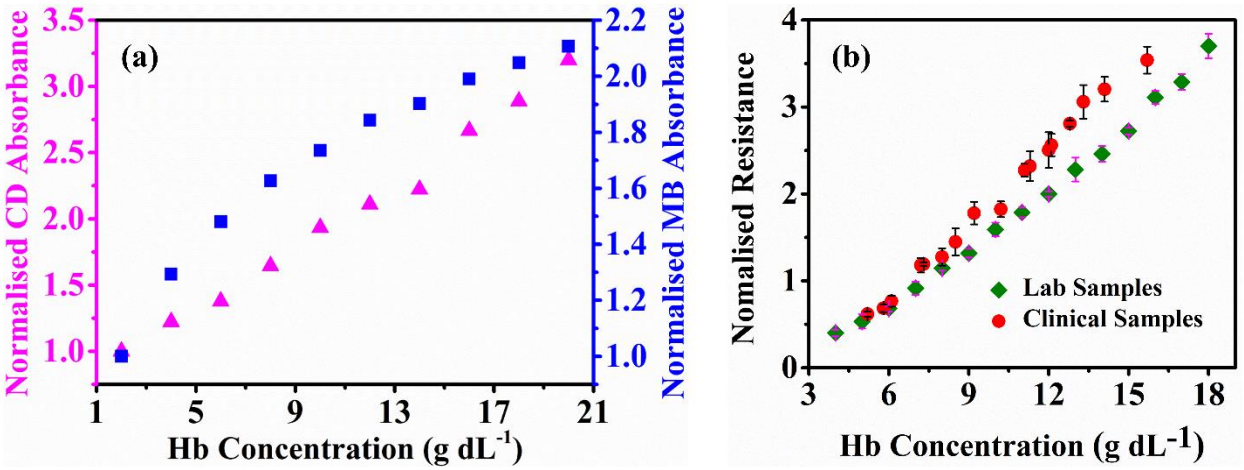

Figure 5.9 Plot **(a)** shows the response of UV-Vis for different concentration of Hb, normalized absorbance values of CDs peak (magenta triangle) and the normalized absorbance values of MB_{ox} (blue square dots). Plot **(b)** shows the response of the optical device of lab samples (green square dots) for a wide range of hemoglobin concentrations (4 g dL^{-1} to 18 g dL^{-1}), and clinical samples (red dots) for different concentration of Hb (5.2 to 15.7 g dL^{-1}).

We aimed to develop a hand-held low-cost device. To address this, experiments were performed with the fabricated 3D printed device for the known concentrations of Hb in milli-Q water ranging from ~ 4 g dL^{-1} to ~ 18 g dL^{-1} to prepare the calibration curve. Reported values of the normal range of Hb in human venous blood is 12–18 g dL^{-1} [21]. 2 mL of the complex reaction matrix solution was taken into a cuvette and 15 µL of Hb solution was added into it. After mixing thoroughly, the intensity of the transmitted light was recorded by LDR. The LDR resistance was measured using a digital multimeter (DMM). **Figure 5.10a** shows the normalized resistance response (the normalized resistance as defined in section 5.4.6) of the complex reaction matrix for a wide concentration range of Hb samples. The change in resistance with the change in the concentration of the Hb was systematically recorded with the help of DMM. It was observed that for a lower concentration of Hb in the solution, LDR recorded lower resistance due to the higher intensity of transmitted light from the samples placed in the cuvette, which was

reflected as lower resistance on the DMM. For the higher concentration of Hb in the solution, LDR showed higher resistance because of the lower intensity of transmitted light from the samples placed in the cuvette, and therefore DMM recorded higher resistance. The calibration curve thus prepared can be used to find the Hb concentration of unknown samples. These data points were fitted with a linear curve having $R^2 \sim 0.99$. The function of this device was verified by human blood samples obtained from a local hospital. The normalized resistance obtained from different human samples from the hospital was checked with our device. The reading obtained from the hospital's conventional method for Hb detection was compared with the results obtained from our device (**Figure 5.10b**).

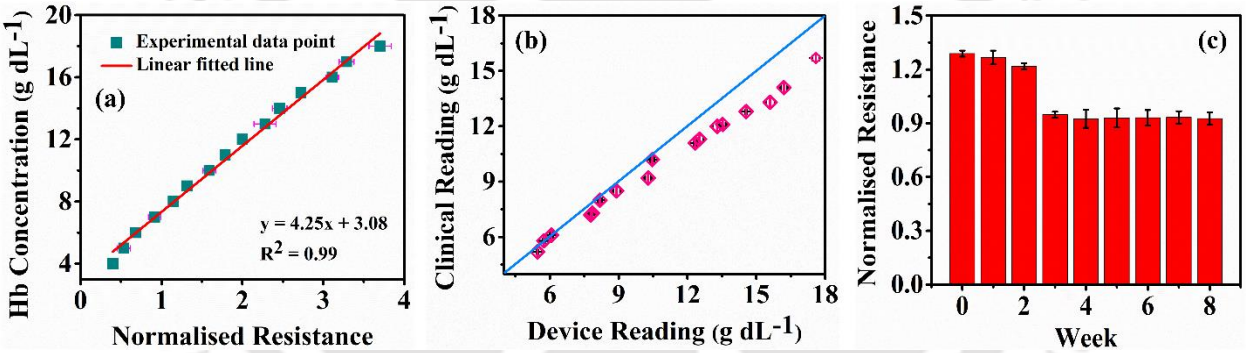

Figure 5.10 (Colour online) **(a)** Calibration curve for the Hb concentration (4 g dL^{-1} to 18 g dL^{-1}) as a function of the normalized resistance. Plot **(b)** shows the comparison of the clinical reading (obtained from a local hospital) of Hb concentration from 17 patients with the readings obtained from the optical device developed in this work using the calibration curve **(a)**. Deviation from the diagonal blue line indicates the deviation between hospital readings and the device reading. **(c)** Depicts the stability of the complex reaction matrix: response of the device for a particular concentration of Hb (9 g dL^{-1}) over the period of 8 weeks.

We tested with 17 human samples and for all the cases, the relative error of detection, when compared with reported values from the hospital, was less than ~ 7% for lower Hb concentrations. For the Hb concentration above 11 g dL^{-1} our device report higher values with more relative errors. Further optimization of the device based on a huge medical trial is expected.

The errors in determining the Hb concentration in clinical human samples may originate from two facts: first, although the interference test (as discussed earlier) showed results in favor of the detection methods adopted here, it is undeniable that there may be some components in human blood which may slightly influence the test results. Secondly, in the case of human blood samples, there is a possibility of systematic human errors at both the measuring ends: at the hospital diagnostic end and the laboratory end using our developed device. This may impart higher relative errors of the obtained results. These limitations can be overcome and the device calibration may be further improved by collecting and testing a large number of human blood samples. Along with this, the knowledge of the health conditions of the patient, applying machine learning techniques to analyze the data, the device can be improved significantly. Obviously, this will open up the pathways for a large volume of data validations and commercial device fabrication.

5.4.9 Quantification of Hb on a microfluidic platform

Figure 5.11 illustrates the design and operation of the paper-based Hb assay. We report a simple and cost effective microfluidic (filter paper) based colorimetric quantification of Hb. Filter paper has inherently designed ~ 1 cm diameter circle to create a constant area for quantification with an image analysis algorithm and prevent potential cross contamination of samples. We performed this paper-based Hb assay by first dispensing 50 µL complex matrix solution onto the filter paper and drying it at a temperature 40 °C. Then we deposited a 20 µL droplet of different concentration of Hb solution on top of the different chemically modified filter paper. This solution spread radially on the paper substrate from the center toward the periphery of the paper due to wicking by capillary action. It was found that, the effect of dilution on the mean color

intensity of the stains produced by Hb on paper is high for higher Hb concentration and vice-versa. Hence, this can be used for proximate quantitative analysis of Hb.

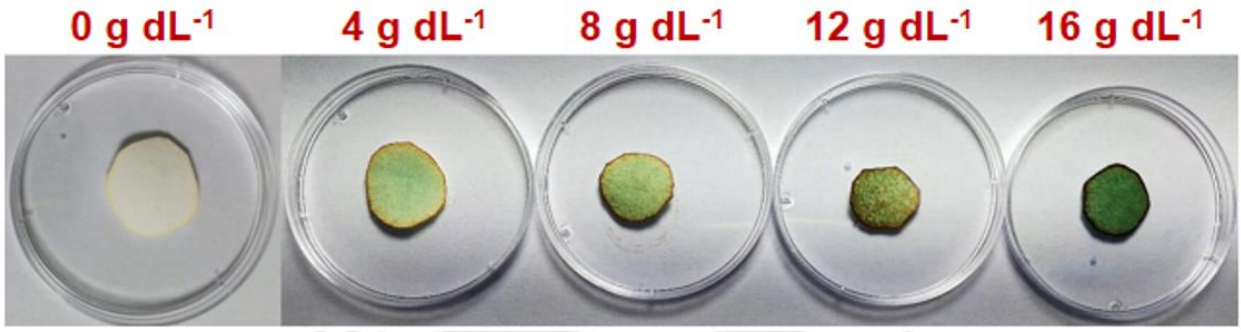

Figure 5.11 shows the Hb quantification on a microfluidic platform.

5.4.10 Storage conditions, stability test, and reproducibility assay

The CDs/Nf/MB_{red} complex reaction matrix was stored in a refrigerator at 5 °C after the preparation of the solution, and the effective resistances were recorded weekly using the optical device for the fixed concentration (9 g dL^{-1}) of Hb solution. The normalized resistance obtained from the device shows that the complex matrix retained the stability of more than 95.0% till the 2nd week, while the result decreased to 74.0 (± 1.71) % after 3rd week and remain so till the end of the 8th week, up to which the stability analysis was performed, **Figure 5.10c**. The considerably excellent shelf-life of the complex matrix in the first two weeks was most likely due to the presence of highly stable CDs in the matrix. This signifies that the chemical modification steps i.e. formation of a complex matrix, do not adversely affect the quantification of Hb. Readings from the device with multiple sets of complex reaction matrices showed the standard deviation < ~ 5% (n=3). This proves the robustness of the matrix formulation. The minor deviation is insignificant and accounts for the slight operational variation during the preparation of CDs, complex matrix, Hb solution, and handling error.

5.4.11 Limit of detection (LOD) calculation of the optical device

Figure 5.12 shows absolute resistance (kΩ) as a function of Hb concentration (g dL^{-1}). In order to calculate the limit of detection (LOD) of the device, a plot of measured absolute resistance (R(C)) values against different concentrations of Hb in a complex matrix, as shown in **Figure 5.12** was prepared. Here R(C) is the resistance at a given concentration (C) of Hb. A blank test was also performed with only the reaction matrix without any Hb. To estimate the LOD, a tangent to the developed R(C) vs C curve at low concentration regime was drawn with equation R(C) = 4.12 C + 19.4 (**Figure 5.12**). The LOD was then estimated using the following equation [50]:

$$LOD = \frac{Mean_{blank} + 1.645(SD_{blank}) + 1.645(SD_{low\ concentration\ sample}) - Intercept}{Slope\ of\ \text{the}\ curve} \quad (5.3)$$

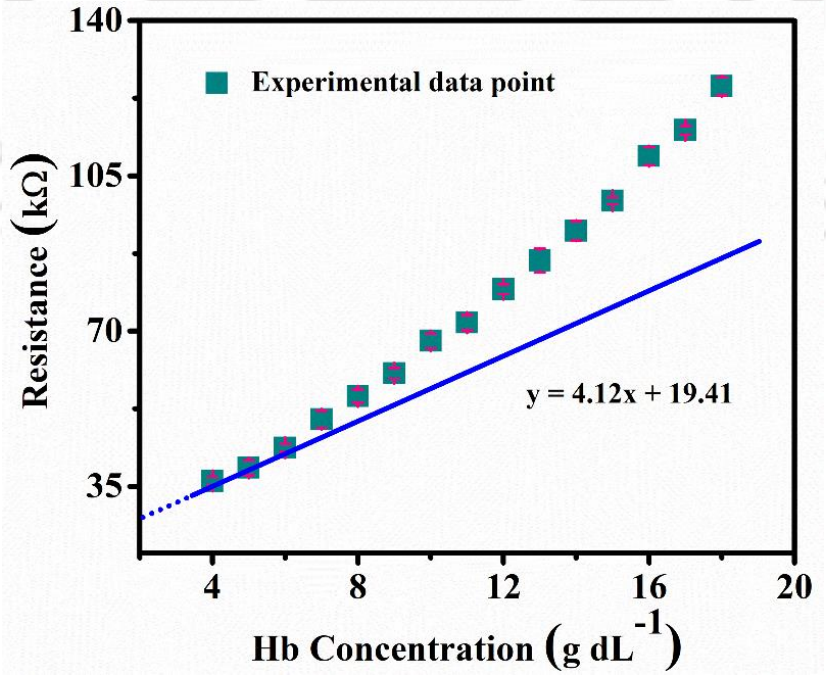

Figure 5.12 Plot shows the response of the optical device of lab samples (dark cyan square dots) for a wide range of hemoglobin concentrations (4 g dL^{-1} to 18 g dL^{-1}).

Where, SD_{blank} is the standard deviation of blank and $SD_{low\ concentration\ sample}$ denotes standard deviation at lower concentration i.e at 4 g dL^{-1}. Using equation 5.3, the calculated value of LOD was found to be ~ 2 g dL^{-1}.

5.4.12 Comparison of methods adopted for the quantification of Hb

The limit of detection (LOD) of the Hb quantification device was estimated to be ~ 2 g dL^{-1} [50]. The LOD, linear range, practical range, and device fabrication of some recently published articles are compared with our work (**Table 5.1**). Among all the reports, only this work probes the practical range of Hb in human blood samples. Although the LOD of our developed device is slightly higher compared to other studies, for all practical purpose of detecting anemia and other Hb concentration related complications, the operating range of the device is well suited. Moreover, as this device doesn't require any expensive materials or complicated probe preparation, unlike other methods, simple and easy quantification of Hb, make this inexpensive device a potential candidate for a frugal point of care device.

Table 5.2: Comparison of detection methods from various published works

Detection method	**Probe**	**LOD**	**Linear range**	**Normal Practical range (7.5 – 11.2 mM) (Yes/No)**	**Device (Yes/ No)**	**Refer-ence**
Fluorimetry	G-quadruplex/hemin complex	2 nM	5 – 200 nM	No	No	[51]
Fluorimetry	G-quadruplex structure aptamer and reduced graphene oxide mixture	50 nM	0.31 – 2.5 µM	No	No	[52]
Fluorimetry	Luminescent terbium complexes	–	0.77 – 62 µM	No	No	[53]

Amperometry	MB/Nf/microcylinder	2 µM	5 – 50 µM	No	No	[54]
Amperometry	Toluidine blue O/microcylinder carbon fiber electrode	–	8.0 – 800 µM	No	No	[55]
Amperometry	Cu-based metal organic frameworks confined in macroporous carbon	3.5 µM	0.01 – 2.4 mM	No	No	[56]
Colorimetry	Curcumin nanoparticle	1.55 nM	15.5 – 620 nM	No	No	[57]
Colorimetry	CDs/MB_{red}/Nf complex matrix	**1.2** mM	**2.4 – 11.2** mM	**Yes**	**Yes**	**This work**

5.5 Conclusions

In the present work, we have developed a prototype hand-held device for the quantitative detection of Hb exploiting optical properties of CDs and its interaction with Hb. The key findings of the work are summarized as follows,

- CDs showed a characteristic peak at ~ 347 nm, which was intensified on the addition of Hb with a slight red shift to ~ 355 nm. Electronic Interaction of CDs with Hb was found to be optically responsive and the same was used for the quantitative analysis.
- An alternative approach for the quantification of Hb was discussed for the same system by exploiting the redox reaction of MB_{ox} to quantify Hb. MB_{ox} (blue colored) was converted to its reduced form (colorless) by using H_2A, and the subsequent addition of Hb made the absorbance peak reappear gradually at ~ 664 nm.
- Utilizing the absorbance of the CDs mixture (corresponding to ~ 355 nm), we developed a portable device, based on a simple colorimetric principle, by integrating a light source (LED)

and a detector (LDR). A calibration curve was prepared using this device to quantify the Hb concentration.

- Interference study with inorganics salts and proteins present in the blood sample was performed and the specificity of the device towards the Hb was demonstrated.
- Using the calibration curve for our developed portable device analysis for real blood samples was demonstrated. A comparison of the device reading with the local hospital data showed close agreement. It was seen that the device could predict the Hb concentration with good accuracy and the maximum error in detection was less than 7% for ~ 80 percent of the tested samples with the values reported by the Hospital.

Concisely, the present technique is based on the green chemistry of low-cost abundant CDs and MB with minimal environmental hazards. The designed portable device is also economic and easy to use without any mandate of clinical expertise, thus suitable for point of care frugal quantification of Hb by common people in developing countries.

References

[1] J.D. Cohen, L. Li, Y. Wang, C. Thoburn, B. Afsari, L. Danilova, C. Douville, A.A. Javed, F. Wong, A. Mattox, R.H. Hruban, C.L. Wolfgang, M.G. Goggins, M.D. Molin, T.L. Wang, R. Roden, A.P. Klein, J. Ptak, L. Dobbyn, J. Schaefer, N. Silliman, M. Popoli, J.T. Vogelstein, J.D. Browne, R.E. Schoen, R.E. Brand, J. Tie, P. Gibbs, H.L. Wong, A.S. Mansfield, J. Jen, S.M. Hanash, M. Falconi, P.J. Allen, S. Zhou, C. Bettegowda, L.A. Diaz, C. Tomasetti, K.W. Kinzler, B. Vogelstein, A.M. Lennon, N. Papadopoulos, Detection and localization of surgically resectable cancers with a multi-analyte blood test, *Science.* 359 (**2018**) 926–930.

[2] L. Van Neste, R.J. Hendriks, S. Dijkstra, G. Trooskens, E.B. Cornel, S.A. Jannink, H. de Jong, D. Hessels, F.P. Smit, W.J.G. Melchers, G.H.J.M. Leyten, T.M. de Reijke, H. Vergunst, P. Kil, B.C. Knipscheer, C.A. Hulsbergen-van de Kaa, P.F.A. Mulders, I.M. van Oort, W. Van Criekinge, J.A. Schalken, Detection of High-grade Prostate Cancer Using a Urinary Molecular Biomarker–Based Risk Score, *Eur. Urol.* 70 (**2016**) 740–748.

[3] A.T. Hastie, F.J. Martinez, J.L. Curtis, C.M. Doerschuk, N.N. Hansel, S.A. Christenson, N. Putcha, V.E. Ortega, X. Li, R.G. Barr, E.E. Carretta, D.J. Couper, C.B. Cooper, E.A. Hoffman, R.E. Kanner, E.C. Kleerup, W.K. O'Neal, R. Paine, S.P. Peters, N.E. Alexis, P.G. Woodruff, M.L.K. Han, D.A. Meyers, E.R. Bleecker, W.H. Anderson, R.C. Boucher, R.P. Bowler, A.P. Comellas, G.J. Criner, R.G. Crystal, M.T. Dransfield, C.M. Freeman, R.J. Kaner, J.A. Krishnan, L.M. LaVange, S.C. Lazarus, J.D. Newell, E.C. Oelsner, S.I. Rennard, D.P. Tashkin, M.B. Scholand, J.M. Wells, R.A. Wise, Association of sputum and blood eosinophil concentrations with clinical measures of COPD severity: an analysis of the SPIROMICS cohort, *Lancet Respir. Med.* 5 (**2017**) 956–967.

[4] F.J. Accurso, F. Van Goor, J. Zha, A.J. Stone, Q. Dong, C.L. Ordonez, S.M. Rowe, J.P. Clancy, M.W. Konstan, H.E. Hoch, S.L. Heltshe, B.W. Ramsey, P.W. Campbell, M.A. Ashlock, Sweat chloride as a biomarker of CFTR activity: Proof of concept and ivacaftor clinical trial data, *J. Cyst. Fibros.* 13 (**2014**) 139–147.

[5] N. von Thun und Hohenstein-Blaul, S. Funke, F.H. Grus, Tears as a source of biomarkers for ocular and systemic diseases, *Exp. Eye Res.* 117 (**2013**) 126–137.

[6] M.C. Hu, M. Shi, J. Zhang, H. Quiñones, C. Griffith, M. Kuro-o, O.W. Moe, Klotho deficiency causes vascular calcification in chronic kidney disease, *J. Am. Soc. Nephrol.* 22 (**2011**) 124–136.

[7] A. Küchler, M. Yoshimoto, S. Luginbühl, F. Mavelli, P. Walde, Enzymatic reactions in confined environments, *Nat. Publ. Gr.* 11 (**2016**) 409–420.

[8] M.H.V. Van Regenmortel, D. Altschuh, J. Chatellier, L. Christensen, N. Rauffer-Bruyère, P. Richalet-Secordel, J. Witz, G. Zeder-Lutz, Measurement of antigen-antibody interactions with biosensors, *J. Mol. Recognit.* 11 (**1998**) 163–167.

[9] Y. Xiao, A.A. Lubin, A.J. Heeger, K.W. Plaxco, Label-free electronic detection of thrombin in blood serum by using an aptamer-based sensor, *Angew. Chemie - Int. Ed.* 44 (**2005**) 5456–5459.

[10] M.S. Steiner, A. Duerkop, O.S. Wolfbeis, Optical methods for sensing glucose, *Chem. Soc. Rev.* 40 (**2011**) 4805–4839.

[11] R. Cush, J.M. Cronin, W.J. Stewart, C.H. Maule, J. Molloy, N.J. Goddard, The resonant mirror: a novel optical biosensor for direct sensing of biomolecular interactions Part I: Principle of operation and associated instrumentation, *Biosens. Bioelectron.* 8 (**1993**) 347–354.

[12] E. Matysiak, M. Donten, A. Kowalczyk, M. Bystrzejewski, I.P. Grudzinski, A.M. Nowicka, A novel type of electrochemical sensor based on ferromagnetic carbon-encapsulated iron nanoparticles for direct determination of hemoglobin in blood samples, *Biosens. Bioelectron.* 64 (**2015**) 554–559.

[13] L.G. Carrascosa, M. Moreno, M. Álvarez, L.M. Lechuga, Nanomechanical biosensors: A new sensing tool, *TrAC - Trends Anal. Chem.* 25 (**2006**) 196–206.

[14] C. Berggren, B. Bjarnason, G. Johansson, Capacitive biosensors, *Electroanalysis.* 13 (**2001**) 173–180.

[15] E. Beutler, J. Waalen, The definition of anemia: What is the lower limit of normal of the blood hemoglobin concentration?, *Blood.* 107 (**2006**) 1747–1750.

[16] S. Wu, C. Zheng, S. Chen, X. Cai, Y. Shi, B. Lin, Y. Chen, Overexpression of long non- coding RNA HOTAIR predicts a poor prognosis in patients with acute myeloid leukemia, *Oncol. Lett.* 10 (**2015**) 2410–2414.

[17] D.M. Bissell, K.E. Anderson, H.L. Bonkovsky, Porphyria, *N. Engl. J. Med.* 377 (**2017**) 862-872.

[18] S. Kradtap, B. Srisawang, P. Kongtawelert, D. Christian, K. Grudpan, Review on screening and analysis techniques for hemoglobin variants and thalassemia, *Talanta.* 65 (**2005**) 1149–1161.

[19] T. Options, Anemia and Chronic Heart Failure, *J. Am. Coll. Cardiol.* 52 (**2008**) 501–511.

[20] M. Chonchol, C. Nielson, Hemoglobin levels and coronary artery disease, *Am. Heart J.* 155 (**2008**) 494–498.

[21] Path, Anemia Detection Methods in Low-Resource Settings: A Manual For Health Workers, Http//Www.Path.Org/Publications/Files/TS_anemia_guide_ Heal. (**1997**).

[22] S. Zhu, Q. Meng, L. Wang, J. Zhang, Y. Song, H. Jin, K. Zhang, H. Sun, H. Wang, B. Yang, Highly photoluminescent carbon dots for multicolor patterning, sensors, and bioimaging, *Angew. Chemie - Int. Ed.* 52 (**2013**) 1–6.

[23] S. Mowry, P.J. Ogren, Kinetics of Methylene Blue Reduction by Ascorbic Acid, *J. Chem. Educ.* 76 (**1999**) 970–974.

[24] T. Snehalatha, K.C. Rajanna, P.K. Saiprakash, Methylene blue-ascorbic acid: An undergraduate experiment in kinetics, *J. Chem. Educ.* 74 (**1997**) 228–233.

[25] H. Ding, J.S. Wei, P. Zhang, Z.Y. Zhou, Q.Y. Gao, H.M. Xiong, Solvent-Controlled Synthesis of Highly Luminescent Carbon Dots with a Wide Color Gamut and Narrowed

Emission Peak Widths, *Small.* 14 (**2018**) 1–10.

[26] M.C. Ortega-Liebana, N.X. Chung, R. Limpens, L. Gomez, J.L. Hueso, J. Santamaria, T. Gregorkiewicz, Uniform luminescent carbon nanodots prepared by rapid pyrolysis of organic precursors confined within nanoporous templating structures, *Carbon N. Y.* 117 (**2017**) 437–446.

[27] Y. Dong, H. Pang, H. Bin Yang, C. Guo, J. Shao, Y. Chi, C.M. Li, T. Yu, Carbon-based dots co-doped with nitrogen and sulfur for high quantum yield and excitation-independent emission, *Angew. Chemie - Int. Ed.* 52 (**2013**) 7800–7804.

[28] M. Zheng, Z. Xie, D. Qu, D. Li, P. Du, X. Jing, Z. Sun, On-off-on fluorescent carbon dot nanosensor for recognition of chromium(VI) and ascorbic acid based on the inner filter effect, *ACS Appl. Mater. Interfaces.* 5 (**2013**) 13242–13247.

[29] L. Li, G. Wu, G. Yang, J. Peng, J. Zhao, J.J. Zhu, Focusing on luminescent graphene quantum dots: Current status and future perspectives, *Nanoscale.* 5 (**2013**) 4015–4039.

[30] S. Qu, X. Wang, Q. Lu, X. Liu, L. Wang, A biocompatible fluorescent ink based on water-soluble luminescent carbon nanodots, *Angew. Chemie - Int. Ed.* 51 (**2012**) 12215–12218.

[31] J. Ye, R.P. Baldwin, Catalytic Reduction of Myoglobin and Hemoglobin at Chemically Modified Electrodes Containing Methylene Blue, *Anal. Chem.* 60 (**1988**) 2263–2268.

[32] R.P. Smith, C.D. Thron, Hemoglobin, methylene blue and oxygen interactions in human red cells., *J. Pharmacol. Exp. Ther.* 183 (**1972**) 549–558.

[33] D.L. Pavia, G.M. Lampman, G.S. Kriz, Introduction to Spectroscopy third edition, *Thomson Learn. Inc.* (**2001**).

[34] M.T. Taghizadeh, M. Vatanparast, Preparation and evaluation of Nafion/SnO2 nanocomposite for improving the chemical durability of proton exchange membranes in fuel cells, *RSC Adv.* 6 (**2016**) 56819–56826.

[35] Z. Liang, W. Chen, J. Liu, S. Wang, Z. Zhou, W. Li, G. Sun, Q. Xin, FT-IR study of the microstructure of Nafion® membrane, *J. Memb. Sci.* 233 (**2004**) 39–44.

[36] V. Di Noto, R. Gliubizzi, E. Negro, G. Pace, Effect of SiO2 on relaxation phenomena and mechanism of ion conductivity of [Nafion/(SiO2)x] composite membranes, *J. Phys. Chem. B.* 110 (**2006**) 24972–24986.

[37] K. Charradi, C. Forano, V. Prevot, D. Madern, A.B.H. Amara, C. Mousty, Characterization of hemoglobin immobilized in MgAl-layered double hydroxides by the coprecipitation method, *Langmuir.* 26 (**2010**) 9997–10004.

[38] Z. Yu, S.S.C. Chuang, Probing methylene blue photocatalytic degradation by adsorbed ethanol with in situ IR, *J. Phys. Chem. C.* 111 (**2007**) 13813–13820.

[39] C. Garnero, M. Longhi, Study of ascorbic acid interaction with hydroxypropyl-β-cyclodextrin and triethanolamine, separately and in combination, *J. Pharm. Biomed. Anal.* 45 (**2007**) 536–545.

[40] K.G.H. Desai, H.J. Park, Encapsulation of vitamin C in tripolyphosphate cross-linked

chitosan microspheres by spray drying, *J. Microencapsul.* 22 (**2005**) 179–192.

[41] A.S. Kumar, P. Swetha, Ru(DMSO)4Cl2 nano-aggregated Nafion membrane modified electrode for simultaneous electrochemical detection of hypoxanthine, xanthine and uric acid, *J. Electroanal. Chem.* 642 (**2010**) 135–142.

[42] S. George, H.K. Lee, Direct electrochemistry and electrocatalysis of hemoglobin in nafion/carbon nanochip film on glassy carbon electrode, *J. Phys. Chem. B.* 113 (**2009**) 15445–15454.

[43] A. Senthil Kumar, P. Gayathri, P. Barathi, R. Vijayaraghavan, Improved electric wiring of hemoglobin with impure-multiwalled carbon nanotube/nafion modified glassy carbon electrode and its highly selective hydrogen peroxide biosensing, *J. Phys. Chem. C.* 116 (**2012**) 23692–23703.

[44] R. Sinha, N. Roy, R. Rajasekhar, A. Karnawat, T.K. Mandal, N-doped carbon dot from cigarette-tobacco: Picric acid sensing in real water sample and synthesis of CD-MWCNT nano-composite for UV-photodetection, *J. Environ. Chem. Eng.* 9 (**2021**) 104971.

[45] N. V. Bhagavan, C.-E. Ha, Essentials of Medical Biochemistry, Second Edi, *Elsevier,* **2011**.

[46] T.R. Shah, A. Misra, in: Challenges in delivery of therapeutic genomics and Proteomics, Elsevier, (**2011**) 387–427.

[47] E.M. McDonagh, J.M. Bautista, I. Youngster, R.B. Altman, T.E. Klein, PharmGKB summary: Methylene blue pathway, Pharmacogenet. *Genomics.* 23 (**2013**) 498–508.

[48] S. Pakapongpan, R. Palangsuntikul, W. Surareungchai, Electrochemical sensors for hemoglobin and myoglobin detection based on methylene blue-multiwalled carbon nanotubes nanohybrid-modified glassy carbon electrode, *Electrochim. Acta.* 56 (**2011**) 6831–6836.

[49] H.A. KREBS, Chemical composition of blood plasma and serum., *Annu. Rev. Biochem.* 19 (**1950**) 409–430.

[50] D.A. Armbruster, T. Pry, Limit of blank, limit of detection and limit of quantitation., *Clin. Biochem. Rev. 29 (Suppl)* 1 (**2008**) S49-52.

[51] S. Pang, S. Liu, X. Su, A novel fluorescence assay for the detection of hemoglobin based on the G-quadruplex/hemin complex, *Talanta.* 118 (**2014**) 118–122.

[52] Y. Shi, W.T. Huang, H.Q. Luo, N.B. Li, A label-free DNA reduced graphene oxide-based fluorescent sensor for highly sensitive and selective detection of hemin, *Chem. Commun.* 47 (**2011**) 4676–4678.

[53] F. Morgner, Detecting free hemoglobin in blood plasma and serum with luminescent terbium complexes †, *Phys. Chem. Chem. Phys.* 17 (**2015**) 1740–1745.

[54] H.Y. Chen, H.X. Ju, Y.G. Xun, Methylene Blue/Perfluorosulfonated Ionomer Modified Microcylinder Carbon Fiber Electrode and Its Application for the Determination of Hemoglobin, *Anal. Chem.* 66 (**1994**) 4538–4542.

[55] H. Ju, L. Dong, H. Chen, Electrochemical behaviour of toluidine blue O covalently modified microcylinder carbon fiber electrode and amperometric determination of hemoglobin in whole blood, *Anal. Lett.* 29 (**1996**) 587–599.

[56] Y. Zhang, A. Nsabimana, L. Zhu, X. Bo, C. Han, M. Li, L. Guo, Metal organic frameworks/macroporous carbon composites with enhanced stability properties and good electrocatalytic ability for ascorbic acid and hemoglobin, *Talanta.* 129 (**2014**) 55–62.

[57] N. Pourreza, H. Golmohammadi, Hemoglobin detection using curcumin nanoparticles as a colorimetric chemosensor, *RSC Adv.* 5 (**2015**) 1712–1717.

CHAPTER 6

Overall Conclusions and Recommendations for Future Work

CHAPTER 6

Overall Conclusions and Recommendations for Future Work

This chapter draws appropriate conclusions based on the investigations carried out in the present study. This chapter also provides some useful recommendations for future research in the relevant field.

6.1 Major Conclusions

The present thesis unravels some of the salient features of the microfluidic reactor & crystallizer, separation of surfactants, extraction of dye, and quantification of Hemoglobin in the human blood samples. The major findings from these studies are narrated chapter wise as follows:

- The second chapter shows the resolution of enantiomers in a continually in a microfluidic platform where S-(-)-α-phenylethylamine was separated from its racemic mixture using L-(+)-tartaric acid as a resolving agent via diastereomeric salt formation. The synthesized diastereomeric crystals thus obtained were as pure or better than the crystals obtained from the batch process. Assuming the identical purity of the salt crystal, the recovered S-(-)-α-phenylethylamine obtained from such salt crystals was ~ 89%. The optimum resolution conditions were determined such as reactor temperature, feed concentration, feed flow rate, etc. and a crystal shape map was developed using concentration and the flow rate as process parameters. The total time required for the formation of highly pure diastereomeric crystal is at most 130 min which is 33 fold less compared to the batch process (~ 4320 min). Moreover, one can control the purity (needle-like or prism-like) by controlling the

appropriate flow rate and concentration of the feed. It follows a facile one-step workflow that is fully adaptable for industrial application with VLSI to achieve high throughput production.

- In the third chapter, we demonstrated a sustainable separation process for the removal of surfactants from wastewater. The goal is to improve the existing physical and chemical processes for industrial wastewater treatment (e.g., chemical precipitation, synthetic organic resins, adsorption on active coal, etc.). A localized non-invasive DC electric voltage integrated microchannel can facilitate the separation of charged molecules in and around the flow stream. Due to strong electrostatic interactions between the oppositely charged head groups of the cationic and anionic surfactants, the variations in the intensity of the DC voltage can further improve the separation ability. At higher voltage, an electrolysis phenomenon occurred and microbubbles were also observed in the microchannel. Higher retention time shows a higher degree of separation of the surfactants. Moreover, separation efficiency was good for the solution concentration at or below the critical micelle concentration (CMC) level.
- The fourth chapter explores the pathways to enhance the extraction efficiency of methylene blue dye from the aqueous phase to the organic phase in a microchannel under the influence of an external electric field. It is intuitive that the surface-to-volume ratio increases as we do hydrodynamic two-phase flows in a microscale system which speeds up any kind of transport process. An electric field creates instability at the interface of the two-phase system in a microchannel which enhances the extraction efficiency of methylene blue in microscale systems. It was observed that extraction efficiency was increased by increasing the number of electrodes and vice-versa for the same electric field intensity. A high degree of non-uniformity lowers the timescale required to achieve predetermined extraction kinetics.

- In the fifth chapter, we report the development of a hand-held device for the quantitative detection of Hb exploiting the optical properties of CDs and its interaction with Hb. CDs showed a characteristic peak at ~ 347 nm, which was intensified on the addition of Hb with a slight red shift to ~ 355 nm. Electronic Interaction of CDs with Hb was found to be optically responsive and the same was used for the quantitative analysis. Utilizing the absorbance of the CDs mixture, we developed a portable device, based on a simple colorimetric principle, by integrating a light source (LED) and a detector (LDR). A calibration curve was prepared using this device to quantify the Hb concentration. Using this calibration curve analysis on real blood samples was done and cpmpared with the local hospital data which showed close agreement. It was seen that the device could predict the Hb concentration with good accuracy and the maximum error in detection was less than 7% for ~ 80 percent of the tested samples with the values reported by the Hospital.

6.2 Recommendations for Future Research Work

The research presented in this thesis reveals various characteristics of research projects that could be further investigated in the future. The following are the future research scopes:

- Enzymatic resolution of enantiomers on a microfluidic platform using fungus (*Beauveria bassiana MTCC 984*) can be studied.
- Simultaneous separation of cationic, anionic, and non-ionic charged molecules can be investigated in a microchannel using the external electric field.
- The separation of cationic and anionic dye in a microchannel under the influence of an external electric field can be studied.

- An electrochemical sensor can be developed for the quantification of Hemoglobin in human blood using the same complex matrix materials with optimized parameters.

Research Output

Journal Publications

1. **Singh, S.K.**, Gogoi, P., Deb, A., Gooh Pattader, P.S., "Chiral Resolution of Racemic Amines in μ-Reactor-Crystallizer", *Chemical Engineering Science,* 256 (2022) 117686.

2. **Singh, S.K.**, Srinivasan, A., Mitra, S., Gooh Pattader, P.S., "Carbon Dots and Methylene Blue Facilitated Photometric Quantification of Hemoglobin", *Spectrochimica Acta Part A: Molecular and Biomolecular Spectroscopy,* 271 (2022) 120906.

3. **Singh, S.K.**, Deb, A., Murmu, K, Gogoi, P., Gooh Pattader, P.S., Separation of Anionic and Cationic Surfactant in a Microchannel Using Ultra-Low Electric Field. (Manuscript under preparation).

4. **Singh, S.K.**, Murmu, K, Gogoi, P., Deb, A., Banerjee, T., Gooh Pattader, P.S., Liquid-Liquid Efficient Micro Extraction of Dye in a Microfluidic Platform by creating Electric Field Induced Instability at the Interface of fluids. (Manuscript under preparation).

Conferences

1 **Singh, S.K.**, Gooh Pattader, P.S., Resolution of Enantiomers on a Microfluidic Platform, Research Conclave, IIT Guwahati, March 8-11, 2018 (**Poster**).

2 **Singh, S.K.**, Gooh Pattader, P.S., Resolution of Tartaric Acid by Excess Enantiomeric Method, Research Conclave, IIT Guwahati, March 14-17, 2019 (**Poster**).

3 **Singh, S.K.**, Gooh Pattader, P.S., Separation of Enantiomers by Preferential Crystallization Method, Advances in Chemical Engineering, Assam Engineering College, Guwahati, August 30, 2019 (**Oral**).

4 **Singh, S.K.**, Srinivasan, A., Mitra, S., Gooh Pattader, P.S., Hemoglobin Quantification Using Carbon Dots, Recent Trends in Chemical and Allied Industries Technology, Economics and Related Issues, University of Calcutta, Kolkata, September 13, 2019 (**Oral**).

5 **Singh, S.K.**, Srinivasan, A., Mitra, S., Gooh Pattader, P.S., Portable Digital Device for Colorimetric Quantification of Hemoglobin Using Carbon Dots and Methylene Blue Dye, International Conference on Advances in Chemical Engineering, UPES Dehradun, February 5–7, 2020 (**Oral**).

Awards and Achievements

1. **Best oral presentation** (**1st position**), International Conference on Advances in Chemical Engineering, UPES Dehradun, February 5–7, 2020 (**Oral**).